Alternative Concepts for Electron Acceptor and Transparent Conducting Electrode in Organic Photovoltaics

DISSERTATION

zur Erlangung des akademischen Grades
eines Doktors der Naturwissenschaften (Dr. rer. nat.)
im Promotionsprogramm
Photophysik synthetischer und multichromophorer Systeme
der Bayreuther Graduiertenschule für Mathematik und Naturwissenschaft

vorgelegt von
Christoph Rainer Hunger

geboren in Pößneck / Deutschland

Bayreuth, 2015

Die vorliegende Arbeit wurde in der Zeit von März 2011 bis September 2015 in der Arbeitsgruppe Angewandte Funktionspolymere am Lehrstuhl für Makromolekulare Chemie I der Universität Bayreuth unter der Betreuung von Herrn Prof. Dr. Mukundan Thelakkat angefertigt.

Vollständiger Abdruck der von der Bayreuther Graduiertenschule für Mathematik und Naturwissenschaften (BayNAT) der Universität Bayreuth genehmigten Dissertation zur Erlangung des akademischen Grades eines Doktors der Naturwissenschaften (Dr. rer. nat.).

Dissertation eingereicht am:	01.10.2015
Wissenschaftliches Kolloquium:	11.02.2016
Amtierender Direktor der Graduiertenschule:	Prof. Dr. Stephan Kümmel

Prüfungsausschuss:

Prof. Dr. Mukundan Thelakkat	(Erstgutachter)
Prof. Dr. Markus Retsch	(Zweitgutachter)
Prof. Dr. Anna Köhler	(Vorsitz)

Table of Content

1 Summary

Organic photovoltaics (OPV) has been established as a potential regenerative energy conversion method over the last years. In contrast to the omnipresent – often silicon based – inorganic photovoltaics, OPV consists of carbon based molecules or polymers. Likewise, these are able to absorb light followed by charge carrier generation. The advantages of OPV arise directly from its material properties: For instance, they exhibit absorption coefficients several orders of magnitudes higher than that of silicon. Consequently, the photoactive layer can be fabricated much thinner and even on flexible substrates. They are also suitable for stretchable and bendable applications. The fabrication is often carried out from solution and is suitable for many large area coating methods. However, OPV commercialization is still at the beginning, which is due to the moderate power conversion efficiency and the low lifetime. In addition, some of the materials are highly energy demanding in production and hence expensive. For instance, the fullerene based phenyl-C_{61}-butyric acid methyl ester (PCBM) – a widely used efficient electron acceptor in the photoactive layer and indium tin oxide (ITO), which serves as a transparent conducting electrode (TCE) are both together responsible for more than 60% of the energy requirement of the overall solar cell. The search for alternative materials is therefore crucial for the competitiveness of OPV.

The dissertation contributes to that aspect and deals with alternative material concepts to replace both, PCBM and ITO. The thesis consists therefore of two parts: In the first one, two perylene bisimides (PBIs) as potential electron acceptors are investigated in the blend with three different donor polymers. The focus lies on the morphology formation between the two components and the charge carrier recombination dynamics as well as their photovoltaic performance in order to understand the potential of PBIs. In the second part of this thesis, a novel transparent metal network electrode was developed, characterized and successfully integrated into OPV. This electrode is highly transparent and exhibits good electrical conductance. In contrast to ITO, the metal network electrode is not only suitable for front, but also for back electrode and hence enables the fabrication of ITO-free semitransparent solar cells. In the following the major findings on these two topics are summarized.

PBI is a potential electron acceptor, since it fulfills basic requirements such as suitable energy levels and high electron mobility. It also exhibits excellent light absorption, whereas the synthesis and purification is easier compared to PCBM and it is also suitable for large scale production. Moreover, it is easy to chemically modify PBIs, which enables precise tuning of energetic and photophysical properties. The solubility of the usually poorly soluble PBI core can be enhanced via solubilizing substituents, whereas they influence also the miscibility between PBI and the donor polymer. The aim of this thesis is to examine the correlation between solubilizing substituents and miscibility with donor polymers. Therefore, two PBIs were selected either with nonpolar alkyl or polar oligoethylene glycole (OEG) substituent and were investigated in blend systems with three different donor polymers. The corresponding solar cells showed differences in current density – voltage (*J*-*V*) characteristics depending on the chain used in PBI. The investigation of the morphology was carried out using atomic force microscopy (AFM). A higher degree of intermixing between donor and acceptor was found when both components carry alkyl chains, whereas a higher degree of phase separation was found for the donor polymer having alkyl side chains and the PBI having an OEG chain. However, this finding could not be correlated with the obtained *J*-*V* characteristics. This discrepancy was fully resolved by using transient absorption spectroscopy (TAS). Via TAS it is possible to determine the remaining density of charge carriers on nanosecond to microsecond time scale after photoexcitation as well as their recombination dynamics. In the course of this thesis, a sensitive TAS-setup covering the time range from several nanoseconds up to milliseconds was installed. Prior to the TAS experiments, methods to measure the radical cation and anion spectra of the donor and acceptor via spectroelectrochemistry and chemical oxidation were worked out. These radical ion spectra were then used to analyze the TAS spectra. Finally, combining TAS and AFM, it was shown that the alkyl/OEG interaction usually leads to higher phase separation and a higher charge carrier density inside the blend. Here the charge carriers are long-lived compared to blend systems having a high degree of intermixing due to the favorable alkyl/alkyl interaction. However, when the degree of phase separation is too high, the charge carrier density is extremely reduced. This is because the exciton is no more able to reach the donor-acceptor interface within its diffusion length for charge carrier generation. Thermal annealing was proved to be a suitable method to induce phase separation in a highly intermixed alkyl/alkyl blend system. Consequently, a reduced recombination dynamics and hence more long-lived charge carriers were observed.

In the second part of this thesis a novel metal network as a TCE in OPV was developed. The fabrication is based on a colloidal polymer dispersion, which forms cracks during drying. This cracked polymer layer served as a template and was afterwards metalized. Finally, the polymer template was lifted off, whereas a fine structured metal network remained. This metal network is highly transparent and exhibits at the same time good electrical conductance – two basic requirements for a TCE. In the first step the metal network was fabricated on glass substrate and characterized with regard to optical transmittance and sheet resistance. Both parameters depend on the lateral feature sizes as well as the height of the metal network. An increase in optical transmittance led to an increase in sheet resistance and hence an optimal compromise between both was realized. Using scanning electron microscopy (SEM) we found that the typical thickness of 45 nm zinc oxide (ZnO) layer was not sufficient anymore to cover the metal network completely leading to electrical shorts in the respective devices. A subsequent optimization led to a ZnO layer thickness of 135 nm. Using that thickness allowed us to fabricate devices, which were comparable to the ITO-reference devices.

The successful integration of the transparent metal network in OPV motivated us to consider the metal network not only as a replacement for ITO at the front side, but also as a potential back electrode. For that the metal network had to be fabricated on top of the poly(3,4-ethylenedioxythiophene) polystyrene sulfonate (PEDOT:PSS) coated photoactive layer. The implementation of the idea posed two questions: 1. Will the cracking process on PEDOT:PSS be similar to that on glass substrate? 2. How can the lift off process of the polymer template be realized without destroying the underlying soluble layers? In the investigations, no significant differences in the cracking process on the PEDOT:PSS were observed. Additionally, the haze, a property describing the optical scattering, was determined. A low haze is especially interesting for applications as semitransparent solar cell. The haze of the transparent metal network electrode could be decreased to 5%. Afterwards the transparent metal network was fabricated on top of the complete solar cell device. The challenge was to lift off the polymer template after metallization without damaging the underneath layers. Thereby we found that the polymer template could be easily dissolved by ethyl acetate under ultra-sonication, while keeping the underlying layers intact. Thus we were able to integrate the transparent metal network successfully as front and as back electrode in OPV which consequently leads to ITO-free semitransparent solar cell devices with good photovoltaic performance. The transparent metal network represents therefore a realistic alternative to current TCEs, especially to ITO, and is moreover suitable for large area production.

Zusammenfassung

Die organische Photovoltaik (OPV) hat sich in den letzten Jahren zu einer ernstzunehmenden regenerativen Energiequelle etabliert. Im Gegensatz zur allgegenwärtigen oft auf Silizium basierten anorganischen Photovoltaik, besteht sie im Kern aus kohlenstoffbasierten Molekülen oder Polymeren. Diese sind ebenso in der Lage, Licht zu absorbieren und elektrische Ladungen zu generieren. Dabei ergeben sich die Vorteile der OPV unmittelbar aus den Eigenschaften der verwendeten Materialien: So besitzen diese einen um Größenordnungen höheren Absorptionskoeffizient als Silizium und dementsprechend kann die photoaktive Schicht sehr dünn und sogar auf flexiblen Substraten gestaltet werden. Die Herstellung erfolgt zudem oft aus Lösung und ist geeignet für viele großflächige Beschichtungsverfahren. Dennoch steht die OPV noch am Beginn ihrer kommerziellen Verwendung, was zum einen am moderaten Wirkungsgrad und an der niedrigen Lebensdauer liegt, zum anderen aber auch an Materialien, die ihrer Herstellung noch energieintensiv und damit zu teuer sind. Die zwei energieintensivsten Materialien sind das Fullerene basierte [6,6]-Phenyl-C_{61}-Buttersäuremethylester (PCBM) – ein weitverbreiteter Elektronenakzeptor in der photoaktiven Schicht – und Indium Zinn Oxid (ITO), welches als transparente leitfähige Elektrode (TCE) fungiert. Beide Komponenten machen in ihrer Herstellung über 60% des Energiebedarfs einer kompletten organischen Solarzelle aus. Die Suche nach alternativen Materialien ist daher von entscheidender Bedeutung für die Konkurrenzfähigkeit der OPV.

Diese Dissertation leistet dazu einen Beitrag und beschäftigt sich mit alternativen Materialkonzepten um PCBM und ITO zu ersetzen. Sie besteht daher aus zwei Teilen: Im ersten Teil werden zunächst zwei Perylene Bisimide (PBI) als potentielle Elektronakzeptoren in Verbindung mit drei verschiedenen Donorpolymeren untersucht. Hier liegt der Fokus auf der Ausbildung der Morphologie zwischen beiden Komponenten und deren Einfluss auf die Rekombinationsdynamik der Ladungsträger sowie der Solarzellencharakteristik um das Potential der PBIs zu verstehen. Im zweiten Teil der Arbeit wurde eine neuartige Metallnetzwerkelektrode entwickelt, charakterisiert und erfolgreich in die OPV integriert. Diese Elektrode ist hoch transparent und gut elektrisch leitfähig. Sie kann im Vergleich zu ITO zudem auf Vorder- und Rückseite der Solarzelle zum Einsatz kommen und ermöglichte dadurch die Herstellung von ITO-freien semitransparenten Solarzellen.

Im Folgenden werden die wichtigsten Erkenntnisse dieser zwei Themenkomplexe kurz vorgestellt.

PBI ist ein potentieller Elektronenakzeptor, weil er nicht nur über Grundvoraussetzungen wie geeignete energetische Lagen und hohe Elektronenmobilität verfügt, sondern zudem eine hervorragende Lichtabsorption zeigt. Außerdem ist die Synthese und Aufreinigung im Vergleich zu PCBM einfacher und in großen Maßstab umsetzbar. Des Weiteren kann man PBIs leicht chemisch modifizieren und so die energetischen und photophysikalischen Eigenschaften genau anpassen. Die Löslichkeit des sonst wenig löslichen PBI Kerns lässt sich durch löslichkeitsvermittelnden Substituenten erhöhen, wobei diese dann auch auf die Mischbarkeit des PBIs mit dem Donorpolymer Einfluss nimmt. Das Ziel der vorliegenden Arbeit ist es, diesen Zusammenhang zwischen löslichkeitsvermittelnden Substituenten und Mischbarkeit mit dem Donorpolymer näher zu beleuchten. Dazu wurden zwei PBIs mit je einem unpolaren Alkyl- oder polaren Oligoethylenglycol- (OEG) Substituenten gewählt und im Blend mit drei verschiedenen Donorpolymeren untersucht. Die entsprechenden Solarzellen zeigten unterschiedliche Strom-Spannungs- (*J*-*V*) Kennlinien in Abhängigkeit der verwendeten Substituenten am PBI. Die Untersuchung der Morphologie erfolgte mittels Rasterkraftmikroskopie (AFM). Es zeigte sich eine höhere Vermischung zwischen Donor und Akzeptor, wenn beide Komponenten Alkylketten trugen, wohingegen eine höhere Phasenseparation im Fall von Alkylseitenketten am Donorpolymer und einer OEG-Kette am PBI. Jedoch korrelierte dieser Befund nicht mit dem Verhalten der *J*-*V*-Kennlinien. Diese Diskrepanz konnte mit transienter Absorptionsspektroskopie (TAS) vollständig aufgeklärt werden. Mittels TAS kann man sowohl die verbleibende Dichte der Ladungsträger nach Photoanregung bestimmen, als auch deren Rekombinationsdynamik. Innerhalb dieser Arbeit wurde dazu ein sensitiver TAS-Aufbau in Betrieb genommen, der den Zeitbereich von einigen Nanosekunden bis zu Millisekunden abdeckt. In Vorbereitung zur TAS Messung wurden zudem Möglichkeiten zur Messung von Radikalspektren der Kationen und Anionen von Donor und Akzeptor mittels Spektroelektrochemie und chemischer Oxidation erarbeitet. Diese Radikalionenspektren wurden dann zur Auswertung der TAS Spektren herangezogen. Abschließend konnte durch die TAS in Verbindung mit AFM gezeigt werden, dass eine Alkyl/OEG Wechselwirkung zwischen Polymer und PBI zu einer besseren Phasenseparation und auch zu einer erhöhten Ladungsträgerdichte im Blend führt. Die Ladungsträger sind dabei stabiler und langlebiger im Vergleich zu den Blendsystemen mit hoher Vermischung aufgrund von der bevorzugten Alkyl/Alkyl Wechselwirkung. Es konnte aber auch gezeigt werden, dass ein zu hoher Grad an Phasenseparation die Ladungsträgerdichte extrem verringert, da hier die

Exzitonen nicht mehr die Donor-Akzeptorgrenzfläche innerhalb ihrer Diffusionslänge erreichen. Außerdem erwies sich das Tempern eines hoch vermischten Alkyl/Alkyl Blendsystems als potentielle Methode um Phasenseparation zu induzieren. Folglich konnten in diesem Blend mittels TAS eine verlangsamte Rekombinationsdynamik und damit stabilere Ladungsträger beobachtet werden.

Im zweiten Themenkomplex der Dissertation wurde ein neuartiges Metallnetzwerk für die Verwendung als TCE in OPV entwickelt. Die Herstellung beruht auf einer kolloidalen Polymerdispersion, die beim Trocknen auf einem Substrat feinste Risse ausbildet. Dieser rissige Polymerfilm dient als Template und wird anschließend metallisiert. Zuletzt wird das Polymertemplate mit einem Lösungsmittel abgelöst und übrig bleibt ein feines Metallnetzwerk. Dieses ist hoch transparent und besitzt gleichzeitig eine hohe elektrische Leitfähigkeit – zwei Grundvoraussetzungen für die TCE. Im ersten Schritt wurde das Metallnetzwerk auf einem Glasträgersubstrat hergestellt und in Hinblick auf optische Transmission und Flächenwiederstand charakterisiert. Beide Parameter hängen von der lateralen Strukturgröße und der Höhe des Metallnetzwerkes ab. Eine Erhöhung der optischen Transparenz führte zu einer Erhöhung des Flächenwiederstandes und ein optimaler Kompromiss zwischen beiden konnte realisiert werden. Es zeigte sich allerdings mittels Rasterelektronenmikroskop (SEM), dass die übliche Schichtdicke von 45 nm Zinkoxid (ZnO) nicht ausreichte um die Netzwerk vollständig zu überdecken, was in den entsprechenden Solarzellen zu elektrischen Kurzschlüssen führt. Eine anschließende Optimierung ergab eine Schichtdicke von 135 nm ZnO. Unter Verwendung dieser Schichtdicke konnten Solarzellen hergestellt werden, die in ihrer OPV-Performance vergleichbar mit der entsprechenden ITO-Referenzsolarzelle waren.

Der die erfolgreiche Integration der Metallnetzwerkelektrode in die OPV ermutigte uns diese nun nicht nur als Ersatz zur ITO Elektrode zu sehen, sondern auch für die gegenüberliegende Rückelektrode zu verwenden. Dazu musste die Metallnetzwerkelektrode auf der mit Poly(3,4-ethylendioxythiophen)polystyrolsulfonat (PEDOT:PSS) überzogenen photoaktiven Schicht hergestellt werden. Die Umsetzung dieser Idee warf zwei Fragen auf: 1. Verhält sich die Rissbildung auf PEDOT:PSS ähnlich wie der auf dem Glassubstrat? 2. Wie kann ein Ablösen des Polymertemplates erfolgen, ohne die darunter löslichen Schichten zu zerstören? In der folgenden Untersuchung zeigten sich jedoch keine großen Unterschieden in der Rissbildung auf PEDOT:PSS. Zudem wurde der Haze bestimmt – eine Eigenschaft, die das optische Streuverhalten beschreibt. Ein niedriger Haze ist insbesondere für Anwendungen als

semitransparente Solarzelle interessant. Der Haze der transparenten Netzwerkelektroden war überraschend gering und lag bei 5%. Anschließend wurde die transparente Netzwerkelektrode auf einer kompletten Solarzelle hergestellt. Die Herausforderung bestand darin, das Polymertemplate nach der Metallisierung wieder abzulösen ohne die darunterliegenden Schichten zu zerstören. Das Ablösen in Ethylacetat in Verbindung mit Ultraschall stellte sich dafür als erfolgreiche Methode heraus. Schließlich war es uns möglich das transparente Metallnetzwerk sowohl als untere als auch als obere Elektrode erfolgreich in OPV zu integrieren, was unmittelbar zu einer ITO-freien semitransparenten Solarzelle mit guter Performance führt. Das transparente Metallnetzwerk stellt daher eine echte Alternative zu bisherigen TCEs dar, allen voran zu ITO, und ist darüber hinaus leicht auf eine großflächige Produktion übertragbar.

2 Introduction

2.1 Organic solar cells – a motivation

At the EXPO 2015 in Milan, Italy, the German pavilion[1a] (Figure 1) made the great progress of the last years in organic photovoltaics (OPV) visible by showing, how versatile this new technology for building integration can be.[1b] With properties such as flexibility, lightweight and semitransparency, OPV can enter new markets and applications, where their silicon based counterparts cannot. This is due to the properties of material used for organic solar cells. Organic materials exhibit much higher molar absorption coefficients than inorganic materials[2] and hence a very thin photoactive layer in the range of 100 to 300 nm is sufficient for proper light absorption. Furthermore, they are not brittle like inorganic materials, which make them interesting for flexible applications. A roll to roll production enables cheap and fast production on flexible polymer substrate on large scale.[3] In addition, the color of the photoactive layer can be easily tuned by careful selection of the photoactive materials. This is especially interesting for semitransparent solar cells for building integrated photovoltaics and automotive applications.[4]

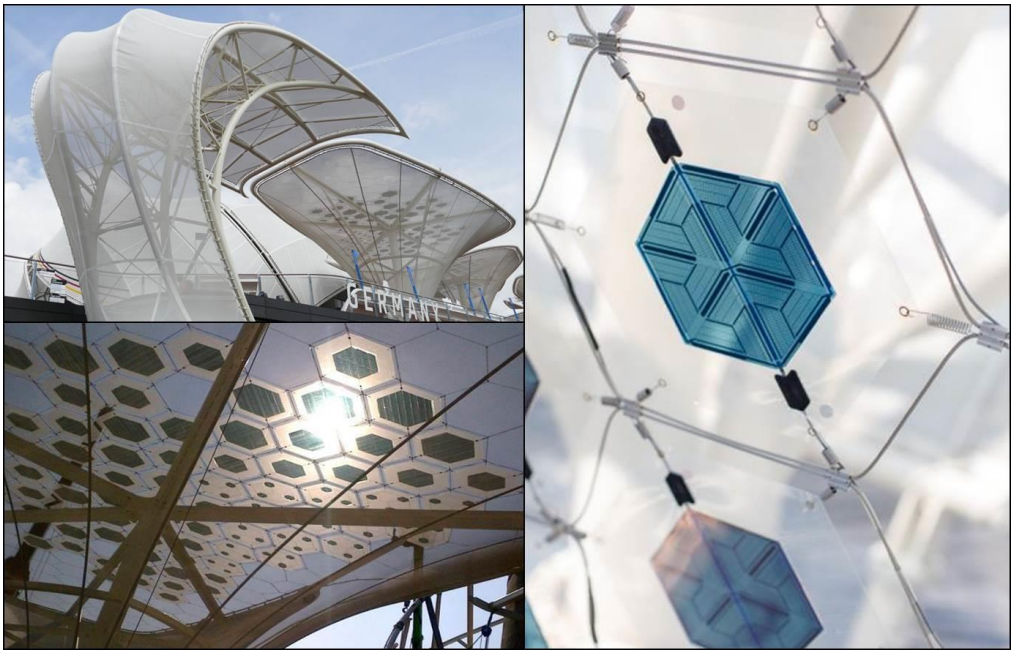

Figure 1. *Photographs of the German pavilion at the EXPO 2015 in Milan (Italy) taken from multiple perspectives to highlight the potential of flexible semitransparent OPV in architecture.*[1a]

It is a fact, that OPV still needs to be improved in terms of power conversion efficiency (PCE) and long-term stability, however, a number of new companies try to enter niche markets at this early state of commercialization. Darling and You describe scenarios for the next 10 years and longer regarding the OPV market and emphasize, that up to date with respect to energy payback time, global warming potential and the abundance of elements only silicon and organic photovoltaics are suitable for large area power plants in terawatt scale.[5] The energy payback time is a key factor for the economic evaluation of OPV and depends on the PCE on the one hand and the energy requirement for production on the other hand. It is therefore important to keep an eye on the energy demand to enable OPV commercialization in niche markets, e.g. for mobile applications, even if the PCE and lifetime is limited. In Figure 2 the energy demand of typical polymer bulk heterojunction solar cells is given. It is obvious, that both phenyl-C_{61}-butyric acid methyl esters (PCBM) – a common electron acceptor – as well as indium tin oxide (ITO) as transparent electrode are responsible for more than 60 % of the whole solar cell energy demand.[6] Hence, search for alternative materials to PCBM and ITO is required. This thesis therefore deals on the one hand with perylene bisimides (PBIs) as potential alternative to PCBM and on the other hand, with developing and studying a novel metal network as transparent conducting electrode as replacement for ITO.

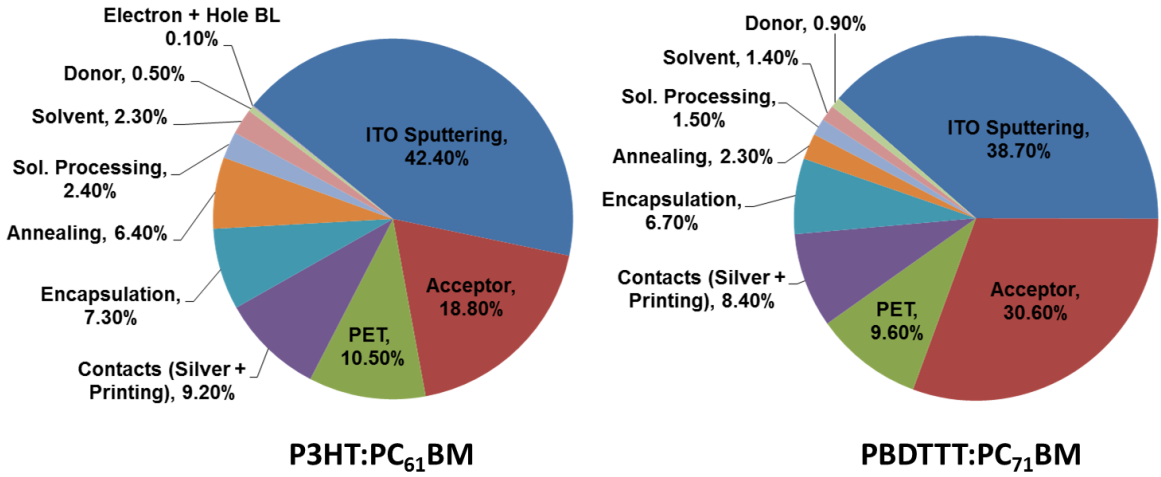

***Figure 2**. Proportion of each component to the cumulative energy requirement for fabrication of two common solution processed polymer solar cells P3HT:PC_{61}BM and PBDTTT:PC_{71}BM (reproduced from [6]).*

In the following sections of this chapter a brief insight into function, fundamental processes and measurement of OPV is given. Special attention is paid in section 1.5 to PBI as a potential alternative electron acceptor for PCBM and ITO-free transparent electrodes.

2.2 Device architecture and function of solar cells

During the last decades of OPV research organic solar cells underwent an intensive development including different architectures, material compositions and device concepts. Simultaneously a better understanding of fundamental processes in organic semiconductors in general also evolved. In organic semiconductors sp^2-hybridized carbons are connected via alternating single and double bonds, whereas the p_z orbital is perpendicular to the sp^2-plane of each carbon. According to the linear combination of atomic orbitals (LCAO) a combination of two p_z atom orbitals leads to a bonding π and an antibonding π* molecular orbital. The bonding π molecular orbital is also called the highest occupied molecular orbital (HOMO) filled by the two p_z electrons, whereas the antibonding π* molecular orbital is empty and therefore also called the lowest unoccupied molecular orbital (LUMO). Depending on the number N of participating π-bonds in the conjugated π-system, a set of HOMOs (HOMO, HOMO-1, HOMO-2, …, HOMO-$\frac{1}{2}N$) as well as a set of LUMOs (LUMO, LUMO+1, LUMO+2, …, LUMO+$\frac{1}{2}N$) is formed. The energetic difference between the HOMO band and the LUMO band is called the fundamental gap and it decreases with increasing N.[7] The energetic level of the HOMO and LUMO and so the fundamental gap can be tuned furthermore by integrating heteroatoms into the π-conjugated system. The HOMO-LUMO gap is typically in the range of 1 to 3 eV which allows the π-system to absorb light in the visible spectrum to transfer one electron from the HOMO to energetic higher lying LUMO while leaving a hole in the HOMO. Such an electron-hole pair, so-called singlet exciton, is strongly bound via the columbic force resulting in a high exciton binding energy. The exciton binding energy is much higher than in inorganic semiconductors due to the lower effective dielectric constant of 2 to 4 in organic semiconductors. The question arises, how to overcome the exciton binding energy in order to split the exciton into free charges. The very first organic solar cells in the late 70s consist of only one organic semiconductor sandwiched between two metal electrodes with different work functions.[8] At the contact between the organic semiconductor and the metal, a Schottky barrier is formed where the electric field is strong enough to split the exciton into free charges. However, only a very small fraction of excitons reach the metal contact due to limited exciton diffusion length, whereas the majority of the excitons recombine.[9] A new concept to split the exciton more efficiently was introduced by Tang *et al.* in 1986. He combined a p-type with a n-type organic semiconductor to form a bilayer which was sandwiched between the respective electrodes.[10] The p-type material, also called electron donor, exhibits energetic higher lying HOMO and LUMO levels

compared to the n-type material or the so-called electron acceptor. In Figure 2a, the HOMO and LUMO levels of the donor and the acceptor are shown with respect to the vacuum level. The energetic value of the HOMO levels correspond than to the (vertical) ionization potential (*IP*) and the energetic value of the LUMO levels to the electron affinity (*EA*), respectively. Experimental accessible are both values via ultraviolet photoelectron spectroscopy (UPS) for *IP* and inverse photoemission spectroscopy (IPES) for *EA*. The difference between *IP* and *EA* represents the HOMO-LUMO band gap, also called the transport gap E_{trans}.[7] For simplicity we consider in the following the exciton to be generated only in the donor material. However, exciton generation takes place in both donor and acceptor. Absorption of a photon in the donor leads to a donor exciton while the lowest optical transition is defined as optical gap E_{opt}. Experimental E_{opt} is estimated from the thin film UV / Vis absorption onset.[11] In excitonic materials such as used here for donor and acceptor, the optical gap is lower in energy than the transport gap.[12] The difference between both is defined as exciton binding energy E^b_{exc}. In order to overcome E^b_{exc} and to split the exciton into free charges the exciton has to reach the donor acceptor interface. There takes place a one electron transfer from the excited donor (donor exciton) to the acceptor LUMO.

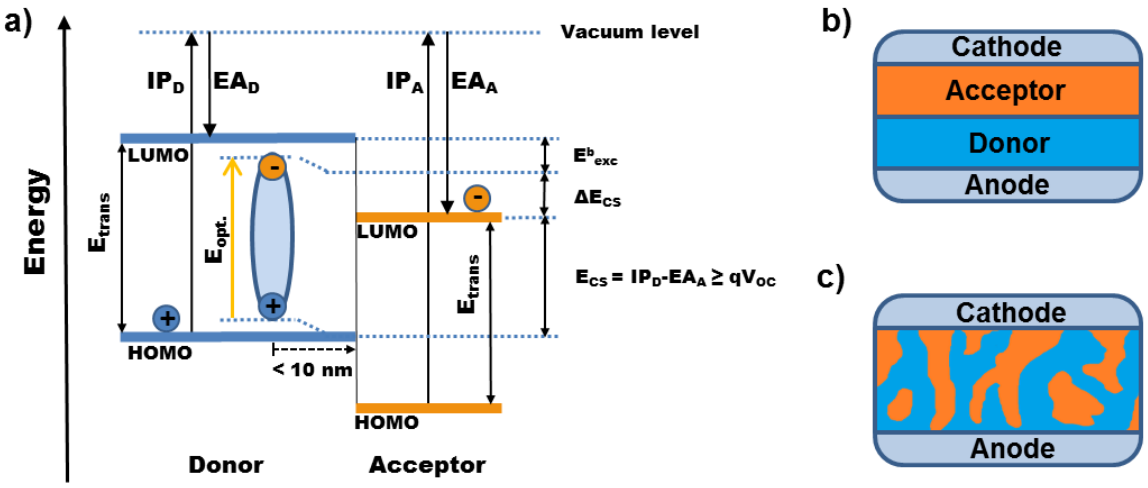

Figure 3. *a) Principle of photocharge generation in donor / acceptor organic solar cells based on their energy levels considering photoexcitation in the donor material*[10, 11] *and simplified architecture of b) bilayer and c) bulk heterojunction solar cell.*

A charge transfer exciton or a charge transfer state, which may appear as an intermediate between the donor exciton and the free charges will be discussed in section 1.3. The available driving force for charge separation with respect to the exciton is given by the energy

difference ΔE_{CS} and is derived from the energy of the separated charges E_{CS} and the optical gap E_{opt} according to Eq. 1, whereas E_{CS} is calculated from ionization potential of the donor (IP_D) and electron affinity of the acceptor (EA_A) (Eq. 2).

$$-\Delta E_{CS} = E_{CS} - E_{opt} \quad (1)$$

$$E_{CS} = IP_D - EA_A \quad (2)$$

$$-\Delta E_{CS} = (IP_D - EA_A) - E_{opt} \quad (3)$$

$$-\Delta E_{CS} > E^b{}_{exc} \quad (4)$$

Roughly spoken, for a successful splitting of the exciton into free charges at the donor acceptor interface, the driving force ΔE_{CS} has to be greater than the exciton binding energy $E^b{}_{exc}$ (Eq. 4). This is necessary but might be not sufficient. From Eq. 3 it is clearly seen, that the success of light induced charge generation depend not only on the optical gap E_{opt} but also on the HOMO-LUMO transport levels of both the donor and the acceptor in general, given by the *IP* and *EA* respectively.[11] After charge separation the free charges will be transported towards the electrodes for charge extraction, whereas holes are transported via the donor HOMO transport levels and electrons are transported via the acceptor LUMO transport levels. In Figure 2a, the exciton diffusion length of 10 nm is depicted to emphasize that only excitons generated within this exciton diffusion length are able to reach the donor acceptor interface for charge generation. However, for sufficient light absorption photoactive layers of at least 100 nm are required. Coming back to Tangs bilayer type solar cell (Figure 2b) it is now clear, that only a small fraction of excitons contribute to the photocurrent when the photoactive layer is much thicker than the exciton diffusion length, whereas the majority recombines e.g. either radiatively via photoluminescence or via thermal relaxation. This is one reason for the poor photocurrent in Tangs solar cell resulting in relatively poor efficiency of 1 %.[10] On the other hand, it should be noted, that once the free charge carriers are generated, they likely migrate through the pure donor and acceptor phase in a bilayer device towards the electrodes rather than recombine. The concept of bilayers is today therefore mainly applied successfully for vacuum processed organic solar cells using small molecules, where the photoactive layer can be fabricated in the range of some nanometers and multi junction structures can be precisely created. For solution processed organic solar cells the bilayer type is usually not practicable, since the thicknesses of tens of nanometers are hard to control. Additionally, the required orthogonal solvent for fabrication e.g. the donor layer on top of the acceptor layer limits the variety of suitable photoactive materials. In 1992 Heeger *et al*. presented a new

concept by fabricating the photoactive layer from a solvent containing both, the donor and acceptor material[13] which was then realized in an organic solar cell in 1995.[14] Surprisingly this resulted in a donor acceptor blend structure with an increased interface layer, the so-called bulk heterojunction (Figure 2c). Here phase domains in the range of the exciton diffusion length guarantee, that almost each exciton reaches the donor acceptor interface. This leads to a higher photocurrent with respect to the bilayer type and high power conversion efficiency of up to 10 % are reported recently using improved photoactive layer materials.[15] However, due the blending of donor and acceptor, the chance for recombination of opposite free charges on the way towards the electrodes is increased with respect to a bilayer solar cell.[16, 17] An engineering of the optimal blend morphology is therefore crucial to ensure both, a high donor acceptor interface for charge generation and for percolation pathways towards the electrodes for fast charge carrier extraction.

2.3 Elementary processes in the photoactive layer

To understand, what influences the solar cell performance, we take a deeper look into the elementary processes inside the photoactive layer of a bulk heterojunction solar cell. As mentioned above, the photoactive layer is a blend consisting of an electron donor material and an electron acceptor material. In Figure 3a a sketch of the blend illustrates the elementary processes including the involved intermediate species such as singlet exciton, charge transfer exciton, polaron pair or free polaron. The transition probability between the intermediate species depends highly on their molecular state energy. A respective schematic molecular state diagram is given in Figure 3b.

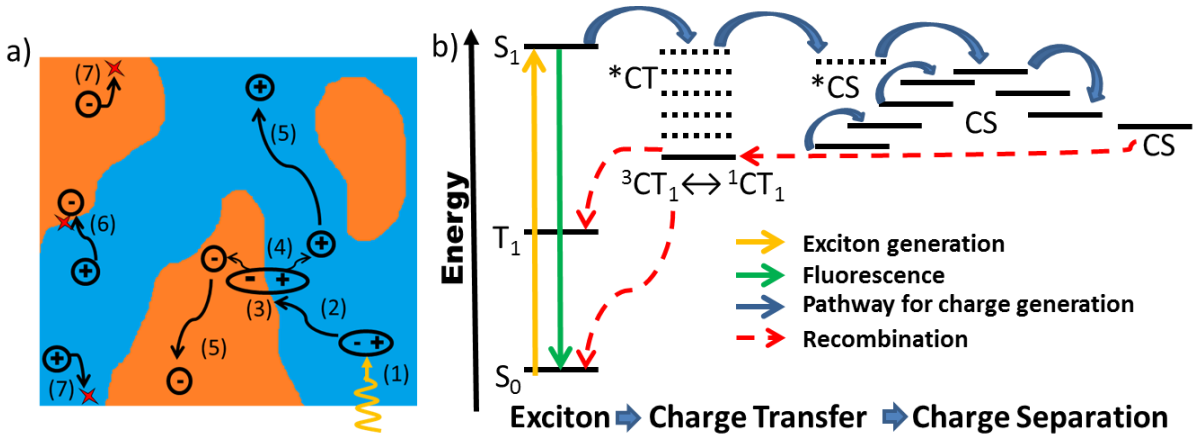

Figure 4. *Photocharge generation process illustrated by a) insight into bulk heterojunction photoactive layer with elementary processes and b) molecular state diagram (modified from [9] and [18]).*

The elementary processes and possible loss mechanisms numbered in Figure 3a can be described as follows:

(1) Exciton formation

When the photoactive layer is exposed to light, a photon gets absorbed by the donor leading to a donor excitation. In terms of molecular energy states the photon absorption corresponds to transition from the electronic ground state S_0 to the first excited state S_1 of the donor leading to a singlet exciton formation. Due to the low relative dielectric constant in organic semiconductors, the singlet exciton can be considered as a strongly coulomb bound electron-hole pair, a so-called “frenkel-exciton”.

(2) Exciton diffusion

The exciton is electrically neutral and its diffusion length L therefore depends only on its lifetime τ and the diffusion coefficient D according to $L = \sqrt{D \cdot \tau}$.[19] Typical exciton diffusion lengths in organic semiconductor are in the range of 5 to 10 nm.[20] Within this diffusion length or exciton lifetime the exciton may reach the donor / acceptor interface (3) or recombine radiatively under fluorescence back to the S_0 ground state. A transition from the singlet exciton S_1 to a triplet exciton T_1 is spin forbidden and rather ineffective in organic materials without heavy atoms.

(3) In case the S_1 singlet exciton reaches the donor / acceptor interface within the exciton diffusion length, an electron transfer from the donor to the acceptor leads to a singlet charge transfer state (^{1}CT). This transfer occurs typically on a very fast timescale of 10 to 100 fs.

(4) If the thermalization length exceeds the coulomb capture radius, the CT state is able to split off into free charges represented in Figure 3b by a charge separated state (CS). The hole is located at the HOMO transport level in the donor, whereas the electron is at the LUMO transport level of the acceptor.

(5) The free charges, also called polarons, are now able to migrate through its respective transport levels towards the electrodes. These molecular transport levels are not equal in energy but rather described by a Gaussian distribution of density of energy (DOS). The charge transport is than dominated by a charge hopping process between these energy states.

(6) As mentioned already before, due to the donor-acceptor blend structure in BHJ solar cells, there is a certain probability for the free charges to recombine non-geminate before reaching the electrodes. Due to spin statistics, a ratio between singlet ^{1}CT to triplet ^{3}CT states of one to three is proposed. A ^{1}CT state can recombine directly to the ground state S_0, whereas a ^{3}CT may include a triplet state T_1 of the acceptor followed by a relaxation to the ground state S_0. For both, the ^{1}CT and the ^{3}CT, dissociation back to free charge carriers is possible and it depends upon the time constant between these processes.[21]

(7) Free charges may also reach the opposite and hence “wrong” electrode resulting in surface recombination. This is especially the case at low internal electric field condition near the open circuit voltage, where the current is controlled by diffusion rather than by internal electrical field. To prevent this, interlayers serving as hole and electron blocking layer are used successfully (more about such blocking layers in section 1.5.2).

2.4 Measurement & Characterization

The current-voltage (*J-V*) characteristic in dark of solar cell is similar to that of a diode. In the reverse bias region only a very weak dark current is observed, whereas in the forward bias region the current increases rapidly at certain applied bias (Figure 5). Under illumination the current increases in the reverse bias region due to the additional photocurrent. From the *J-V* curve under illumination the characteristic parameters short circuit current (J_{SC} – maximal cell current) and open circuit voltage (V_{OC} – maximal cell voltage) are obtained. The ideal power of the solar cell would be the product of J_{SC} and V_{OC} – represented by the white rectangle in Figure 4. However, the ideal power is never reached and the maximum power P_{max} is given therefore at the maximum power point (MPP), where the product of J_{MPP} and V_{MPP} – represented by the blue rectangle – maximizes. The fill factor is the ratio between both products and a measure for the "squareness" of the *J-V* curve (Eq. 5).

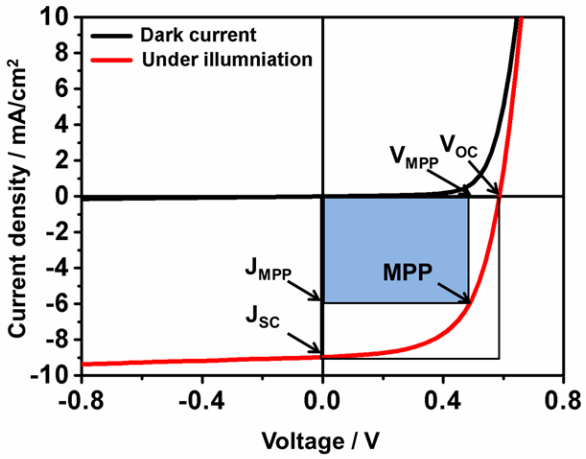

$$FF = \frac{J_{MPP} \cdot V_{MPP}}{Jsc \cdot Voc} = \frac{Pmax}{Jsc \cdot Voc} \qquad (5)$$

$$PCE = \frac{Pmax}{P_L} = \frac{FF \cdot Jsc \cdot Voc}{P_L} \qquad (6)$$

Figure 5. *J-V characteristic of a typical P3HT:PCBM organic solar cell in dark and under illumination including characteristic parameters J_{SC}, FF and V_{OC} as well as the maximum power point (MPP).*

The unique parameter of the solar cell is the power conversion efficiency (PCE), which ultimately describes the ratio between the incoming light power P_L and the obtained maximal electrical power P_{max} (Eq. 6). In order to measure under standardized lab conditions, P_L is defined as 1 sun with a power surface density of 1000 W/m^2. This represents the overall yearly average of solar irradiation under a zenith angle of 48.2°. Under this angle the sun light has to travel in average trough 1.5 air masses (AM 1.5). In laboratory a calibrated xenon arc lamp with suitable filters is used to simulate 1 sun conditions for measurement. The measurement under illumination should be furthermore carried out using a shadow mask to

define the active area and restrict measured photocurrent from additional contribution by light scattering or high conductive interlayers.[22]

Another important characterization method is the determination of the external (EQE) and internal quantum efficiency (IQE). The EQE is defined as the ratio of the numbers of collected charges (electrons) N_e to the number of incident photons at a given wavelength $N_{ph}\,(\lambda)$ (Eq. 7), whereas the IQE is defined as the ratio of the number of collected charges N_e to the number of absorbed photons by the photoactive layer $N_{ph}^{abs}(\lambda)$ (Eq. 8). EQE and IQE are connected via the absorptivity A in percentage of the photoactive layer (Eq. 9). A precise determination of the IQE spectra considers the parasitic absorption (due to interlayer etc.) by simulation.[92] An EQE spectra as well as an IQE spectra of a typical P3HT:PCBM organic solar cell is shown in Figure 5.

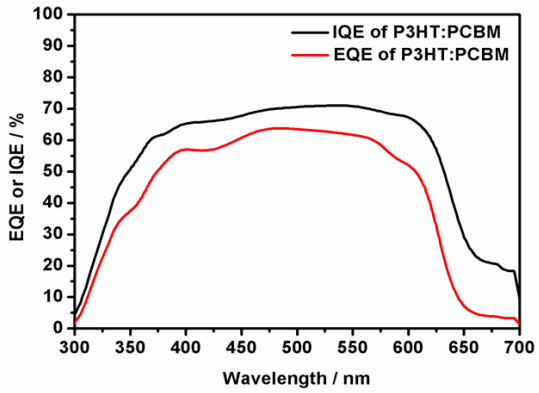

$$EQE\,(\lambda) = \frac{N_e}{N_{ph}\,(\lambda)} \qquad (7)$$

$$IQE\,(\lambda) = \frac{N_e}{N_{ph}^{abs}(\lambda)} \qquad (8)$$

$$EQE\,(\lambda) = IQE(\lambda) \cdot A(\lambda) \qquad (9)$$

Figure 6. *Comparison between EQE (red) and IQE (black) spectra of a typical P3HT:PCBM organic solar cell showing that at 500 nm nearly 63 % of the incident photons are converted into collected charges (from EQE spectrum). In contrast to that, the respective IQE spectrum shows, that 70 % of the absorbed photons are converted into collected charges at the same wavelength.*

Knowing both, the *J-V* curve including their characteristic parameters and the IQE spectrum helps to understand loss mechanism in organic solar cells.

2.5 Materials

This section will give an overview of commonly used and high efficiency materials for solution processed bulk heterojunction solar cells including materials for the photoactive layer, interlayers and electrodes. Special attention is paid to perylene bisimide (PBI) as an alternative small molecule acceptor on the one hand and the variety of transparent conduction electrodes (TCE) on the other hand, since both topics will be addressed in the main part of this thesis.

An unique property of all the materials used as particular layers in organic solar cells is the position of their energy levels with respect to the vacuum level. In Figure 6a a typical organic solar cell in normal geometry is shown including the energy levels for poly(3-hexylthiophene-2,5-diyl) (P3HT) and phenyl-C_{61}-butyric acid methyl ester (PCBM) as a common electron donor and acceptor respectively. As mentioned in section 1.2, the energy levels of interest for donor and the acceptor are the HOMO and LUMO transport levels. After photoinduced charge generation, holes have to travel through the transport HOMO levels towards the anode, whereas electrons have to travel through the LUMO transport levels towards the cathode.

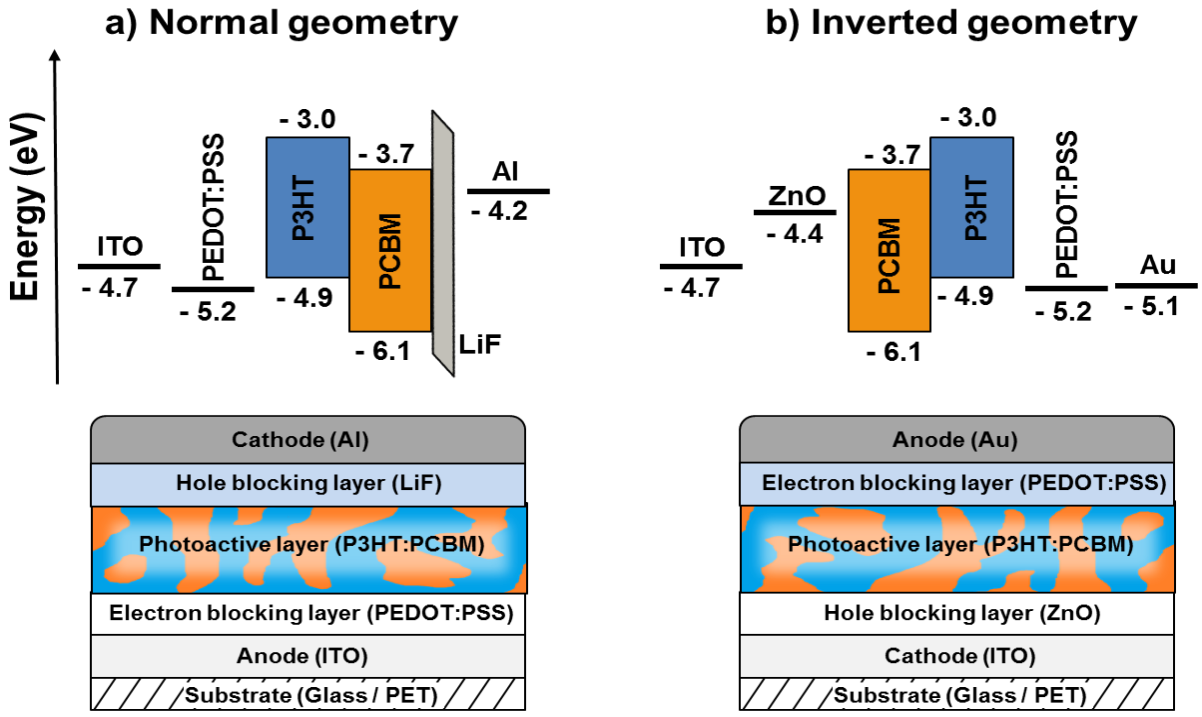

Figure 7. *Energy level diagram and cross-section with the particular layers and materials of an organic bulk heterojunction solar cell in a) normal and b) inverted device geometry.*

On the anode side in normal geometry, indium tin oxide (ITO) serves as a TCE and enables both, light passage towards the photoactive layer and charge carrier collection. Between ITO and the photoactive layer a hole blocking layer – usually poly(3,4-ethylenedioxythiophene) polystyrene sulfonate (PEDOT:PSS) – reduces surface recombination between hole from the photoactive layer and already extracted electrons as mentioned in section 1.3. For the cathode a low work function metal is used for electron extraction and collection. Additionally, the opaque metal layer enables reflection of non-absorbed light back into the photoactive layer leading to increased photocurrent. However, in contrast to normal geometry, an inverted geometry with inverse layer structure as shown in Figure 6b might be also suitable for many cases and was first applied by Shirakawa *et al.*[23] Between a high work function metal anode (e.g. Au) and the photoactive layer, again PEDOT:PSS serves as hole extraction layer / electron blocking layer. In addition, zinc oxide (ZnO) is fabricated between ITO and the photoactive layer as an electron extraction layer and hole blocking layer. Such interlayers do not only prevent surface recombination, but also define mainly the built in voltage. Indeed, efficient organic solar cells are published using silver electrodes as both, the anode and the cathode. A drawback of low work function metals is their oxidation which reduces the long term stability of such devices. The question about the choice between normal and inverted geometry concerns not only long term stability, but has also a huge impact on the photoactive layer during processing, due to preferential interaction of either the donor or the acceptor with either of the interlayers or the air. The following sections present common materials for each layer.

2.5.1 Photoactive layer

This section presents a selection of common donor and acceptor materials for the photoactive layer with a focus on PBIs as promising alternative electron acceptors. The structures of the donor and acceptor materials are shown in Figure 7 and 8, respectively.

The very first bulk heterojunction solar cell was published by Heeger *et al*. in 1995 using poly[2-methoxy-5-(2-ethylhexyloxy)-1,4-phenylenevinylene] (MEH-PPV) as a donor polymer and a fullerene derivative PCBM as small molecule acceptor.[14] Using a structurally related donor polymer poly[2-methoxy-5-(3′,7′-dimethyloctyloxy)-1,4-phenylenevinylene] (MDMO-PPV), Sariciftci *et al*. achieved an almost three fold enhancement in PCE of 2.5 % in 2001 due to a more intimate mixed morphology using chlorobenzene (CB) instead of toluene.[24] Indeed the morphology plays a crucial role as already mentioned in section 1.3 and it needs to be optimized. One of the best investigated systems also in terms of morphology is definitely a blend using P3HT as donor polymer and PCBM as acceptor. A lot of work was done to investigate the influence of solvent and solvent additives, PCBM content and thermal annealing. But also P3HT itself was optimized by variation of the polydispersity, molecular weight or regioregularity[25] and including device optimization a high PCE of 6.5% was reported for this system.[26] A further milestone in order to improve the performance of OPV was achieved using the so-called low band gap (LBG) polymers. Having electron rich and electron deficient units, a mixing of their respective molecular orbitals leads to a decrease in electronic and hence optical gap resulting in a bathochromic shift of the absorption onset. Taking the photon flux of the sun into account, it is obvious that consequently more photons will be absorbed leading to a potentially higher J_{SC} .[27] Typical high efficient LBG polymers classified according to their electron deficient units are based on diketopyrrolopyrrole (PDPP5T)[28], thieno[3,4-c]pyrrole-4,6-dione (PBDTTPD)[29], thienothiophene (PBDTTT-C-T[30], PBDTT-F-TT[31] and PTB7[32]) or benzothiadiazole (PCPDTBT)[33] with 5 to 8 % PCEs. Based on benzothiadiazole, highly efficient low band gap polymers were recently published exhibiting PCE over 10 %.[15] Following the low band gap approach, also small donor molecules were synthesized such as F-DTS with a high PCE of 7 %.[34] Most of the donor materials mentioned above were blended with acceptors based on fullerene and its derivatives such as PCBM. Indeed, PCBM is up to date one of the most efficient acceptor for organic photovoltaics due to its high electron affinity and mobility.

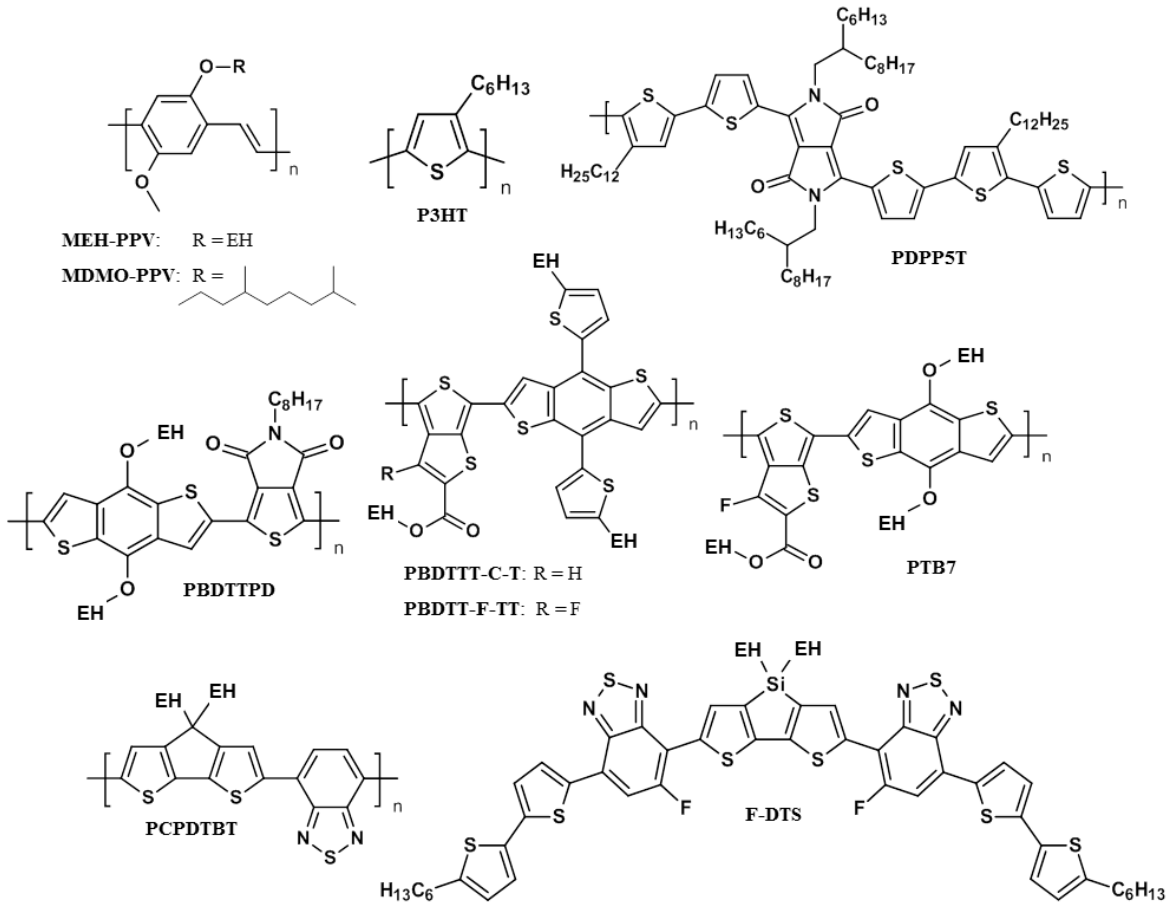

Figure 8. *A selection of common donor materials for OPV. Note that EH stands for 2-ethylhexyl – a common alkyl solubilizing side chain.*

On the other hand, the high electron affinity results in a relatively low LUMO level with respect to the LUMO level of P3HT, at the cost of the attainable V_{OC}. This issue was solved by the indene-C_{60} bisadduct (ICBA) having a LUMO level 0.17 eV higher than that of $PC_{[61]}BM$. In consequence a remarkable high V_{OC} of 0.84 V and hence an increase to 5.44 % PCE when blended with P3HT was observed, whereas the reference cell with $PC_{[61]}BM$ exhibits a V_{OC} of 0.58 V and a PCE of 3.88% PCBM.[35] After the optimization, the P3HT:ICBA blend achieved even a PCE of 6.48 %.[36] However, the light absorption properties of fullerene based electron acceptors are in general poor. Additional challenging synthesis and purification after chemical modification make fullerenes and its derivatives a cost intensive material for large area photovoltaics. This motivated researchers to look for alternative electron acceptors[37, 38], whereas PBI is one of the most promising one for several reasons: PBI exhibit high extinction coefficients of 10^4 – 10^5 M^{-1} cm^{-1} in the visible range from 400 to 600 nm combined with suitable electron affinity of – 3.9 eV.[39] Both, optical and

electronic properties can be tuned via chemical modification of the π-conjugated core or through extension of the conjugated system.[40, 41] Furthermore, an electron mobility as high as 2.1 cm^2 V^{-1} s^{-1} were measured by OFET.[42] The synthesis and purification is easier and cheaper compared to fullerene derivatives and can be carried out on large scale. Additionally, PBI is known for its high photostability and hence used for dyes and pigments for many years.[43] In OPV, a PBI based acceptor was already used by Tang *et al*. in the very first vacuum processed organic bilayer solar cell. For bulk heterojunction solar cells PBI can be blended with a donor polymer such as P3HT. A prominent one is the PBI 1 shown in Figure 8, which was first blended with P3HT by Friend *et al*.[44] Here, also a huge impact of the solvent on the morphology was observed: A blend of P3HT and PBI 1 spin coated from CB showed large crystals of PBI due to its high tendency to aggregate, whereas the same blend system results in an intermixed network when spin coated from chloroform (CF). This was ascribed to the fast evaporation of CF giving not enough time for the PBI to aggregate. Additional optimization of the CF spin coated blend was done and a combination of hot substrate spin coating, annealing and cooling in liquid nitrogen was found to give the highest J_{SC} resulting in an overall PCE of 0.25 %.[45] However, in both cases, the PCE was poor compared to a P3HT:PCBM blend solar cell. Similar findings were obtained by Howard *et al*.: a polymer:PBI 1 blend spin coated from CF showed well intermixing of both components leading to strong non-geminate recombination. In contrast to that, spin coating of the same blend from toluene results in large PBI aggregates. He found, that excitons generated inside the PBI aggregates rather convert into intermolecular states, which do not contribute to further charge generation. It was also shown, that such intermolecular states with excimer like emission at 620 nm[46] exhibit much shorter diffusion length compared to the exciton state,[47] which would in consequence need much smaller domain sizes for charge generation. Indeed, the strong ability of the PBI to aggregate via π-π steaking, causing big domain sizes, turned out to be a serious issue in polymer:PBI blend systems. Beside the intermolecular state formation, the charge transport suffers from grain boundaries and poor interconnection between large PBI crystals. Therefore two concepts were applied to control the nanomorphology and to allow excited state diffusion (exciton or excimer) towards the donor / acceptor interface layer for charge generation: First, control over aggregation by chemical modification of PBI 1 to inhibit intermolecular state formation and guarantee relatively long exciton diffusion lengths and second, reducing the PBI domain size in the range of the intermolecular state diffusion length, while keeping the chemical structure of PBI 1.

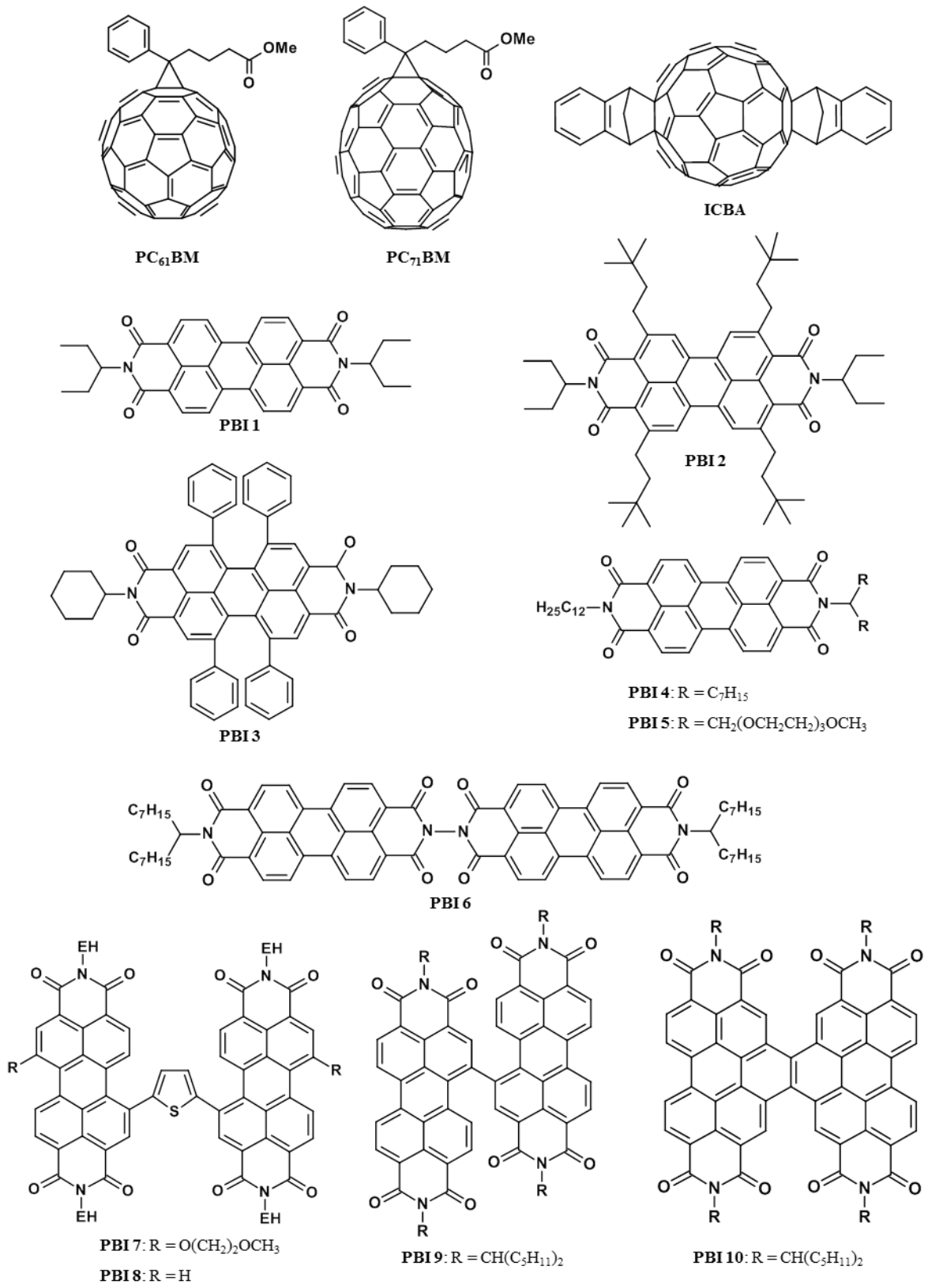

Figure 9. *A selection of common acceptor materials based on fullerene and perylene bisimides for organic solar cells.*

Following the first concept, Kamm *et al*. introduced branched alkyl substituents to the PBI core and achieved for PBI 2 an exciton like emission peaking at 590 nm, whereas PBI 1 showed an excimer like emission at 640 nm. As expected, the J_{SC} was slightly higher for PBI 2, when blended with P3HT resulting in a PCE of 0.5 %.[48] Additionally, it was shown, that core substitution not only suppresses the crystallinity but also enables tuning of the PBI phase size.[49] For instance, phenyl substituents at the bay position in PBI 3 cause twisting of the PBI core and hence inhibit aggregation, which finally leads to a PCE of 4.1 % using PTB7 as donor polymer.[50] Another approach considers the fact, that the intermolecular state in PBI is almost exclusively found in H-aggregates, whereas exciton diffusion length up to 96 nm where measured for J-aggregates.[51] Following that approach, Marks *et al*. presented slip stacked PBI aggregates with different slip angles depending on the core substituent. Increasing the slip angle leads to an increase of J_{SC} and the overall efficiency. However, with increasing the slip angles also the LUMO level of the PBI decreases and hence providing more excess energy for charge separation, which could also explain the higher J_{SC}.[52]. As mentioned already before, core substitution does not only affect the aggregation but also the photophysical and electronic properties of the PBI, which makes an analysis of the particular contribution of a PBI excimer to the increased J_{SC} complex in this system.

Following the second concept, several approaches turned out to be suitable in order to reduce domain size of PBI 1. Rajaram *et al*. used for instance a P3HT:PBI diblock copolymer as compatibilizer to reduce the PBI 1 domain size resulting in a higher PCE of 0.55 % due to higher J_{SC} compared to a PCE of 0.37 % without compatibilizer.[53] Thermal annealing was also found to have a huge impact of the PBI 1 domain size, where increasing temperature leads to an increased intermolecular state emission due to larger PBI 1 domains.[54] However, adjusting the PBI 1 domain size by thermal annealing to the intermolecular state diffusion length quenched this emission at the donor / acceptor interface and lead to higher photocurrent generation.[55] Furthermore solvent additives were used to control the morphology in both PTB7:PBI 1 and F-DTS:PBI 1 blend system.[56] Using diiodooctane (DIO) as solvent additive, the PBI domain size in a PBDTTT-CT:PBI 1 blend could be significantly reduced resulting in a PCE of 3.64 % compared to a PCE of 2.67 % without DIO. The authors mentioned, that not only the smaller PBI domain size causes the higher PCE, but also an improved electronic coupling of the adjacent PBI aggregates and a balanced charge transport between holes and electrons.[57] The impact of using DIO as additive was even more shown in a blend of PBI 1 with the small molecule donor F-DTS, where the PCE increased dramatically from 0.13 % (without DIO) to 3.1 % (with DIO).[58, 59] This blend

system could be further optimized by changing the F-DTS:PBI 1 ratio to 1.3:1 resulting in a surprising high PCE of 5.1 %.[60] This is remarkable, since PBI 1 is known for its high tendency to aggregate in large crystals as mentioned above. However, in blend systems with F-DTS high miscibility with PBI 1 was found and almost no aggregation. Here DIO allows PBI aggregation and higher crystallinity in both phases, donor and acceptor was observed, leading to a higher photocurrent and hence photovoltaic performance. It should be noted, that especially in blends with LBG donor materials, such as PBDTTT-CT or F-DTS, energy transfer from PBI 1 to the donor might contribute significantly to the photocurrent, since the emission of PBI 1 (excitons and excimer) overlaps with the donor absorption. Although the PCE of PBDTTT-CT:PBI 1 and F-DTS:PBI 1 are high for PBI based solar cells, they are still significantly lower than the respective blends with fullerene based acceptors.[30, 34] The lower PCE was attributed to the lower photocurrent represented by the relatively low IQE of only 45% in F-DTS:PBI 1 compared to 90 % in F-DTS:PCBM. The IQE value was rather independent on the light intensity suggesting a low non-geminate recombination. In contrast to that, the IQE value was found to increase to 60 % at reverse applied voltage of -10V, an indication for electrical field dependent charge generation or charge transport.[58, 59] The PBI crystalline correlation length (a measure of the distance over which crystalline order is preserved) in F-DTS: PBI 1 blend was found to be 7.4 ± 3.3 nm,[59] which might not be sufficient for efficient charge separation and charge delocalization / stabilization.[61]

The efficiency of charge separation based on the CT-state at the donor:PBI interface depends highly on the order of the PBI and a certain electronic coupling between the adjacent PBI molecules seems to be necessary to take the charge fast away from the interface and hence avoid recombination. This should be especially keep in mind for the first concept, since here the chemical modification of the PBI disturbs the aggregation and likewise the electronic coupling. Asbury *et al*. has shown in a P3HT blend system, that non-crystalline PBI derivate exhibits activated charge separation, whereas charge separation with PCBM occurs through barrierless pathway. He proposed an improved charge separation with reduced activation energy in case of highly crystalline PBI phase.[62] Indeed, a crystalline PBI derivative exhibiting higher electron mobility than PCBM has shown to be more efficient in charge photogeneration even at low energetic driving forces with respect to PCBM.[63] This was furthermore confirmed for a series of aggregating PBI derivatives leading to the same result.[64] However, the high mobility expected for crystalline PBI phase might not be maintained through the whole bulk when blended with a polymer like PBDTTT-CT due to missing percolation pathways between the PBI domains. Consequently this poor charge

transport in bulk limits the performance of PBDTTT-CT:PBI solar cells compared to PBDTTT-CT:$PC_{71}BM$, even if charge-separation and non-geminate recombination dynamics were observed to be strikingly similar for both blend systems.[65] One way to solve the conflict of avoiding crystallinity while keeping the charge mobility high is the approach of liquid crystals. Liquid crystals are known for their supramolecular assembly and high electron mobilities of 1.3 cm^2 V^{-1} s^{-1} in SCLC,[66] while at the same time showing a reduced crystallinity and self-healing properties leading to reduction of structural defects like grain boundaries.[67] With respect to PBIs, Thelakkat *et al*. observed a different behavior in terms of charge mobility between the crystalline PBI 4 and the liquid crystalline PBI 5. Both PBIs exhibit similar electron mobility in as-cast films. However, annealing allows structural reorganization which leads to an increase of two orders of magnitude in the case of the liquid crystalline PBI 5, whereas the electron mobility of the crystalline PBI 4 decreases by a factor of four.[68] Based on this result in chapter 3, the impact of crystallinity versus liquid crystallinity on the charge carrier yield and non-geminate recombination for these two PBIs when blended with P3HT is investigated.

It was also reported that the efficiency of CT-state formation and CT-dissociation depends on the electronic structure of the acceptor and fundamental differences between PBI with PCBM were found. For instance, Bredas *et al*. calculated that the CT-recombination in a α-sexithienyl/PBI system is much faster than in a α-sexithienyl/PCBM system and hence competes with CT-dissociation. It is worth to note, that this theoretical calculation was applied just on the single donor / acceptor system and did not involve any aggregation effects e.g. of the acceptor.[69] Troisi *et al*. calculated the rate constant for CT-state formation based on a donor exciton and provides an explanation why PCBM as acceptor leads to high rate constants compared to other small molecule acceptors such as PBI. In particular, he considers the charge transfer in the Marcus inverted region, where an increase of the Gibbs free energy leads to an increase in activation energy and hence a decreased rate for the electron transfer reaction. However, in PCBM the access to low lying excited states in the anionic form of PCBM leads to decreased Gibbs free energy and consequently an increased rate constant for these excited states, respectively. With regard to PBI, he suggests to link two PBI units via a methylene bridge in order to create low lying excited states for an increase of CT-formation.[70] Such low lying exited states could be already found experimentally in linked PBI dimers.[71]

In OPV the concept of linked PBIs was first realized by Narayan *et al*. by connecting two PBIs directly at the N-terminal leading to PBI 6. In a blend with PBDTTT-CT as donor he observed a 10-fold increase in J_{SC} for the linked PBI when compared to the non-linked PBI as reference. However, the increase J_{SC} was attributed to the disturbed stacking of PBI 6 leading also to smaller PBI domain sizes and an increase in dimensionality, whereas the role of possible low lying excited states for the PBI 6 anionic form was not discussed.[72] Following detailed studies on the same blend system confirmed an intermittent mixing where both, donor and acceptor contribute equally to the photocurrent and an overall PCE of 3.20 % was found.[73] Yao *et al*. linked two PBIs at the bay position via a thiophene bridge resulting in PBI 7. Also here the PBI 7 domain size was dramatically reduced to approximately 30 nm compared to 200-700 nm of the monomeric analog of PBI in blend with PBDTTT-CT. Consequently, an increase in *FF* and an over 25-fold increase in J_{SC} were observed for PBI 7 resulting in a remarkable high PCE of 4.03 %. It is worth to note, that DIO is again essential as additive and leaving out DIO leads to a PCE of only 0.77 %.[74] A detailed optimization of the DIO content in combination with solvent annealing to reconstruct the morphology for the same blend system leads to further increase in J_{SC} to 12.8 mA/cm^2 and *FF* to 56.4 % and an overall PCE of 6.1 %.[75] Using F-DTS as small molecule donor, the impact of additives on the PBI 8 domain size was controlled and finally, a direct correlation between the PBI domain size and J_{SC} was found.[76] Subsequently a number of other dimeric PBIs were synthesized predominately to top the PCE and to demonstrate the potential of this approach, whereas an understanding of the structural and photophysical consequences is often fragmentary. However, the following additional candidates are presented to highlight the progress in linking PBI units for high efficient small molecule acceptors. Zhan *et al*. investigated the impact of the length of the thiophene bridge and the number of thiophenes was varied from zero up to three units. Using PBDTTT-CT as donor polymer the PBI dimer with only one thiophene unit was found to give the best performance of 3.6 % PCE, whereas direct linking of two PBIs result in poor performance of 0.7 % PCE. This was attributed to the high dihedral angle of 62.7° in direct linked PBIs, which does not allow π-π steaking leading to inability to form PBI domains and conversely, large crystalline PBDTTT-CT domains were found. As a result hole transport was promoted, whereas electron transport was restricted.[77] However, taking the same donor polymer PBDTTT-CT and after small changes to the solubilizing chains of the direct linked PBI result in PCE enhancement to 3.63 % for PBI 9.[78] This clearly shows the impact of solubilizing chains on the morphology which is supported by further examples at the end of this section. A very similar but more suitable donor polymer for PBI 9

seems to be PBDTT-F-TT due to a deeper HOMO level and red-shifted absorption with respect to PBDTTT-CT resulting in a PCE for normal device geometry of 4.21 % and for inverted device geometry of 5.31 %.[79] PBI 9 was also blended with others donor polymers and high efficiencies between 4 to 5 % are reported.[80, 81, 82] Another candidate for high efficient PBI based acceptors was presented by Nuckolls *et al*. and was formed by fusion of two PBI units with a two-carbon bridge. In combination with PTB7 or PBDTT-TT as donor polymer high PCEs between 4.5 and 6.1 % were obtained, whereas photocharge generation was found to originate from both, donor as well as acceptor excitons.[83] Beside PBI dimers also trimers and tetramers were synthesized, motivated by an expected improved three dimensional charge transport.[84, 85, 86, 87] In order to get the highest PCE not only an optimal matching of the photophysical and energetic properties between donor and acceptor, but also a balance between miscibility and aggregation of the components for a beneficial morphology is necessary. This enables especially PBI based acceptors more opportunities for chemical fine-tuning and thus was shown also for PBI-dimers to gain improved photovoltaic performance.[88, 89]

2.5.2 Interlayers and electrodes

As seen from Figure 6 the photoactive layer is, no matter if in normal or inverted geometry, sandwiched between interlayers, in particular hole and electron blocking layers, and the electrodes for charge collection. In this section the interlayers and electrodes will be treated together, since they appear often also as hybrids. This is especially the case for a series of transparent conducting electrodes (TCEs), which will be discussed in detail here.

The reasons to use interlayers between the photoactive layer and the electrodes instead of sandwiching the photoactive layer directly between metallic electrodes are manifold. The main reason to use interlayers is to prevent recombination of charges at the opposite electrode. This is especially important for bulk heterojunction solar cells, since here donor and acceptor phase are distributed over the whole photoactive layer. When the acceptor phase is in direct contact with the anode and electrons from the acceptor LUMO may recombine with already extracted holes. However, when an electron blocking layer is integrated exhibiting a higher LUMO level than the acceptor, this recombination is heavily suppressed. Similarly, a hole blocking layer at the cathode having a deeper energy level as the donor hinders holes from the donor to recombine with previous extracted electrons at the cathode. As a consequence of the suppressed recombination high photocurrent densities can be achieved even at weak electric field resulting in an improved *FF* and an overall better PCE.[90] Depending upon the blocking layer material, e.g. in case of metal oxides, the energy level is described by conduction band and valence band rather than HOMO and LUMO respectively. Beside the blocking effect of opposite charges, the interlayers are of course also responsible for the extraction of the desired charges. The involved energy levels for charge extraction predominantly define the built in voltage of the device and hence the electric field strength. High electric field strength is needed for high charge carrier extraction efficiency and to restrict recombination processes inside the photoactive layer. The selection of interlayers has therefore a direct impact on the device PCE. For instance, the PCE of a device based on a P3HT:PCBM blend varies from 2.3 % to 4.2 % using different interlayers.[91] Common interlayers are based on both, organic and inorganic materials and depending on their energy levels, they are used for hole extracting layer (e.g. MoO_3, NiO, PEDOT:PSS) or electron extracting layers (e.g. TiO_x, ZnO). The choice of suitable interlayers depends not only on their energy levels but also on their processability. In this context the surface energy plays an important role, when the photoactive layer is processed on top of the interlayer and vice versa. Additional to that, the so-called self-assembled monolayers (SAMs) are used to control both, work function via formation of dipoles and surface energy. A requirement for all interlayers is a high

transparency to minimize parasitic absorption and thus maximize light absorption in the photoactive layer.[92] An overview of the several interlayer materials and their functions is given in literature reviews.[91, 93, 94] Finally, electrodes are needed for charge collection and no matter, whether normal or inverted geometry is used, one can define the electrode right on top of the substrate as front electrode and the counter electrode as back electrode (Figure 10). For the front electrode usually, ITO is used as TCE to allow light transmission towards the photoactive layer. Depending on the device geometry, the back electrode is made either from a low (for anode) or high (for cathode) work function metal (Figure 10a). As seen in Figure 10a, the metal back electrode allows reflection of the light back to photoactive layer and interlayers such as titanium oxides (TiOx) are also used as optical spacer to adjust the maximum of light intensity within the photoactive layer.[95] In contrast to that, using a transparent back electrode enables the fabrication of OPV devices on non-transparent substrates such as paper (Figure 10b). Having front and back electrodes transparent lead to semitransparent OPV devices and opens up new applications for windows in building integrated photovoltaics and automotive roofs (Figure 10c).

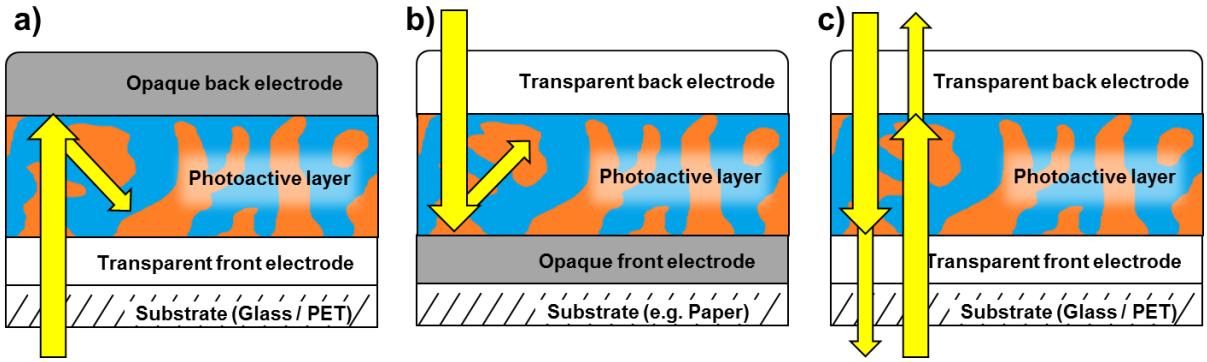

Figure 10. *Possible arrangements of transparent conducting electrode as a) front electrode, b) back electrode and c) front & back electrode.*

In the following, currently used efficient TCEs especially for OPV will be briefly demonstrated to illustrate the variety of materials and its applications. Two elementary properties are essential for a high performing TCE: high optical transparency and low sheet resistance ($R_{\square}$). The optical transparency is of course necessary for high light transmittance (T) and can be easily measured by UV / Vis absorption spectroscopy. Typically, T is given for 550 nm, which corresponds to the maximum of human eye luminosity curve.[96] A low $R_{\square}$ is needed for fast charge collection over the entire size of the photoactive area. An increase in $R_{\square}$ may increase the probability for recombination at the electrode / photoactive interface,

leading to a decreased photovoltaic performance. $R_{\square}$ depends on the material specific resistivity ρ and the thickness d of the electrode layer according to Eq. 10. Usually $R_{\square}$ is measured by a four-point probe method, but can be also determined by a two-point probe method as deduced in the following.

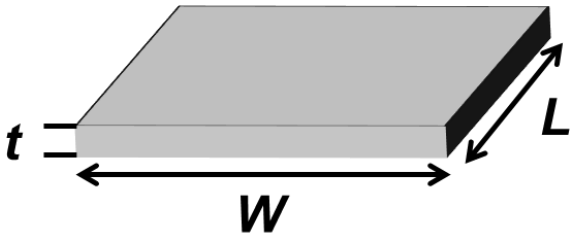

$$R_{\square} = \frac{\rho}{t} \qquad (10)$$

$$R = \frac{\rho}{t} \cdot \frac{L}{W} \qquad (11)$$

$$R = R_{\square} \cdot \frac{L}{W} \qquad (12)$$

Figure 11. *Illustration to derive the sheet resistance $R_{\square}$ of a thin conducting layer having the thickness t, width W and length L.*

In Figure 11 the respective electrode is defined by the thickness *t*, the width *W* and the length *L*. The resistance *R* along *L* can be then measured and it is connected to the resistivity ρ of the material and *L* as well as the cross section $t \cdot W$ according to Eq. 11. Combining Eq. 10 and Eq. 11 leads to Eq. 12 and for $L = W$, the resistance measured between the edges perpendicular to *L* equals to $R_{\square}$. However, as seen from Eq. 10, $R_{\square}$ depends on *t* and the thicker the electrode layer is, the smaller is $R_{\square}$, but also the lower is *T*. Therefore, a compromise between low $R_{\square}$ and high *T* has to be found for the optimal electrode thickness *t*. A quantitative way to connect the optical transparency with the sheet resistance is ratio of electrical (σ_{DC}) and optical (σ_{OP}) conductivity, the so called figure of merit (FOM) given by the Eq. 13.[97] Here Z_0 is the impedance of free space (377 Ω)[98], $R_{\square}$ is the sheet resistance and *T* corresponds to the transmittance.

$$FOM = \frac{\sigma_{DC}}{\sigma_{OP}} = \frac{Z_0}{2R_{\square}\,(T^{(-0.5)}-1)} \qquad (13)$$

For instance, commercial ITO having *T*=97% and $R_{\square}$ = 15 – 30 Ω/□ exhibits FOM values of 400–800.[97] However, it should be noted, that also other definitions of FOM were proposed,[99] while the one presented here is the most popular.[100]

Thus the high *T* along with a sufficiently low $R_{\square}$ of ITO is the reason, why ITO is one of the most common TCE not only for OPV, but also for organic light emitting diodes, displays and

touchscreens. Beside ITO, also other tin oxide based TCE are known such as fluorine doped tin oxide (FTO) or aluminum doped zinc oxide (AZO). FTO requires high deposition temperatures above 600°C, which makes the use of FTO for flexible polymer substrates difficult,[99] whereas AZO is attacked easily by acid or alkaline chemical groups and therefore also by the acidic PEDOT:PSS.[101] In contrast to that, ITO is much more resistant against acids or bases[99] and can be deposited also on flexible substrates such as PET, although a higher thickness is required to achieve a $R_{\square}$ of 12.6 Ω/□ at the cost of T.[102] On the other hand, transparent conducting oxides are brittle and form cracks on flexible substrates after bending and a significant increase in resistance with increasing strain for ITO on polymer substrates was found.[103] In addition, indium is a rare and expensive element[99] and the production of ITO is highly energy demanding. Considering a complete organic solar cell, a share of over 35% for ITO on the overall energy demand in production was determined.[6] This may hamper OPV to be produced inexpensively on large flexible substrate, which motivated researchers to look for alternative TCEs. Based on preliminary studies on carbon nanotubes (CNTs) and their optical and electrical properties in thin films,[104, 105] Gruner *et al*. replaced ITO by a 30 nm CNT thin film coated on PET (T=85%, $R_{\square}$ =200 Ω/□), whereas PEDOT:PSS was used to smooth the surface and to further decrease $R_{\square}$ to 160 Ω/□. Finally, a PCE of 2.5 % using a P3HT:PCBM blend was achieved, whereas the ITO reference device exhibits 3 % PCE.[106] Additionally, the sheet resistance was reduced using chemical dopants and through mechanical pressing to improve the contact between the CNTs.[107] Although CNT electrodes were proposed for cheap large area production, the intercalation of CNTs into the active layer lowers significantly the device performance.[108] Using a PTB7:$PC_{71}BM$ blend Matsuo *et al*. achieved 6.04 % PCE which is 83% of the ITO reference device (PCE of 7.48%) with a MoO_x doped and PEDOT:PSS over coated CNT electrode. However, it was found that MoO_x forms cracks through bending, which leads to a decreased in PCE.[109] In contrast to that, a graphene based TCE (T=92%, $R_{\square}$ =300 Ω/□) was quite stable even after 100 bending cycles using again PTB7:$PC_{71}BM$ as photoactive layer. Graphene was used for both, anode and cathode and PCEs of 6.1 % and 7.1 % were achieved.[110] Analogous to CNT, $R_{\square}$ in graphene TCE can be further reduced with increasing number of graphene layers, but only at the cost of T, or by chemical doping resulting in a $R_{\square}$ of 30 Ω/□.[111] However, a big drawback of using graphene for TCE is the high cost due to the sophisticated syntheses and issues in maintaining high quality.[112] Beside CNT and graphene also highly doped PEDOT:PSS (T=98.1 %, $R_{\square}$ =145 Ω/□) itself was successfully used as TCE resulting in 4.1 % PCE for a P3HT:PCBM blend system, which is actually the same as achieved for the ITO reference

(4.11 % PCE).[113] At the first instance, it is surprising that the mentioned alternative TCEs with $R_{\square}$ much higher than that of ITO still gives quite similar performance. However, this is only possible due to the small device areas and it should be noted, that the power loss (P_{loss}) depends on $R_{\square}$ and the device area ($L \cdot W$) according to Eq. 14.

$$P_{loss} = (J \cdot L \cdot W)^2 \cdot R_{\square} \cdot \frac{W}{3 \cdot L} \qquad (14)$$

There is J the current density, L is the length and W is the width as defined in Figure 11 and $R_{\square}$ is the sheet resistance. Having for instance J_{MPP} = 8 mA/cm^2 and V_{MPP} = 500 mV, the fraction of power loss P_{loss} / ($J_{MPP} \cdot L \cdot W \cdot V_{MMP}$) is limited to 10 % for $R_{\square}$ = 10 Ω/□, when W is kept below 1.4 cm, whereas for $R_{\square}$ = 160 Ω/□, only when W is below 0.34 cm.[106] A further decrease of $R_{\square}$ especially for larger device areas is therefore needed.

As mentioned above, carbon based TCEs such as CNT, graphene and PEDOT:PSS needs often to be doped in order to increase the charge carrier density and hence the conductivity. This is not the case for metal based TCEs due to the intrinsic high charge carrier density of metals. Thin metal films are known as semitransparent electrode with $R_{\square}$ below 20 Ω/□ for a long time.[114] Unfortunately, ultrathin metal films exhibit generally only a very low transmittance for sufficiently low $R_{\square}$ values, leading to lower J_{SC}.[115] Ag nanowires are used similar to CNT as TCE, whereas much lower $R_{\square}$ in the range of 9 Ω/□ (T = 89%) to 69 Ω/□ (T=95%) is observed. To reduce the conduction resistance between Ag nanowires, further treatments such as pressing or nano-welding is required.[116] Additional over coating with PEDOT:PSS significantly improved the performance and a PCE even higher than for the ITO reference were obtained.[117] However, similar to CNT, Ag nanowires may lead to shorts especially in roll-to-roll fabrication and breakdown of Ag nanowires due to current induced heating reduces the performance during the time.[118] Beside Ag nanowires, also Cu nanowires are suitable for TCE in OPV[119] and furthermore TCEs based on electro spun nanofibers exhibits reasonable low $R_{\square}$ between 15 and 21 Ω/□ while having high T of approximately 90% or higher for Cu, Au and Ag and roughly 70 % for Al.[120] Apart from that, metals grids in combination with high conducting PEDOT:PSS are used as front TCE on flexible substrates with comparable performance to ITO.[121] The grid is often inkjet printed from an Ag ink resulting e.g. in 130 nm high lines, which needs to be over coated or embedded into the substrate and because of a line width of 100 µm and more, the grid is still visible to the naked eye.[122]

An elegant method to fabricate a non-visible metal network (T_{550nm}=86 %, $R_{\square}$ =10 Ω/□) is part of this thesis and presented in chapter 5. The metal network was successfully incorporated in OSCs, which exhibits a similar performance like the ITO reference. The big advantage of this metal network is the potential for easy and cheap production on a large scale and the variety of materials, which may be used for the network.

Many of the TCEs presented here for the front electrode (Figure 10a) can be fabricated also on top of the photoactive layer (Figure 10b), which is especially interesting for non-transparent substrates such as paper.[123, 124] Having both front and back electrode transparent (Figure 10c) enables semitransparent organic solar cells, where the color can be tuned through selection of the photoactive layer material, respectively. This opens new application and markets for building integrated OPV and automotive roof top applications. Many semitransparent OPV devices reported in the literature use ITO as front electrode and Ag nanowires,[125, 126, 127, 128, 129] metal / metal oxide[130, 131, 132] or PEDOT:PSS[133, 134, 135, 136] as back electrode. However, due to the drawbacks of ITO mentioned above, ITO-free semitransparent OSC are of special interest and there are a few examples in the literature as well. Jen *et al*. used PEDOT:PSS based front and back electrodes for a P3HT:$PC_{[61]}$BM system, but achieved a rather low PCE of only 0.5 %.[137] More successful was a combination of Ag nanowires and PEDOT:PSS or metal oxides for both electrodes leading to PCEs between 2.0 and 2.3% when P3HT as donor polymer is used[138, 139] and a PCE of 2.9 % using a LBG-polymer.[140] Current collecting grids printed from Ag inks in combination with PEDOT:PSS are well established as front and back electrodes for large area roll-to-roll fabrication of ITO-free OPV. However, here the dimensions of the grid ranging from 200 to 300 µm are visible to the naked eye and hence not ideal for window applications,[141] where a complete transparent electrode is desired.

Based on the presented work in chapter 5, the metal network was successfully fabricated on top of a photoactive layer exhibiting a low haze and a high FOM. The combination with the metal network front electrode from chapter 5 leads to an ITO-free semitransparent OPV device as presented in chapter 6.

References

[1] (a) http://www.solarte.de/index.php/de/#galerie, 28.09.2015
(b) http://www.solarte.de/index.php/de/?file=files/theme_data/pdf/PI_Expo_20150507_en.pdf, 28.09.2015

[2] Schlenker, C. W.; Thompson, M. E., The molecular nature of photovoltage losses in organic solar cells. *Chem. Commun.*, **2011**, *47*, 3702-3716.

[3] Søndergaard, R.; Hösel, M.; Angmo, D.; Larsen-Olsen, T. T.; Krebs, F. C., Roll-to-roll fabrication of polymer solar cells. *Mater. Today*, **2012**, *15* (1-2), 36-49.

[4] Forberich, K.; Guo, F.; Bronnbauer, C.; Brabec, C. J., Efficiency Limits and Color of Semitransparent Organic Solar Cells for Application in Building-Integrated Photovoltaics. *Energy Technol.*, **2015**.

[5] Darling, S. B.; You, F., The case for organic photovoltaics. *RSC Adv.*, **2013**, *3*, 17633-17648.

[6] Anctil, A.; Babbitt, C. W.; Raffaelle, R. P.; Landi, B. J., Cumulative energy demand for small molecule and polymer photovoltaics. *Prog. Photovolt. Res. Appl.*, **2013**, *21* (7), 1541-1554.

[7] Bredas, J.-L., Mind the gap! *Mater. Horiz.*, **2014**, *1*, 17-19.

[8] Chamberlain, G. A., Organic solar cells: A review. *Solar Cells*, **1983**, *8* (1), 47-83.

[9] Deibel, C.; Dyakonov, V., Polymer–fullerene bulk heterojunction solar cells. *Rep. Prog. Phys.*, **2010**, *73* (9), 096401.

[10] Tang, C- W., Two layer organic photovoltaic cell. *Appl. Phys. Lett.*, **1986**, *48*, 18.

[11] Savoie, B. M.; Jackon, N. E.; Marks, T. J.; Ratner, M. A., Reassessing the use of one-electron energetics in the design and characterization of organic photovoltaics. *Phys. Chem. Chem. Phys.*, **2013**, *15*, 4538-4547.

[12] Deibel, C.; Mack, D.; Gorenflot, J.; Schöll, A.; Krause, S.; Reinert, F.; Rauh, D.; Dyakonov, V., Energetics of excited states in the conjugated polymer poly(3-hexylthiophene). *Phys. Rev. B*, **2010**, *81*, 085202.

[13] Sariciftci, N. S.; Smilowitz, L.; Heeger, A. J.; Wudl. F., Photoinduced Electron Transfer from a Conducting Polymer to Buckminsterfullerene. *Science*, **1992**, *258* (5087), 1474-1476.

[14] Yu, G.; Gao, J.; Hummelen, J. C.; Wudl, F.; Heeger, A. J., Polymer Photovoltaic Cells: Enhanced Efficiencies via a Network of Internal Donor-Acceptor Heterojunctions. *Science*, **1995**, *270* (5243), 1789-1791.

[15] Liu, Y.; Zhao, J.; Li, Z.; Mu, C.; Ma, W.; Hu, H.; Jiang, K.; Lin, H.; Ade, H.; Yan, H., Aggregation and morphology control enables multiple cases of high-efficiency polymer solar cells. *Nat. Commun*., **2014**, *5*, 5293.

[16] Sánchez-Días, A.; Burtone, L.; Riede, M.; Palomares, E., Measurements of Efficiency Losses in Blend and Bilayer-Type Zinc Phthalocyanine/C60 High-Vacuum-Processed Organic Solar Cells. *J. Phys. Chem. C*, **2012**, *116* (31), 16384-16390.

[17] Shoaee, S.; Mahraeen, S.; Labram, J. G.; Bredas, J.-L., Bradley, D. C. D.; Coropceanu, V.; Anthopoulos, T. D.; Durrant, J. R., Correlating Non-Geminate Recombination with Film Structure: A Comparison of Polythiophene: Fullerene Bilayer and Blend Films. J. *Phys. Chem. Lett*., **2014**, *5* (21), 3669-3676.

[18] Bredas, J.-L-; Norton, J. E.; Cornil, J.; Coropceanu, V., Molecular Understanding of Organic Solar Cells: The Challenges. *Acc. Chem. Res.*, **2009**, *42* (11), 1691-1699.

[19] Menke, S. M.; Holmes, R. J., Exciton diffusion in organic photovoltaic cells. E*nergy Environ. Sci.*, **2014**, *7*, 499-512.

[20] Mikhnenko, O. V.; Blom, P. W. M.; Nguyen, T.-Q., Exciton diffusion in organic semiconductors. *Energy Environ. Sci.*, **2015**, *8*, 1867-1888.

[21] Rao, A.; Chow, P. C. Y.; Gélinas, S.; Schlenker, C. W.; Li, C.-Z.; Yip, H.-L.; Jen, A. K.-Y.; Ginger, D. S.; Friend, R. H., The role of spin in the kinetic control of recombination in organic photovoltaics. *Nature*, **2013**, *500*, 435-439.

[22] Snaith, H. J., How should you measure your excitonic solar cells. *Energy Environ. Sci*, **2012**, *5*, 6513-6520.

[23] Shirakawa, T.; Umeda, T.; Hashimoto, Y.; Fujii, A.; Yoshino, K., Effect of ZnO layer on characteristics of conducting polymer/C_{60} photovoltaic cell. *J. Phys. D: Appl. Phys*., **2004**, *37* (6), 37847.

[24] Shaheen, S. E.; Brabec, C. J.; Sariciftci, N. S.; Padinger, F.; Fromherz, T.; Hummelen, J. C., 2.5% efficient organic plastic solar cells. *Appl. Phys. Lett.*, **2001**, *78*, 841.

[25] Dang, M. T.; Hirsch, L.; Wantz, G., P3HT:PCBM, Best Seller in Polymer Photovoltaic Research. *Adv. Mater.*, **2011**, *23* (31), 3597-3602.

[26] Lee, S.-H.; Kim, D.-H.; Kim, J.-H.; Lee, G.-S.; Park, J.-G., Effect of Metal-Reflection and Surface-Roughness Properties on Power-Conversion Efficiency for Polymer Photovoltaic Cells. *J. Phys. Chem. C*, **2009**, *113* (52), 21915–21920.

[27] Bundgaard, E.; Krebs, F. C., Low band gap polymers for organic photovoltaics. *Sol. Energ. Mat. Sol. Cells*, **2007**, *91* (11), 954-985.

[28] Li, W.; Roelofs, W. S. C.; Wienk, M. M.; Janssen, R. A. J., Enhancing the Photocurrent in Diketopyrrolopyrrole-Based Polymer Solar Cells via Energy Level Control. *J. Am. Chem. Soc.*, **2012**, *134* (33), 13787-13795.

[29] Cabanetos, C.; El Labban, A.; Bartelt, J. A.; Douglas, J. D.; Mateker, W. R.; Frechet, J. M. J.; McGehee, M. D.; Beaujuge, P. M., Linear Side Chains in Benzo[1,2-b:4,5-b′] dithiophene–Thieno[3,4-c]pyrrole-4,6-dione Polymers Direct Self-Assembly and Solar Cell Performance. *J. Am. Chem. Soc.*, **2013**, *135* (12), 4656-4659.

[30] Huo, L.; Zhang, S.; Guo, X.; Xu, F.; Li, Y.; Hou, J., Replacing Alkoxy Groups with Alkylthienyl Groups: A Feasible Approach To Improve the Properties of Photovoltaic Polymers. *Angew. Chem. Int. Ed.*, **2011**, *50* (41), 9697-9702.

[31] Cui, C.; Wong, W.-Y.; Li, Y.,Improvement of open-circuit voltage and photovoltaic properties of 2D-conjugated polymers by alkylthio substitution. *Energy Environ. Sci.*, **2014**, *7*, 2276-2284.

[32] Liang, Y.; Xu, Z.; Xia, J.; Tsai, S.-T.; Wu, Y.; Li, G.; Ray, C.; Yu, L., For the Bright Future – Bulk Heterojunction Polymer Solar Cells with Power Conversion Efficiency of 7.4%. *Adv. Mater.*, **2010**, *22* (20), E135-E138.

[33] Peet, J. ; Kim, J. Y.; Coates, N. E.; Ma, W. L.; Moses, D.; Heeger, A. J.; Bazan, G. C., Efficiency enhancement in low-bandgap polymer solar cells by processing with alkane dithiols. *Nat. Mater.*, **2007**, *6*, 497-500.

[34] van der Poll, T. S.; Love, J. A.; Nguyen, T.-Q.; Bazan, G. C., Non-Basic High-Performance Molecules for Solution-Processed Organic Solar Cells. *Adv. Mater.*, **2012**, *24* (27), 3646-3649.

[35] He, Y.; Chen, H.-Y.; Hou, J.; Li, Y., Indene-C60 Bisadduct: A New Acceptor for High- Performance Polymer Solar Cells. *J. Am. Chem. Soc.*, **2010**, *132* (4), 1377-1382.

[36] Zhao, G.; He, Y.; Li, Y., 6.5% Efficiency of Polymer Solar Cells Based on poly(3-hexylthiophene) and Indene-C_{60} Bisadduct by Device Optimization. *Adv. Mater.*, **2010**, *22* (39), 4355-4358.

[37] Lin, Y.; Zhan, X., Non-fullerene acceptors for organic photovoltaics: an emerging horizon. *Mater. Horiz.*, **2014**, *1*, 470-488.

[38] Eftaiha, A., F.; Sun, J.-P.; Hill, I. G.; Welch, G. C., Recent advances of non-fullerene, small molecular acceptors for solution processed bulk heterojunction solar cells. *J. Mater. Chem. A*, **2014**, *2*, 1201-1213.

[39] Ford, W. E.; Hiratsuka, H.; Kamat, P. V., Photochemistry of 3,4,9,10-perylenetetracarboxylic dianhydride dyes. 4. Spectroscopic and redox properties of oxidized and reduced forms of the bis(2,5-di-tert-butylphenyl)imide derivative. *J. Phys. Chem.*, **1989**, *93* (18), 6692-6696.

[40] Marder, S. R.; Huang, C.; Barlow, S., Perylene-3,4,9,10-tetracarboxylic Acid Diimides: Synthesis, Physical Properties, and Use in Organic Electronics. *J. Org. Chem.*, **2011**, *76* (8), 2386-2407.

[41] Wicklein, A.; Kohn, P.; Ghazaryan, L.; Thurn-Albrecht, T.; Thelakkat, M., Synthesis and structure elucidation of discotic liquid crystalline perylene imide benzimidazole. *Chem. Commun.*, **2010**, *46* (13), 2328-2330.

[42] Tatemichi, S.; Ichikawa, M.; Koyama, T.; Taniguchi, Y., High mobility n-type thin-film transistors based on N,N′-ditridecyl perylene diimide with thermal treatments. *Appl. Phys. Lett.*, **2006**, *89*, 112108.

[43] Herbst, W.; Hunger, K., Industrial Organic Pigments: Production, Properties, Applications, 3rd edn., WILEY-VCH, Weinheim, **2004**.

[44] Dittmer, J. J.; Marseglia, E. A.; Friend, R. H., Electron Trapping in Dye/Polymer Blend Photovoltaic Cells. *Adv. Mater.*, **2000**, *12* (17), 1270-1274.

[45] Guo, X.; Bu, L.; Zhao, Y.; Xie, Z.; Geng, Y.; Wang, L., Controlled phase separation for efficient energy conversion in dye/polymer blend bulk heterojunction photovoltaic cells. *Thin Solid Films*, **2009**, *517*, (16), 4654-4657.

[46] Howard, I. A.; Laquai, F.; Keivanidis, P. E.; Friend, R. H.; Greenham, N. C., Perylene Tetracarboxydiimide as an Electron Acceptor in Organic Solar Cells : A Study of Charge Generation and Recombination. *J. Phys. Chem. C*, **2009**, *113*, 21225-21323.

[47] Vertsimakha, Y.; Lutsyk, P.; Palewska, K.; Sworakowski, J.; Lytvyn, O.; Optical and photovoltaic properties of thin films of N,N′-dimethyl-3,4,9,10-acid diimide. *Thin Solid Films*, **2009**, *515* (20-21), 7950-7957.

[48] Kamm, V.; Battagliarin, G.; Howard, I. A.; Pisula, W.; Mavrinskiy, A.; Li, C.; Müllen, K.; Laquai, F., Polythiophene:perylene diimide solar cells - The impact of alkyl-substitution on the photovoltaic performance. *Adv. Energy Mater.*, **2011**, *1*, 297-302.

[49] Zhang, X.; Jiang, B.; Zhang, X.; Tang, A.; Huang, J.; Zhan, C.; Yao, J., Cooperatively Tuning Phase Size and Absorption of Near IR Photons in P3HT: Perylene Diimide Solar Cells by Bay-Modi fi cations on the Acceptor. *J. Phys. Chem. C*, **2014**, *118*, 24212-24220.

[50] Cai, Y.; Huo, L.; Sun, X.; Wei, D.; Tang, M.; Sun, Y., High Performance Organic Solar Cells Based on a Twisted Bay-Substituted Tetraphenyl Functionalized Perylenediimide Electron Acceptor. *Adv. Energy Mater.*, **2015**, *5* (11), 1500032 (1-5).

[51] Marciniak, H.; Li, X.-Q.; Würthner, F.; Lochbrunner, S., One-Dimensional Exciton Diffusion in Perylene Bisimide Aggregates. *J. Phys. Chem. A*, **2011**, *115* (5), 648–654.

[52] Hartnett, P. E.; Timalsina, A.; Matte, H. S. S. R.; Zhou, N.; Guo, X.; Zhao, W.; Facchetti, A.; Chang, R. P. H.; Hersam, M. C.; Wasielewski, M. R.; Marks, T. J., Slip-Stacked Perylenediimides as an Alternative Strategy for High Efficiency Nonfullerene Acceptors in Organic Photovoltaics. *J. Am. Chem. Soc.*, **2014**, *136* (46), 16345–16356.

[53] Rajaram, S.; Armstrong, P. B.; Bumjoon, J. K.; Fréchet, J. M. J., Effect of Addition of a Diblock Copolymer on Blend Morphology and Performance of Poly(3-hexylthiophene):Perylene Diimide Solar Cells. *Chem. Mater.*, **2009**, *21*, (9), 1775-1777.

[54] Singh, R.; Giussani, E.; Mróz, M. M.; Di Fonzo, F.; Fazzi, D.; Cabanillas-González, J.; Oldridge, L.; Vaenas, N.; Kontos, A. G.; Falaras, P.; Grimsdale, A. C.; Jacob, J.; Müllen, K.; Keivanidis, P. E., *Org. Electron.*, **2014**, *15*, 1347-1361.

[55] Ye, T.; Singh, R.; Butt, H.-J.; Floudas, G.; Keivanidis, P. E., ACS Applied Materials & Interfaces, **2013**, *5*, 11844-11857.

[56] Li, M.; Liu, J.; Cao, X.; Zhou, K.; Zhao, Q.; Yu, X.; Xing, R.; Han, Y., *Phys. Chem. Chem. Phys.*, **2014**, *16*, 26917-26928.

[57] Singh, R.; Aluicio-Sarduy, E.; Kan, Z.; Ye, T.; MacKenzie, R. C. I.; Keivanidis, P. E., *J. Mater. Chem. A*, **2014**, *2*, 14348-14353.

[58] Sharenko, A.; Proctor, C. M.; van der Poll, T. S.; Henson, Z. B.; Nguyen, T-Q.; Bazan, G. C., A High-Performing Solution-Processed Small Molecule:Perylene Diimide Bulk Heterojunction Solar Cell. *Adv. Mater.*, **2013**, *25* (32), 4403-4406.

[59] Sharenko, A.; Gehring, D.; Laquai, F.; Nguyen, T.-Q., The Effect of Solvent Additive on the Charge Generation and Photovoltaic Performance of a Solution-Processed Small Molecule:Perylene Diimide Bulk Heterojunction Solar Cell. *Chem. Mater.*, **2014**, *26* (14), 4109-4118.

[60] Chen, Y.; Zhang, X.; Zhan, C.; Yao, J., In-depth understanding of photocurrent enhancement in solution-processed small-molecule:perylene diimide non-fullerene organic solar cells. *Physica Status Solidi A*, **2015**, 1-8.

[61] Veldman, D.; Ipek, Ö.; Meskers, S. C. J.; Sweelssen, J.; Koetse, M. M.; Veenstra, S. C.; Kroon, J. M.; van Bavel, S. S.; Loos, J.; Janssen, R. A. J., Compositional and Electric Field Dependence of the Dissociation of Charge Transfer Excitons in Alternating Polyfluorene Copolymer/Fullerene Blends. *J. Am. Chem. Soc.*, **2008**, *130* (24), 7721-7735.

[62] Pensack, R. D.; Guo, C.; Vakhshouri, K.; Gomez, E. D.; Asbury, J. B., Influence of Acceptor Structure on Barriers to Charge Separation in Organic Photovoltaic Material. *J. Phys. Chem. C*, **2012**, *116* (7), 4824-4831.

[63] Shoaee, S.; An, Z.; Zhang, X.; Barlow, S.; Marder, S. R.; Duffy, W.; Heeney, M.; McCulloch, I.; Durrant, J. R., Charge photogeneration in polythiophene–perylene diimide blend films. *Chem. Commun.*, **2009**, 5445-5447.

[64] Shoaee, S.; Clarke, T. M.; Huang, C.; Barlow, S.; Marder, S. R.; Heeney, M.; McCulloch, I.; Durrant, J. R., Acceptor Energy Level Control of Charge Photogeneration in Organic Donor/Acceptor Blends. *J. Am. Chem. Soc.*, **2010**, *132* (37), 12919-12926.

[65] Shoaee, S.; Deledalle, F.; Tuladhar, P. S.; Shivanna, R.; Rajaram, S.; Narayan, K. S.; Durrant, J. R., A Comparison of Charge Separation Dynamics in Organic Blend Films Employing Fullerene and Perylene Diimide Electron Acceptors. *J. Phys. Chem. Lett.*, **2015**, *6* (1), 201-205.

[66] An, Z.; Yu, J.; Jones, S. C.; Barlow, S.; Yoo, S.; Domercq, B.; Prins, P.; Siebbeles, L. D. A.; Kippelen, B.; Marder, S. R., High Electron Mobility in Room-Temperature Discotic Liquid-Crystalline Perylene Diimides. *Adv. Mater.*, **2005**, *17* (21), 2580-2583.

[67] Pisula, W.; Zorn, M.; Chang, J. Y.; Müllen, K.; Zentel, R., Liquid Crystalline Ordering and Charge Transport in Semiconducting Materials. *Macromol. Rapid Commun.*, **2009**, *30* (14), 1179-1202.

[68] Muth, M.-A.; Gupta, G.; Wicklein, A.; Carrasco-Orozco, M.; Thurn-Albrecht, T.; Thelakkat, M., Crystalline vs Liquid Crystalline Perylene Bisimides: Improved Electron Mobility via Substituent Alteration. *J. Phys. Chem. C*, **2014**, *118* (1), 92-102.

[69] Yi, Y.; Coropceanu, V.; Bredas, J.-L.; A comparative theoretical study of exciton-dissociation and charge-recombination processes in oligothiophene/fullerene and oligothiophene/perylenediimide complexes for organic solar cells. *J. Mater. Chem.*, **2011**, *21*, 1479-1486.

[70] Liu, T.; Troisi, A., What Makes Fullerene Acceptors Special as Electron Acceptors in Organic Solar Cells and How to Replace Them. *Adv.Mater.*, **2013**, *25* (7), 1038-1041.

[71] Jiang, W.; Xiao, C.; Hao, L.; Wang, Z.; Ceymann, H.; Lambert, C.; Di Motta, S.; Negri, F., Localization/Delocalization of Charges in Bay-Linked Perylene Bisimides. *Chem. Eur. J.*, **2012**, *18* (22), 6764–6775.

[72] Rajaram, S.; Shivanna, R.; Kandappa, S. K.; Narayan, K. S., *J. Phys. Lett.*, **2012**, *3*, 2405- 2408.

[73] Shivannna, R.; Shoaee, S.; Dimitrov, S.; Kandappa, S. K.; Rajaram, S.; Durrant, J. R.; Narayan, K. S., Charge generation and transport in efficient organic bulk heterojunction solar cells with a perylene acceptor. *Energy Environ. Sci.*, **2014**, *7*, 435-441.

[74] Zhang, X.; Lu, Z.; Ye, L.; Zhan, C.; Hou, J.; Zhang, S.; Jiang, B.; Zhao, Y.; Huang, J.; Zhang, S.; Liu, Y.; Shi, Q.; Liu, Y.; Yao, J., A Potential Perylene Diimide Dimer-Based Acceptor Material for Highly Efficient Solution-Processed Non-Fullerene Organic Solar Cells with 4.03% Efficiency. *Adv. Mater*., **2013**, *25*, 5791–5797.

[75] Zhang, X.; Zhan, C.; Yao, J., Non-Fullerene Organic Solar Cells with 6.1% Efficiency through Fine-Tuning Parameters of the Film-Forming Process. *Chem. Mater.*, **2015**, *27*, 166−173.

[76] Chen, Y.; Zhang, X.; Zhan, C.; Yao, J., Origin of Effects of Additive Solvent on Film-Morphology in Solution- Processed Nonfullerene Solar Cells. *ACS Appl. Mater. Interfaces*, **2015**, *7*, 6462−6471.

[77] Wang, J.; Yao, Y.; Dai, S.; Zhang, X.; Wang, W.; He, Q.; Han, L.; Lin, Y.; Zhan, X., Oligothiophene-bridged perylene diimide dimers for fullerene- free polymer solar cells: Effect of bridge length. *J. Mater. Chem. A*, **2015**, *3* (24), 13000-13010.

[78] Jiang, W.; Ye, L.; Li, X.; Xiao, C.; Tan, F.; Zhao, W.; Hou, J.; Wang, Z., Bay-linked perylene bisimides as promising non-fullerene acceptors for organic solar cells. *Chem. Commun.*, **2014**, *50*, 1024-1026.

[79] Zang, Y.; Li, C.-H.; Chueh, C.-C.; Williams, S. T.; Jiang, W.; Wang, Z.-H.; Yu, J.-S.; Jen, A. K.-Y., Integrated Molecular, Interfacial, and Device Engineering towards High-Performance Non-Fullerene Based Organic Solar Cells. *Adv. Mater.*, **2014**, *26* (32), 5708-5714.

[80] Ye, L.; Jiang, W.; Zhao, W.; Zhang, S.; Qian, D.; Wang, Z.; Hou, J., Selecting a Donor Polymer for Realizing Favorable Morphology in Efficient Non-fullerene Acceptor-based Solar Cells. *Small*, **2014**, *10* (22), 4658–4663.

[81] Ye, L.; Jiang, W.; Zhaoa, W.; Zhanga, S.; Cui, Y.; Wang, Z.; Houa, J., Toward e fficient non- fullerene polymer solar cells: Selection of donor polymers. *Org. Electron.* **2015**, *17*, 295-303.

[82] Zhao, J.; Li, Y.; Lin, H.; Liu, Y.; Jiang, K.; Mu, C.; Ma, T.; Lai, J. Y. L.; Hu, H.; Yuc, D.; Yan, H., High-efficiency non-fullerene organic solar cells enabled by a difluorobenzothiadiazole-based donor polymer combined with a properly matched small molecule acceptor. *Energy Environ. Sci.*, **2015**, *8* (2), 520-525.

[83] Zhong, Y.; Trinh, M. T.; Chen, R.; Wang, W.; Khlyabich, P. P.; Kumar, B.; Xu, Q.; Nam, C.-Y.; Sfeir, M. Y.; Black, C.; Steigerwald, M. L.; Loo, Y.-L.; Xiao, S.; Ng, F.; Zhu, X.-Y.; Nuckolls, C., Efficient Organic solar cells with helical perylene diimides Electron acceptors. *J. Am. Chem. Soc*., **2014**, *136* (43), 15215–1522.

[84] Lin, Y.; Wang, Y.; Wang, J.; Hou, J.; Li, Y.; Zhu, D.; Zhan, X., A Star-Shaped Perylene Diimide Electron Acceptor for High-Performance Organic Solar Cells. *Adv. Mater*., **2014**, *26* (30), 5137-5142.

[85] Liu, Y.; Lai, J. Y. L.; Chen, S.; Li, Y.; Jiang, K.; Zhao, J.; Li, Z.; Hu, H.; Ma, T.; Lin, H.; Liu, J.; Zhang, J.; Huang, F.; Yuc, D.; Yan, H., Efficient non-fullerene polymer solar cells enabled by tetrahedron-shaped core based 3D-structure small-molecular electron acceptors. *J. Mater. Chem. A*, **2015**, *3*, 13632-13636.

[86] Liu, S.-Y.; Wu, C.-H.; Li, C.-Z.; Liu, S.-Q.; Wei, K.-H.; Chen, H.-Z.; Jen, A. K.-Y., A Tetraperylene Diimides Based 3D Nonfullerene Acceptor for Efficient Organic Photovoltaics. *Adv. Sci.*, **2015**, *2*, 1500014 (1-7).

[87] Chen, W.; Yang, X.; Long, G.; Wan, X.; Chen, Y.; Zhang, Q., A perylene diimide (PDI)- based small molecule with tetrahedral configuration as a non-fullerene acceptor for organic solar cells. *J. Mater. Chem. C*, **2015**, *3*, 4698-4705.

[88] Lu, Z.; Zhang, X.; Zhan, C.; Jiang, B.; Zhang, X.; Chen, L.; Yao, J., Impact of molecular solvophobicity vs. solvophilicity on device performances of dimeric perylene diimide based solution-processed non-fullerene organic solar cells. P*hys. Chem. Chem. Phys.*, **2013**, *15*, 11375-11385.

[89] Ye, L.; Sun, K.; Jiang, W.; Zhang, S.; Zhao, W.; Yao, H.; Wang, Z.; Hou, J., Enhanced Efficiency in Fullerene-Free Polymer Solar Cell by Incorporating Fine-designed Donor and Acceptor Materials. *ACS Appl. Mater. Interfaces*, **2015**, *7* (17), 9274–9280.

[90] Servaites, J. D.; Ratner, M. A.; Marks, T. J., Organic solar cells: A new look at traditional models. *Energy Environ. Sci.*, **2011**, *4*, 4410-4422.

[91] Lai,T.-H.; Tsang, S.-W.; Manders, J. R.; Chen, S.; So, F., Properties of interlayers for organic photovoltaics. *Mater. Today*, **2013**, *16* (11), 424-432.

[92] Armin, A.; Velusamy, M.; Wolfer, P.; Zhang, Y.; Burn, P. L.; Meredith, P.; Pivrikas, A., Quantum Efficiency of organic solar cells: Electro – optical cavity considerations. *ACS Photonics*, **2014**, *1* (3), 173-181.

[93] Steim, R.; Kogler, F. R.; Brabec, C. J., Interface materials for organic solar cells. *J. Mater. Chem.*, **2010**, *20*, 2499-2512.

[94] Chen, L.-M.; Xu, Z.; Hong, Z.; Yang, Y., Interface investigation and engineering – achieving high performancepolymer photovoltaic devices. *J. Mater. Chem*., **2010**, *20*, 2575-2598.

[95] Park, S. H.; Roy, A.; Beaupré, S.; Cho, S.; Coates, N.; Moon, J. S.; Moses, D.; Leclerc, M.; Lee, K.; Heeger, A. J., Bulk heterojunction solar cells with internal quantum efficiency approaching 100 %. *Nat. Photon*., **2009**, *3*, 297-302.

[96] Ellmer, K., Past achievements and future challenges in the development of optically transparent electrodes. *Nat. Photon*., **2012**, *6*, 809-817.

[97] De, S.; Higgins, T. M.; Lyons, P. E.; Doherty, E. M.; Nirmalraj, P. N.; Blau, W. J.; Boland, J. J.; Coleman, J. N., Silver Nanowire Networks as Flexible, Transparent, Conducting Films: Extremely High DC to Optical Conductivity Ratios. *ACS Nano*, **2009**, *3* (7), 1767-1774.

[98] Glover, R. E.; Tinkham, M., Conductivity of Superconducting Films for Photon Energies between 0.3 and 40kTc. *Phys. Rev*., **1957**, *108* (2), 243.

[99] Gordon, R. G., Criteria for Choosing Transparent Conducting Electrodes. *MRS Bulletin*, **2000**, *25* (8), 52-57.

[100] Pekker, Á.; Kamarás, K., A general figure of merit for thick and thin transparent conductive carbon nanotube coatings. *J. Appl. Phys.*, **2010**, *108* (5).

[101] Park, J.-H.; Kang, S. J.; Na, S.-I.; Lee, H. H.; Kim, S.-W.; Hosono, H.; Kim, H.-K., Indium-free, acid-resistant anatase Nb-doped TiO2 electrodes activated by rapid-thermal annealing for cost-effective organic photovoltaics. *Sol. Energ. Mat. Sol. Cells*, **2011**, *95* (8), 2178-2185.

[102] Hao, L.; Diao, X.; Xu, H.; Gu, B.; Wang, T., Thickness dependence of structural, electrical and optical properties of indium tin oxide (ITO) films deposited on PET substrates. *Appl. Surf. Sci.*, **2008**, *254* (11), 3504-3508.

[103] Cairns, D. R.; Witte, R. P.; Sparacin, D. K.; Sachsman, S. M.; Paine D. C.; Crawford, G. P.; Newton R. R., Strain-dependent electrical resistance of tin-doped indium oxide on polymer substrates. *Appl. Phys. Lett.*, **2000**, *76*, 1425.

[104] Hu, L.; Hecht, D. S.; Grüner, G., Percolation in Transparent and Conducting Carbon Nanotube Networks. *Nano Lett.*, **2004**, *4* (12), 2513-2517.

[105] Wu, Z.; Chen, Z.; Du, X.; Logan, J. M.; Sippel, J.; Nikolou, M.; Kamaras, K.; Reynolds, J. R.; Tanner, B. D.; Hebard, A. F.; Rinzler, A. G.,Transparent, Conductive Carbon Nanotube Films. *Science*, **2004**, *305* (5688), 1273-1276.

[106] Rowell, M. W.; Topinka, M. A.; McGehee, M. D.; Prall, H.-J.; Dennler, G.; Sariciftci, N. S.; Hu, L.; Grüner, G., Organic solar cells with carbon nanotube network electrodes. *Appl. Phys. Lett*., **2006**, *88*, 233506.

[107] Zhang, D.; Ryu, K.; Liu, X.; Polikarpov, E.; Ly, J.; Topmsos, M. E.; Zhou, C., Transparent, Conductive, and Flexible Carbon Nanotube Films and Their Application in Organic Light-Emitting Diodes. *Nano Lett*., **2006**, *6* (9), 1880-1886.

[108] Tenent, R. C.; Barnes, T. M.; Bergeson, J. D.; Ferguson, A. J.; To, B.; Gedvilas, L. M.; Heben, M. J.; Blackburn, J. L., Ultrasmooth, Large-Area, High-Uniformity, Conductive Transparent Single-Walled-Carbon-Nanotube Films for Photovoltaics Produced by Ultrasonic Spraying. *Adv. Mater*., **2009**, *21* (31), 3210-3216.

[109] Jeon, I.; Cui, K.; Chiba, T.; Anisimov, A.; Nasibulin, A. G.; Kauppinen, E. I.; Maruyama, S.; Matsuo, Y., Direct and Dry Deposited Single-Walled Carbon Nanotube Films Doped with MoO_x as Electron-Blocking Transparent Electrodes for Flexible Organic Solar Cells. *J. Am. Chem. Soc.*, **2015**, *137* (25), 7982-7985.

[110] Park, H.; Chang, S.; Zhou, X.; Kong, J.; Palacios, T.; Gradečak, S., Flexible Graphene Electrode-Based Organic Photovoltaics with Record-High Efficiency. *Nano Lett*., **2014**, *14* (9), 5148-5154.

[111] Bae, S.; Kim, H.; Lee, Y.; Xu, X.; Park, J.-S.; Zheng, Y.; Balakrishnan, J.; Lei, T.; Kim, H. R.; Song, Y.; Kim, Y.-J.; Kim, K. S.; Özyilmaz, B.; Ahn, J.-H.; Hong, B. H.; Iijima, S., Roll-to-roll production of 30-inch graphene films for transparent electrodes. *Nat. Nanotechnol.*, **2010**, *5*, 574-578

[112] Ren, W.; Cheng, H.-M., The global growth of graphene. *Nat. Nanotechnol.*, **2014**, *9*, 726-730.

[113] Mengistie, D. A.; Ibrahem, M. A.; Wang, P.-C.; Chu, C.-W., Highly Conductive PEDOT:PSS Treated with Formic Acid for ITO-Free Polymer Solar Cells. *ACS Appl. Mater. Interfaces*, **2014**, *6* (4), 2292-2299.

[114] Haacke, G.,Transparent Conductive Coatings. *Annu. Rev. Mater. Sci.*, **1977**, *7*, 73-93.

[115] O´Connor, B.; Haughn, C.; An, K.-H.; Pipe, K. P.; Shtein, M., Transparent and conductive electrodes based on unpatterned, thin metal films. *Appl. Phys. Lett.*, **2008**, *93*, 223304.

[116] Lee, J.; Lee, P.; Lee, D.; Lee, S. S.; Ko, S. H., Very long Ag nanowire synthesis and its application in a highly transparent, conductive and flexible metal electrode touch panel. *Nanoscale*, **2012**, *4*, 6408-6414.

[117] Gaynor, W.; Burkhard, G. F.; McGehee, M. D.; Peumans, P., Smooth Nanowire/Polymer Composite Transparent Electrodes. *Adv. Mater.*, **2011**, *23* (26), 2905-2910.

[118] Zhao, J.; Sun, H.; Dai, S.; Wang, Y.; Zhu, J., Electrical Breakdown of Nanowires. *Nano Lett.*, **2011**, *11* (11), 4647-4651.

[119] Sachse, C.; Weiß, N.; Gaponik, N.; Müller-Meskamp, L.; Eychmüller, A.; Leo, K., ITO-Free, Small-Molecule Organic Solar Cells on Spray-Coated Copper-Nanowire-Based Transparent Electrodes. *Adv. Energy Mater*., **2014**, *4* (2).

[120] Wu, H.; Kong, D.; Ruan, Z.; Hsu, P.-C.; Wang, S.; Yu, Z.; Carney, T. J.; Hu, L.; Fan, S.; Cui, Y.; A transparent electrode based on a metal nanotrough network. *Nat. Nanotechnol.*, **2013**, *8*, 421-425.

[121] Aernouts, T.; Vanlaeke, P.; Geens, W.; Poortmans, J.; Heremans, P.; Borghs, S.; Mertens, R.; Adriessen, R.; Leenders, L., Printable anodes for flexible organic solar cell modules. *Thin Solid Films*, **2004**, *451-452*, 22-25.

[122] Burgués-Ceballos, I.; Kehagias, N.; Sotomayor-Torres, C. M.; Campoy-Quiles, M.; Lacharmoise, P. D., Embedded inkjet printed silver grids for ITO-free organic solar cells with high fill factor. *Sol. Energ. Mat. Sol. Cells*, **2014**, *127*, 50-57.

[123] Hübler, A.; Trnovec, B.; Zillger, T.; Ali, M.; Wetzold, N.; Mingebach, M.; Wagenpfahl, A.; Deibel, C.; Dyakonov, V., Printed Paper Photovoltaic Cells. *Adv. Energy Mater.*, **2011**, *1* (6), 1018-1022.

[124] Leonat, L.; White, M. S.; Głowacki , E. D.; Scharber, M. C.; Zillger, T.; Rühling, J.; Hübler, A.; Sariciftci, N. S., 4% Efficient Polymer Solar Cells on Paper Substrates. *J. Phys. Chem. C*, **2014**, *118* (30),16813–16817.

[125] Reinhard, M.; Eckstein, R.; Slobodskyy, A.; Lemmer, U.; Colsmann, A., Solution-processed polymer–silver nanowire top electrodes for inverted semi-transparent solar cells. *Org. Electron.*, **2013**, *14* (1), 273-277.

[126] Zilberger, K.; Gasse, F.; Pagui, R.; Polywka, A.; Behrendt, A.; Trost, S.; Heiderhoff, R.; Görrn, P.; Riedl, T., Highly Robust Indium-Free Transparent Conductive Electrodes Based on Composites of Silver Nanowires and Conductive Metal Oxide. *Adv. Funct. Mater.*, **2014**, *24* (12), 1671-1678.

[127] Beiley, Z. M.; Christoforo, M. G.; Gratia, P.; Bowring, A. R.; Eberspacher, P.; Margulis, G. Y.; Cabanetos, C.; Beaujuge, P. M.; Salleo, A.; McGehee, M. D., Semi-Transparent Polymer Solar Cells with Excellent Sub-Bandgap Transmission for Third Generation Photovoltaics. *Adv. Mater.*, **2013**, *25* (48), 7020-7026.

[128] Chen, C.-C.; Dou, L.; Zhu, R.; Chung, C.-H.; Song, T.-B.; Zheng, Y. B.; Hawks, S.; Li, G.; Weiss, P. S.; Yang, Y., Visibly Transparent Polymer Solar Cells Produced by Solution Processing. *ACS Nano*, **2012**, *6* (8), 7185-7190.

[129] Lee, J.-Y.; Connor, S. T.; Cui, Y.; Peumans, P., Semitransparent Organic Photovoltaic Cells with Laminated Top Electrode. *Nano Lett.*, **2010**, *10* (4), 1276-1276.

[130] Winkler, T.; Schmidt, H.; Flügge, H.; Nikolayzik, F.; Baumann, I.; Schmale, S.; Weimann, T.; Hinze, P.; Johannes, H.-H.; Rabe, T.; Hamwi, S.; Riedl, T.; Kowalsky, W., Efficient large area semitransparent organic solar cells based on highly transparent and conductive ZTO/Ag/ZTO multilayer top electrodes. *Org. Electron.*, **2011**, *12* (10), 1612-1618.

[131] Chen, K.-S.; Salinas, J.-F.; Yip, H.-L.; Huo, L.; Hou, J.; Jen, A. K.-Y., Semi-transparent polymer solar cells with 6% PCE, 25% average visible transmittance and a color rendering index close to 100 for power generating window applications. *Energy Environ. Sci*., **2012**, *5*, 9551-9557 .

[132] Colsmann. A.; Puetz, A.; Bauer, A.; Hanisch, J.; Ahlswede, E.; Lemmer, U., Efficient Semi-Transparent Organic Solar Cells with Good Transparency Color Perception and Rendering Properties. *Adv. Energy Mater*., **2011**, *1* (4), 599-603.

[133] Colsmann. A.; Reinhard, M.; Kwon, T.-H.; Kayser, C.; Nickel, F.; Czolk J.; Lemmer, U.; Clark, N.; Jasieniak, J.; Holmes, A. B.; Jones, D., Inverted semi-transparent organic solar cells with spray coated, surfactant free polymer top-electrodes. *Sol. Energ. Mat. Sol. Cells*, **2012**, *98*, 118-123.

[134] Czolk J.; Puetz, A.; Kutsarov, D.; Reinhard, M.; Lemmer, U.; Colsmann. A., Inverted Semi-transparent Polymer Solar Cells with Transparency Color Rendering Indices approaching 100. *Adv. Energy Mater.*, **2013**, *3* (3), 386-390.

[135] Hau, S. K.; Yip, H.-L.; Zou, J.; Jen, A. K.-Y., Indium tin oxide-free semi-transparent inverted polymer solar cells using conducting polymer as both bottom and top electrodes. *Org. Electron.*, **2009**, *10* (7), 1401-1407.

[136] Kim, H. P.; Lee, H. J.; Yusoff, A. R. bin Mohd; Jang, J., Semi-transparent organic inverted photovoltaic cells with solution processed top electrode. *Sol. Energ. Mat. Sol. Cells*, **2013**, *108*, 38-43.

[137] Hau, S. K.; Yip, H.-L.; Zou, J.; Jen, A. K.-Y., Indium tin oxide-free semi-transparent inverted polymer solar cells using conducting polymer as both bottom and top electrodes. *Org. Electron.*, **2009**, *10* (7), 1401-1407.

[138] Guo, F.; Zhu, X.; Forberich, K.; Krantz, J.; Stubhan, T.; Salinas, M.; Halik, M.; Spallek, S.; Butz, B.; Spieker, E.; Ameri, T.; Li, N.; Kubis, P.; Guldi, D. M.; Matt, G. J.; Brabec, C. J., ITO-Free and Fully Solution-Processed Semitransparent Organic Solar Cells with High Fill Factors. *Adv. Energy Mater*., **2013**, *3* (8), 1062-1067.

[139] Yim, J. H.; Joe, S.-Y.; Pang, C.; Lee, K. M.; Jeong, H.; Park, J.-Y.; Ahn, Y. H.; de Mello, J. C.; Lee, S., Fully Solution-Processed Semitransparent Organic Solar Cells with a Silver Nanowire Cathode and a Conducting Polymer Anode. *ACS Nano*, **2014**, *8* (3), 2857-2863.

[140] Guo, F.; Kubis, P.; Stubhan, T.; Li, N.; Baran, D.; Przybilla, T.; Spieker, E.; Forberich, K.; Brabec, C. J., Fully Solution-Processing Route toward Highly Transparent Polymer Solar Cells. *ACS Appl. Mater. Interfaces*, **2014**, *6* (20), 18251-18257.

[141] Carlé, J. E.; Helgesen, M.; Madsen, M. V.; Bundgaard, E.; Krebs, F. C., Upscaling from single cells to modules – fabrication of vacuum- and ITO-free polymer solar cells on flexible substrates with long lifetime. *J. Mater. Chem. C*, **2014**, *2*, 1290-1297.

3 Overview

Organic photovoltaics (OPV) owns a great potential as a source for renewable energy and a big progress was made over the last decades in terms of understanding the fundamental photophysical processes and device engineering. Both are necessary to establish OPV as inexpensive and environment friendly alternative to current photovoltaic technologies. For OPV commercialization several aspects need to be considered such as cost of material and fabrication, power conversion efficiency and device lifetime. Also environmental friendliness and carbon foot print are important factors. Thus the choice of suitable OPV materials, which should be also available in large scale, is crucial. However, phenyl-C_{61}-butyric acid methyl ester (PCBM) – the state-of-the-art electron acceptor in solution processed OPV – is one of the most expensive components and its large scale production needs great effort in synthesis and purification. Likewise, indium tin oxide (ITO), a common transparent conducting electrode, suffers from the limited abundance and high costs of indium. Additionally, ITO is not the best choice for flexible substrates, since it is brittle and forms cracks which lower the electrical conductance. Therefore, alternative material and device concepts are needed to make solution processed OPV competitive and to enable large scale production.

The aim of this thesis is to provide alternative concepts for both, PCBM and ITO. Therefore, the thesis deals with detailed study of perylene bisimides (PBI) as a small molecule electron acceptor to replace PCBM. PBIs exhibit a higher light absorption efficiency compared to PCBM and its color can also be easily tuned. The color of photoactive materials again is an interesting aspect for semitransparent OPV, since it allows a variety in design by selecting suitable colors of photoactive materials. On the other hand, this thesis presents a concept to fabricate a novel transparent conducting electrode based on transparent metal networks which can replace ITO. The dissertation contains four individual manuscripts, each represented by one chapter.

Chapter 3 and chapter 4 regard PBI as potential electron acceptor in bulk heterojunction polymer blends solar cells. Here the impact of alkyl vs. oligo ethylene glycol (OEG) solubilizing substituents on morphology, charge carrier recombination dynamics and consequently OPV device performance was investigated. We found, that solubilizing substituents have a large impact on the miscibility and hence on the phase separation between donor and acceptor. We could correlate the different degrees of phase separation to changes in charge carrier recombination dynamics. Based on these findings, we could explain the

difference in photovoltaic performance of two differently aggregating PBIs in combination with two different donor polymers. The methods used here, i.e. atomic force microscopy (AFM) and transient absorption spectroscopy (TAS) represent a powerful combination to analyze the effect of phase separation on charge carrier recombination dynamics and hence help to understand the loss mechanisms in OPV using PBI.

Chapter 5 and chapter 6 deal with a novel concept to fabricate transparent metal network electrodes, which were successfully integrated into OPV devices as both, front and back transparent conducting electrode (TCE). The metal network was fabricated with the help of a cracked polymer template by thermal evaporation of a metal (e.g. Ag) followed by removal of the polymer template. We have developed methods to easily incorporate this metal network electrode not only as front electrode on a glass substrate, but also as back electrode, where the whole fabrication of the metal network had to be carried out on sensitive organic photoactive layers. Therefore, the metal network electrode was not only used to replace ITO successfully, but also to provide a transparent back electrode. Having both front and back electrode made by transparent metal network electrodes leads to an ITO-free semitransparent organic solar cell. Since the metal network can be fabricated at low cost and in large scale, this concept is relevant for industrial production of large area OPV including the opportunity for semitransparency, which is especially interesting for building integrated OPV and automobile roof top applications.

Studying concepts based on novel material for electron transport as well as transparent electrodes, this thesis contributes to novel device concepts and applications.

Controlling phase separation in donor polymer-PBI blend systems via hydrophobic vs. hydrophilic side chains and their impact on non-geminate recombination (Chapter 3 and 4)

The photoactive layer is the heart of a solar cell device. The charge carriers are generated within the photoactive layer and thus the careful selection of photoactive materials i.e. the electron donor and acceptor materials decides the overall photovoltaic performance of the device. A milestone of OPV development is the introduction of the bulk heterojunction concept, where the electron donor and acceptor is blended to form a morphology suitable for efficient exciton diffusion to the donor/acceptor interface, charge generation and charge carrier transport towards the extracting electrodes. Thereby, not only photophysical and electronic properties such as absorption, energy alignment and charge carrier mobility are important, but also the donor-acceptor miscibility and the capability to undergo favorable phase separation. Several concepts are known to control the morphology such as thermal and solvent annealing as well as the use of solvent additives. Solubilizing side chains of the donor and acceptor material have also a huge impact on the miscibility and hence phase separation between both and offer further possibilities to control aggregation and morphology. However, in many of the organic solar cell devices, the donor polymer is designed to suit the state-of-the-art PCBM acceptor, since PCBM itself has only very limited potential for chemical modification without losing its electron accepting properties. Additional drawbacks of PCBM such as very poor light absorption, tendency to agglomerate and high costs due to sophisticated synthesis and purification motivated researchers to look for alternative electron acceptors. PBI is a prominent candidate, since it possesses high light absorption, excellent electron accepting and transport properties and it is easy to synthesize in large scale. With regard to morphology control, PBI allows fine tuning through chemical modification of not only the photophysical and energetic properties, but also aggregation behavior and phase separation in combination with a donor polymer. However, the effect of PBI solubilizing substituents on the phase separation in polymer blends is not well investigated. To do this, two unsymmetrical PBIs both having a linear alkyl chain on one of the imide positions, whereas the other imide position is either functionalized with an alkyl (PBI 1) or OEG (PBI 2) swallow tail. The chemical structures of PBI 1 and PBI 2 are shown in Figure 1. Substitution of the imide position does not affect the photophysical and energetic properties.

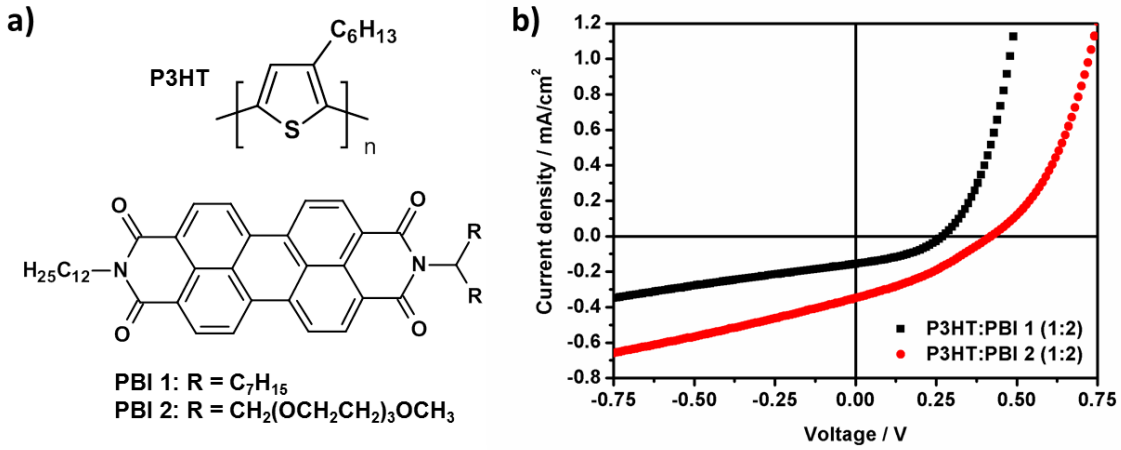

Figure 1. *a) Chemical structure of the two investigated perylene bisimides PBI 1 and PBI 2 as electron acceptors and the respecting donor polymer P3HT. b) J-V characteristics of normal organic solar cells under illumination using P3HT as donor polymer and PBI 1 (black) or PBI 2 (red) as small molecule acceptor. The P3HT:PBI ratio was 1:2 by weight in each case.*

This allowed a direct comparison of the results based on the different side chains. Starting point of the investigation (chapter 3) was the different photovoltaic behavior observed for PBI 1 compared to PBI 2 when blended with P3HT (Figure 1b). Here, the PBI 2 blend showed much higher short circuit current (J_{SC}) and open circuit voltage (V_{OC}) compared to the PBI 1 blend. Although the power conversion efficiency (PCE) of both blend systems was low, the difference was significant and the question arose, whether this can indeed be attributed to the different structural features of PBI 1 and PBI 2 which can cause different morphologies. We therefore focused on investigation of the photoactive blend itself including methods such as UV / VIS spectroscopy, AFM imaging and TAS. In addition, we study the effect of thermal annealing in both PBI blend systems, since this in known considerably influence the phase separation and thereby charge carrier recombination dynamics.

First, the results of the as-cast blend system are discussed and based on that the changes upon thermal annealing at selected temperatures are referred. Following the assumption that the different side chains of PBI lead to changes in blend morphology, AFM images were taken. It is obvious, that the topography of PBI 1 blend (RMS roughness = 0.6 nm) is very smooth compared to that of PBI 2 blend (RMS roughness = 6.4 nm). We ascribed this to a well intermixed morphology due to high P3HT - PBI 1 miscibility mediated by similar alkyl side chains in both components. In contrast to that, PBI 2 having polar OEG side chains leads to phase separation featuring larger domains. The high degree of intermixing in PBI 1 blend versus phase separation in PBI 2 blend was expected to have a big impact in the charge carrier

recombination dynamics. Hence, time resolved TAS in the nanosecond to microsecond time scale was carried out. In preliminary studies, radical cation and anion spectra were taken for donor and acceptor materials either by spectroelectrochemistry or by chemical oxidation. This is helpful to interpret the polaron bands in transient absorption spectra. In Figure 2a the P3HT polaron band of the PBI 1 blend is shown, which is in line with data from literature. The P3HT polaron band having a maximum at 970 nm was selected for analyzing the charge carrier recombination dynamics in both blend systems, hence the evolution of ΔOD upon time (note that ΔOD here at each time is proportional to the charge carrier density in the blend system). In Figure 2b the charge carrier recombination dynamics for both blend systems are shown in a log-log plot. The change in ΔOD upon time was well described by a power law having the order of $(\lambda+1)$ and a decay rate constant k, which is typical for charge carrier non-geminate recombination and consequently the decay dynamics could be fitted using the integrated power law Eq. 1.

$$\Delta OD(t) = (\Delta OD_0^{-\lambda} + k \cdot \lambda \cdot t)^{-1/\lambda} \quad (1)$$

The different decay dynamics are shown in Figure 2b for PBI 1 and PBI 2 blend including the best fit according to Eq. 1. For P3HT:PBI 1, a decay rate constant k being two orders of magnitude higher than for P3HT:PBI 2 was observed, indicating a faster decay dynamics in the PBI 1 blend. The faster decay was ascribed to the high degree of intermixing as confirmed by AFM images. In addition, the decay order $(\lambda+1)$ in PBI 1 blend was exceeding two (2.49) and significantly higher than in the PBI 2 blend (1.71). This was ascribed to a higher density of trap states and lower domain crystallinity in PBI 1 blend.

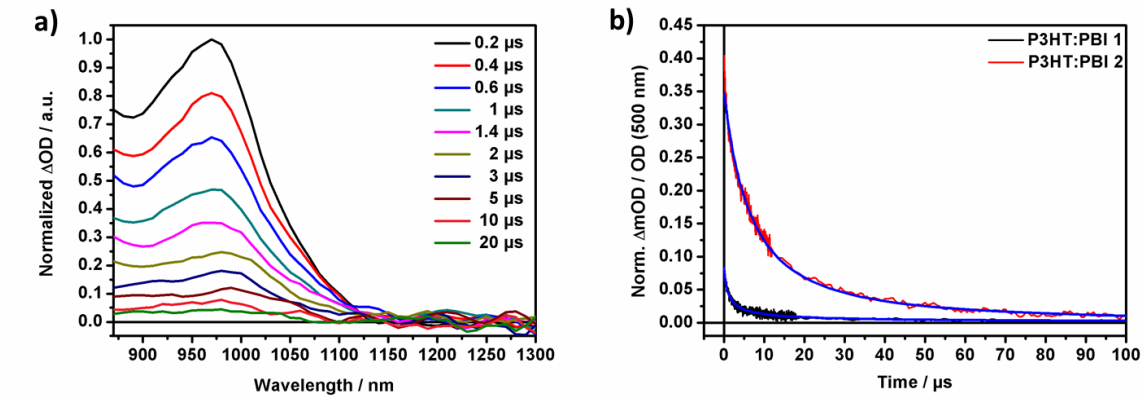

Figure 2. *Transient absorption a) spectrum of P3HT:PBI 1 blend and b) decay dynamics at 970 nm monitoring the maximum of P3HT polaron absorption for PBI 1 (black) and PBI 2 (red) blend including the best power law fit (blue) according to Eq. 1.*

Using thermal annealing at selected temperatures the phase separation in P3HT:PBI 1 was increased as confirmed by AFM images. Interestingly, significant changes in steady state absorption spectra were observed indicating structural reorganizations of either the P3HT or PBI or both. This probably also causes higher degree of crystallinity (Figure 3a). Likewise, we observed different recombination dynamics upon thermal annealing, which is shown in Figure 3b. As an example, the P3HT:PBI 1 blend annealed at 170°C was analyzed and two different decay dynamics were found; one between 0.35 to 5.5 µs and the second between 6.5 to 450 µs illustrated by the black lines in Figure 3b. Both time regimes could be described by power law and are ascribed in accordance to literature to a non-geminate recombination between free charge carriers for the early time regime and to trap limited non-geminate recombination for the later time regime.

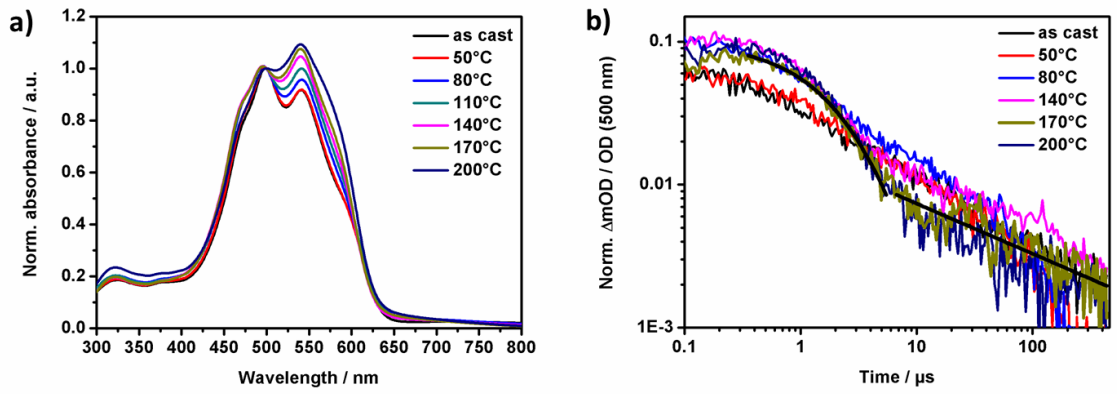

Figure 3. *a) normalized steady state absorption spectra and b) transient absorption decay dynamics at 970 nm for P3HT:PBI 1 blend for as-cast and thermal annealed film at selected temperatures.*

However, for P3HT:PBI 2 blend neither in steady state absorption nor in transient decay dynamics significant changes upon thermal annealing were observed. Only a decreasing charge carrier density with increasing annealing temperature was found. In accordance to the higher degree of phase separation upon thermal annealing, this could be explained by decreased photocharge generation due to a smaller donor-acceptor interface.

Thus the big impact of solubilizing side chains in PBI on the phase separation and thus on morphology was clearly demonstrated here. It is shown that the different degree of intermixing in both PBI 1 and PBI 2 blend systems directly affects the recombination dynamics and thus the photovoltaic performance. Using thermal annealing large phase separation was induced leading to decelerated recombination dynamics in P3HT:PBI 1 compared to the as-cast blend system.

In chapter 4, the morphological impacts of the same two PBI compounds in combination with two different donor copolymers were studied. It was an open question, whether the findings from chapter 3 can be generalized also to other donor polymers. The selected donor polymers, having both alkyl solubilizing side chains, OPV32 and PDPP5T are depicted in Figure 4.

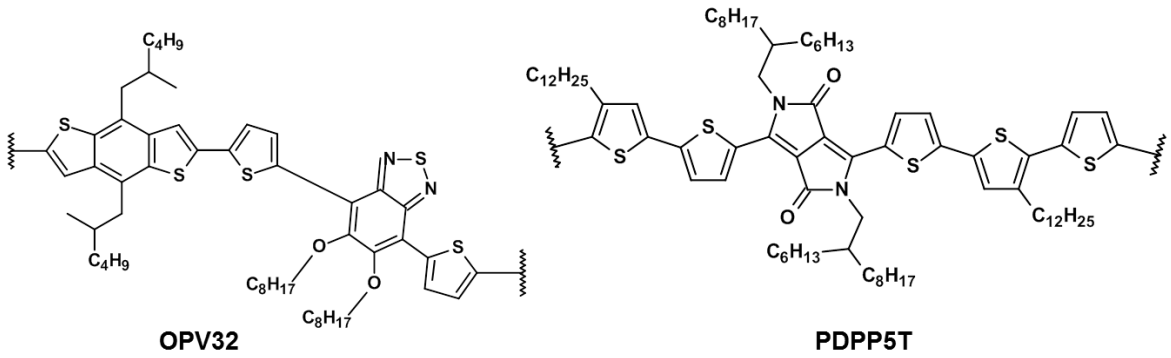

Figure 4. *Chemical structures of the donor polymer* ***OPV32*** *and* ***PDPP5T*** *for the PBI blends.*

According to chapter 3 one could assume, that both donor polymers will show high intermixing when blended with PBI 1, whereas coarse phase separation will occur when blended with PBI 2 due to the alkyl/alkyl versus alkyl/polar OEG interaction of the blend systems, respectively. The aim of this chapter is to verify this assumption including the investigation of photovoltaic behavior, morphology and charge carrier recombination. The optimization of the OPV32:PBI solar cells as well as their blend characterization using AFM images was published before elsewhere.[1] Here the PDPP5T:PBI blend was optimized first for solar cell performance and investigated including UV/VIS spectroscopy, and morphology using AFM. However, analysis of the recombination dynamics by TAS is provided for both the blend systems using different polymers; OPV32:PBI (1:1) as well as PDPP5T:PBI (1:2).

From a previous doctoral thesis in our group[1] it was known, that a OPV32:PBI 2 blend performs much better in OPV device than the respective OPV32:PBI 1 blend. This result was similar to the conclusion drawn for P3HT:PBI 1 in chapter 3 which can be ascribed to the high degree of intermixing between OPV32 and PBI 1 and could be supported by AFM images showing a very smooth film. In contrast to that OPV32:PBI 2 exhibited clear phase separation between both components leading to higher J_{SC} and finally, improved PCE. The explanation for the different morphology is again the alkyl/alkyl versus alky/polar OEG interaction of the solubilizing side chains in OPV32 and PBI. Similarly, from the chemical structure of PDPP5T in Figure 4 one could assume a high degree of intermixing with PBI 1. Consequently, the PDPP5T:PBI 2 blend should result in higher phase separation due to

unfavored alkyl/polar OEG substituent interaction of both components. The question was, whether the higher phase separation again leads to higher J_{SC} values and an overall better photovoltaic performance. Surprisingly, the blend using PBI 1 exhibited always higher J_{SC} and a much better photovoltaic performance compared to PBI 2.

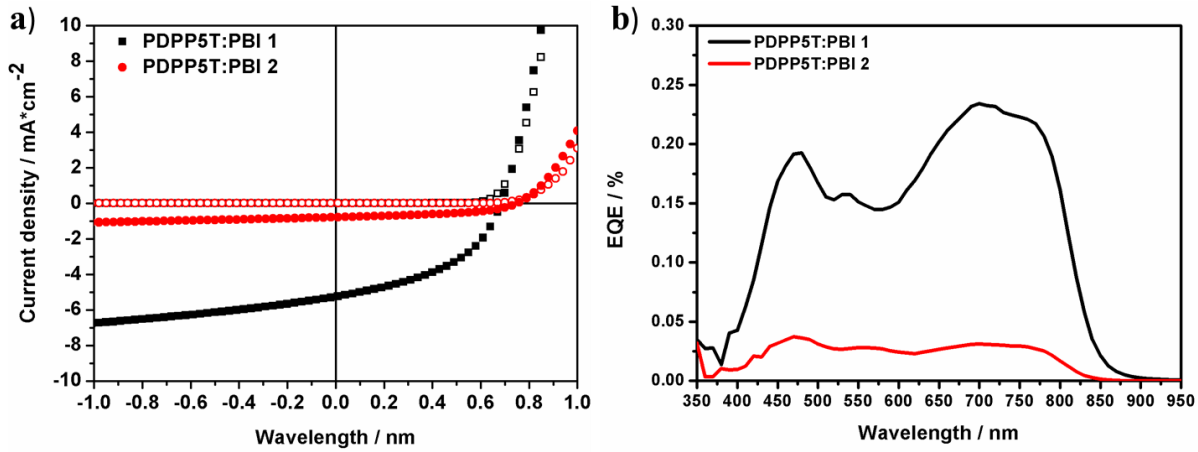

Figure 5. *a) J-V characteristics of PDPP5T blends using PBI 1 (black) or PBI 2 (red) as electron acceptor in dark (open symbols) and under illumination (filled symbols) and b) EQE spectra of PDPP5T blends using PBI 1 (black) and PBI 2 (red) as electron acceptor. The PDPP5T:PBI ratio was 1:2 by weight in each case and both devices were in inverted geometry.*

Figure 5a shows the optimized inverted solar cells having a J_{SC} of 5.03 mA/cm^2 and a PCE of 1.56 % for PBI 1 blend which is much better than for the PBI 2 blend (J_{SC} of 0.76 mA/cm^2 and PCE of 0.27 %). In addition, the EQE spectra are given in Figure 5b emphasizing a much higher photocurrent extraction for the PBI 1 blend over the whole range of the blend absorption spectrum (not shown here). This is surprising since PBI 1 was expected to intermix with PDPP5T leading to an unfavored morphology for photocharge generation and extraction. The AFM images shown in Figure 6b confirm our initial assumption and a much coarser phase separation could be found for the PBI 2 blend. Nevertheless, also the PBI 1 blend exhibits a certain degree of phase separation as seen in Figure 6a, which might be favorable for photocharge generation.

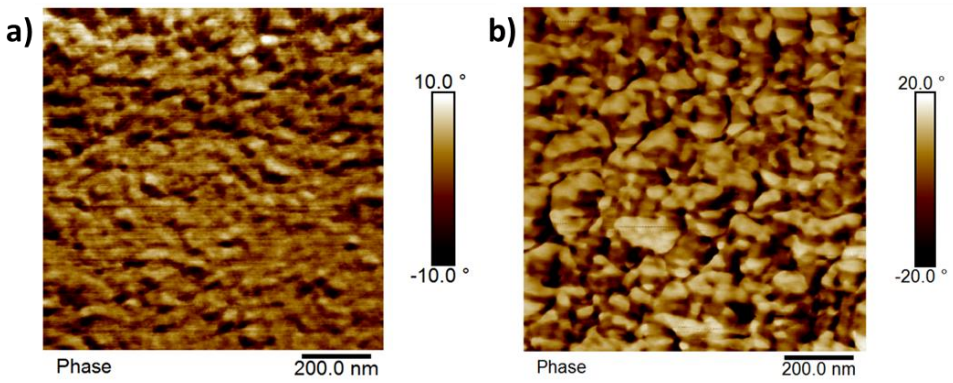

Figure 6. *AFM phase images of PDPP5T blends using a) PBI 1 or b) PBI 2 as electron acceptor. The PDPP5T:PBI ratio was 1:2 by weight in each case*.

Finally, time resolved TAS was performed to monitor and compare the charge carrier non-geminate recombination dynamics in both kinds of blend systems. The decay dynamics for OPV32:PBI 1 in Figure 7a is much faster compared to OPV32:PBI 2 blend indicating faster non-geminate recombination dynamics caused by a higher degree of intermixing in the former as confirmed by AFM images. This is totally different for PDPP5T:PBI blend systems (Figure 7b). Whereas the PBI 1 blend exhibits also a polaron decay dynamics, this is not observed for the case of PBI 2 blend. Almost no or very little amount of charges were generated in the PBI 2 blend which can be explained by having again a closer look at the AFM images in Figure 6b: a very coarse macro phase separation is most probably responsible for poor exciton diffusion towards the donor/acceptor interface leading to a very limited photocharge generation.

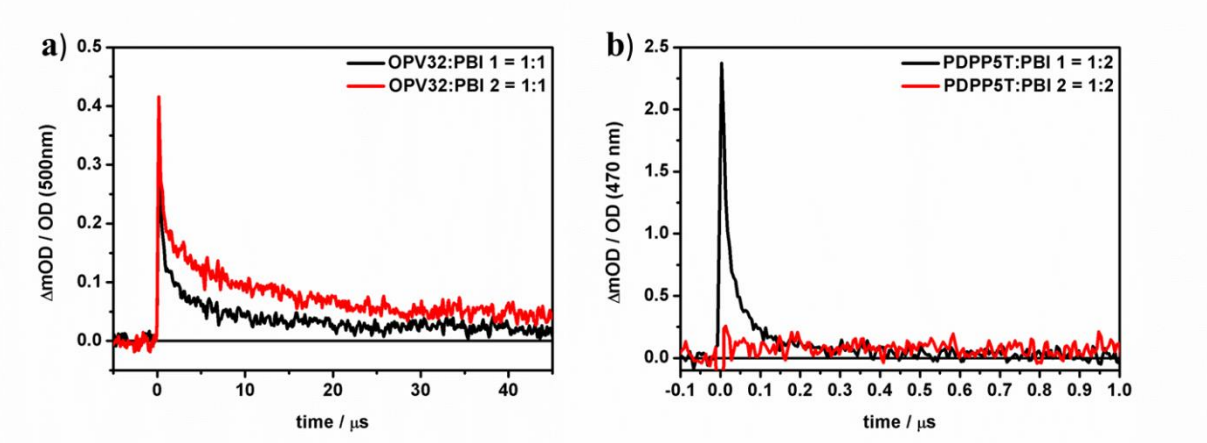

Figure 7. *Transient absorption decay of PBI 1 (black) and PBI 2 (red) blend system monitored at 970 nm using either a) OPV32 or b) PDPP5T as donor polymer. The transient signal was normalized to the steady state absorption at the excitation wavelength, which was 500 nm for a) and 470 nm for b). The excitation density was 30μJ/cm^2 in each case.*

Thus within this study it was shown that the nature of solubilizing side chains has a huge impact on blend morphology and hence on the overall device performance. In contrast to chapter 3 we found, that PBI 1 having alkyl side chains does not always result in high intermixing with donor polymers which also have alkyl side chains. Here in the case of PDPP5T:PBI blend system, the PBI 1 blend exhibits sufficient phase separation, whereas PBI 2 blend system results in domains sizes probably much larger than the exciton diffusion lengths leading finally to limited photocharge generation. Thus, these two chapters address the potential and complexities to use PBIs instead of fullerene derivatives in bulk heterojunction devices. The results indicate the need to adapt the donor & acceptor structures to each other in order to obtain desired phase separation and morphology.

A cracked polymer templated metal network as a transparent conduction electrode for ITO-free semitransparent organic solar cells (chapter 5 and 6)

Transparent conducting electrodes (TCEs) are essential in OPV, since they are necessary for light incoupling and transmission towards the photoactive layer while at the same time they have to ensure high conductivity for loss-free photocurrent collection. ITO fulfills these requirements very efficiently and is therefore the state-of-the-art TCE not only for OPV, but also organic light emitting diodes, liquid crystal displays, touch screens and inorganic thin film solar cells. However, ITO has also a number of drawbacks. It is brittle and forms cracks on stretchable or bendable flexible substrates, which limits its utilization for large area roll-to-roll fabrication and flexible applications. The fabrication of ITO requires high temperature and indium itself is a rare and therefore expensive element. Many alternatives to ITO were proposed such as graphene, carbon nanotubes, and silver nanowires. However, they suffer from high resistance and need further treatments such as pressing or filling with other conductive materials. Current collecting grids printed from silver inks do not have these problems, but they are visible to the naked eye, since they exhibit large feature sizes. In chapter 5 development of a novel transparent metal network electrode for OPV application is presented. The metal network exhibits low sheet resistance and high transmittance, while its structural features remain invisible to the naked eye. Furthermore, it is seamless and the fabrication is suitable for large area fabrication, even on flexible substrates. The principle of fabrication is schematically shown in Figure 8. It starts with the coating of an acrylic resin colloidal polymer suspension on glass, where a polymer cracked template is formed during a fast drying process. The template is fully cracked down to the substrate to form of U-grooves and the cracks are highly interconnected with >5 µm features (Figure 8a).

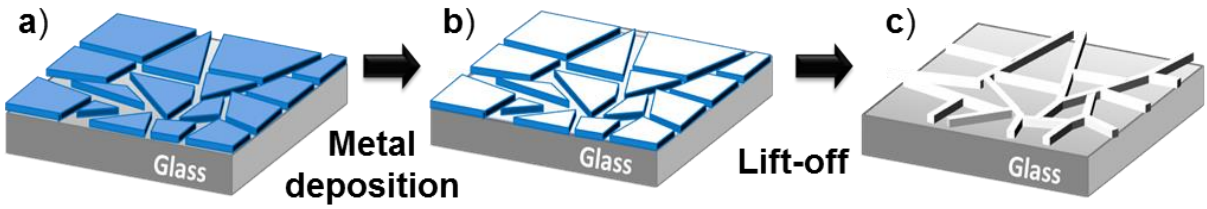

Figure 8. *Schematic illustration of the process for transparent metal network fabrication consisting of a) crack template formation from coating and drying of a colloidal precursor polymer suspension, b) metal deposition onto the polymer template and c) final silver metal network emerges after lift-off of the polymer template by dissolving the polymer in chloroform.*

In a second step 55 nm of silver is deposited by vacuum evaporation on the cracked polymer template (Figure 8b). Finally, the polymer template is washed away by dissolving it in chloroform, while consequently the submicron metal network remains on the glass substrate (Figure 8c). The structure of metal network was afterwards characterized by optical microscope, optical profiler (Figure 9a) and scanning electron microscope (Figure 9b). The metal fill factor, which describes the ratio of deposited metal area with respect to the total substrate area, was estimated to be approximately 20%. The structural width varied between some hundreds of nm and 1-2 µm, the spacing between the silver structures was in the range of 20 to 60 µm. With these structural dimensions the metal network is invisible to the naked eye, which is important for certain applications. The sheet resistance was 10 Ω/□ which is slightly better than that of ITO reference (16 Ω/□) whereas the transmittance at 550 nm was 86% and therefore a bit lower compared to that of ITO (93%). However, as seen from Figure 9c, the transmittance of the metal network is quite constant over a large wavelength range with significantly higher transmittance in the UV region. It is worth to note, that the transmittance and sheet resistance of the metal network depends highly on the metal fill factor as well as on its thickness. A reduction in metal fill factor leads general to an increase in transmittance but on the other side also to an increase in sheet resistance. A fine tuning of the structural dimensions of the metal network is therefore essential to find a compromise between high transmittance and low sheet resistance. This fine tuning was realized by adjustment of the precursor polymer suspension as well as the template fabrication process parameters. Likewise, an increase in metal network thickness adjusted by thermal evaporation leads to a decrease in sheet resistance. However, the maximal thickness is limited due to the fact that the metal network needs to be over coated by the subsequent layer, which is in our case a hole blocking layer made from zinc oxide (ZnO). A thickness of 55 nm Ag was found to give a sufficiently low sheet resistance.

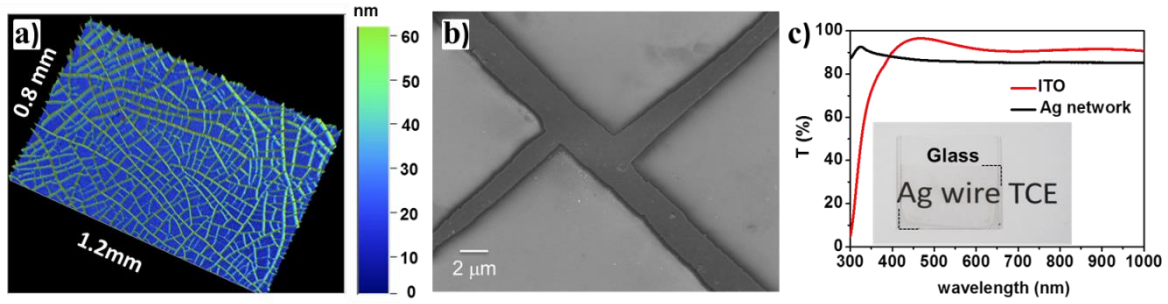

Figure 9. *a) Optical profile meter image in 3D view and b) SEM image of the network junction showing the structural dimensions of the Ag metal network. c) Comparison of transmittance spectra of Ag metal network and ITO. The inset shows a photograph of the Ag network on a glass substrate*.

The overcoating with ZnO is necessary to avoid electrical shorts through the device. The commonly used ZnO layer thickness of 45 nm turned out to not cover the metal network completely as seen from the SEM images in Figure 10a. Therefore, the ZnO layer thickness was increased stepwise and 135 nm ZnO was found to be the optimal thickness (Figure 10b). Figure 10c compares the *J-V* characteristics of the optimized Ag network electrode having 135 nm ZnO with an ITO device as reference with 45 nm ZnO, whereas all other layers were kept the same. In particular, the solar cell parameters are almost same for the Ag network and the ITO device. This emphasizes the potential of transparent Ag metal network electrode as suitable replacement for ITO transparent conducting electrode.

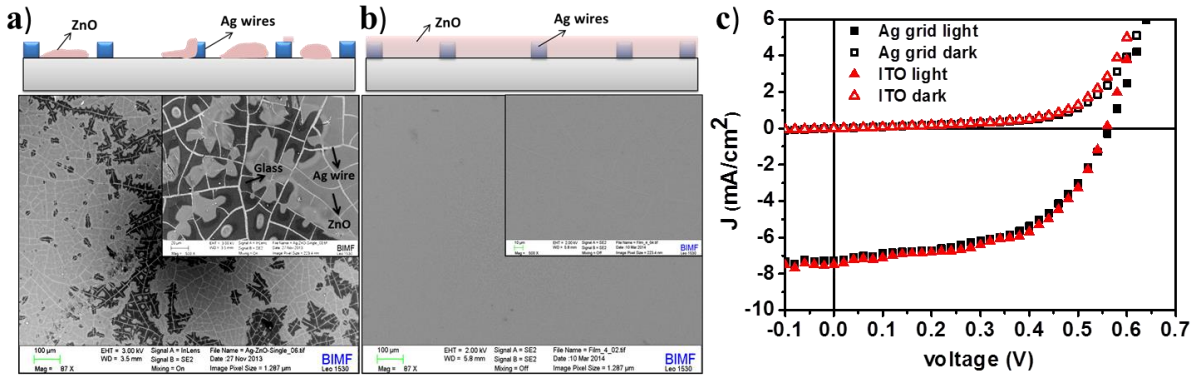

Figure 10. *SEM image and schematic illustration of the Ag metal network on glass substrate covered by a) 45 nm and b) 135 nm ZnO. c) Comparison of J-V characteristics of ITO (black) and Ag network (red) front electrode in dark (open symbols) and under illumination (filled symbols). Note, that the ZnO layer thickness was 45 nm for ITO device and 135 nm for Ag network device. All other layers were kept same.*

Chapter 6 is an extension of the concept based on the successful integration of Ag metal networks as a replacement for ITO as the front transparent electrode. The central question here is, whether the metal network can be processed also on top of the organic photoactive layer leading to a transparent back electrode. In case of having both front and back electrodes transparent, a semitransparent organic solar cell can be realized. The color of such a semitransparent solar cell can be then tuned by the choice of the photoactive layer materials. The semitransparency of OPV is of special interest in the field of window applications in building integrated photovoltaics or for automobile roof tops. The color tunability opens up a completely new freedom in design which is not realizable with other photovoltaic technologies.

The fabrication of the metal network follows the polymer template method from the previous chapter which is schematically shown in Figure 8. However, the fabrication of the metal network electrode on top of soluble organic layers is a quite challenging task, since the polymer template needs to be removed by solvents without dissolving the underneath layers. In an inverted device, the underlying layer is PEDOT:PSS as hole transporting layer on top of the photoactive layer. For this purpose, a 50 nm thick PEDOT:PSS layer was spin coated on a glass substrate. After the polymer template fabrication on top of this PEDOT:PSS layer, it turned out that the cracking characteristic is very similar to that found on glass substrate in the previous chapter. The polymer template was metallized with Ag or Au by thermal evaporation and afterwards dissolved in different organic solvents. Chloroform, acetone and ethyl acetate were suitable solvents to dissolve the polymer template fully while retaining the PEDOT:PSS layer. As a typical example, Au was chosen and the impact of selected Au network thicknesses in the range of 20 to 60 nm on both the transmittance and the sheet resistance were studied in detail. In addition, the haze for all thicknesses was determined, which is an important parameter for determining the effect of light scattering. This is especially interesting for applications, where light scattering due to the metal network is undesired. Surprisingly, the Au metal networks on PEDOT:PSS exhibit an ultralow haze of 5% up to 60 nm Au thickness. Finally, the transmittance - sheet resistance relation of the Au metal network electrode was quantified by a figure of merit (FOM) to compare the performance of different transparent conducting electrodes. A high FOM is desired for most of the applications. For the 60 nm thick Au network on PEDOT/PSS having a sheet resistance of 3 Ω/□ and a transmittance of 85 %, a FOM of 756 was obtained which competes well with that for ITO (FOM = 400 to 800).

After characterizing the metal network on top of a PEDOT:PSS layer, complete organic solar cells were fabricated using the back metal electrode. A very short treatment of 10 seconds in ethyl acetate in combination with ultra-sonication was identified as the best method for dissolving the polymer template while keeping the underneath layers intact. Three types of devices were fabricated according to their front/back electrodes: a ITO/opaque metal device as reference, a ITO/metal network device to proof the possibility of using the metal network as back electrode and a metal network/metal network device, where the transparent metal network back electrode was ultimately combined with the optimized transparent metal network front electrode. In Figure 11a an illustration of all three devices is given for Ag metal electrode. A photograph of each device in Figure 11a highlights the semitransparency of the ITO/Ag network and the Ag/Ag network device. Here the underlying text is fully visible and the color of the device is dominated by the photoactive layer which is P3HT:PCBM for these devices. Thus both the front and the back metal network electrode could be easily structured and prepared in the required size only by using suitable shadow mask during the metal evaporation process. In Figure 11b the *J-V* characteristics of all the three devices are compared in dark and under front illumination. It is obvious that the two semitransparent devices (ITO/Ag network & Ag/Ag network) exhibits a lower J_{SC} compared to the ITO/Ag opaque device. This is expectably attributed to the missing back reflection of light at the Ag metal back electrode, because now most of the light which is not absorbed by the photoactive layer is transmitted through the device.

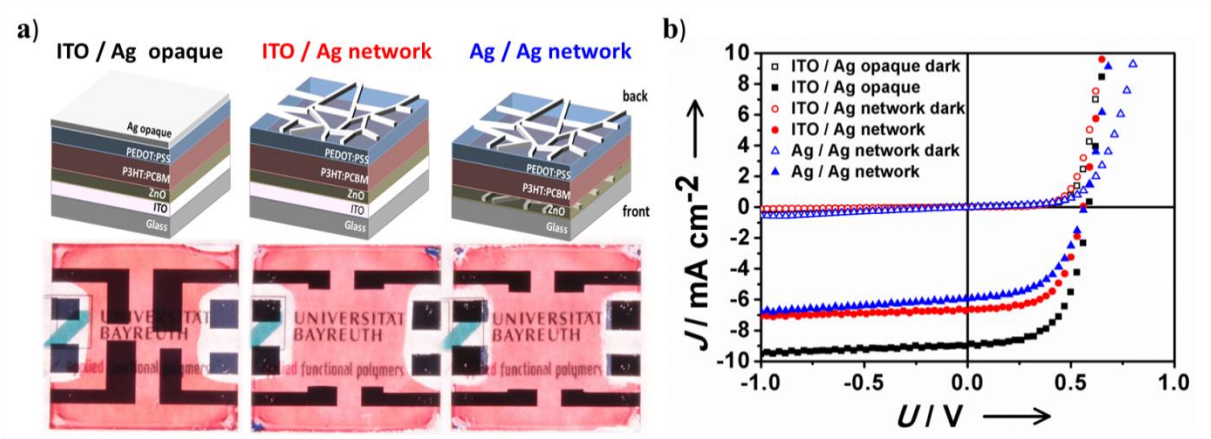

Figure 11. *a) Schematically illustration and photographs and b) J-V characteristics for the three devices having ITO/Ag opaque (black), ITO/Ag network (red) and Ag/Ag network (blue) as front /back electrodes respectively. Note that the J-V characteristics are measured in dark (open symbols) and under front illumination (filled symbols).*

Due to the reduced J_{SC}, we obtained 2.25 % PCE for the ITO/Ag network device and 1.80 % PCE for the Ag/Ag network devices compared to 3.10 % PCE of the reference device. Moreover, the semitransparent devices enables not only front illumination, but also back illumination emphasizing the high transmittance of the metal network/PEDOT:PSS back electrode. It is shown here, that the transparent metal network based TCE is not only just a good replacement for ITO, but also serves as excellent back electrode for ITO-free semitransparent OPV. The easy and fast fabrication and their applicability for large area and flexible substrate make these network electrodes interesting for industrial production.

Reference:

[1] Muth, Mathis-Andreas: Structure-Property Correlation of Electron Transport Materials in Organic Devices, *Dissertation*, University of Bayreuth, **2013**.

Individual contributions to joint publications

The individual contributions of the authors to each manuscript are specified below.

Chapter 3

This manuscript is prepared for submission with the title:

“Controlling phase separation in P3HT-PBI blend systems via hydrophobic vs. hydrophilic side chains and their impact on non-geminate recombination”

by **Christoph Hunger**, Mathis-Andreas Muth and Mukundan Thelakkat.

I prepared as-cast and annealed thin films and measured them by means of UV/Vis spectroscopy and atomic force spectroscopy and transient absorption spectroscopy including their decay analyzes. Additionally, I measured radical anion and cation spectra in solution using spectroelectrochemistry and chemical oxidation. I wrote the manuscript.

Mathis-Andreas Muth synthesized the PBIs, prepared the photovoltaic devices and performed the current density-voltage measurements.

Mukundan Thelakkat supervised the project and was involved in the scientific discussion and corrected the manuscript.

Chapter 4

This manuscript is prepared for submission with the title:

“Phase separation in polymer perylene bisimides blends induced by polar interactions”

by **Christoph Hunger**, Weiwei Li, Martijn M. Wienk, René A. Janssen and Mukundan Thelakkat

I prepared photovoltaic devices and characterized them by current density-voltage characteristics measurements at TU Eindhoven. I also did characterization of thin film sample for UV/Vis spectroscopy, atomic force spectroscopy and transient absorption spectroscopy and analyzed the data. I measured radical anion and cation spectra in solution using spectroelectrochemistry and chemical oxidation. I wrote the manuscript.

Weiwei Li synthesized the donor polymer PDPP5T and was involved in the scientific discussion.

Martijn M. Wienk and René A. Janssen (TU Eindhoven) were involved in the scientific discussion.

Mukundan Thelakkat supervised the project, was involved in the scientific discussion and corrected the manuscript.

Chapter 5

This work is published in *Physical Chemistry Chemical Physics* (**2014**, ***16***, 15107-15110) with the title:

"A cracked polymer templated metal network as a transparent conducting electrode for ITO-free organic solar cells"

by K. D. M. Rao, **Christoph Hunger**, Ritu Gupta, Giridhar U. Kulkarni and Mukundan Thelakkat

I integrated the optimized metal network electrode in solar cells, fabricated the photovoltaic devices and did their characterization by UV/Vis absorption spectroscopy, current density – voltage characteristics and external quantum efficiency measurements. I wrote the photovoltaic devices part in the manuscript.

K. D. M. Rao and Ritu Gupta prepared the transparent metal network electrode including their optimization for the integration in organic photovoltaics. He carried out the characterization of the metal network by means of optical microscope, optical profiler and scanning electron microcopy. They wrote the transparent metal network part in the manuscript.

Giridhar U. Kulkarni and Mukundan Thelakkat supervised the project, were involved in the scientific discussion and corrected the manuscript.

Chapter 6

This work is published in *Energy Technology* (**2015**, *3* (6)**,** 638–645) with the title:

"Transparent Metal Network with Low Haze and High Figure of Merit applied to Front and Back Electrodes in Semitransparent ITO-free Polymer Solar Cells"

by **Christoph Hunger**, K. D. M. Rao, Dr. Ritu Gupta, Chetan R. Singh, Giridhar U. Kulkarni, and Mukundan Thelakkat

I optimized and fabricated the transparent metal network for front and back electrode and integrated them into photovoltaic devices. I characterized the photovoltaic devices by optical microscopy, UV/Vis transmittance and reflectance spectroscopy, current density – voltage characteristics and external quantum efficiency measurements. I wrote the electrode integration and characterization of photovoltaic devices part in the manuscript.

K. D. M. Rao and Ritu Gupta prepared the transparent metal network electrode on PEDOT:PSS and characterized them by scanning electron microscopy, transmittance and optical haze measurements. They wrote the transparent metal network preparation part in the manuscript.

Chetan R. Singh was involved the scientific discussion regarding the impact of measuring the devices with mask vs. without mask.

Giridhar U. Kulkarni and Mukundan Thelakkat supervised the project, were involved in the scientific discussion and corrected the manuscript.

4 Controlling phase separation in P3HT-PBI blend systems via hydrophobic vs. hydrophilic side chains and their impact on non-geminate recombination

*Christoph Hunger, Mathis-Andreas Muth and Mukundan Thelakkat**

*corresponding author

Prof. Dr. Mukundan Thelakkat, Applied Functional Polymers, Macromolecular Chemistry I, University of Bayreuth, D-95440 Bayreuth, Germany.

E-mail: mukundan.thelakkat@uni-bayreuth.de

This manuscript is prepared for submission.

Abstract

Two unsymmetrical perylene bisimides PBI 1 and PBI 1 were studied in blend with poly(3-hexylthiophene-2,5-diyl) (P3HT) as donor polymer in terms of photovoltaic performance, morphology and charge carrier recombination dynamics. The PBIs have a linear alkyl chain at the one imide position while the other imide position was substituted by either a hydrophobic alkyl swallow tail (PBI 1) or a hydrophilic oligo ethylene glycol (OEG) swallow tail (PBI 2). Even through the photophysical properties of both PBIs are very similar, significant differences in photovoltaic performance were found. We observed a much higher short circuit current (J_{SC}) and open circuit voltage (V_{OC}) for PBI 2 blend compared to PBI 1 blend. Investigation of the blend morphology by atomic force microscopy (AFM) showed a very smooth topography for PBI 1 blend whereas a coarse surface was found for PBI 2 indicating a higher degree of phase separation in this blend. We ascribed the different morphology to the favored hydrophobic alkyl / alkyl vs. unfavored hydrophobic alkyl / hydrophilic OEG interactions of the different substituents in P3HT and PBI, respectively. The impact of the different morphology on the photovoltaic performance was confirmed by measuring the charge carrier recombination dynamics in both PBI blend using transient absorption spectroscopy. The high degree of donor/acceptor intermixing found in PBI 1 blend leads to faster charge carrier recombination dynamics and a lower charge carrier density compared to PBI 2 blend, where a high degree of phase separation was found. Finally, phase separation of the PBI 1 was induced by thermal annealing as confirmed by AFM leading to decelerated charge carrier recombination dynamics. We emphasize here the importance of donor and acceptor substituent as a powerful tool to control the phase separation in P3HT:PBI blend systems.

Introduction

Organic photovoltaics (OPV) underwent a rapid development in terms of power conversion efficiency and a deep understanding of the fundamental processes over the last decades. A large number of photoactive materials especially for solution processed bulk heterojunction solar cells were investigated with regard to their photovoltaic performance. However, beside fundamental aspects such as absorption properties, energy alignment and charge carrier mobility also a control of the morphology and thus a defined intermediate phase separation of donor and acceptor phase are crucial for high efficient devices. This can be realized by

thermal[1] or solvent annealing[2] and using solvent additives.[3] For instance, Yan *et al.* presented recently polymer solar cells having over 10 % power conversion efficiency (PCE), which was achieved by temperature-dependent aggregation of the donor polymer.[4] Additionally, block copolymers were used as compatibilizer between donor and acceptor phase[5] or to build up by itself a micro phase separated morphology.[6] The solubilizing side chains of the donor polymer were also found to have a huge impact on the phase separation and their fine tuning allows optimization of morphology thus leading consequently to higher photovoltaic performance. Moreover, Sariciftci *et al.* has shown that the length of the solubilizing side chain in Poly-3-alkylthiophene affects not only the phase separation but does also the phenyl-C61-butyric acid methyl ester (PCBM) diffusion and an increasing PCBM diffusion rate with longer alkyl sidechains was found.[7] In contrast to that, PCBM has only limited possibilities in chemical modification, since each additional substituent to the fullerene core will change its energy levels and hence electron accepting properties. In addition, purification of such multiple substituted fullerene acceptors is highly sophisticated. Even through PCBM is still one of the most efficient electron acceptor in OPV, it has several drawbacks. As mentioned above, PCBM show diffusion and aggregation which leads to instabilities in blend morphology and consequently to limited device lifetime. In addition, PCBM possess only low molecular extinction coefficient and hence contribute less to the photocurrent generation than the donor polymer.[8] The synthesis and in particular the purification of PCBM is highly sophisticated making PCBM a cost intensive component in organic solar cells.[9] Therefore a series of alternative electron acceptors for OPV were proposed in the last years.[10, 11] Among these, perylene bisimides (PBI) is a promising candidate, since it shows high light absorption, is highly photostable, and exhibits sufficient electron mobility and electron accepting properties. The chemistry allows a fine tuning of each property by structural modification.[12] Most of all PBI based acceptors can be synthesized cheap and in large scale.[13] As a special feature, PBI tends to self-assembly via π-π stacking, which opens new opportunities for building up a controlled morphology or one dimensional charge carrier transport in OPV.[14] At the same time the strong π-π stacking property leads often to formation of large crystalline aggregates in polymer:PBI blends which result in unfavorable blend morphology. In consequence, photocurrent generation is reduced for phase domains much larger than the exciton diffusion length and the charge carrier transport between large aggregates is limited, as found for poly(3-hexylthiophene-2,5-diyl) (P3HT) blends.[15] Additionally, excitons in large PBI aggregates are converted into immobile excimer states followed by excimer radiative relaxation rather than charge carrier generation

at the donor/acceptor interface.[16] A control of the PBI aggregate formation and phase domain size is therefore a determining factor for its applications. On the basis of the above mentioned factors for polymer blend systems, morphology tuning was realized by using a P3HT-PBI block copolymer as compatibilizer,[17] solvent additives [18-20] or by thermal annealing. [21-23] Furthermore, linking PBI cores covalently together is a successful way to reduce the PBI aggregation and hence building up a well-defined morphology. Highly efficient polymer:PBI-dimer solar cells having PCE up to 6.05 % were published.[24] As mentioned above tuning of the solubilizing side chains offers opportunities to control the donor and acceptor miscibility and hence the blend morphology. In contrast to PCBM, chemical modification via side chains can be realized much easier in both PBI-monomer and PBI-dimer acceptors. In this context Lu *et al.* investigated the impact of hydrophilic ethylene glycol side chains at the bay position with respect hydrophobic alkyl side chain at the N-terminal of a PBI dimer on the phase separation in a blend with P3HT as donor polymer.[25] However, differences in photovoltaic performance of this study were not only attributed to the different side chains and its effect on phase separation, but also to the changes in the photophysical and electronic properties since the functionalization of the aromatic core always influences these properties.[26] Thus a systematic study about the impact of different side chains in PBI without core substitution to keep the photophysical and energetic properties is still needed. Additionally, non-geminate recombination dynamics have a huge impact on photovoltaic performance and are very sensitive to any change in phase separation. An investigation of different side chain impact on the morphology including the charge carrier recombination dynamics will help to understand the role of donor-acceptor miscibility and phase separation not only for PBI blend systems but for OPV materials in general. This is the aim of this study presented in this manuscript.

As an example we chose two PBI molecules each with a different substituted side chain at the N-atom position of the imide part, while leaving the PBI core unsubstituted to keep the photophysical and energetic properties constant. In Figure 1a, both PBIs are shown, having a linear alkyl chain at one imide position, while either an alkyl (PBI 1) or oligo ethylene glycol (OEG) (PBI 2) swallow tail at the other imide position. The two PBIs exhibit very similar light absorption as well as electron mobility in pristine thin film.[27] Here we address the question, how these different swallow tail substituents will affect the morphology when blended with P3HT – a typical donor polymer in OPV. The influence will be discussed in the context of photovoltaic performance, AFM images and time resolved transient absorption spectroscopy. The study includes also the effect of thermal annealing on morphology and charge carrier recombination dynamics.

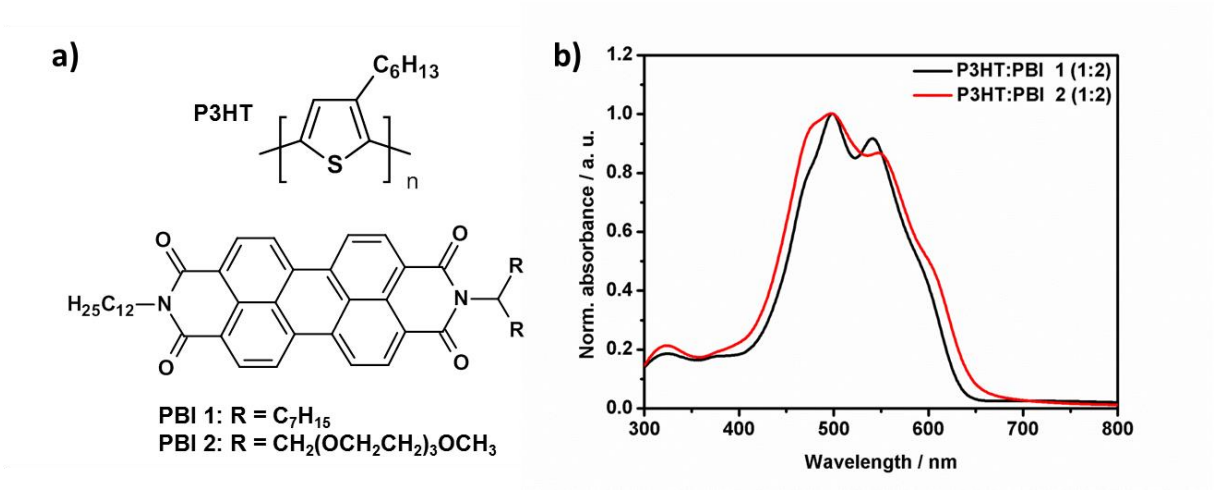

Figure 1. *a) Chemical structure of the donor polymer P3HT and the two investigated perylene bisimides PBI 1 and PBI 2 as electron acceptors. b) Thin film normalized UV / Vis absorbance spectra of a blend using PBI 1 (black) or PBI 2 (red) as electron acceptors and P3HT as donor polymer in each case.*

Experimental Part

Chemicals: The synthesis of PBI 1 and PBI 2 is published elsewhere.[27, 28] PBI 1 is crystalline up to 182 °C, whereas PBI 2 exhibits a liquid crystalline phase up to 136 °C. P3HT (4002-EE) was used as purchased from Rieke Metals. Chloroform ($CHCl_3$) (anhydrous with crowncap, 99%), ortho-dichlorobenzene (oDCB), tetrahydrofuran (THF), tetrabutylammonium hexafluorophosphate (TBA[PF_6]) and antimony pentachloride ($SbCl_5$) were purchased from Sigma-Aldrich. Poly(3,4-ethylenedioxythiophene) polystyrene sulfonate (PEDOT:PSS - Clevios P VP Al 4083) was purchased from Heraeus.

Thin film sample preparation: Thin film samples for UV/VIS spectroscopy, AFM images and time resolved transient absorption measurements were fabricated on glass substrates, which were cleaned in ultrasonic bath using the following sequence of solvents: detergent, water, acetone and 2-propanol. A solution of P3HT:PBI (1:2 wt/wt) in chloroform (30 mg/ml) was afterwards spin coated at 1000 rpm on glass substrate. Annealing of the thin film was carried out under nitrogen at selected temperatures between 50°C and 200°C on hot plate for 15 min. UV-Vis spectroscopy was carried out using a JASCO V-670 spectrometer.

Photovoltaic device preparation: OPV cells were fabricated using a standard device architecture: glass/ ITO/ PEDOT:PSS/ photoactive Layer/ Ca/ Al. Commercial ITO coated glass substrates with a sheet resistance of 13 Ω/□ (Lumtec) were cleaned using following sequence in an ultrasonic bath: detergent, water, acetone and 2-propanol. After ozone

treatment of the substrates for 5 min, PEDOT:PSS was spin-coated on the ITO surface and dried at 130 °C for 30 min. All the following steps were carried out under nitrogen atmosphere with water and oxygen levels ≤ 0.1 ppm. After cooling the substrate, the active layer was blade coated at 35 °C from $CHCl_3$ solution (20mg/ml) on an ErichsenCoatmaster 509MC (40mm/s, gap: 30µm) leading to a photoactive layer thickness of 80 to 90 nm. The substrates were then put in a thermal evaporation chamber to evaporate the top electrodes (30 nm Ca/ 100 nm Al) under high vacuum ($1 \cdot 10^{-6}$ mbar) through a shadow mask (active area 4 mm^2). The current-voltage characteristics of the devices were measured using a Keithley 2420 (I-V) Digital SourceMeter at 25 °C under AM1.5 solar irradiation. The power of the solar simulator was calibrated using a reference silicon solar cell.

Radical ion spectra: Radical anion spectra for PBI 1 and PBI 2 were taken by spectroelectrochemical cell kit provided by ALS-japan at low concentration ($c=10^{-5}$ $molL^{-1}$) in THF solution having 0.1 $molL^{-1}$ $TBA[PF]_6$ as electrolyte. For this qualitative measurement, no reference electrode was used and bias was applied as stated. Radical cation spectra of P3HT were taken in oDCB by adding stepwise antimony pentachloride. Changes in absorption in each case were recorded using a JASCO V-670 spectrometer.

Time resolved transient absorption: Nano- to microsecond timescale transient absorption of the thin film blend samples was measured using the LKS80 spectrometer (Applied Photophysics). The P3HT:PBI blend samples under controlled atmosphere were photoexcited at 500 nm by an optical parametric oscillator (Rainbow, 4-8 ns pulse duration – Quantel) which was pumped with the 3rd harmonic oscillation of a Nd:YAG laser (Brilliant – Quantel). The excitation energy density for analyses of the recombination dynamics was 30 µJ/cm^2, whereas for capturing the transient absorption spectra it was 280 µJ/cm^2 for P3HT:PBI 1 and 130 µJ/cm^2 for P3HT:PBI 2 blend system to have a sufficient signal to noise ratio. The different excitation energy densities in each case were controlled by neutral density filters and an attenuator consisting of two air-spaced Glan-Taylor calcite polarizers. Additionally, suitable filters were used in the laser beam to cut off the fundamental wavelength at 1064 nm and in the probe light beam to cut off any visible light up to 850 nm. Changes of transient absorption were measured in the visible wavelength using the photomultiplier tube R928 (Hamamatsu) or NIR wavelength range using the InGaAs photodiode HCA-S-200M-IN (Femto), both supplied by Applied Photophysics). The data were collected using a DSOS104A oscilloscope (Keysight Technologies).

Results and Discussion

As mentioned already, PBI 1 and PBI 2 (Figure 1a) exhibit similar thin film absorption spectra in the as-cast film ranging mainly from 420 nm to 630 nm.[27] Since P3HT absorbs also in a similar wavelength region from 300 nm to 650 nm (Figure S1) the P3HT:PBI blend absorption result from contributions of both components. The normalized absorption of the as-cast 1:2 (wt/wt) blend films using P3HT and PBI 1 or PBI 2 is shown in Figure 1b. Organic solar cells in normal geometry were made to obtain an initial idea about the photovoltaic potential of both blends. The P3HT:PBI ratio was 1:2 (wt/wt) in each case. Chloroform was used as solvent for the photoactive layer, since it is fast evaporating and consequently giving the PBI no time to form large aggregates as it was observed in the case of chlorobenzene.[15] The *J-V* characteristics for both blend solar cells are shown in Figure 2 and a difference in photovoltaic performance between both is obvious: P3HT:PBI 1 exhibits a J_{SC} of only 0.16 mA/cm^2 and a V_{OC} of 280 mV. In contrast to that, the J_{SC} in P3HT: PBI 2 is more than doubled to 0.34 mA/cm^2 while at the same time the V_{OC} increased to 420 mV. The parameters of both devices are summarized in Table 1.

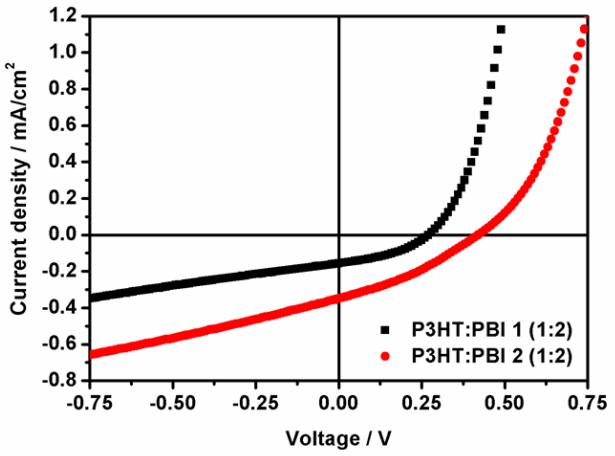

Figure 2. *J-V characteristics of organic solar cells under illumination in normal geometry using P3HT as donor polymer and PBI 1 (black) or PBI 2 (red) as small molecule acceptor. The P3HT:PBI ratio was 1:2 (wt/wt) in each case. The photoactive layer thickness in both devices was about 80 to 90 nm.*

Table 1. *Summarizes the solar cell parameters for P3HT:PBI blend systems according to Figure 2.*

Blend system (1:2 wt/wt)	J_{SC} [mA·cm^{-2}]	V_{OC} [V]	FF [%]	PCE [%]
P3HT : PBI 1	0.16	0.28	40	0.02
P3HT : PBI 2	0.34	0.42	32	0.05

The PCE of both devices is much less than that usually obtained from P3HT:PCBM solar cells[1] and it is also lower than those for other P3HT:PBI solar cells.[15] However, the difference in behavior of PBI 1 and PBI 2 in photovoltaic performance is significant and needs to be explained. Since different swallow tail substituents are placed at the N-atom terminal of the PBI core, it does not affect the photophysical and energetic properties of the PBI molecules.[12] Therefore, an explanation of the differences in photovoltaic parameters due to possible different HOMO or LUMO levels fails. It was shown that the swallow tail influences the packing behavior of the PBI. The packing of PBI 1 and PBI 2 in bulk and pristine films is well studied and it was found, that the π-π stacking distance in both PBIs is similar.[27] With respect to the donor polymer it is known, that side chains have a huge impact on miscibility between donor polymer and PBI acceptor and hence on the morphology and in particular on the PBI domain size.[25] Due to difference in nature of the swallow tail substituents in PBI 1 and 2 (hydrophobic alkyl in PBI 1 vs. hydrophilic OEG in PBI 2), we expect different PBI domain sizes and different morphologies when blended with P3HT.

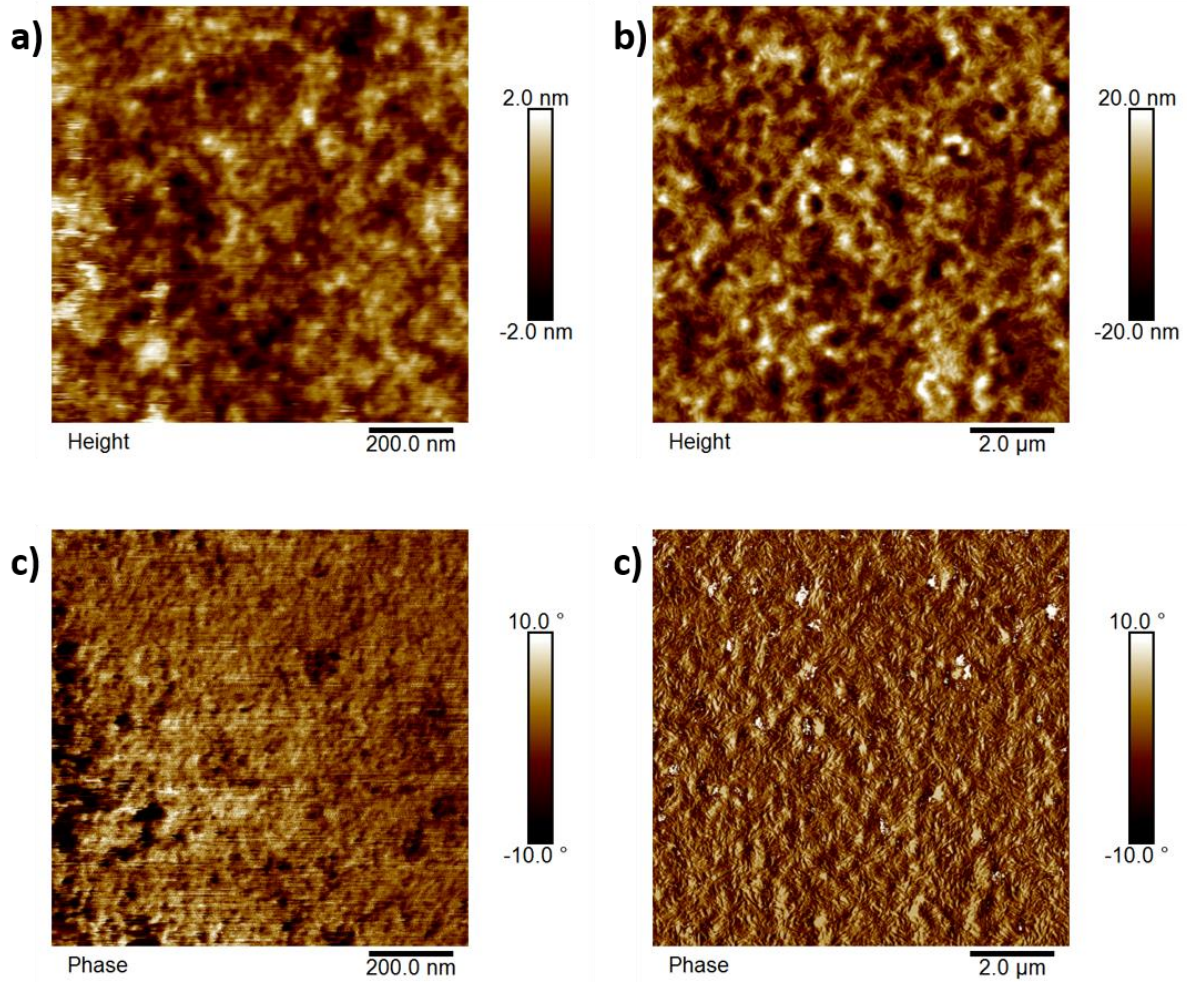

Figure 3. *AFM height (**a** and **b**) and phase (**c** and **d**) images of P3HT:PBI blends (1:2 wt/wt) for PBI 1 (**a** and **c**) and PBI 2 (**b** and **d**) as-cast from chloroform on glass slide. Note the different scale bars.*

This assumption was confirmed by AFM images for both P3HT:PBI blend systems. The samples used for AFM images are the same as for UV / Vis spectroscopy. As seen from the AFM height images in Figure 3, both P3HT:PBI blends exhibit phase separation, however, on quite different scales: The blend using PBI 1 show rather small features having a RMS roughness of only 0.6 nm. In contrast to that, the PBI 2 blend forms large phase separation exhibiting increase in RMS roughness to 6.4 nm (note the difference in scale of the AFM image of 10 x 10 µm). For comparison a 1 x 1 µm AFM image is given in Figure S2a for PBI 2 blend having a RMS roughness of 4.8 nm. Additionally, some structural features are visible in Figure 3b which may originate from highly aggregated PBI 2 domains. The structural features are even more noticeable in the respective AFM phase image in Figure 3d (see Figure S2b for the 1 x 1 µm AFM phase image). As seen from the AFM phase image in Figure 3c, the PBI 1 blend does not exhibit such structural features. Together with low roughness obtained from the AFM height images it can be concluded, that PBI 1 exhibits a higher miscibility with P3HT mediated most probably trough the alkyl side chains in PBI 1 and P3HT. In contrast to that, the hydrophilic OEG side chain in PBI 2 prevents intermixing with the P3HT phase and hence leading to formation of large PBI 2 domains.

Charge carrier recombination dynamics are very sensitive to difference in morphology and have a huge impact on the *J-V* characteristics. For instance, V_{OC} does not only depend on energy levels of the donor / acceptor system or the charge extraction layers but was found to be affected by the charge carrier recombination dynamics inside the photoactive layer.[29]

We therefore performed transient absorption spectroscopy in the nanosecond to microsecond timescale using a laser flash photolysis setup to monitor the recombination dynamics. This time regime is dominated by non-geminate recombination of separated charges remaining at this time and geminate recombination of singlet exciton states or singlet charge transfer states appearing usually at shorter timescale can be neglected. To identify the separated charges (radical cations or anions) or the so-called polarons from the transient absorption spectra, usually the radical cation spectra of the donor and radical anion spectra of the acceptor is measured before in steady state by electrochemical doping or by spectroelectrochemical measurement. In Figure 4a, the PBI radical anion of PBI 1 in THF solution measured by spectroelectrochemistry is shown. The concentration of the PBI was kept in the range of 10^{-5} mol L^{-1} to prevent any aggregation effects.

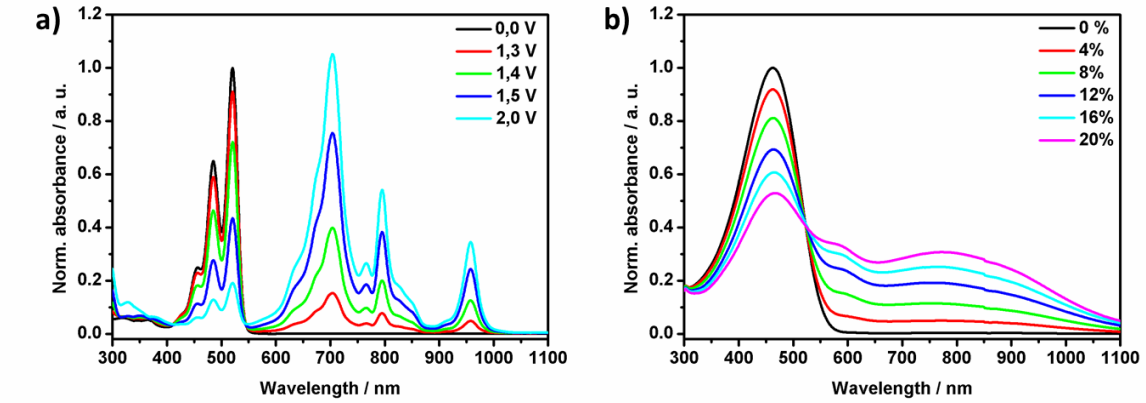

Figure 4. *a) Normalized spectroelectrochemical spectra of PBI 1 radical anion in THF (c = 10^{-5} mol L^{-1}) with an applied bias ranging between 0.0 V and 2.0 V. For spectroelectrochemical spectra of PBI 2 see Figure S3. b) Normalized absorbance spectra of chemical oxidation of P3HT in oDCB with different amounts of $SbCl_5$ given in wt% with respect to P3HT.*

When no bias is applied to the electrodes (black line) only the steady state absorption spectra of the non-aggregated neutral PBI 1 appears between 400 and 550 nm with the characteristic vibronic bands at 456 nm (0-2), 485 nm (0-1) and 520 nm (0-0), which are typical for the $S_0 \rightarrow S_1$ electronic transition in PBI (Figure 4a). After applying an electrical bias of 1.3 V new bands between 550 nm and 1000 nm emerge with three maxima at 704 nm, 795 nm and 958 nm. These bands are specific for the PBI radical anion and are in line with published data on PBI radical anion spectra.[30] With increasing bias from 1.3 V up to 2 V the absorption intensity of the neutral PBI 1 species between 400 and 550 nm decreases, while at the same time the absorption intensity for the PBI 1 radical anion between 550 and 1000 nm increases. This conversion from the neutral species of PBI 1 to the radical anion is even more obvious with increasing bias between 1.3 V up to 2 V. A very similar spectra for PBI 2 in neutral and radical anion form was obtained (Figure S3) and both spectra were also very similar to PBI anion spectra from the literature, which supports that the different side chains at the N-atom does not affect the photophysical properties of the PBI. The P3HT cation spectrum was not measured by spectroelectrochemistry, since P3HT was precipitating upon electrical oxidation. Therefore, the P3HT cation spectrum was obtained by chemical oxidation using $SbCl_5$ (Figure 4b) which is a common way to estimate the polaron spectrum for polymers.[31] Upon chemical oxidation the steady state absorption of P3HT reduces, whereas a new broad band between 600 and 1700 nm appears which was attributed to the P3HT radical cation spectra in solution. Both PBI and P3HT radical spectra confirm the findings from others in literature[30, 32] and help to identify the polaron absorption band in the transient absorption spectra. It is worth to

note, that the polaron band of P3HT in thin film is red shifted with respect to its cation spectra in solution due to aggregation effects. A broad polaron band centred at 980 nm is usually observed for P3HT in the NIR wavelength range.[33]

With the knowledge about the radical absorption spectra of P3HT, PBI 1 and PBI 2 we now turn to the transient absorption spectroscopy measurement of both blend systems P3HT:PBI 1 and P3HT:PBI 2. We focus here in this study on the P3HT polaron band between 900 and 1100 nm for technical reasons explained under Figure S4. For that, the same samples used in UV / Vis absorption spectra measurements in Figure 1b were used. To exclude any saturation effect due to high laser excitation, we first analyzed the ΔOD dependence upon laser excitation energy, which should be linear. Any further measurement was than performed within the linear regime.[34] The transient absorption decay was measured therefore for both blend systems at 970 nm which is dominated by the P3HT polaron absorption. In Figure 5a the ΔOD value as a function of laser excitation density is given. The ΔOD values were taken at 500 ns after photoexcitation and were normalized to the ground state optical density at 500 nm. Two information can be obtained from this plot: First, the PBI 2 blends exhibits much higher ΔOD values at a given excitation density, indicating higher charge densities with respect to the PBI 1 blend, since ΔOD is proportional to the charge density n (here ascribed to the P3HT polaron density) according lambert beers law (Eq.1), where d is the film thickness and ε_p is the extinction coefficient of the polaron.[34]

$$\Delta OD = n \cdot d \cdot \varepsilon_P \qquad (1)$$

Second, the different slope of the linear regime and the fact that the ΔOD at 970 nm starts to saturate at different excitation densities with for the two blends is an indication for different recombination dynamics in both blend systems (Figure 5a).

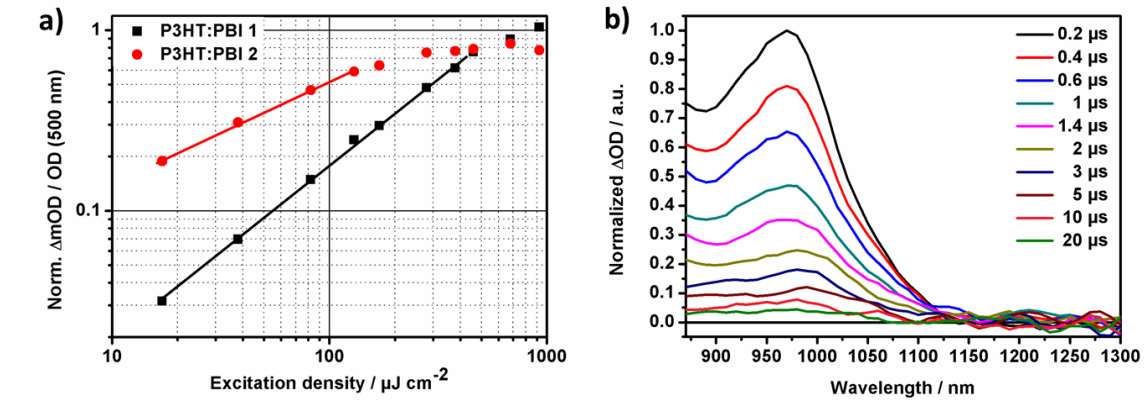

Figure 5. *a) Normalized (with respect to the steady state optical density at 500nm) ΔOD at 970 nm and 500 ns time delay versus laser excitation density between 17 and 925 µJ·cm^{-2} at 500 nm for PBI 1 (black) and PBI 2 (red) blends. Straight lines illustrating the linear regime (below 460 µJ·cm^{-2} for PBI 1 and 130 µJ·cm^{-2} for PBI 2 blend) where no saturation due to high laser excitation energy occurs. b) Normalized transient absorption spectra between 870 and 1300 nm for P3HT:PBI 1 blend after laser excitation at 500 nm with 280 µJ·cm^{-2}. For P3HT:PBI 2 blend see Figure S4 in supporting information.*

In a next step, we measured the transient spectra in the NIR region for both blend systems, whereas the excitation density was chosen to be 280 µJ·cm^{-2} for the PBI 1 blend and 130 µJ·cm^{-2} for the PBI 2 blend to have a sufficient high signal to noise ratio especially apart from the polaron maximum, while still being in the linear regime to prevent saturation effects. Figure 5b is showing the transient absorption spectra for P3HT:PBI 1 blend between 870 and 1300 nm having a maximum around 970 nm, which was earlier ascribed mainly to the P3HT polaron.[35] Note that PBI^{-} exhibits also certain radical anion absorption at 958 nm as seen from Figure 4a and may partially contribute to the transient absorption in this region. The transient absorption spectrum of P3HT:PBI 2 (Figure S4) is very similar, however, it appears a little bit narrower and redshifted to that of P3HT:PBI 1. Following the temporal evolution it is obvious, that the dynamics in P3HT:PBI 1 is much faster than in P3HT:PBI 2 indicating a faster charge recombination dynamics for the PBI 1 blend. Note that both spectra were smoothed and normalized to 1. A comparison of original data and smoothed data at early time is given in Figure S5 for both blends.

We now take a deeper look at the temporal evolution of the transient absorption around 970 nm to understand the recombination dynamics in both blend systems. The laser excitation density was kept at 30 µJ·cm^{-2} (excitation wavelength = 500 nm), to minimize fast recombination due to high charge densities, since it was shown, that the recombination

dynamics depend highly on the charge density. To ensure, that triplet states were not significantly involved in the recombination process, we measured the temporal dynamics of the transient absorption at 970 nm for both blend systems under nitrogen and under air. In case of significant triplet contribution to the transient absorption, we expect in oxygen an accelerated recombination dynamics due to triplet-triplet energy transfer from any triplet state in the photoexcited blend to the triplet oxygen.[36] Additionally, a mono exponential decay of the transient absorption would be a possible indication for geminate recombination dominated transient absorption decay.[35]

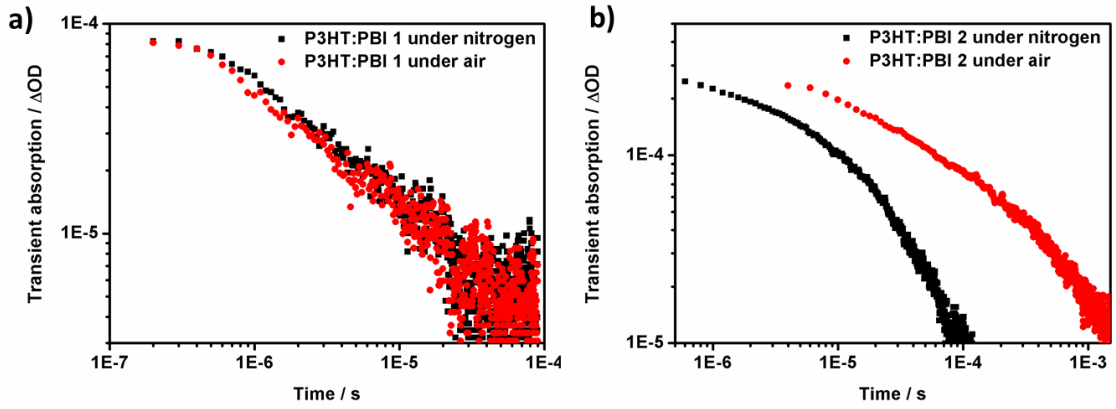

Figure 6. *Decay of transient absorption at 970 nm after laser excitation at 500 nm with 30 µJ·cm^{-2} for a) P3HT:PBI 1 and b) P3HT:PBI 2 under nitrogen (black) and air (red). The date shown here are as measured without any normalization.*

In Figure 6a, the decay of transient absorption in P3HT:PBI 1 blend under nitrogen and air is shown. No differences between the measurement under nitrogen and air are observed, hence triplet states does not play a significant role in the decay dynamics of this blend system. Furthermore the linear decay from the log-log plot indicates a non-geminate recombination of charge carriers according to power law as it was found also in P3HT:PCBM blend systems rather than a mono exponential decay indicating geminate recombination or triplet states.[35] Such power law behavior was also found for the P3HT:PBI 2 blend system under air especially in the time domain between 20 and 100 µs (Figure 6b). However, an analogous measurement under air leads to prolonged recombination dynamics, as it was not expected and to the best of our knowledge such behavior was also not published earlier. We assign this prolonged recombination to the formation of charge trapping caused by hygroscopic nature of the OEG side chains and hence leading to decelerated recombination dynamics in air. Ethylene glycol is known for its high hygroscopicity. Using PBI 1 in blend (no OEG side

chains) such a behavior was not found under air. As mentioned already, triplet state would accelerate the decay dynamics due to triplet state quenching by oxygen. However, this is not the case for the P3HT:PBI 2 blend. We assign therefore the decay characteristics observed for both blends under nitrogen to recombination of charge carriers between holes from the P3HT donor domain with electrons from the PBI acceptor domain. The rate of recombination *R*, hence the decay of charge carrier density upon time *dn/dt* can be written as Eq. 1, where *n* and *p* are the charge carrier densities for electron and hole respectively and β is the recombination rate constant.

$$R = \frac{dn}{dt} = -\beta \cdot n \cdot p \qquad (2)$$

$$R = \frac{dn}{dt} = -\beta \cdot n^2 \qquad (3)$$

$$R = \frac{dn}{dt} = -\beta \cdot n^{(\lambda+1)} \qquad (4)$$

$$n(t) = (n_0^{-\lambda} + \beta \cdot \lambda \cdot t)^{-1/\lambda} \quad (5)$$

Under the assumption that intrinsic charge carrier densities are negligible, the number of both charge carriers should be equal, since each electron will leave one hole during the photoinduced charge generation process. Having $n = p$, Eq. 1 simplifies to a second order power law (Eq. 2), which emphasize a pure bimolecular nature of recombination. However, it was shown, that often recombination orders beside 2 are observed.[37] Therefore a general power law equation having an order of $(\lambda+1)$ was introduced (Eq.3). Integration of Eq. 3 leads to Eq. 4, which represents the charge density at a given time. As mentioned above in Eq. 1, ΔOD is directly proportional to *n* and hence Eq. (5) can be rewritten as

$$\Delta OD(t) = (\Delta OD_0^{-\lambda} + k \cdot \lambda \cdot t)^{-1/\lambda} \quad (6)$$

with *k* being the rate constant for the ΔOD decay. Using Eq. (6) we were able to fit both decay dynamics for PBI 1 and PBI 2 blend systems. In Figure 7, the measured decays for both blend systems are shown including the best fit according to Eq. 6. Different decay dynamics between PBI 1 and PBI 2 are obvious indicating different recombination dynamics in these blend systems. Note that all data from Figure 7 were also normalized to the steady state optical density of the sample at 500 nm. In Table 2 all the parameters from the best fit according to Eq. (6) are shown. Additional α is given, which corresponds to the slope of the power low linear regime in the log-log plot and is based on the relation $n(t) \sim t^{-\alpha}$, with $\alpha = -(1/\lambda)$.

Table 2. *Summarizes the parameters from decay data in Figure 7 using a best fit based on Eq. (6). The parameter α was calculated from λ according to α = -(1/λ).*

blend	ΔOD_0	k [s^{-1}]	(λ+1)	α
P3HT:PBI 1	8.3 E-5	4.0 E-5	2.49	-0.40
P3HT:PBI 2	3.5 E-4	3.2 E-7	1.71	-0.58

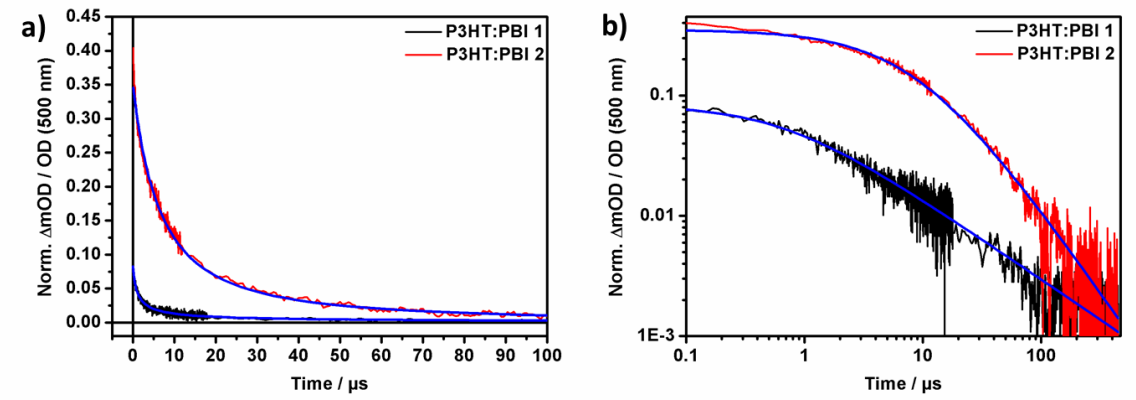

Figure 7. *Normalized (with respect to the steady state optical density at 500 nm) decay of transient absorption at 970 nm after laser excitation at 500 nm with 30 µJ·cm^{-2} for P3HT:PBI 1 (black) and P3HT:PBI 2 (red) under nitrogen in a) linear-linear scale between 0 and 100 µs and b) log-log scale between 0.1 and 500 µs. The blue line represents the best fit according to power law Eq. (6).*

From the linear-linear plot (Figure 7a) one can already see that the initial signal given in *ΔmOD* for PBI 1 blend is much smaller than for PBI 2 blend as it was found already from the excitation density dependent measurement shown in Figure 5a and which again corresponds to a smaller charge carrier density for PBI 1 blend at the time of measurement. Two reasons might explain the differences in initial charge density: 1.) A certain crystallinity and domain size might be needed to ensure fast transport away from the interface in PBI blend systems which minimize geminate recombination. Taking the results from AFM images in Figure 3 into account, the high intermixing found in P3HT:PBI 1 might lead to an increased geminate recombination due to the inability to transport the charges carriers away from the interface and to stabilize the charge carriers in sufficient large PBI domains. In consequence, the efficiency of charge carrier separation is reduced. 2.) Meredith *et al.* has shown recently an enhancement of dielectric constant in a small molecule acceptor by substituting the alkyl side chain with OEG side chains.[38] A higher dielectric constant reduces the Coulomb force and hence higher the efficiency of exciton dissociation at the donor acceptor interface into charge

transfer states and further into separated charge carriers. We therefore expect PBI 2 having OEG side chains to exhibit higher dielectric constant compared to PBI 1, which consequently leads to an increase in separated charge carrier generation due to reduced Coulomb binding force. Similarly differences in the decay constant *k* can be explained: First, the high intermixing found in P3HT:PBI 1 increases the probability for opposite charge carriers to meet and hence increases the recombination rate. Second, the recombination rate reduces with increasing dielectric constant, which is theoretically described by the Langevin expression and was experimental shown by Jen *et al.*[39] Therefore the OEG side chain in PBI 2 might be again responsible for a decay constant *k* being two orders of magnitude lower than for PBI 1 due to a higher degree of phase separation for charge carrier stabilization and a higher dielectric constant which leads in both cases to a reduced non-geminate recombination rate. The recombination order of the power law ($\lambda+1$) was also obtained from the best fit. Based on the relation mentioned above, α was calculated from λ. Alternatively α can be determined by the slope of the linear regime in the log-log plot shown in Figure 7b. In literature both, the order of power law ($\lambda+1$) as well as the power law slope in log-log plot α is used to discuss the underlying recombination dynamics. For instance, a recombination order of one was ascribed to Shockley-Hall-Read recombination via interface states or trap states, whereas second order recombination is explained by Langevin recombination of free charge carriers as found for example in neat P3HT. Consequently a recombination order between one and two (1.71), as found for the P3HT:PBI 2 blend, is explained by a combination of both recombination types. In contrast to that, P3HT:PBI 1 exhibits a recombination order of 2.49. Such recombination orders higher than two were also reported for P3HT:PCBM blend systems and their origin is still under discussion.[37, 40, 41] Deibel *et al*. took several effects into account to explain super-second-order kinetics, whereby the effect of interfacial states was found to provide the most complete explanation. Such interfacial states originate from close donor/acceptor interaction in the presence of a third mixed phase beside pure donor and acceptor domains.[37] This might explain the higher recombination order found in P3HT:PBI 1, since presence of higher intermixing between PBI 1 and P3HT was already demonstrated by AFM images (Figure 3c and d). However, a full explanation for the effect of involved trap states for both blend systems is still needed. While indeed an increase in recombination orders where found with increasing density of trapped charges, e.g. at low temperatures[37] or through photodegradation,[41] a higher exponent α was found after thermal annealing in P3HT:PCBM blend systems and consequently was attributed to a reduction in the fraction of deep traps through increased crystallinity of the film.[33] Thus, the higher

exponent α (similarly the lower recombination order) found in P3HT:PBI 2 is an indication for lower density of trapped charges and a higher crystallinity inside the blend of either the donor or acceptor or both with respect to P3HT:PBI 1. This is in line with the results from the AFM measurements, where structural features were found (Figure 3b and 3d). We are now able to explain the lower J_{SC} in P3HT:PBI 1 with a lower initial charge carrier density and a faster recombination dynamics, which is a result of the high degree of intermixing as confirmed by AFM images. In addition, Durrant *et al*. found the V_{OC} to be linked quantitatively to the recombination rate constant, where a larger recombination rate constant leads to a lower V_{OC}. The larger recombination rate constant was explained to be a consequence of poor phase separation between donor and acceptor,[35] which is in line with our results. Consequently an increase in phase separation at least for the intermixed P3HT:PBI 1 blend should lead to a smaller recombination rate constant.

It was shown earlier, that phase separation and hence PBI domain size can be controlled by thermal annealing in Polymer:PBI blend systems.[21-23] We therefore annealed both P3HT:PBI blend systems for 15 minutes at selected temperatures to investigate changes in morphology and non-geminate recombination dynamics. In Figure 8 the absorption normalized at 500 nm for both P3HT:PBI blend system is shown. Interestingly the shape of the absorption spectrum in PBI 1 blend changes upon thermal treatment most obviously from a rising peak at 540 nm with respect to the peak at 500 nm with increasing annealing temperature (Figure 8a). This is a strong indication for structural changes inside the PBI 1 blend. Possible reasons for that might be the crystallization of P3HT or changes in the monomer to aggregate ratio of PBI 1. In contrast to that, no significant spectral changes could be observed for the PBI 2 blend (Figure 8b).

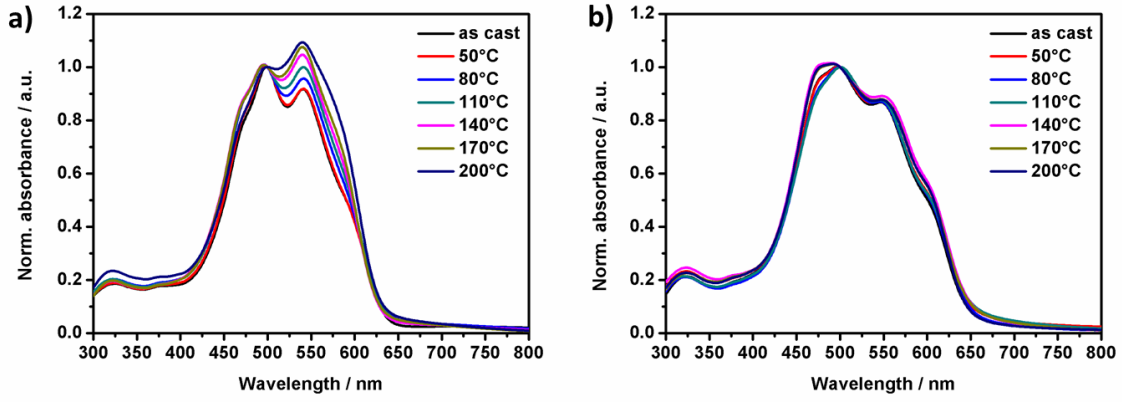

Figure 8. *Normalized absorbance of a) P3HT:PBI 1 and b)P3HT:PBI 2 annealed for 15 minutes at different annealing temperatures. Normalization of the absorption was applied at 500 nm which is the absorption maximum for the as-cast film for both PBI blends.*

Usually thermal annealing of polymer:PBI blends leads to higher surface roughness indicating an increase in phase separation or in particular an increase in PBI domain size.[21-23] To verify whether the film roughness of the P3HT:PBI blends increases upon thermal annealing, AFM images were taken and compared to the as-cast film shown in Figure 3. As an example, AFM images of both PBI blend films after 15 minutes at 170°C are shown (Figure 9). The RMS roughness of PBI 1 blend was 1.31 nm, whereas for PBI 2 blend it was 10.8 nm. The difference is similar to the as-cast films in Figure 3 mainly based on the different side chains. However, compared to the as-cast film, both PBI blend systems exhibits an increase in RMS roughness as seen also by comparing the respective AFM height images (Figure 3 and Figure 9). This is similar to the finding from literature for polymer:PBI systems and can be explained by thermally driven grow of PBI domains and / or an increased formation of P3HT crystalline phases.

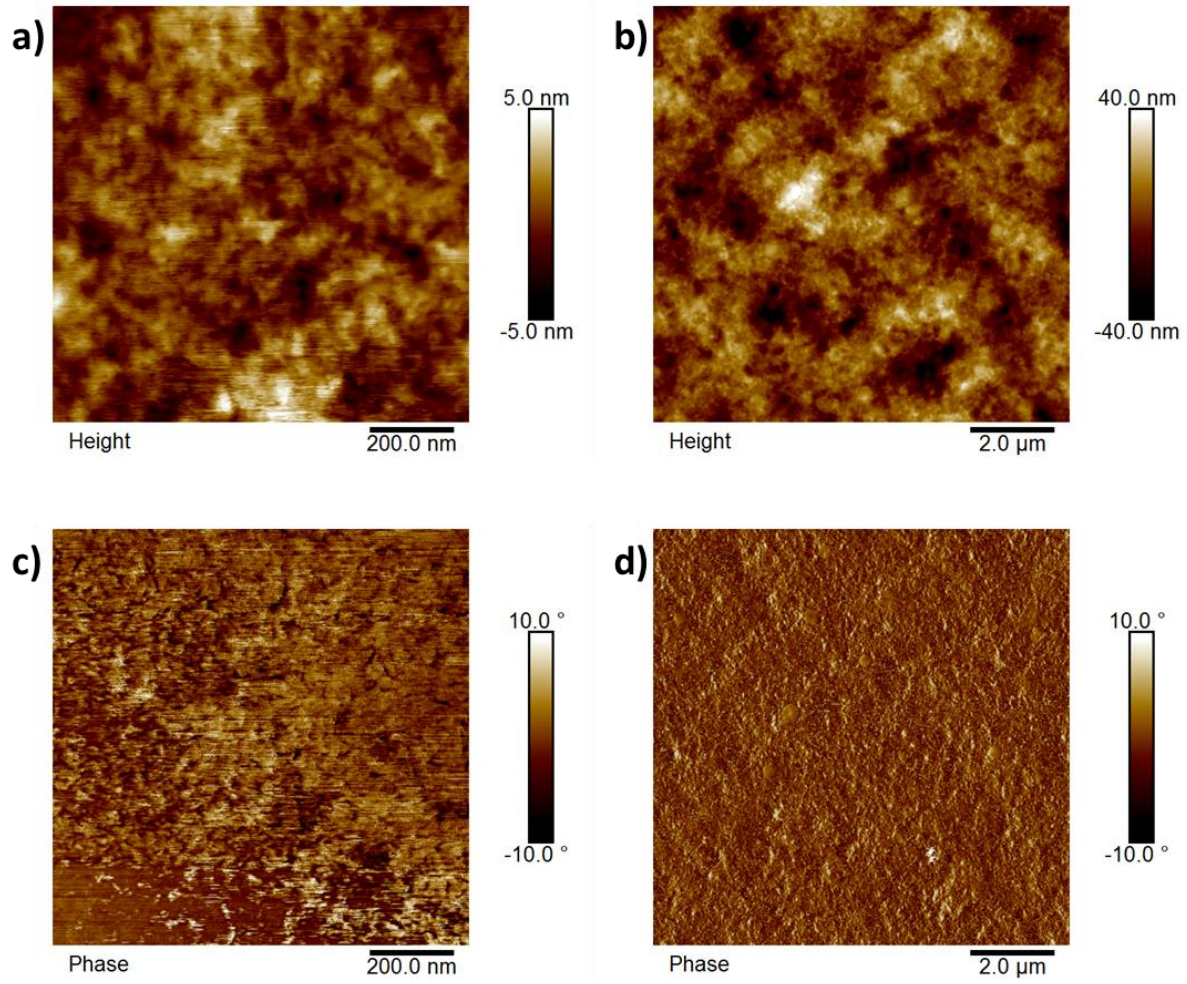

Figure 9. *AFM height (**a** and **b**) and phase (**c** and **d**) images of P3HT:PBI blends (1:2 wt/wt) for PBI 1 (**a** and **c**) and PBI 2 (**b** and **d**) annealed at 170°C for 15 minutes . Note the different scale bars. An 1 x 1 µm AFM images of the P3HT:PBI 2 blend is available in Figure S7.*

The increased RMS roughness of the P3HT:PBI blend film topography upon thermal annealing is an indication for an increased phase separation compared to the as-cast blend films. We again performed transient absorption spectroscopy to verify the impact of thermal annealing on the non-geminate recombination dynamics. The decay dynamics of transient absorption monitored at 970 nm for annealed P3HT:PBI 1 blends is shown in Figure 10a. No differences in decay dynamics are observed for as-cast and at 50°C annealed blend films. However, starting from 80°C and above, annealed blend film exhibit two different decay dynamics; the first one at early times between 0.35 to 5.5 µs was ascribed to the non-geminate recombination between free charge carriers, whereas the linear tail in the log-log plot between 6.5 to 450 µs was referred to trap limited non-geminate recombination of a free and a trapped charge carrier.[41] This is particularly pronounced for the blend film annealed at 170°C and 200°C. As an example, the two different decay dynamics of the blend film annealed at 170°C were fitted to power law decay. The first decay dynamics between 0.35 to 5.5 µs was fitted using Eq. 6, whereas for the second decay dynamics between 6.5 to 450 µs a simple linear fit in the log-log plot was used to estimate the slope α. The fits of the two time regimes are shown in Figure 10a as black line following the decay dynamics for the blend film annealed at 170°C. According to the power law fit between 0.35 to 5.5 µs, a decay rate constant of $k \approx$ 1.2 E-6 s^{-1} was found, which is indeed one order of magnitude smaller than for the as-cast P3HT:PBI 1 blend (Table1). This is a strong indication for decelerated non-geminate recombination dynamics for the blend film annealed at 170°C most probably through more crystalline domains as assumed from the absorption spectra (Figure 8a) and a higher degree of phase separation which is in line with the increased roughness found by AFM images (Figure 9a). Both effects help to stabilize the charge carriers in the respective domains and prevent them from fast non-geminate recombination as it is the case for as-cast highly intermixed P3HT:PBI 1 blend. The recombination order ($\lambda+1$) is 1.3 for this early time regime, whereas it is 2.9 for the later time regime between 6.5 to 450 µs; which is obtained from the slope of the linear fit in the log-log plot α = -0.35. Such high recombination orders observed from the later time regime are typical for trap limited non-geminate recombination from deep trap states.[41]

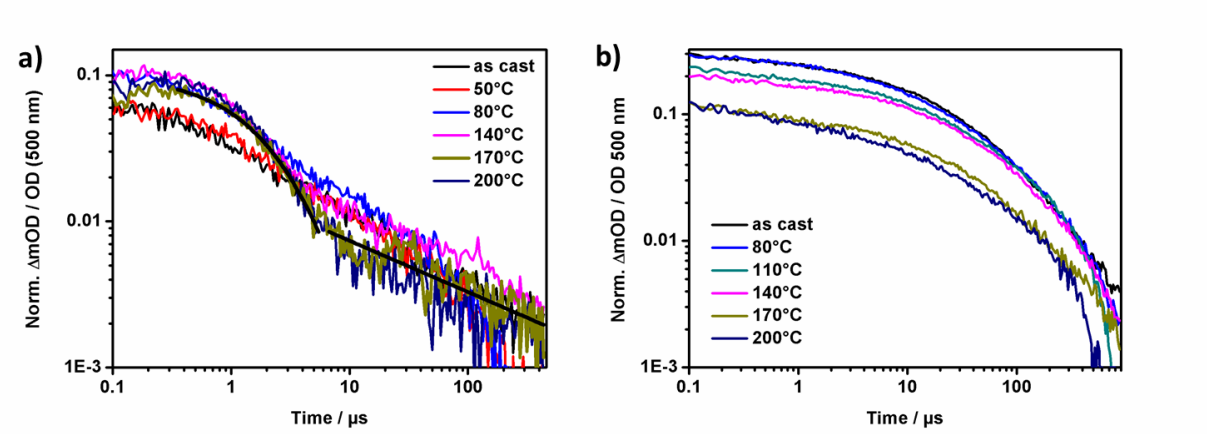

Figure 10. *Normalized (with respect to the steady state optical density at 500 nm) decay transient absorption decay dynamics monitored at 970 nm after excitation at 500 nm (excitation density was 30 µJ/cm2) of a) P3HT:PBI 1 and b) P3HT:PBI 2 of as-cast film and after annealing at different temperatures. The black lines in a) reflect the best fit for the film annealed at 170°C using either Eq. 6 (0.35 µs to 5.5 µs) or linear fit of in log-log plot to estimate α according to ΔmOD(t)~t-α (6.5 µs to 450 µs).*

In contrast to that, the P3HT:PBI 2 blend system does not show significant changes in decay dynamics upon thermal annealing as can be seen from Figure 9b. Hence no significant changes in crystallinity or structure could be observed upon thermal annealing, which affect neither the absorption spectra (Figure 8b) nor the decay dynamics in transient absorption (Figure 10b). However, the initial *ΔmOD* signal decreases with increasing annealing temperature indicating decreasing charge carrier density upon thermal annealing. We attribute this to the increasing roughness at higher annealing temperature as confirmed by AFM image (Figure 9b). The increased phase separation leads consequently to a decreased donor-acceptor interface and hence and lower photocharge generation.

Finally, using time-dependent transient absorption spectroscopy and AFM images, we could explain the impact of hydrophobic alkyl versus hydrophilic OEG solubilizing side chains in P3HT:PBI blend system on the charge recombination dynamics and morphology and consequently we were able to explain the differences observed in photovoltaic performance. Furthermore, we could monitor the impact of thermal annealing on steady state absorption, morphology and recombination dynamics for both PBI blend systems.

Conclusion

We have studied two different PBI small molecule acceptors containing either alkyl (PBI 1) or OEG (PBI 2) side in a blend with P3HT. Both PBIs show similar photophysical and energetic properties, however, PBI 2 show better photovoltaic performance when blended with P3HT. From AFM images we observed a very smooth surface for the PBI 1 blend indicating a high degree of intermixing with P3HT. In contrast to that, the roughness of the PBI 2 blend was dramatically increased, which is an evidence for high phase separation between PBI 2 and P3HT. Additionally, structural features were found indicating large PBI aggregates. Using time dependent transient absorption spectroscopy in nano- to microsecond time scale we were able to monitor the dynamics of charge carrier recombination. We observed a much faster dynamics with lower initial charge carrier density and a higher recombination order indicating a higher density of trap states for the P3HT:PBI 1 blend. The faster dynamics and the lower initial charge carrier density were attributed to the high degree of intermixing as confirmed by AFM images. The high recombination order might be a sign for a third mixed phase between donor and acceptor. Further experiments are necessary to support this hypothesis. For the P3HT:PBI 2 blend a slower dynamics together with a higher initial charge carrier density was found, which can be explained by higher phase separation and stabilization as seen from AFM images and by the higher dielectric constant due to OEG side chains, leading to an improved charge generation efficiency while reduced recombination due to reduced coulomb binding force. The lower recombination order found in PBI 2 blend might origin from lower density of traps caused by a higher degree of crystallinity e.g. from PBI aggregates as proposed from AFM images. Using thermal annealing, we were able to increase the crystallinity and phase separation also in P3HT:PBI 1 blend system as confirmed by steady state absorption spectroscopy and AFM images. Consequently the recombination of an annealed P3HT:PBI 1 film was found to be lowered by one order of magnitude compared to the as-cast film indicating a decelerated recombination dynamic.

Acknowledgements

The financial support from the Bavarian State Ministry of Science, Research, and Arts for the collaborative Research Network ‘‘Solar Technologies go Hybrid’’ is gratefully acknowledged. Christoph Hunger acknowledges for financial support from DFG (GRK 1640) and give thanks to Andreas Schedl (University of Bayreuth) for support in AFM measurements.

References

[1] Dang, M. T.; Hirsch, L.; Wantz, G., P3HT:PCBM, Best Seller in Polymer Photovoltaic Research. *Adv. Mater.*, **2011**, *23* (31), 3597-3602.

[2] Li, G.; Yao, Y.; Yang, H.; Shrotriya, V.; Yang, G.; Yang, Y., Solvent Annealing Effect in Polymer Solar Cells Based on Poly(3-hexylthiophene) and Methanofullerenes. *Adv. Funct. Mater.*, **2007**, *17*, 1636–1644.

[3] Lee, J. K., Ma, W. L., Brabec, C. J., Yuen, J., Moon, J. S., Kim, J. Y., Lee, K.; Bazan, G. C.; Heeger, A. J., Processing additives for improved efficiency from bulk heterojunction solar cells. *J. Am. Chem. Soc.*, **2008**, *130* (11), 3619-3623.

[4] Liu, Y.; Zhao, J.; Li, Z.; Mu, C.; Ma, W.; Hu, H.; Jiang, K.; Lin, H.; Ade, H.; Yan, H., Aggregation and morphology control enables multiple cases of high-efficiency polymer solar cells. *Nat. Commun.*, **2014**, *5*, (9), 1-8.

[5] Sun, Z.; Xiao, K.; Keum, J. K.; Yu, X.; Hong, K.; Browning, J.; Ivanov, I. N.; Chen, J.; Alonzo, J.; Li, D.; Sumpter, B. G. & Geohegan, D. B., PS-b-P3HT Copolymers as P3HT/PCBM Interfacial Compatibilizers for High Efficiency Photovoltaics. *Adv. Mater.*, **2011**, *23* (46), 5529-5535.

[6] Sommer, M.; Lindner, S. M.; Thelakkat, M., Microphase-Separated Donor–Acceptor Diblock Copolymers: Influence of HOMO Energy Levels and Morphology on Polymer Solar Cells. *Adv. Funct. Mater.*, **2007**, *17* (9), 1493-1500.

[7] Nguyen, L. H.; Hoppe, H.; Erb, T.; Guenes, S.; Gobsch, G.; Sariciftci, N. S.. Effects of Annealing on the Nanomorphology and Performance of Poly (alkylthiophene): Fullerene Bulk-Heterojunction Solar Cells. *Adv. Funct. Mater.*, **2007**, *17* (7), 1071-1078.

[8] Nicolaidis, N. C.; Routley, B. S.; Holdsworth, J. L.; Belcher, W. J.; Zhou, X.; Dastoor, P. C., Fullerene Contribution to Photocurrent Generation in Organic Photovoltaic Cells. *J. Phys. Chem. C*, **2011**, *115*, (15), 7801-7805.

[9] Anctil, A.; Babbitt, C. W.; Raffaelle, R. P.; Landi, B. J., Material and energy intensity of fullerene production. *Environ. Sci. Technol.*, **2011**, *45*, (6), 2353-2359.

[10] Sonar, P.; Fong Lim, J. P.; Chan, K. L., Organic non-fullerene acceptors for organic photovoltaics. *Energ. Environ. Sci.*, **2011**, *4*, (5), 1558- 1574.

[11] Lin, Y.; Zhan, X., Non-fullerene acceptors for organic photovoltaics: an emerging horizon. *Mater. Horiz.*, **2014**, *1* (5), 470-488.

[12] Marder, S. R.; Huang, C.; Barlow, S., Perylene-3,4,9,10-tetracarboxylic Acid Diimides: Synthesis, Physical Properties, and Use in Organic Electronics. *J. Org. Chem.*, **2011**, *76* (8), 2386-2407.

[13] Herbst, W.; Hunger, K., Industrial Organic Pigments: Production, Properties, Applications, 3rd edn., WILEY-VCH, Weinheim, **2004**.

[14] Oh, J. H.; Wong, L.; Yu, H.; Park, Y. J.; Min Kim, J.; Bao, Z., Observation of orientation-dependent photovoltaic behavior in aligned organic nanowires. *Appl. Phys. Lett.*, **2013**, *103*, 053304-053301.

[15] Guo, X.; Bu, L.; Zhao, Y.; Xie, Z.; Geng, Y.; Wang, L., Controlled phase separation for efficient energy conversion in dye/polymer blend bulk heterojunction photovoltaic cells. *Thin Solid Films*, **2009**, *517*, (16), 4654-4657.

[16] Howard, I. A.; Laquai, F.; Keivanidis, P. E.; Friend, R. H.; Greenham, N. C., Perylene Tetracarboxydiimide as an Electron Acceptor in Organic Solar Cells: A Study of Charge Generation and Recombination. *J. Phys. Chem. C*, **2009**, *113*, 21225-21323.

[17] Rajaram, S.; Armstrong, P. B.; Bumjoon, J. K.; Fréchet, J. M. J., Effect of Addition of Diblock Copolymer on Blend Morphology and Performance of Poly(3-hexylthiophene):Perylene Diimide Solar Cells. *Chem. Mater.*, **2009**, *21*, (9), 1775-1777.

[18] Li, M.; Liu, J.; Cao, X.; Zhou, K.; Zhao, Q.; Yu, X.; Xing, R.; Han, Y., Achieving balanced intermixed and pure crystalline phases in PDI-based non-fullerene organic solar cells via selective solvent additives. *Phys. Chem. Chem. Phys.*, **2014**, *16*, 26917-26928.

[19] Singh, R.; Aluicio-Sarduy, E.; Kan, Z.; Ye, T.; MacKenzie, R. C. I.; Keivanidis, P. E., Fullerene-free organic solar cells with an efficiency of 3.7% based on a low-cost geometrically planar perylene diimide monomer. *J. Mater. Chem. A*, **2014**, *2*, 14348-14353.

[20] Sharenko, A.; Gehring, D.; Laquai, F.; Nguyen, T.-Q., The Effect of Solvent Additive on the Charge Generation and Photovoltaic Performance of a Solution-Processed Small Molecule:Perylene Diimide Bulk Heterojunction Solar Cell. *Chem. Mater.*, **2014**, *26* (14), 4109-4118.

[21] Keivanidis, P. E.; Howard I. A.; Friend, R. H., Intermolecular Interactions of Perylene diimides in Photovoltaic Blends of Fluorene Copolymers: Disorder Effects on Photophysical Properties, Film Morphology and Device Efficiency. *Adv. Funct. Mater.*, **2008**, *18* (20), 3189-3202.

[22] Ye, T.; Singh, R.; Butt, H.-J.; Floudas, G.; Keivanidis, P. E., Effect of Local and Global Structural Order on the Performance of perylene diimide excimeric solar cells. *ACS Appl. Mater. Interfaces*, **2013**, *5*, 11844-11857.

[23] Singh, R.; Giussani, E.; Mróz, M. M.; Di Fonzo, F.; Fazzi, D.; Cabanillas-González, J.; Oldridge, L.; Vaenas, N.; Kontos, A. G.; Falaras, P.; Grimsdale, A. C.; Jacob, J.;

Müllen, K.; Keivanidis, P. E., On the role of aggregation effects in the performance of perylene-diimide based solar cells. *Org. Electron.*, **2014**, *15*, 1347-1361.

[24] Zhong, Y.; Trinh, M. T.; Chen, R.; Wang, W.; Khlyabich, P. P.; Kumar, B.; Xu, Q.; Nam, C.-Y.; Sfeir, M. Y.; Black, C.; Steigerwald, M. L.; Loo, Y.-L.; Xiao, S.; Ng, F.; Zhu, X.-Y.; Nuckolls, C., Efficient Organic Solar Cells with Helical Perylene Diimide Electron Acceptors. *J. Am. Chem. Soc.*, **2014**, *136*, (43), 15215–15221.

[25] Lu, Z.; Zhang, X.; Zhan, C.; Jiang, B.; Zhang, X.; Chen, L.; Yao, J., Impact of molecular solvophobicity *vs.* solvophilicity on device performances of dimeric perylene diimide based solution-processed non-fullerene organic solar cells. *Phys. Chem. Chem. Phys.*, **2013**, *15*, 11375-11385.

[26] Huang, C.; Barlow, S.; Marder, S. R., Perylene-3, 4, 9, 10-tetracarboxylic acid diimides: Synthesis, physical properties, and use in organic electronis. *J. Org. Chem.*, **2011**, *76*, (8), 2386-2407.

[27] Muth, M.-A.; Gupta, G.; Wicklein, A.; Carrasco-Orozco, M.; Thurn-Albrecht, T.; Thelakkat, M., Crystalline vs Liquid Crystalline Perylene Bisimides: Improved Electron Mobility via Substituent Alteration. *J. Phys. Chem. C*, **2013**, *118*, 92-102.

[28] Wicklein, A.; Lang, A.; Muth, M.; Thelakkat, M., Swallow-tail substituted liquid crystalline perylene bisimides: synthesis and thermotropic properties. *J. Am. Chem. Soc*., **2009**, *131* (40), 14442-14453.

[29] Maurano, A.; Hamilton, R.; Shuttle, C. G.; Ballantyne, A. M.; Nelson, J.; O'Regan, B.; Zhang, W.; McCulloh, I.; Azimi, H; Morana, M.; Brabec, C. J.; Durrant, J. R., Recombination dynamics as a key determinant of open circuit voltage in organic bulk heterojunction solar cells: a comparison of four different donor polymers. *Adv. Mater*., **2010**, *22* (44), 4987-4992.

[30] Salbeck, J., An electrochemical cell for simultaneous electrochemical and spectroelectrochemical measurements under semi-infinite diffusion conditions and thin-layer conditions. *J. Electroanal. Chem.*, **1992**, *340* (1), 169-195.

[31] Williams, E.; Ang, T.; Ooi, Z.; Sonar, P.; Lin, T.; Neo, W.; Song, J.; Hobley, J., Optical Characterization of the Hole Polaron in a Series of Diketopyrrolopyrrole Polymers Used for Organic Photovoltaics. *Polymers* **2015**, *7*, 69-90.

[32] Tautz, R.; Da Como, E.; Limmer, T.; Feldmann, J.; Egelhaaf, H.-J.; Von Hauff, E.; Lemaur, V.; Beljonne, D.; Yilmaz, S.; Dumsch, I.; Allard, S.; Scherf, U., Structural correlations in the generation of polaron pairs in low-bandgap polymers for photovoltaics. *Nat. Commun.* **2012**, *3*, 970.

[33] Clarke, T. M.; Ballantyne, A. M.; Nelson, J.; Bradley, D. D.; Durrant, J. R., Free energy control of charge photogeneration in polythiophene/fullerene solar cells: the influence of thermal annealing on P3HT/PCBM blends. *Adv. Funct. Mater*., **2008**, *18* (24), 4029-4035.

[34] Clarke, T. M.; Lungenschmied, C.; Peet, J.; Drolet, N.; Mozer, A. J., A Comparison of Five Experimental Techniques to Measure Charge Carrier Lifetime in Polymer/Fullerene Solar Cells. *Adv. Energ. Mater*., **2015**, *5* (4).

[35] Shoaee, S.; Eng, M. P.; Espildora, E.; Delgado, J. L.; Campo, B.; Martin, N.; Vanderzande, D.; Durrant, J. R., Influence of nanoscale phase separation on geminate versus bimolecular recombination in P3HT: fullerene blend films. *Energ. Environ. Sci*., **2010**, *3* (7), 971-976.

[36] Soon, Y. W.; Cho, H.; Low, J., Bronstein, H.; McCulloch, I., Durrant, J. R., Correlating triplet yield, singlet oxygen generation and photochemical stability in polymer/fullerene blend films. *Chem. Commun.*, **2013**, *49* (13), 1291-1293.

[37] Gorenflot, J.; Heiber, M. C.; Baumann, A.; Lorrmann, J.; Gunz, M.; Kämpgen, A.; Dyakonov, V.; Deibel, C., Nongeminate recombination in neat P3HT and P3HT: PCBM blend films. *J. Appl. Phys.*, **2014**, *115* (14), 144502.

[38] Donaghey, J. E.; Armin, A.; Burn, P. L.; Meredith, P., Dielectric constant enhancement of non-fullerene acceptors via side-chain modification. *Chem. Commun.*, **2015**, *51* (74), 14115-14118.

[39] Cho, N.; Schlenker, C. W.; Knesting, K. M.; Koelsch, P.; Yip, H. L.; Ginger, D. S.; Jen, A. K. Y., High-Dielectric Constant Side-Chain Polymers Show Reduced Non-Geminate Recombination in Heterojunction Solar Cells. *Adv. Energ. Mater.*, **2014**, *4* (10).

[40] Rauh, D.; Deibel, C.; Dyakonov, V., Charge density dependent nongeminate recombination in organic bulk heterojunction solar cells. *Adv. Funct. Mater.*, **2012**, *22* (16), 3371-3377.

[41] Rauh, D., Impact of Charge Carrier Density and Trap States on the Open Circuit Voltage and the Polaron Recombination in Organic Solar Cells. *Dissertation*, University of Würzburg, **2013**.

Supporting information

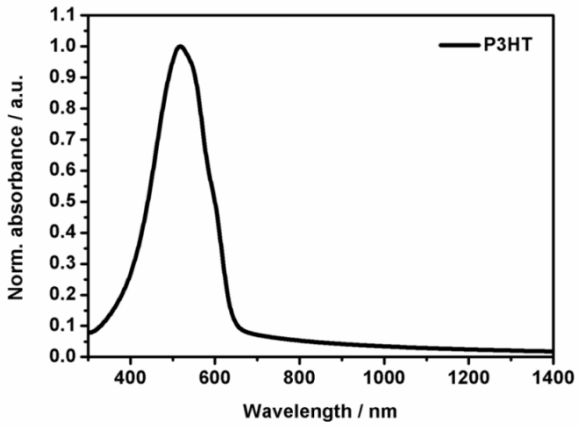

Figure S1. *Normalized absorbance spectrum of as-cast P3HT thin film on glass substrate spin coated from chloroform.*

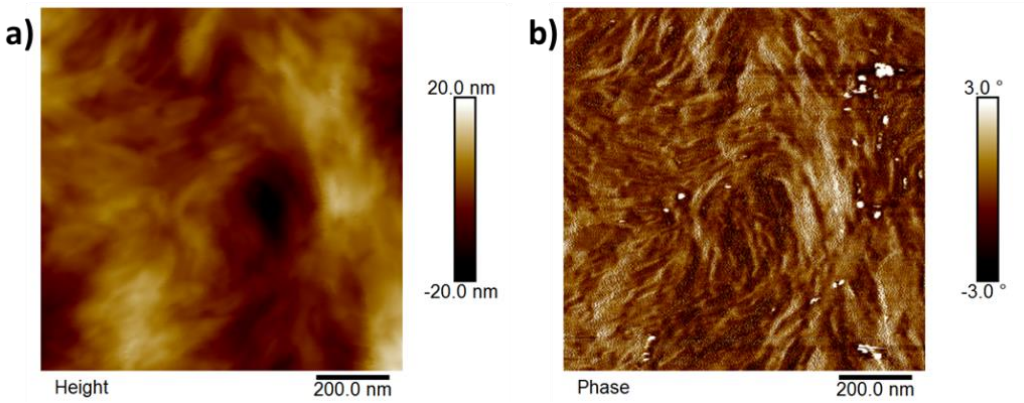

Figure S2. *AFM (1 µm x 1 µm) height (**a**) and phase (**b**) image of P3HT:PBI 2 blend (1:2 wt%) from as-cast chloroform on glass slide. The RMS roughness here was 4.8 nm.*

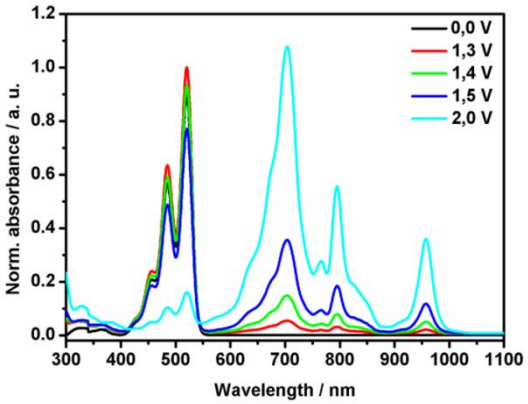

Figure S3. *Normalized spectroelectrochemical spectra of PBI 1 radical anion in THF ($c = 10^{-5}$ mol L^{-1}) with an applied bias ranging between 0.0 V and 2.0 V. Note that the spectrum at 0.0 V bias (black) is hidden behind the spectrum at 1.4 V bias (green) between 400 and 550 nm.*

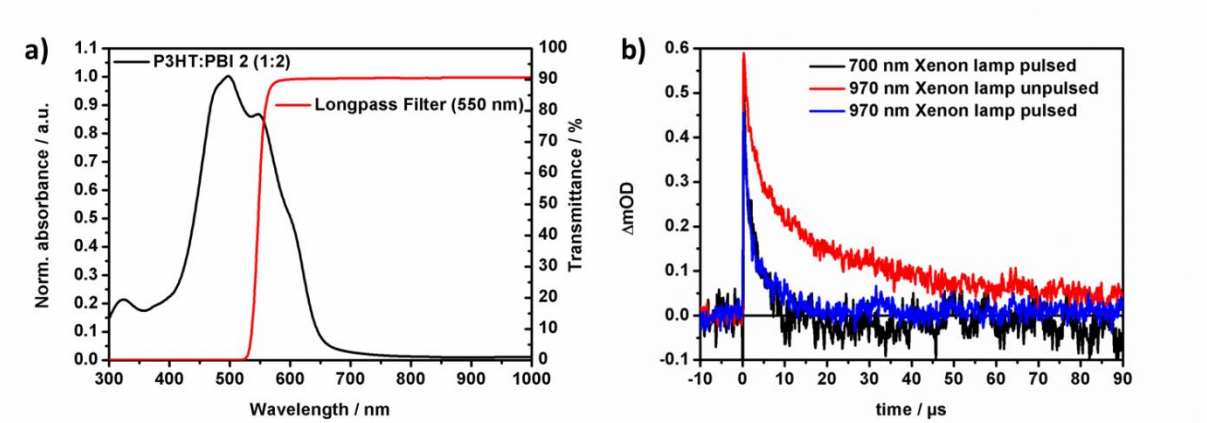

Figure S4. *a) Normalized absorbance spectrum of P3HT:PBI 2 (1:2) (black) and transmittance spectrum of a longpass filter having cut-on wavelength at around 550 nm. b) Transient absorption decay data for P3HT:PBI 2 blend obtained after excitation at 500 nm with an density of 130 µJ / cm^2 and after 100 averages. The data were taken at 700 nm (black) and 970 nm (blue) under pulsed xenon lamp and at 970 nm (red) under non-pulsed xenon lamp. For all three measurements the same filter shown in a) was used.*

Explanation: The available transient absorption setup uses for the visible wavelength range (250 nm to 850 nm) a photomultiplier tube and thus the xenon lamp needs to be pulsed to achieve sufficient light intensity. In contrast to that, for the NIR wavelength range, an InGaAs photodiode is used which works properly without pulsing the xenon lamp. The pulse mode has two drawbacks: First, the measurement takes much longer, since the arc lamp pulser needs a certain time to be recharged before giving the next pulse. A measurement with a high number of averages for sufficient signal to noise ratio is then very time consuming and additionally, the life time of the arc lamp shortens dramatically. Secondly, one has to carefully select a suitable filter to prevent the sample from high light intensities. But this is not just a question about possible photobleaching reactions. Especially in organic photovoltaic devices the recombination dynamics depends highly on the charge carrier density. However, each photon from the Xenon lamp which reached the sample prior to the actual measurement by the laser shot might get absorbed and create a charge carrier. To keep charge carrier density as low as possible before laser excitation, the sample has to be protected by a suitable filter from light, which might get absorbed by the blend system. In Figure S4a a longpass filter having a cut-on wavelength at around 550 nm does not sufficiently blocks all the photons and light from the xenon lamp between 550 and 800 nm which will be then absorbed by the sample leads consequently to an increase of charge carrier density prior the actual laser pulse. This effect of having high charge carrier densities can be clearly seen from the decay dynamics in Figure S4b. The black decay was recorded at 700 nm using the Xenon lamp pulsing mode, which is necessary in this wavelength range as mentioned above. The red decay at 970 nm

without pulsed Xenon lamp shows much longer decay dynamics. However, the blue decay also at 970 nm using now Xenon lamp pulsing mode shows the same fast dynamics as observed to 700 nm (black decay). Since in all three cases, the same longpass filter with cut-on wavelength at 550 nm was used, the faster decay dynamics can be clearly ascribed to high charge carrier densities due to photon absorption by high lamp pulsing prior to laser excitation. A nearly suitable filter for the example in Figure S4a should have a cut-on wavelength at 690 nm to block most of the light <690 nm, while measuring at >700 nm to monitor e.g. polaron band from PBI as well as from P3HT.

Since we measure the transient absorption for detailed recombination dynamics analysis at low excitation energy (30µJ/cm^2), we decided to focus on the P3HT polaron band at 970 nm. Here we are able to carry out a high number of averages for a sufficient signal to noise ratio. In addition, the chosen longpass filter having a cut-on wavelength of 850 nm blocks most of the white light in the visible range.

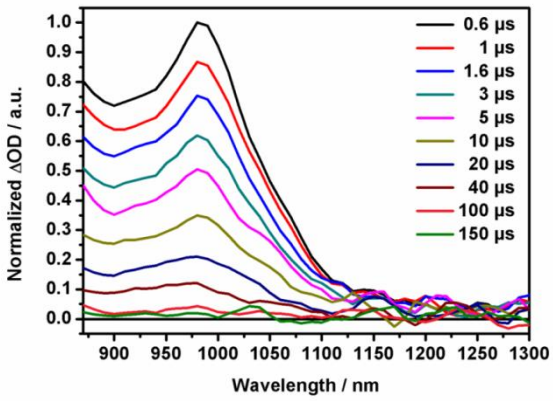

Figure S5. *Normalized to 1 transient absorption spectra between 870 and 1300 nm for P3HT:PBI 2 blend after laser excitation at 500 nm with 130 µJ·cm^{-2}.*

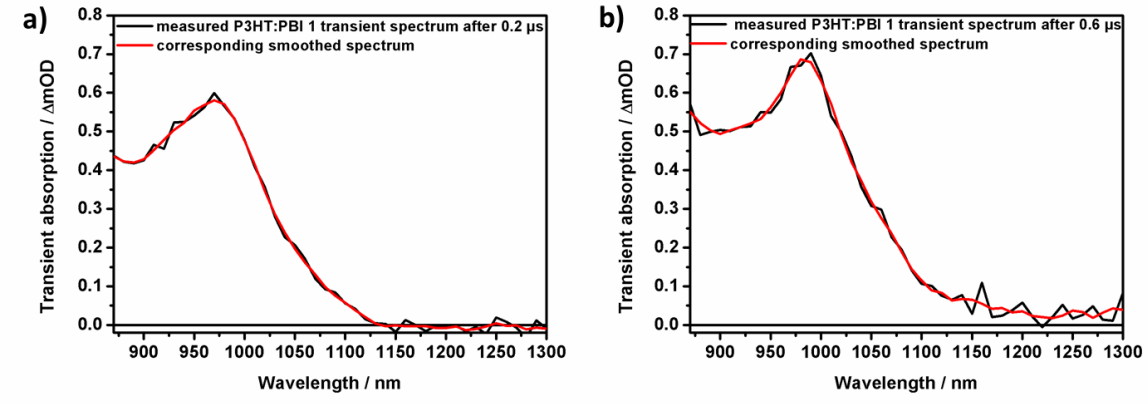

Figure S6. *Comparison between measured transient absorption spectrum (black) and smoothed spectrum (red) for a) P3HT:PBI 1 and b) P3HT:PBI 2 at early times (0.2µs and 0.6µs respectively). In both cases the excitation wavelength was 500 nm, whereas the excitation density was 280 µJ·cm^{-2} for P3HT:PBI 1 and 130 µJ·cm^{-2} for P3HT:PBI 2. Smoothing of the measured data was done using the Savitzky-Golay-filter with a second polynomial order.*

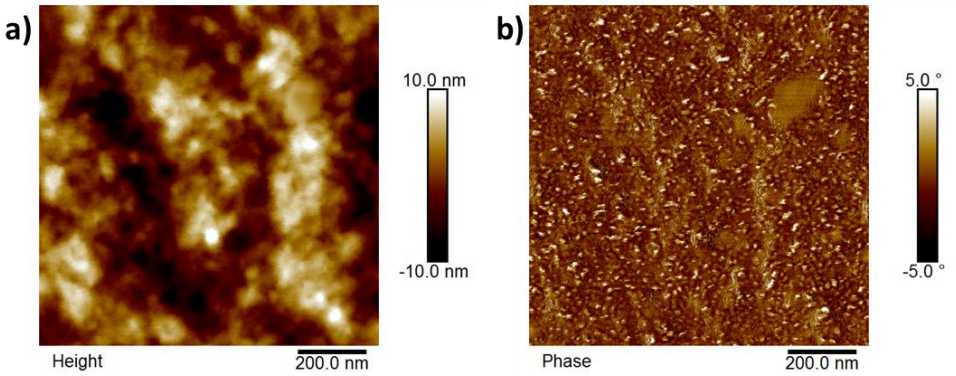

Figure S7. *AFM (1 µm x 1 µm) height (**a**) and phase (**b**) image of P3HT:PBI 2 blend (1:2 wt%) thermal annealed for 15 minutes at 170°C on glass slide. The RMS roughness here was 3.8 nm.*

5 Phase separation in polymer perylene bisimides blends induced by polar interactions

*Christoph Hunger[a], Weiwei Li[b], Martijn M. Wienk[b], René A. Janssen[b] and Mukundan Thelakkat[a]**

*corresponding author

[a] Prof. Dr. Mukundan Thelakkat, Applied Functional Polymers, Macromolecular Chemistry I, University of Bayreuth, D-95440 Bayreuth, Germany.

E-mail: mukundan.thelakkat@uni-bayreuth.de

[b] Prof. Dr. René A. Janssen, Molecular Materials and Nanosystems, Institute of Complex Molecular Systems, Eindhoven University of Technology, P.O. Box 513, 5600 MB Eindhoven, The Netherlands.

This manuscript is prepared for submission.

Abstract

The non-polar vs. polar interaction of two donor polymers with two unsymmetrical perylene bisimides (PBI) PBI 1 and PBI 2 as acceptor were studied in blend. Both PBIs are substituted with a linear alkyl chain at the one imide position, whereas with a hydrophobic alkyl swallow tail (PBI1 1) or hydrophilic oligo ethylene glycol (OEG) swallow tail (PBI 2) at the other imide position. From previous studies it is known, that the hydrophilic substituent in PBI 2 induces phase separation in blend with hydrophobic alkyl side chain substituted donor polymers leading to a higher photovoltaic performance compared to PBI 1. Here we found, that this cannot be generalized, since a higher photovoltaic performance was observed for PBI 1 for one of the donor polymers. However, using atomic force spectroscopy (AFM) we confirmed, that the unfavored interaction between hydrophobic alkyl side chain of the polymer and hydrophilic OEG swallow tail of PBI 2 still leads to higher phase separation for each blend system compared to PBI 1. This discrepancy could by fully resolved by analysis of charge carrier recombination dynamics using time resolved transient absorption spectroscopy (TAS), which leads us to the following conclusion: phase separation in polymer:PBI blends can be indeed induced by hydrophobic vs. hydrophilic interactions of the solubilizing chains of both components and helps to generate long living stabilized charge carriers. However, a too coarse morphology with domain sizes much larger than the exciton diffusion length leads to limited charge carrier generation as confirmed by TAS. The results from TAS of each polymer:PBI blend system presented here explain fully the differences in the respective photovoltaic devices.

Introduction

Solution processed organic photovoltaic (OPV) devices exceed already the 10 % power conversion efficiency (PCE) mark.[1] Fullerene derivatives are still one of the most common acceptors in high efficiency solar cells due to its good electron affinity and charge carrier mobility. However, light absorption occurs mainly in the donor material, since fullerenes show weak light absorption and their contribution to the photocurrent is therefore less compared to the donor polymer.[2] Additionally, when it comes to commercialization, fullerene based acceptors are rather expensive and involve energy intensive syntheses.[3] Moreover, they diffuse or tend to agglomerate in a blend which leads to instability of the donor / acceptor morphology and finally shortens the device lifetime. These aspects have

motivated researchers to look for alternative electron acceptors in OPV.[4, 5] Perylene bisimides (PBI) are one of the most promising alternatives to fullerene for several reason: PBIs exhibit high molar extinction coefficients of 10^4 – 10^5 M^{-1} cm^{-1} [6] in the visible range from 400 – 600 nm,[7] possess high electron mobilities[8] and they are also cheap to synthesize in large amounts. A characteristic property of PBI is the self-assembly through π-π stacking of the PBI core which enables new opportunities for orientated one dimensional charge carrier transport in OPVs.[9] However, in bulk heterojunction solar cells the PBI is - similar to fullerene based acceptors - just blended with a donor polymer, whereby the aggregation and orientation of the PBI aggregates is hard to control. This leads to low photocurrent and low PCE. The main reason for the low PCE of less than 1 % in poly(3-hexylthiophene-2,5-diyl) (P3HT):PBI solar cells[10] is the formation of immobile intermolecular states inside large PBI aggregates after photoexcitation,[11] which finally lead to an excimer formation and relaxation,[12] before reaching the donor / acceptor interface for charge separation. Control of the PBI phase size is therefore crucial and this was demonstrated using a P3HT-PBI diblock copolymer as compatibilizer,[13] solvent additives[14-16] or by thermal annealing.[17, 18] Chen *et al*. found recently a direct correlation between PBI phase size and $J_{SC.}$[19] The phase size was here varied by changing the donor:PBI ratio. Chemical modification of the PBI via side groups at the aromatic core or the N-terminal was done to improve the solubility and / or reduce the aggregation of the PBI core.[20, 21] Another very promising concept was introduced by Rajaram *et al*.,[22] in which two PBI cores were covalently bound via the N-terminals. In this PBI dimer species, the aggregation is heavily reduced, which leads to smaller PBI domains and therefore a 10-fold increase in J_{SC} compared to an analogous monomer PBI molecule. This concept was modified by Zhang *et al*. in such a way, that two PBIs were connected at the bay position via one thiophene group to achieve an efficiency of 4.03 %.[23] The PCE of OPV devices using a bay linked PBI dimer as electron acceptor could be increased since then over 5%[24] and reached recently 6.05%, whereby here the PBI cores are fused directly together.[25] For both, single PBIs and PBI dimers, the N-terminal substituent is used to increase solubility often by alkyl side chains or ethylene glycol.[20, 22, 24-28] The side chains do not only improve the solubility of the PBI in the photoactive layer precursor solution, but also affect the miscibility of the PBI in the donor polymer matrix. Consequently, the side chain may have big influence on the phase separation in a blend and furthermore on the overall photovoltaic performance. The impact of the different numbers of hydrophilic ethylene glycol side chains at the aromatic PBI core with respect of the same hydrophobic alkyl side chain at the N-terminal of a PBI dimer was investigated by Lu *et al*.[29] However,

functionalization of the aromatic PBI core always influences the photophysical and electronic properties.[30] An investigation of the impact of hydrophilic and hydrophobic side chains at the imide N-atoms on the phase separation of a blend is still missing. This helps to keep the photophysical and electric properties of the PBI unit the same. We therefore introduce in Figure 1 two unsymmetrical PBIs with a linear alkyl chain on one imide position and whereas the other imide position is functionalized with either a hydrophobic alkyl swallow tail for PBI 1 or a hydrophilic ethylene glycol swallow tail for PBI 2. As expected, properties such as thin film absorption, molecular energy levels and electron mobility are quite similar for both PBIs.[28, 31] Keeping these properties the same, we are able to investigate the impact of the hydrophobic vs. hydrophilic swallow tail on the phase separation when blended with a donor polymer. In Figure 1 the two donor polymers used in this investigation are shown. Muth *et al*. observed that PBI 1 is very well intermixed with the donor polymer OPV32, giving a smooth featureless film according to atomic force microscopy (AFM) studies. This results in an overall poor OPV device performance most probably due to fast recombination dynamics.[11, 28] In contrast to that, PBI 2 exhibits phase separation when blended with OPV32 resulting in higher short circuit current (J_{SC}) and fill factor (*FF*) leading to improved PCE. In this work we investigate the differences in aggregation of both these PBIs in two different donor polymer materials by studying recombination dynamics. For that we chose PDPP5T as an alternative donor polymer and compared it with OPV32 (Figure 1).

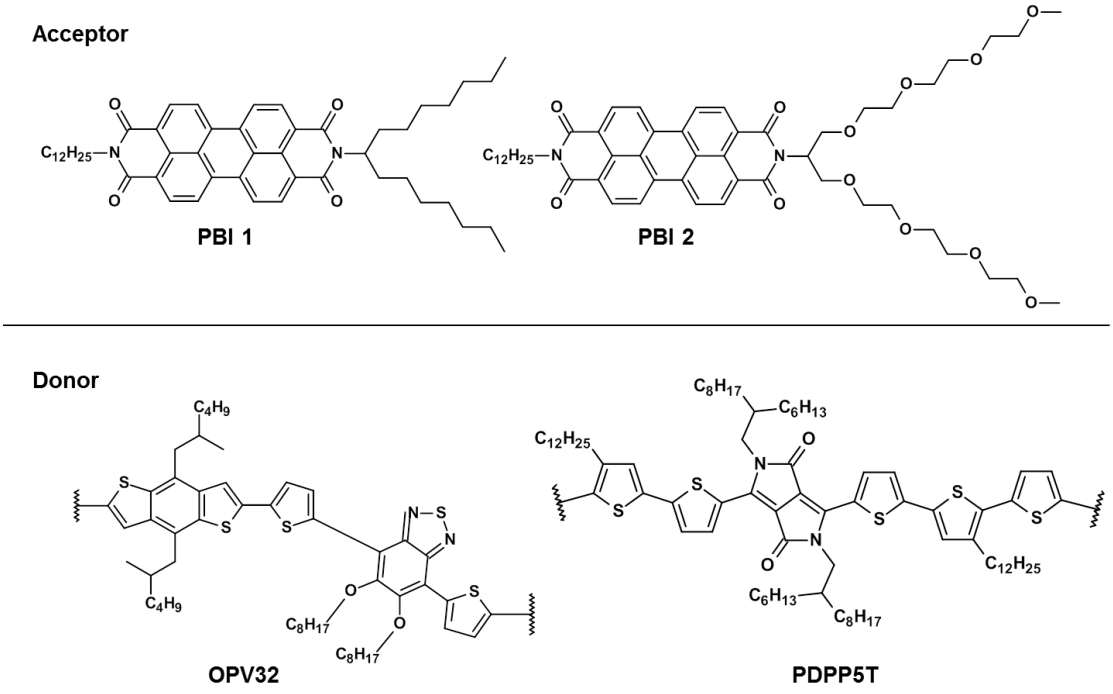

Figure 1. *Chemical structure of the two investigated perylene bisimides PBI 1 and PBI 2 as electron acceptors and the respecting electron donor polymers OPV32 and PDPP5T.*

PDPP5T is a classical low band gap polymer and known to give high PCE of 5.8 % together with $PC_{[70]}BM$ as acceptor.[32] Furthermore its absorption appears mainly between 550 and 850 nm, whereas PBI 1 and 2 absorbs complementarily between 400 and 600 nm.[28] Therefore using PDPP5T as donor polymer should further enhance the photocurrent with respect to OPV32, whose absorption appears only up to 700 nm. Here we fabricated OPV devices from PDPP5T as donor and PBI 1 or PBI 2 as acceptor. The photovoltaic performance of these devices is compared to the devices using OPV32 as donor and differences are discussed based on AFM images and time resolved transient absorption spectroscopy (TAS). We found a strong impact of the hydrophilic vs. hydrophobic side chain of the PBI on the different blend morphology depending on which donor polymer is used. Furthermore, a better photovoltaic performance for the inverted device geometry was found with respect to normal device geometry.

Experimental Part

Chemicals: The synthesis of the acceptor molecule PBI 1 was analogous done to that of PBI 2.[27] The synthesis of the donor polymer PDPP5T is also described elsewhere,[32] whereas the polymer OPV32 was provided by Merck Chemicals Ltd. Poly(3,4-ethylenedioxythiophene) polystyrene sulfonate (PEDOT:PSS) (Clevios P VP Al 4083) was purchased from Heraeus. Zinc acetate dihydrate, methoxyethanole, ethanolamine, diiodooctane (DIO), dichlorobenzene (oDCB) and chloroform ($CHCl_3$) were purchase from sigma Aldrich and used without any further purification.

Thin film sample preparation: Thin film samples for UV/VIS spectroscopy, AFM images and time resolved TAS were fabricated using glass substrates, which were cleaned in ultrasonic bath using the following sequence of solvents: detergent, water, acetone and isopropanol. The photoactive layer of the polymer:PBI blend was fabricated on glass substrate in the same way as for polymer solar cells. UV-Vis spectroscopy was carried out using a Jasco V-670 spectrometer.

Polymer solar cell: Patterned indium tin oxide (ITO) substrates (14 Ω per square, Naranjo substrates) were cleaned with isopropanol and dried with nitrogen gas. For normal device geometry PEDOT:PSS was spin coated with 3000 rpm for 60 s right on top of the cleaned ITO substrates. The photoactive layer was prepared by spin coating right on top of the PEDOT:PSS layer. Different donor:acceptor ratios are calculated by weight whereas any

additive (DIO or oDCB) was added by volume percent (vol %). Variation in thickness was obtained by varying the rotation speed of spin-coating. Lithium fluoride (1 nm) and aluminum (100 nm) was finally evaporated thermally on top of the photoactive layer. For inverted geometry, a zinc acetate solution (109.75 mg zinc acetate dihydrate, 30.5 µl ethanolamine and 1ml methoxyethanole) was mixed, stirred for at least two hours and filtered with 0.2 µm hydrophilic filter. To obtain a 45 nm thick ZnO layer, 100 µl of zinc acetate solution was spin coated on ITO with 4000 rpm for 50 s, followed by heating at 150°C for 5 min to convert zinc acetate into zinc oxide.[33] The photoactive layer was prepared analogous to that of the normal geometry. Molybdenum trioxide (10 nm) and silver (100 nm) was finally deposited on the photoactive layer by thermal vacuum evaporation. The cell area was either 0.091 or 0.162 cm^2. The current-voltage characteristics were measured under the illumination of ~100 mW cm^{-2} white light. Short circuit currents (J_{SC}) under AM1.5G conditions were estimated from the spectral response and convolution with the solar spectrum. The spectral response was measured under simulated 1 sun operation conditions using bias light from a 532 nm solid-state laser (Edmund Optics). Light from a 50 W tungsten halogen lamp (Osram64610) was used as probe light and modulated with a mechanical chopper before passing the monochromator (Oriel, Cornerstone 130) to select the wavelength. The response was recorded as the voltage over a 50 resistance, using a lock-in amplifier (Stanford Research Systems SR 830). The setup was calibrated with a silicon reference. All photovoltaic device measurements were done under nitrogen. The thickness of the photoactive layers was measured on a Veeco Dektak 150 profilometer.

Recombination dynamics: Nano- to microsecond timescale transient absorption of the photoactive blend system was measured using a LKS 80 spectrometer (Applied Photophysics). The photoactive layer was kept for measurements in a thin film holder under N_2 atmosphere. Excitation wavelength of the photoactive layer was either 470 nm (PDPP5T:PBI) or 500 nm (OPV32:PBI) provided by an optical parametric oscillator (Rainbow, 4-8 ns pulse duration – Quantel) which was pumped with the 3rd harmonic oscillation of a Nd:YAG laser (Brilliant – Quantel). The excitation energy of 30 µJ was controlled by neutral density filters and an attenuator consisting of two air-spaced Glan-Taylor calcite polarizers. Additionally, suitable filters were used in the laser beam to cut off the fundamental wavelength at 1064 nm and in the probe light beam to cut off any visible light up to 850 nm. Changes of transient absorption were measured using a fast InGaAs photodiode (HCA-S-200M-IN from Femto, supplied by Applied Photophysics). The data were collected by a DSOS104A oscilloscope (Keysight Technologies).

Results and Discussion

UV-Vis Spectroscopy

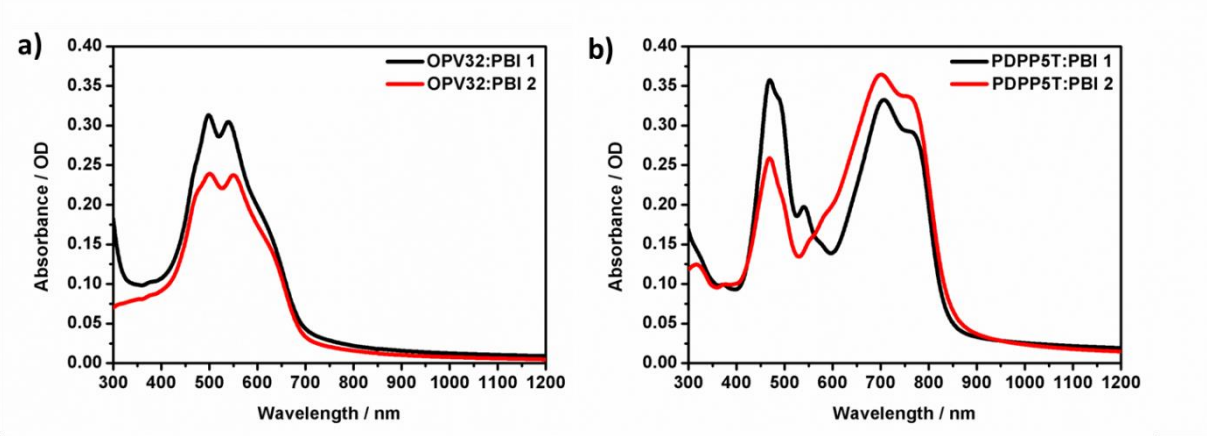

Figure 2. *Thin film UV / Vis absorbance spectra of PBI 1(black) and PBI 2 (red) as electron acceptor in blend with the respective donor polymer a) OPV32 and b) PDPP5T. The polymer:PBI ratio was 1:1 (wt/wt) for OPV32 and 1:2 (wt/wt) for PDPP5T blends.*

Thin films for UV-Vis absorbance measurements were fabricated on glass substrate and they are the same samples as used later for AFM images and TAS measurements. A clear difference in absorption range between the two different blend systems (Figure 2a and 2b) is obvious depending on which polymer is used. Using OPV32 as donor polymer the blend systems absorb mainly between 400 and 700 nm (Figure 2a), whereas PDPP5T:PBI blends show much broader absorption range from 400 up to 850 nm (Figure 2b). This is due to PDPP5T, a low band gap polymer that dominates the absorption between 600 to 850 nm[32] whereas the absorption from 400 to 600 nm originates mainly from the PBI.[28] It is worth to note, that the PBI 2 blend systems are weaker in absorption between 400 to 600 nm compared to the PBI 1 blends. This can be explained by the higher molecular weight of PBI 2 compared to PBI 1 and thus a lower molar concentration of PBI 2 in its blends, since the blend ratio polymer:PBI was calculated by weight (see experimental section for details). This is obvious from the larger swallow tail substituent in PBI 2.

Photovoltaic performance

OPV devices were made to investigate the influence of the hydrophobic vs. hydrophilic side chains of PBI 1 and PBI 2 respectively on the device parameters. Here only devices with PDPP5T as donor polymer are shown and discussed, since the optimization of devices with OPV32 is already published elsewhere.[31] To optimize each PDPP5T:PBI blend system

several experiments were done to estimate the influence of additive content, device geometry, PDPP5T:PBI ratio and photoactive layer thickness on the device performance. Tables S1 to S4 (in ESI) summarize all device parameters for each experiment, which will be discussed in the following. A selected set of data for optimized photovoltaic devices is shown in Table 1 to help the reader to follow the arguments.

Table 1. *Photovoltaic parameters for the optimized PDPP5T:PBI blend devices in normal and inverted device geometry.*

Device Geometry	**PBI**	**Solvent:additive (vol %)**	**d [nm]**	**V_{OC} [V]**	**J_{SC} [mA·cm^{-2}]**	**FF [%]**	**PCE [%]**
normal	PBI 1	$CHCl_3$:oDCB 10%	108	0.58	2.60	32	0.48
	PBI 2	$CHCl_3$:DIO 2.5%	160	0.15	0.27	25	0.01
inverted	PBI 1	$CHCl_3$:oDCB 10%	83	0.69	5.03	45	1.56
	PBI 2	$CHCl_3$:DIO 2.5%	120	0.75	0.76	47	0.27

At first each PDPP5T:PBI blend system was made from $CHCl_3$ and by adding additives of either 2.5 % vol. DIO or 10 % vol. oDCB in a normal device geometry, since these additives are known to have influence on the device performance when PDPP5T and similar donor polymers are blended with $PC_{[70]}BM$.[32] Devices using PBI 1 as acceptor show moderate photovoltaic performance for all three solvent systems. The PCE increases depending on the solvent system in the order $CHCl_3$ (0.12 % PCE) < $CHCl_3$:DIO 2.5 % vol. (0.34 % PCE) < $CHCl_3$:oDCB 10 % vol. (0.48 % PCE) and this increase in PCE originates from an increase in J_{SC} in the same order. Obviously, these additives influences the morphology in polymer:PBI blends and hence their photovoltaic performance. In contrast to that devices using PBI 2 as acceptor show no or very low PCE of 0.01 % for all three solvent systems (Table S1). We expect therefore a fundamental difference between both PBIs with respect to their photovoltaic performance. From several polymer:PBI devices in literature, it is known, that the device geometry in PBI blend systems has a big influence on the photovoltaic performance.[24, 34, 35] It was assumed, that in the case of normal device geometry the PBI electron acceptor is concentrated more to hole conducting layer PEDOT:PSS. In contrast to that, in inverted device geometry, where the underneath layer is ZnO, the PBI concentration was more vertically balanced in thin blend films, leading to a better photovoltaic performance.[35] This could be one reason for the bad performance especially for the hydrophilic PBI 2, which might lead to a favorable interaction with the hydrophilic PEDOT:PSS layer. To proof this, we tested in a next step the blend systems using their

optimized solvent combinations in inverted geometry. For both blend systems we observed a huge improvement of the photovoltaic performance in the inverted geometry. This improvement again originates mainly from a roughly doubled J_{SC} compared to the normal device geometry. However, comparing PBI 1 and PBI 2 in their respective blends, it is apparent that in the PDPP5T:PBI 1 blend leads again to higher J_{SC} of 5.03 mA/cm^2 compared to the PDPP5T:PBI 2 blend with only 0.76 mA/cm^2 (Table 1 and Figure 3).

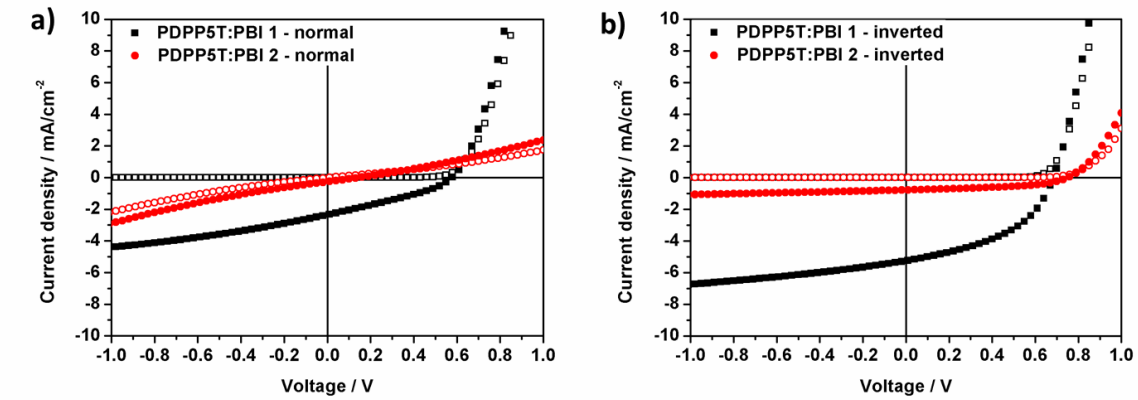

Figure 3. *Optimized PDPP5T:PBI (1:2 wt/wt) blend device under light (filled symbols) and dark (open symbols) for PBI 1 (black) and PBI 2 (red) in a) normal geometry and b) inverted geometry.*

The big difference in J_{SC} is also supported by the EQE spectra for both blend systems as shown in Figure 4. Here the PDPP5T:PBI 1 blend show an EQE value close to 20 % at 470 nm, where the PBI absorption dominates and an EQE value above 23 % in the PDPP5T absorption range with a maximum at 700 nm. The PDPP5T:PBI 2 blend exhibits only EQE values below 4 % over the entire blend absorption range (400 – 850 nm). Nevertheless, for both blend systems it can be concluded that both the donor PDPP5T and the PBI acceptor contribute to the photocurrent. Comparing now the normal with the inverted geometry for both blend systems it is clear, that the bad performance of PBI 2 is not only based on an favorable interaction with a hydrophilic PEDOT:PSS layer. Moreover, in previous studies with the donor polymer OPV32 in normal device geometry, the hydrophilic PBI 2 has performed much better than the hydrophobic PBI 1.[31] We therefore expect the different photovoltaic performance of PBI 1 and PBI 2 to depend additional on differences in phase separation with the respective donor polymer based on hydrophobic – hydrophilic interactions. This is supported by AFM measurements as discussed later. Some further optimizations were carried out for PBI 1 system to check the photovoltaic potential of these systems.

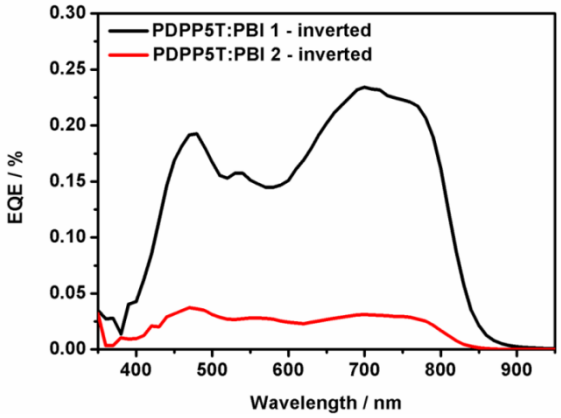

Figure 4. *EQE spectra of optimized PDPP5T:PBI (1:2) blend device for PBI 1 (black) and PBI 2 (red) in inverted geometry.*

The influence of increasing oDCB additive content for the PDPP5T:PBI 1 blend system in an inverted device was investigated, but no further improvement was observed (Table S2). In previous studies with the donor polymer OPV32, it was shown that the polymer:PBI ratio has a big influence on the morphology and consequently on the device efficiency.[31] We therefore varied the PDPP5T:PBI 1 ratio keeping all other optimized parameters in the device the same (Table S3). The different ratios affect the J_{SC} value most and for small J_{SC} values the FF is decreasing, while the V_{OC} stays rather constant. Interestingly, the J_{SC} and therefore the overall PCE is increasing rapidly with increasing PBI content for PDPP5T:PBI 1 ratios from 1:0.5 to 1:2. Analogues to the OPV32:PBI 2 blend systems, two possible effects might be responsible for the increasing J_{SC}: First, an improved electron transport due to the increasing amounts of electron transporting PBI 1 and second an improved morphology, probably due to increasing PBI 1 phase sizes. A further increase of PBI content up to 1:4 leads just to minor changes in J_{SC}. It is worth to note, that with increasing PBI content from 1:0.5 to 1:4, the photoactive layer thickness increases simultaneously from 50 nm up to ~130 nm, which makes a full interpretation of the results difficult. We therefore finally investigated the influence of the photoactive layer thickness for a given ratio of PDPP5T:PBI 1 = 1:2 (wt/wt) (Table S4). Here a clear impact on the J_{SC} is observed: For a 60 nm thick photoactive layer, the light absorption is insufficient leading to a decreased J_{SC}. In contrast to that, in a 167 nm thick photoactive layer, the charge carriers likely recombine non-geminate before reaching the electrodes. This explains the lower J_{SC} and especially the lower *FF* in that device.[36] The optimum thickness in this series was found at 85 nm, where a compromise between light harvesting, charge carrier transport and charge carrier recombination is achieved.

Morphology studies using AFM

AFM measurements of blend films were done to get a better insight into phase size and phase separation between polymer donor and PBI acceptor. Here we focus on the optimized blend system in inverted device geometry for devices shown in Figure 3b using PDPP5T as donor polymer and PBI 1 or PBI 2 as electron acceptor. The thin film samples for each blend system were prepared using the same conditions as for the respective photovoltaic devices. In Figure 5, both AFM height and phase images are shown.

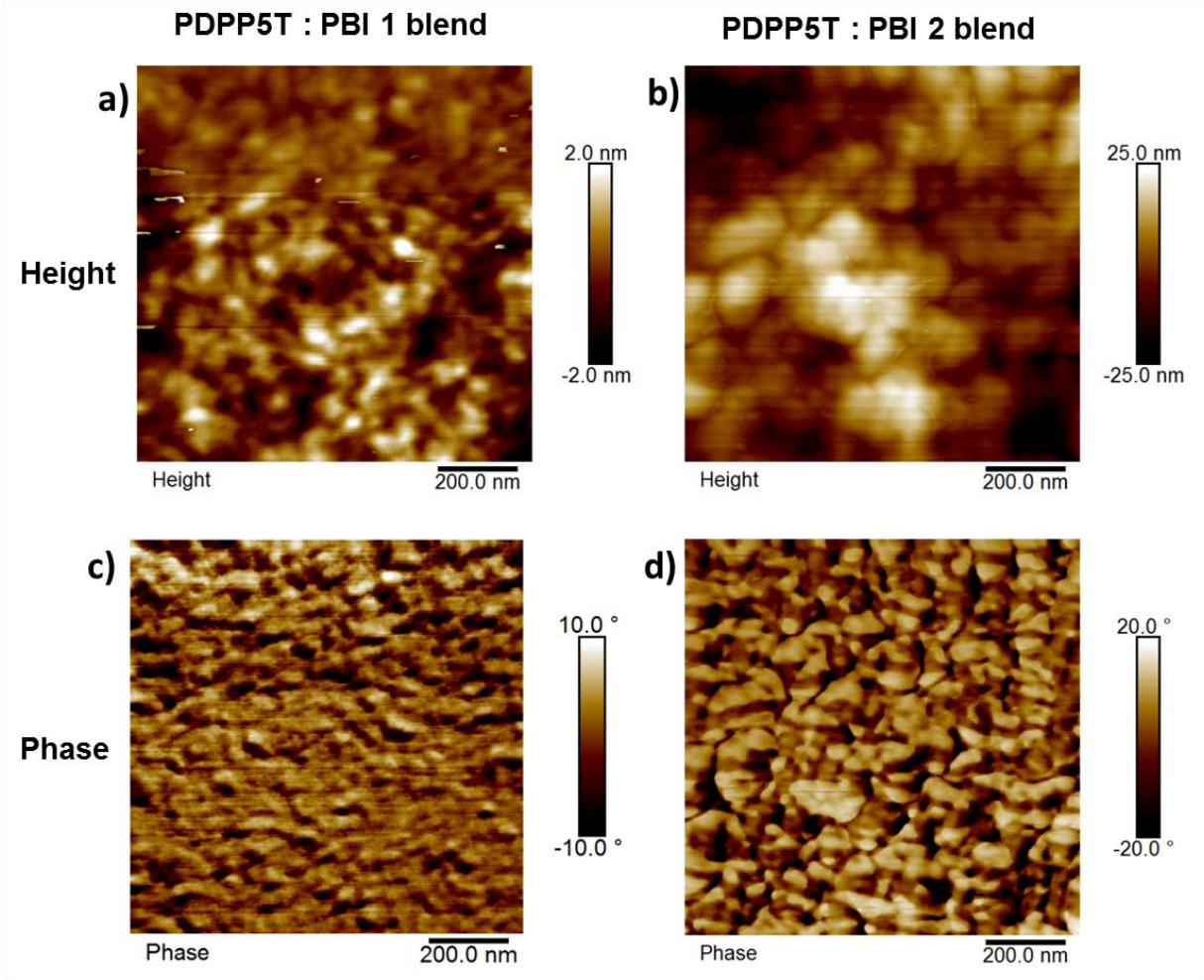

Figure 5. *AFM height (**a** and **b**) and phase (**c** and **d**) images of optimized blends (1:2 wt/wt) for PBI 1 (**a** and **c**) and PBI 2 (**b** and **d**).*

A first impression of the two different domain sizes of both blends systems is given by the AFM height images (Figure 5a and 5b). Here the roughness for the PDPP5T:PBI 1 blend is much smoother than the PDPP5T:PBI 2. Additionally, the former indicates smaller domain sizes. This is further supported by the phase images of the respective blends, where smaller domain sizes are clearly seen in the PDPP5T:PBI 1 blend, whereas PDPP5T:PBI 2 show

larger domain sizes and additionally, a higher phase contrast. The question arises, if the different domain sizes are a result of the hydrophobic vs. hydrophilic swallow tail in PBI 1 vs. PBI 2. Such a correlation was found for these PBI acceptors already in blends with the OPV32 donor polymer.[31] Here a 1:1 blend of OPV32:PBI 1 results in a very smooth film suggesting a high degree of intermixing due to the similar solubilizing alkyl chains in OPV32 and PBI 1. In contrast to that, the OPV32:PBI 2 blend clearly showed phase separated domains with sizes of about some hundreds of nanometers. The hydrophilic swallow tail of PBI 2 prevented an intimate intermixing (as observed with PBI 1) and helps the formation of phase separated morphology with OPV 32 donor polymer. This leads to a higher J_{SC} and therefore better device performance in PBI 2 blend compared to the well intermixed OPV32:PBI 1 blend, where J_{SC} and the overall photovoltaic performance is worse. This is no more the case, when PBI 1 is blended with PDPP5T. Even though PDPP5T exhibits solubilizing alkyl chains as well, a complete intermixing with PBI 1 was not observed. According to AFM phase image in Figure 5d a rather phase separated morphology with estimated domain sizes below 100 nm is found. This explains also the higher J_{SC} observed in this blend compared to the PDPP5T:PBI 2 blend, where the domains probably due to the hydrophilic swallow tail of PBI 2 are much larger than exciton diffusion lengths. In large PBI 2 domains, excitons form rather immobile intermediate states, as mentioned already,[11] than convert into free charges at the donor acceptor interface. Additionally, the larger are the phase domains, the smaller is the donor acceptor interface. Both facts lead to a decrease of J_{SC} and therefore a decrease of the overall PCE as observed for the PDPP5T:PBI 2 blend.

Recombination dynamics using TAS

To better understand the correlation between morphology and J_{SC}, we measured the recombination dynamics of charge separated states or so-called polarons in the blend systems after photoexcitation by TAS in ns to µs timescale. Polarons mean in this context either the positive charges in the polymer domain or the negative charges in the PBI domain. The position of the absorption bands of these polarons in polymer and PBI can be estimated by measuring the radical cation and anion spectra of the donor and acceptor respectively. The radical anion for PBI is known to appear in the visible wavelength range at around 700 nm.[37] However, here we focus on the near infrared (NIR) wavelength range, since the PBI radical anion band at 700 nm lies fully or partially in ground state absorption range of the blend systems (Figure 2) which would lead to an overlapping with the resulting ground state bleach.

The NIR wavelength range is dominated by the polaron spectra of the polymers. In Figure S1 the radical cation spectra of the two donor polymers in solution are shown. Both polymers exhibit a new absorption band of the cation species in the NIR range upon chemical oxidation. Note that the polaron band in thin film might be shifted with respect to the radical cation spectrum obtained from solution due to aggregation effects. Durrant *et al.* reported transient absorption studies of a DPP-thiophene polymer, which is related to the chemical structure of PDPP5T, by monitoring the decay dynamics at 980 nm.[38] In Figure 6a the transient absorption of the PDPP5T:PBI 1 blend between 900 and 1400 nm is shown with selected time intervals after photoexcitation between 8 to 1000 ns. We assign the observed broad absorption band to the polaron of PDPP5T polymer, since a similar broad absorption of the PDPP5T radical cation was found in this region (Figure S1). In contrast to that, the PDPP5T:PBI 2 blend shows no or very weak transient absorption the same wavelength and time range (Figure 6b). A direct comparison of the decay kinetics at 970 nm between the two blend systems is given in Figure 6c. Here it is clearly seen that after photoexcitation at 470 nm the transient absorption in the case of PDPP5T:PBI 1 vanishes after 500 ns, whereas for PDPP5T:PBI 2 no transient absorption and therefore no polarons are observed. This is in good agreement with the J_{SC} values from the respective photovoltaic devices and supports further the assumption, that in PDPP5T:PBI 1 the excitons inside the domains are able to reach the donor / acceptor interface for charge generation much better due to the small domain sizes than in the case of PDPP5T:PBI 2, where bigger domain sizes hinder the exciton to reach the donor / acceptor interface. The decay kinetics at 970 nm for OPV32:PBI blends after photoexcitation at 500 nm are shown in Figure 6d. The decay dynamics in OPV32:PBI 1 blend are a bit faster than the OPV32:PBI 2 blend suggesting a faster recombination dynamics. This can be explained with the higher degree of intermixing between OPV32 and PBI 1 as it was shown by AFM measurements.[31] Thus the recombination dynamics fully support the observed difference in behavior of PBI 1 and PBI 2 in the two different polymer blends. Since the energy levels and charge carrier properties of both PBIs are very similar in as-cast films, the difference in photovoltaic performance in the two different blends can be well explained due to a difference in morphology arising out of the different hydrophobic vs. hydrophilic nature of the two PBIs.

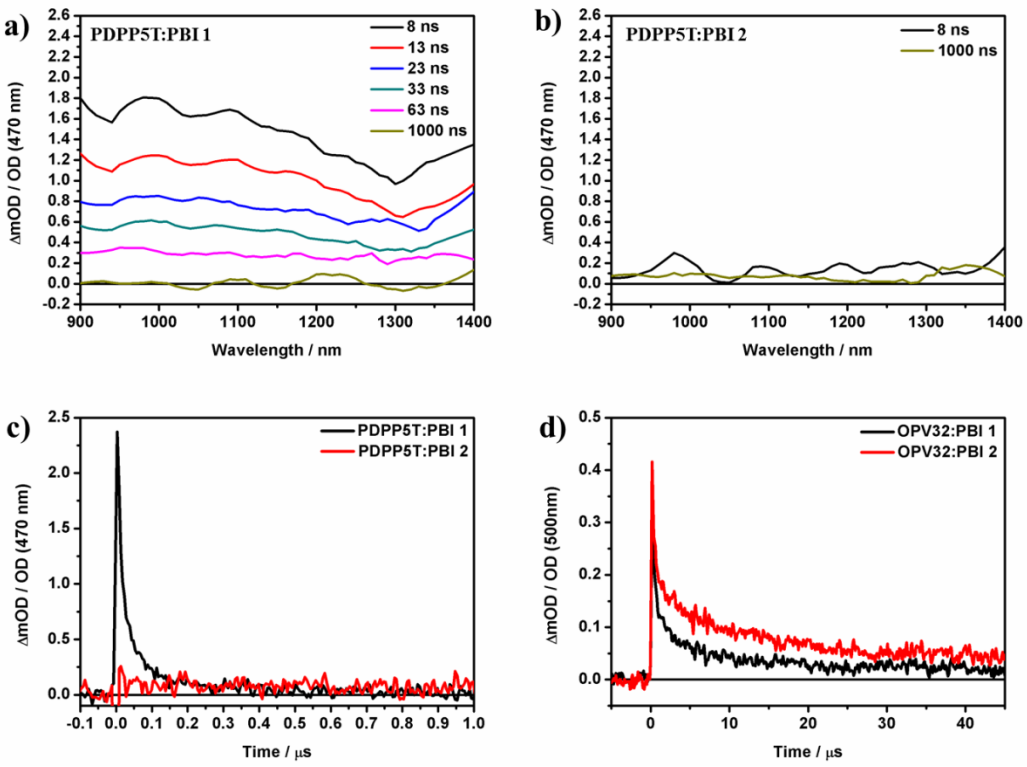

Figure 6. *Transient absorption spectra of a) PDPP5T:PBI 1 and b) PDPP5T:PBI 2 and after excitation at 470 nm. Note that both spectra were smoothed and a comparison of original data and smoothed data for one spectrum is given in Figure S2. Transient absorption decay dynamics at 970 nm are given for PBI 1 (black) and PBI 2 (red) in their respective polymer blends using c) PDPP5T (after excitation at 470 nm) and d) OPV32 (after excitation at 500 nm). All signals shown here were normalized with the ground state optical density at either 470 or 500 nm to have a better comparison in signal intensity. The excitation density 30 μJ cm^{-2} in each case.*

Conclusion

We investigated the different behavior of polymer blend solar cells consisting of two selected donor polymers blended with either the hydrophobic or hydrophilic swallow tail substituted PBIs. Both PBIs have similar energy levels, optical gap and charge carrier transport in as-cast film. However, from previous studies it was known, that the hydrophilic PBI 2 performs much better than the hydrophobic PBI 1 in solar cells with OPV32 as donor polymer. Using PDPP5T as a donor polymer, we observed the opposite case: here PBI 1 show a much higher J_{SC} leading to better PCE compared to PBI 2. We attribute the observed differences in J_{SC} to differences in phase separation and domain sizes as studied by AFM. Together with TAS, where we qualitatively compared the dynamics of the respective charge separated states in polymer, we now come to the following conclusion: The choice of hydrophobic vs.

hydrophilic swallow tail of the PBI acceptor has a big impact on the photoactive layer morphology and it depends furthermore on the miscibility with the respective donor polymer used. Depending on, which PBI and which donor polymer was used, we found that a high intermixing between the polymer and the PBI leads to non-geminate recombination. On the other hand, more phase separation leading to large domains causes reduced photocurrent. This paper addresses the unexpected behavior of similar PBI molecules in different blends causing opposite effects of phase separation or intermixing.

Acknowledgements

The financial support from DFG (SFB 840) is gratefully acknowledged. Christoph Hunger acknowledges for financial support from DFG (GRK 1640) and give thanks to Christian Müller and Christian David Heinrich (University of Bayreuth) for support in EQE and AFM measurements.

References

[1] Liu, Y.; Zhao, J.; Li, Z.; Mu, C.; Ma, W.; Hu, H.; Jiang, K.; Lin, H.; Ade, H.; Yan, H., Aggregation and morphology control enables multiple cases of high-efficiency polymer solar cells. *Nat. Commun.*, **2014**, *5*, (9), 1-8.

[2] Nicolaidis, N. C.; Routley, B. S.; Holdsworth, J. L.; Belcher, W. J.; Zhou, X.; Dastoor, P. C., Fullerene Contribution to Photocurrent Generation in Organic Photovoltaic Cells. *J. Phys. Chem. C*, **2011**, *115*, (15), 7801-7805.

[3] Anctil, A.; Babbitt, C. W.; Raffaelle, R. P.; Landi, B. J., Material and energy intensity of fullerene production. *Environ. Sci. Technol.*, **2011**, *45*, (6), 2353-2359.

[4] Sonar, P.; Fong Lim, J. P.; Chan, K. L., Organic non-fullerene acceptors for organic photovoltaics. *Energy Environ. Sci.*, **2011**, *4*, (5), 1558- 1574.

[5] Lin, Y.; Zhan, X., Non-fullerene acceptors for organic photovoltaics: an emerging horizon. *Mater. Horiz.*, **2014**, *1* (5), 470-488.

[6] Ke, D.; Zhan, C.; Xu, S.; Ding, X.; Peng, A.; Sun, J., Self-Assembled Hollow Nanospheres Strongly Enhance Photoluminescence. *J.Am.Chem.So*c. **2011**, *133*, 11022-11025.

[7] Ford, W. E.; Hiratsuka, H.; Kamat, P. V., Photochemistry of 3,4,9,10-perylenetetracarboxylic dianhydride dyes. 4. Spectroscopic and redox properties of

oxidized and reduced forms of the bis(2,5-di-tert-butylphenyl)imide derivative. *J. Phys. Chem.*, **1989**, *93* (18), 6692-6696.

[8] Zhan, X.; Facchetti, A.; Barlow, S.; Marks, T. J.; Ratner, M. a.; Wasielewski, M. R.; Marder, S. R., Rylene and related diimides for organic electronics. *Adv. Mater.* **2011**, *23*, 268–284.

[9] Oh, J. H.; Wong, L. H.; Yu, H.; Park, Y. J.; Min Kim, J.; Bao, Z., Observation of orientation-dependent photovoltaic behavior in aligned organic nanowires. *Appl. Phys. Lett.*, **2013**, *103*, 053304-053301.

[10] Guo, X.; Bu, L.; Zhao, Y.; Xie, Z.; Geng, Y.; Wang, L., Controlled phase separation for efficient energy conversion in dye/polymer blend bulk heterojunction photovoltaic cells. *Thin Solid Films* **2009**, *517*, (16), 4654-4657.

[11] Howard, I. A.; Laquai, F.; Keivanidis, P. E.; Friend, R. H.; Greenham, N. C., Perylene Tetracarboxydiimide as an Electron Acceptor in Organic Solar Cells: A Study of Charge Generation and Recombination. *J. Phys. Chem. C*, **2009**, *113*, 21225-21323.

[12] Keivanidis, P. E.; Howard, I. A.; Friend, R. H., Intermolecular Interactions of Perylene diimides in Photovoltaic Blends of Fluorene Copolymers: Disorder Effects on Photophysical Properties, Film Morphology and Device Efficiency. *Adv. Funct. Mater.*, **2008**, *18*, 3189-3202.

[13] Rajaram, S.; Armstrong, P. B.; Bumjoon, J. K.; Fréchet, J. M. J., Effect of Addition of Diblock Copolymer on Blend Morphology and Performance of Poly(3-hexylthiophene):Perylene Diimide Solar Cells. *Chem. Mater.*, **2009**, *21*, (9), 1775-1777.

[14] Li, M.; Liu, J.; Cao, X.; Zhou, K.; Zhao, Q.; Yu, X.; Xing, R.; Han, Y., Achieving balanced intermixed and pure crystalline phases in PDI-based non-fullerene organic solar cells via selective solvent additives. *Phys. Chem. Chem. Phys.*, **2014**, *16*, 26917-26928.

[15] Singh, R.; Aluicio-Sarduy, E.; Kan, Z.; Ye, T.; MacKenzie, R. C. I.; Keivanidis, P. E., Fullerene-free organic solar cells with an efficiency of 3.7% based on a low-cost geometrically planar perylene diimide monomer. *J. Mater. Chem. A*, **2014**, *2*, 14348-14353.

[16] Sharenko, A.; Gehring, D.; Laquai, F.; Nguyen, T.-Q., The Effect of Solvent Additive on the Charge Generation and Photovoltaic Performance of a Solution-Processed Small Molecule:Perylene Diimide Bulk Heterojunction Solar Cell. *Chem. Mater.*, **2014**, *26* (14), 4109-4118.

[17] Ye, T.; Singh, R.; Butt, H.-J.; Floudas, G.; Keivanidis, P. E., Effect of Local and Global Structural Order on the Performance of perylene diimide excimeric solar cells. *ACS Appl. Mater. Interfaces*, **2013**, *5*, 11844-11857.

[18] Singh, R.; Giussani, E.; Mróz, M. M.; Di Fonzo, F.; Fazzi, D.; Cabanillas-González, J.; Oldridge, L.; Vaenas, N.; Kontos, A. G.; Falaras, P.; Grimsdale, A. C.; Jacob, J.; Müllen, K.; Keivanidis, P. E., On the role of aggregation effects in the performance of perylene-diimide based solar cells. *Org. Electron.*, **2014**, *15*, 1347-1361.

[19] Chen, Y.; Zhang, X.; Zhan, C.; Yao, J., In-depth understanding of photocurrent enhancement in solution-processed small-molecule:perylene diimide non-fullerene organic solar cells. *Physica Status Solidi A*, **2015**, *9*, 1961-1968.

[20] Kamm, V.; Battagliarin, G.; Howard, I. A.; Pisula, W.; Mavrinskiy, A.; Li, C.; Müllen, K.; Laquai, F.,Polythiophene:Perylene Diimide Solar Cells – the Impact of Alkyl-Substitution on the Photovoltaic Performance. *Adv. Energ. Mater.*, **2011**, *1*, 297-302.

[21] Zhang, X.; Jiang, B.; Zhang, X.; Tang, A.; Huang, J.; Zhan, C.; Yao, J., Cooperatively Tuning Phase Size and Absorption of Near IR Photons in P3HT:Perylene Diimide Solar Cells by Bay-Modifications on the Acceptor. *J. Phys. Chem. C*, **2014**, *118*, 24212-24220.

[22] Rajaram, S.; Shivanna, R.; Kandappa, S. K.; Narayan, K. S., Nonplanar Perylene Diimides as Potential Alternatives to Fullerenes in Organic Solar Cells. *J. Phys. Lett.*, **2012**, *3*, 2405-2408.

[23] Zhang, X.; Lu, Z.; Ye, L.; Zhan, C.; Hou, J.; Zhang, S.; Jiang, B.; Zhao, Y.; Huang, J.; Zhang, S.; Liu, Y.; Shi, Q.; Liu, Y.; Yao, J., A Potential Perylene Diimide Dimer-Based Acceptor Material for Highly Efficient Solution-Processed Non-Fullerene Organic Solar Cells with 4.03% Efficiency. *Adv. Mater.*, **2013**, *25*, 5791-5797.

[24] Zang, Y.; Li, C.-Z.; Chueh, C.-C.; Williams, S. T.; Jiang, W.; Wang, Z.-H.; Yu, J.-S.; Jen, A. K. Y., Integrated Molecular, Interfacial, and Device Engineering towards High-Performance Non-Fullerene Based organic Solar Cells. *Adv. Mater.*, **2014**, *26*, (32), 5708-5714.

[25] Zhong, Y.; Trinh, M. T.; Chen, R.; Wang, W.; Khlyabich, P. P.; Kumar, B.; Xu, Q.; Nam, C.-Y.; Sfeir, M. Y.; Black, C.; Steigerwald, M. L.; Loo, Y.-L.; Xiao, S.; Ng, F.; Zhu, X.-Y.; Nuckolls, C., Efficient Organic Solar Cells with Helical Perylene Diimide Electron Acceptors. *J. Am. Chem. Soc.*, **2014**, *136*, (43), 15215–15221.

[26] Jiang, W.; Ye, L.; Li, X.; Xiao, C.; Tan, F.; Zhao, W.; Hou, J.; Wang, Z., Bay-linked perylene bisimides as promising non-fullerene acceptors for organic solar cells. *Chem. Commun.*. **2014**, *50*, 1024-1026.

[27] Wicklein, A.; Lang, A.; Muth, M.; Thelakkat, M.,Swallow-Tail Substituted Liquid Crystalline Perylene Bisimides: Synthesis and Thermotropic Properties. *J. Am. Chem. Soc.*, **2009**, *131* (40), 14442-14453.

[28] Muth, M.-A.; Gupta, G.; Wicklein, A.; Carrasco-Orozco, M.; Thurn-Albrecht, T.; Thelakkat, M., Crystalline vs Liquid Crystalline Perylene Bisimides: Improved Electron Mobility via Substituent Alteration. *J. Phys. Chem. C*, **2013**, *118*, 92-102.

[29] Lu, Z.; Zhang, X.; Zhan, C.; Jiang, B.; Zhang, X.; Chen, L.; Yao, J., Impact of molecular solvophobicity *vs.* solvophilicity on device performances of dimeric perylene diimide based solution-processed non-fullerene organic solar cells. *Phys. Chem. Chem. Phys.*, **2013**, *15*, 11375-11385.

[30] Huang, C.; Barlow, S.; Marder, S. R., Perylene-3, 4, 9, 10-tetracarboxylic acid diimides: Synthesis, physical properties, and use in organic electronis. *J. Org. Chem.*, **2011**, *76*, (8), 2386-2407.

[31] Muth, M.-A., Structure-Property Correlation of Electron Transport Materials in Organic Devices. *Dissertation*, University of Bayreuth, **2013**.

[32] Li, W.; Roelofs, W. S. C.; Wienk, M. M.; Janssen, R. A. J., Enhancing the photocurrent in diketopyrrolopyrrole-based polymer solar cells via energy level control. *J. Am. Chem. Soc.*, **2012**, *134*, (33), 13787-13795.

[33] Gupta, D.; Wienk, M. M.; Janssen, R. A. J., Efficient Polymer Solar Cells on Opaque Substrates with a Laminated PEDOT:PSS Top Electrode. *Adv. Energy Mater*., **2013**, *3* (6), 782-787.

[34] Lu, Z.; Jiang, B.; Zhang, X.; Tang, A.; Chen, L.; Zhan, C.; Yao, J., Perylene-Diimide Based Non-Fullerene Solar Cells with 4.34% Efficiency through Engineering Surface Donor/Acceptor Composition. *Chem. Mater.*, **2014**, *26*, 2907-2914.

[35] Aluicio-Sarduy, E.; Singh, R.; Kan, Z.; Ye, T.; Baidak, A.; Calloni, A.; Berti, G.; Duò, L.; Iosifidis, A.; Beaupré, S.; Leclerc, M.; Butt, H.-J.; Floudas, G.; Keivanidis, P. E., Elucidating the Impact of Molecular Packing and Device Architecture on the Performance of Nanostructured Perylene Diimide Solar Cells. *ACS Appl. Mater. Interfaces*, **2015**, *7* (16), 8687-8698.

[36] Bartesaghi, D.; Pérez, I. d. C.; Kniepert, J.; Roland, S.; Turbiez, M.; Neher, D.; Koster, L. J. A., Competition between recombination and extraction of free charges determines the fill factor of organic solar cells. *Nat. Commun.*, **2015**, *6* (7083), 1-8.

[37] Salbeck, J., An electrochemical cell for simultaneous electrochemical and spectroelectrochemical measurements under semi-infinite diffusion conditions and thin-layer conditions. *J. Electroanal. Chem.*, **1992**, *340* (1), 169-195.

[38] Soon, Y. W.; Cho, H.; Low, J.; Bronstein, H.; McCulloch, I.; Durrant, J. R., Correlating triplet yield, singlet oxygen generation and photochemical stability in polymer/fullerene blend films, *Chem. Commun.*, **2013**, *49*, 1291-1293.

Supporting information

Table S1. *The photovoltaic parameters for PDPP5T:PBI (1:2 wt/wt) blend devices with different amounts of additives (vol %) and in normal or inverted device geometry.*

Device Geometry	PBI	Solvent:additive (vol %)	d [nm]	V_{OC} [V]	J_{SC} [mA·cm^{-2}]	FF [%]	PCE [%]
normal	PBI 1	$CHCl_3$	141	0.65	0.61	30	0.12
		$CHCl_3$:DIO 2.5%	141	0.65	1.82	28	0.34
		$CHCl_3$:oDCB 10%	108	0.58	2.60	32	0.48
	PBI 2	$CHCl_3$	160	leak			
		$CHCl_3$:DIO 2.5%	160	0.15	0.27	25	0.01
		$CHCl_3$:oDCB 10%	160	leak			
inverted	PBI 1	$CHCl_3$:oDCB 10%	83	0.69	5.03	45	1.56
	PBI 2	$CHCl_3$:DIO 2.5%	~120	0.75	0.76	47	0.27

Table S2. *Photovoltaic parameters for PDPP5T:PBI 1 (1:2 wt/wt) blend devices with different amounts of oDCB as additives in inverted device geometry.*

Solvent	d [nm]	V_{OC} [V]	J_{SC} [mA·cm^{-2}]	FF [%]	PCE [%]
$CHCl_3$:oDCB 10%	83	0.69	5.03	45	1.56
$CHCl_3$:oDCB 20%	106	0.68	~4.32	41	1.21
$CHCl_3$:oDCB 50%	83	0.67	4.15	44	1.23
oDCB	141	0.67	~3.98	42	1.11

Table S3. *Photovoltaic parameters for PDPP5T:PBI 1 blend devices fabricated from $CHCl_3$ and 10 vol % oDCB as additives in inverted device geometry using different donor:acceptor ratios (wt/wt).*

PDPP5T:PBT ratio (wt/wt)	d [nm]	V_{OC} [V]	J_{SC} [mA·cm^{-2}]	FF [%]	PCE [%]
1:0.5	50	0.65	1.71	38	0.43
1:1	73	0.68	3.29	37	0.83
1:2	83	0.69	5.03	45	1.56
1:3	119	0.68	5.04	46	1.59

Table S4. *Photovoltaic parameters for PDPP5T:PBI 1 (1:2 wt/wt) blend devices fabricated from $CHCl_3$ and 10 vol % oDCB as additives in inverted device geometry with different photoactive layer thickness d.*

d [nm]	V_{OC} [V]	J_{SC} [mA·cm^{-2}]	FF [%]	PCE [%]
60	0.68	3.59	45	1.09
85	0.69	5.08	45	1.55
167	0.66	4.25	35	0.97

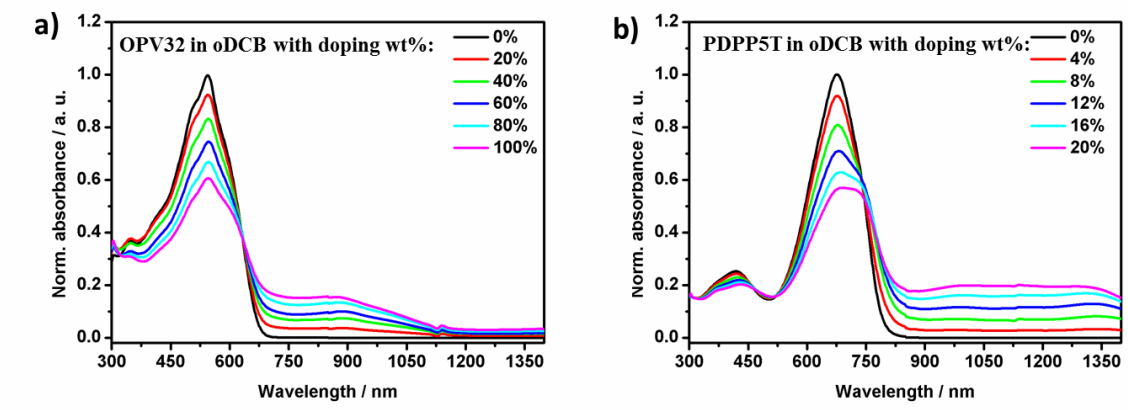

Figure S1. *Normalized absorbance spectra of chemical oxidation of donor polymer a) OPV 32 and b) PDPP5T in oDCB with different amounts of $SbCl_5$ given in wt% with respect to the polymer.*

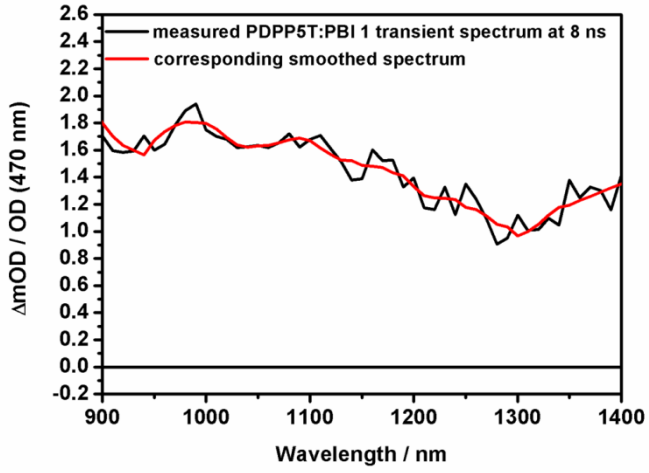

Figure S2. *Comparison between normalized measured transient absorption spectrum (black) and smoothed spectrum (red) for PDPP5T:PBI 1 blend at 8 ns. The excitation wavelength was 470 nm, whereas the excitation density was 30 µJ·cm^{-2}. Smoothing of the measured data was done using the Savitzky-Golay-filter with a second polynomial order.*

6 A cracked polymer templated metal network as a transparent conducting electrode for ITO-free organic solar cells

K. D. M. Rao[a], Christoph Hunger[b], Ritu Gupta[a], Giridhar U. Kulkarni[a] and Mukundan Thelakkat[b]**

* Corresponding authors

[a] Prof. Dr. Giridhar U. Kulkarni, Chemistry & Physics of Materials Unit and Thematic Unit of Excellence in Nanochemistry, Jawaharlal Nehru Centre for Advanced Scientific Research, Jakkur P.O., Bangalore 560 064, India.

E-mail: kulkarni@jncasr.ac.in

[b] Prof. Dr. Mukundan Thelakkat, Applied Functional Polymers, Macromolecular Chemistry I, University of Bayreuth, D-95440 Bayreuth, Germany.

E-mail: mukundan.thelakkat@uni-bayreuth.de

This manuscript is published in *Phys. Chem. Chem. Phys.*, **2014**, *16*, 15107-15110.

We report a highly transparent, low resistance Ag metal network templated by a cracked polymer thin film and its incorporation in an organic solar cell. The performance of this scalable metallic network is comparable to that of conventional ITO electrodes. This is a general approach to replace ITO in diverse thin film devices.

Organic solar cells (OSCs) are an attractive option for large area and inexpensive production of modules. This is because OSCs are well suited to low cost manufacturing due to simple processing[1] steps that are easily translated to roll-to-roll mass production[2] and lead to near commercialization. In the recent past, extensive research has been carried out on the active semiconductor ingredients[3] and electrode optimization[4] in order to improve the OSC performance,[5] which is typically poorer compared to other types of solar cells such as dye sensitized solar cells[6] and silicon based solar cells.[7,8] Nonetheless, OSCs occupy a unique position in the photovoltaic roadmap as solid state, flexible, environmentally benign and ultralight large area devices.[9]

In OSCs, indium tin oxide (ITO) is the most commonly used transparent conducting electrode. Best ITO films exhibit a transmittance of 92% in the visible region and a sheet resistance of 10 ohm $\square^{-1}$.10 Indium is scarce and expensive;[11] ITO requires high temperature processing, is brittle and develops cracks on flexible substrates.[12] In order to address these issues, there has been much effort towards alternative electrodes, as reported in the literature. Graphene,[13] carbon nanotubes (CNTs),[14,15] and Ag nanowires[16,17] have been proposed as alternatives to ITO. Graphene has outstanding optical properties, but a limited sheet resistance of 30 ohm $\square^{-1}$.[13] The CNT networks also exhibit high sheet resistance and in addition, are less stable under ambient conditions.[14,18] Ag nanowire networks show relatively superior performance in terms of transmittance and sheet resistance.[17] But like any other network produced from pre-synthesized nanowires (tubes), they suffer from contact resistance at innumerable crossbar junctions and high roughness.[19,20] Further, the redundant wires/tubes in the network can short the OSCs, which restricts its use in roll-to-roll fabrication. Often, they require an extra treatment, such as mechanical pressing,[21] thermal treatment[20] or poly(3,4-ethylenedioxythiophene) poly(styrenesulfonate) (PEDOT:PSS) coating to improve the performance.[19]

Metal grids offer attractive alternatives to the above TCEs.[22–30] Indeed being free of junctions, they exhibit high performance in terms of transmittance and sheet resistance, and have been successfully used in optoelectronic devices including OSCs. Typically, they are produced by patterning using lithographic techniques such as photolithography,[22] soft

lithography,[23] phase shift lithography[24] and nanoimprint lithography.[25] A technologically relevant and simple alternative is the direct printing of grids using silver nanoparticle inks either by ink-jet printing[26,27] or laser printing[27–29] or flexographic and thermal imprinting.[30] These recipes for Ag grids result in relatively large feature sizes. Such printed patterns are often used as current collecting grids in diverse applications.

Recently, metal meshes have been fabricated based on cracked TiO2 templates and their application in touch screens has been shown.[31,32] Some of us[33] have shown, very recently, selective deposition of Cu by electroplating in the cracked regions of a polymer template to produce Cu mesh based TCEs. These cracked template methods are highly scalable but need to be tested for their applicability and device integration in thin film organic devices such as OSCs, OFETs, etc. One of the basic challenges is to obtain high light transmission maintaining low sheet resistance for such TCEs. Additionally, in thin film devices, the uniformity and connectivity of such meshes are very critical for the reproducibility of such devices.

In this study, we have explored the feasibility of cracking as a tool for the preparation of such metal meshes from inexpensive polymer templates at room temperature and integrating them as TCEs in bulk heterojunction OSCs. Specifically, using a seamless Ag network in the form of a mesh as a replacement for ITO electrodes, several OSCs having an inverted geometry have been made, which exhibited performance comparable to those produced using ITO. We like to note that this work emphasizes the suitability and reproducibility of such an ITO-free TCE in OSCs and not specifically the optimization of efficiency of any kind of device.

The process flow for templating is shown schematically in Figure 1. First, a crack layer is produced by drying an acrylic based colloidal dispersion on a glass substrate wherein highly interconnected cracks are spontaneously obtained.

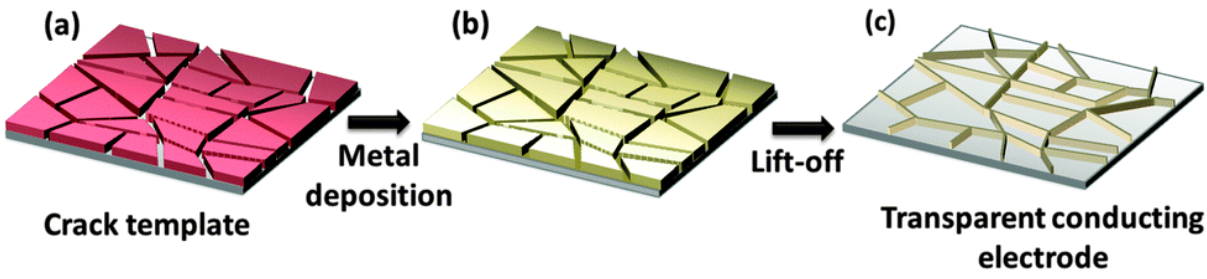

Figure 1. *Schematic illustration of transparent conducting electrode fabrication (a) cracked template (b) deposition of metal on a cracked template and (c) lift-off of the template giving rise to the Ag network based TCE.*

These U-shaped grooves are complete cracks down to the substrate to be distinguished from incomplete cracks.[34] Using the cracked template, the metal (Ag, 55 nm) is deposited by vacuum evaporation and subsequently, the template is washed away with chloroform. As shown in Figure 2a, the Ag mesostructures on glass appear to be well interconnected throughout the network. The metal fill factor is estimated to be ~20% with a structural width of ~2 μm and an average cell size (spacing between the Ag structures) of 20 to 60 μm. The optical profilometric image (1.2 × 0.8 mm^2) in Figure 2b not only reveals the connectivity of the Ag network over a large area but also shows its seamless nature. The surface roughness of the network is estimated to be ~5 nm while the peak-to-valley roughness, which corresponds to the network thickness, is 55 nm. The SEM image in Figure 2c shows a junction where the network surface continues to be smooth and the junction itself is seamless unlike crossbar junctions commonly seen in network TCEs made from pre-synthesized Ag nanowires.[21]

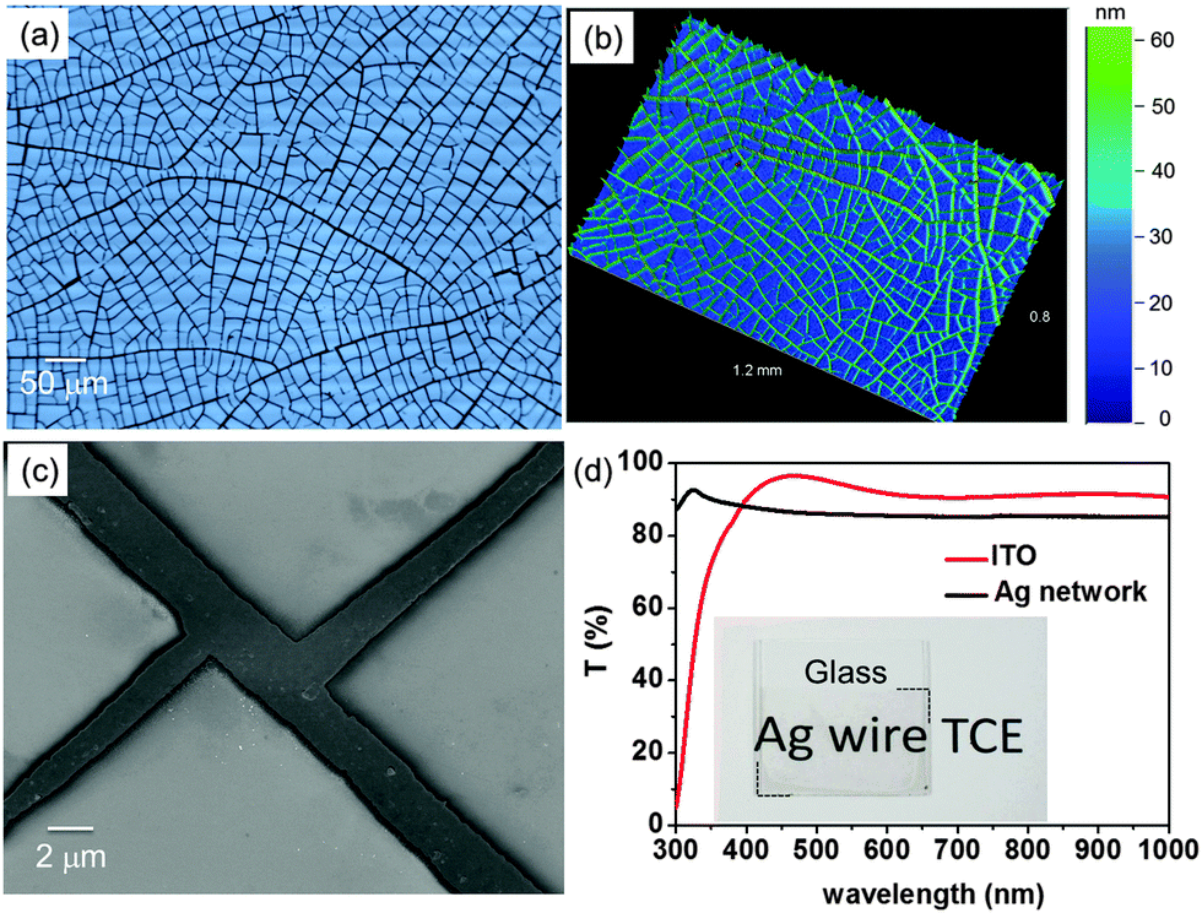

Figure 2. *Characterization of the Ag network derived TCE: (a) the optical microscope image (transmission mode), (b) the optical profiler image in a 3D view, (c) the SEM image of a network junction and (d) comparison of transmittance spectra of Ag metallic network and ITO. The inset shows the photograph of a Ag network TCE on a glass substrate.*

Accordingly, the sheet resistance was found to be ~10 ohm $\square^{-1}$, which is rather low considering the thickness of only 55 nm. The transmittance of the Ag network was ~86% at 550 nm (see Figure 2d) and the overall transmittance is comparable to that exhibited by ITO but, importantly, extends down to the UV region (see the photograph in the inset). ITO, on the other hand, is a good UV absorber. In the next step of solar cell fabrication, the ZnO barrier layer was brought in by decomposing a zinc acetate film at 150 °C in air (see ESI† for experimental details).[35] For a proposed thickness of 45 nm of ZnO, the obtained layer was non-uniform and discontinuous (Figure 3a) as evident from the dark and grey regions, the latter corresponding to the ZnO covered network. Beiley *et al*. described previously the fabrication of a Ag nanowire–ZnO nanoparticle composite to obtain a semi-transparent top electrode and achieved a good power conversion efficiency (PCE) of 4.3% in PBDTTPD/PC70BM devices.[36] Based on this fact, we increased the thickness of the ZnO layer to 95 nm, 135 nm and 230 nm. We observed an increasing degree of covering of the metal network with the increasing thickness of ZnO. For example, in the SEM image of the 135 nm ZnO layer shown in Figure 3b, the ZnO film is seen to be uniformly submerging the entire Ag network. This is found to be the optimal ZnO thickness required to submerge the 55 nm thick Ag network so as to have reproducible devices without shorting.

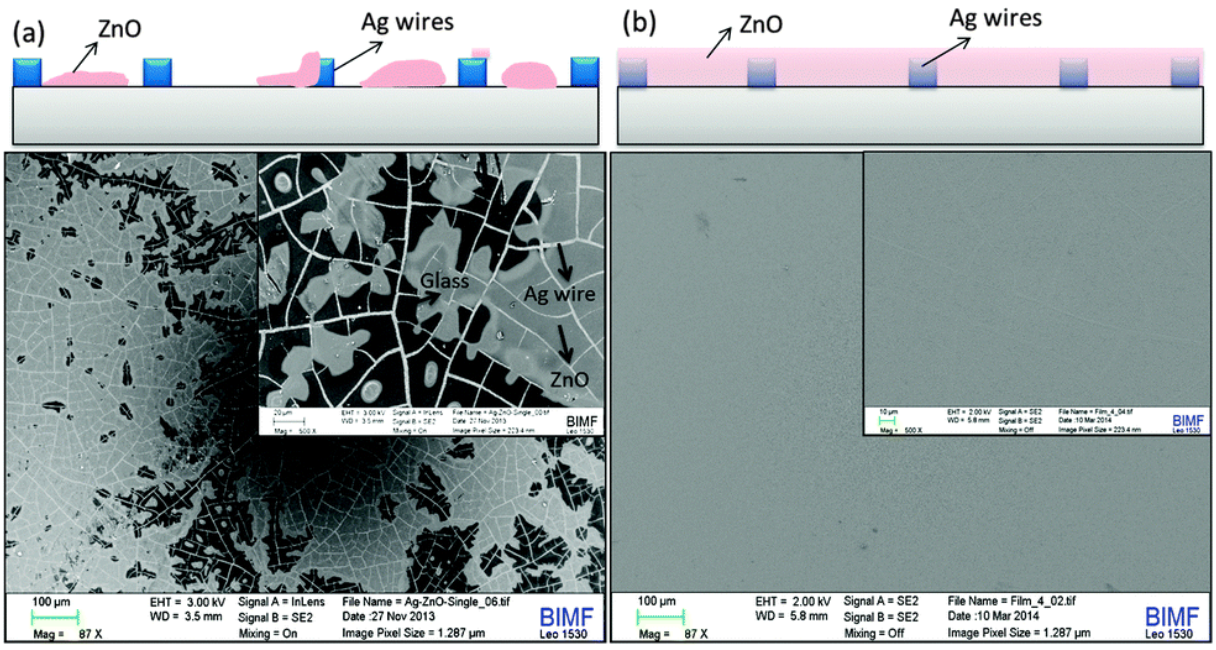

Figure 3. *SEM images and schematic illustrations of the Ag network TCE covered with ZnO layer having a thickness of (a) 45 nm and (b) 135 nm. For more SEM images, see the ESI,† Figure S1.*

Four bottom-illuminated inverted photovoltaic cells (5 devices in each) consisting of poly-3-hexylthiophene (P3HT) and phenyl-C61-butyric acid methyl ester (PCBM) were fabricated on a glass substrate, as shown schematically in Figure 4a using a Ag network derived TCE. The bar graphs of solar cell parameters (V_{OC}, J_{SC}, *FF* and PCE) for all four cells with varying thicknesses of the ZnO barrier layer are shown in Figure 4b. In cell 1, all five devices with a 45 nm ZnO layer were defective due to shorting. For cell 2 with a 95 nm ZnO layer, only two devices were working with moderate efficiencies. On the other hand, for cells 3 and 4 with 135 and 230 nm ZnO barrier layer thicknesses, respectively, all five devices were found to be functioning. Significantly, the five devices with a 135 nm ZnO layer (cell 3), showed uniform performance with an average efficiency of 2.26 ± 0.05%, while those with a 230 nm ZnO layer exhibited some variations in performance with lower efficiency (1.34 ± 0.43%, see Figure 4b).

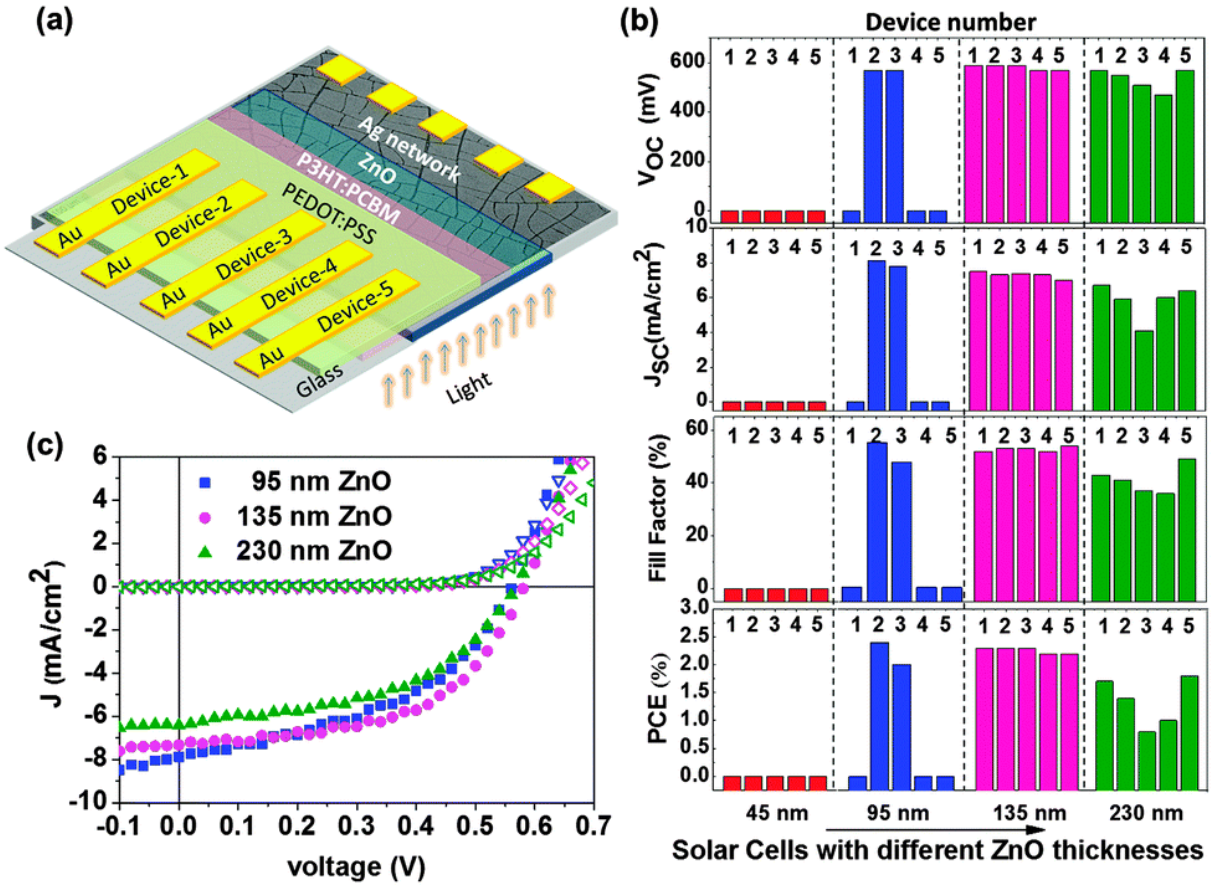

Figure 4. *(a) Schematic illustration of the inverted P3HT–PCBM solar cell with Ag network TCE, (b) bar graph of cell parameters for solar cells of different ZnO layer thicknesses (45, 95, 135 and 230 nm), (c) examples of J-V characteristics of solar cells with different ZnO layer thicknesses in the dark (open symbols) and in light (filled symbols). Note that the best performing solar cell is chosen from each cell.*

The decrease in the cell efficiency for higher ZnO thicknesses can be attributed to higher series resistance of the cell leading to lower current density and fill factor values (see Figure 4b).[35] Indeed, the variations in solar cell parameters among the five devices exhibit a similar trend. The *J-V* characteristics of typical solar cells with different ZnO layer thicknesses (95 nm, 135 nm, and 230 nm) are shown in Figure 4b (see the ESI, Figure S2 for *J-V* characteristics of all working devices).

From Figure 5a, we can compare the *J-V* characteristics of a typical device fabricated using a Ag network (from cell 3) with that produced using ITO as a TCE (ITO: T = 93% and Rs = 16 ohm $\square^{-1}$). The Ag network cell has an optimum ZnO layer thickness of 135 nm. For ITO devices, the thickness of the ZnO blocking layer was kept at 45 nm which is optimum for an inverted solar cell.[35] All other process parameters such as the active layer thickness, top electrode, annealing temperature, etc. were kept the same for all the devices. It is clear from the plot that the Ag network TCE based solar cell follows a similar trend, as the ITO based cell and the derived parameters are quite comparable (see Table 1). Thus, the efficiency of the Ag network TCE based solar cell was 2.14%, while that obtained for ITO based cells under similar ambient conditions was 2.27%.

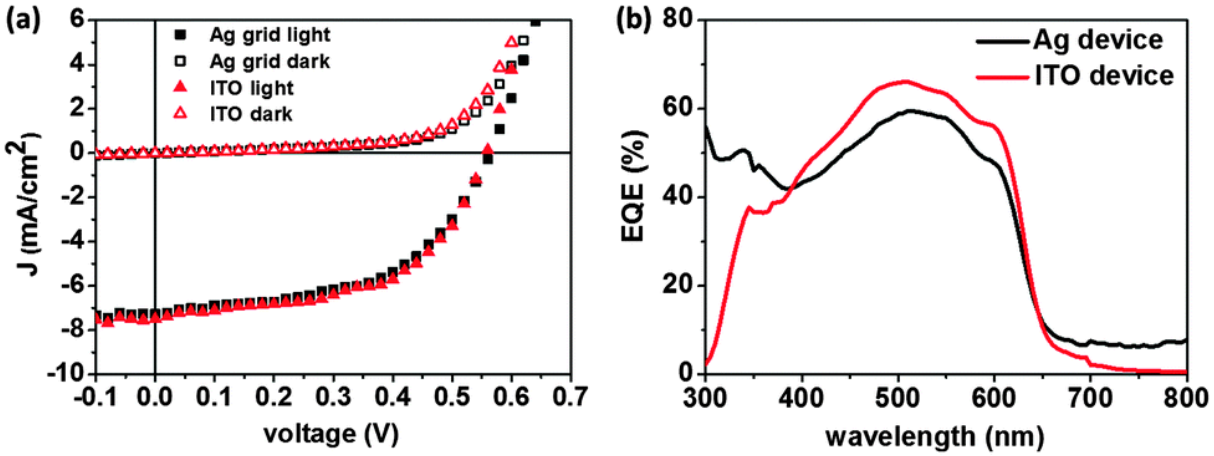

Figure 5. *Comparison of (a) J-V characteristics and (b) EQE for the optimized Ag network and ITO devices.*

Table 1*. Summary of the solar cell parameters corresponding to J-V characteristics shown in Figure 5a. Note, that a Ag grid device has a 135 nm thick ZnO layer, whereas an ITO device has a ZnO layer of only 45 nm.*

TCE	V_{oc} (V)	J_{sc} (mA cm^{-2})	FF (%)	PCE (%)	R_{sh} (Ω cm^{-2})	R_s (Ω cm^{-2})@V_{oc}	R_s (Ω cm^{-2})@P_{max}
Ag grid	0.57	7.2	51.8	2.14	421	8.3	49.7
ITO	0.55	7.5	55.2	2.27	413	6.7	48.6

These results presented here clearly demonstrate the potential of the Ag network based TCE as an alternative to ITO in OSCs. However, a slightly thicker ZnO layer is required to cover the Ag network thickness. Since the ZnO is filled in the interstitial domains between the metallic network, it improves the charge collection properties, which is similar to coating a PEDOT:PSS layer as reported for conventional metal grids.[19] The external quantum efficiency (EQE) measurements (Figure 5b) show that the Ag network TCE based cell exhibits slightly less values in the visible region compared to those derived from ITO cells, but in the UV region, the former excels which makes the overall performance similar for both cells. This can be clearly understood from the differences in transmission of the respective electrodes in the UV region (Figure 2d). The same information can be inferred by comparing the absorption spectra of the two solar cells (ESI, Figure S3) with their EQE spectra.

The method developed in this study for the TCE and associated OSC fabrication has several merits. While the present study has focused on only one type of metallic network, its scope of application can be easily extended to other thin layer devices by varying the template thickness and other parameters in the initial stages of crack template formation. Thus, it is possible to obtain TCEs with different network thicknesses and connectivity and importantly with different metals. Here, Ag was used as a typical example since the work function is favorable for P3HT–PCBM solar cells having an inverted geometry. However, it can be replaced with other metals such as Cu, Al, and Pt depending on the need of application. The metal network based TCE used in the present study works as a current collecting grid at a tens of micrometer scale with a metal fill factor of 20%.

Conclusions

In conclusion, we demonstrated the incorporation of a highly transparent and highly conducting Ag metallic network obtained using a cracked polymer template, in a thin film organic solar cell for the first time. The performance of this highly scalable metal network as a TCE is comparable to that of conventional ITO electrodes. This is a general approach to replace ITO in diverse thin film devices. The crack template approach is universal for any type of metal or substrate material.

Acknowledgements

The financial support from the EU Project "Largecells" (Grant No. 261936), Department of Science and Technology, Government of India and the Bavarian State Ministry of Science, Research, and Arts for the collaborative Research Network "Solar Technologies go Hybrid" is gratefully acknowledged. G.U.K., R.G. and K.D.M.R. are grateful to Professor C. N. R. Rao for his encouragement. K.D.M.R. thanks UGC for the SRF fellowship and C. H. acknowledges financial support from DFG (GRK 1640).

Notes and references

[1] Sun, Y.; Welch, G. C.; Leong, W. J.; Takacs, C. J.; Bazan G. C.; Heeger, A. J., Solution-processed small-molecule solar cells with 6.7% efficiency. *Nat. Mater.*, **2012**, *11*, 44-48.

[2] (*a*) Krebs, F. C., Polymer solar cell modules prepared using roll-to-roll methods: Knife-over-edge coating, slot-die coating and screen printing. *Sol. Energy Mater. Sol. Cells*, **2009**, *93*, 465-475.

(*b*) Gupta, R.; Kiruthika, S.; Rao, K. D. M.; Jørgensen, M.; Krebs, F. C.; Kulkarni, G. U., Screen-Display-Induced Photoresponse Mapping for Large-Area Photovoltaics. *Energy Technol.*, **2013**, *1*, 770-775.

(*c*) Angmo, D.; Gevorgyan, S. A.; Larsen-Olsen, T. T.; Søndergaard, R. R.; Hösel, M.; Jørgensen, M.; Gupta, R.; Kulkarni, G. U.; Krebs, F. C., Scalability and stability of very thin, roll-to-roll processed, large area, indium-tin-oxide free polymer solar cell modules. *Org. Electron.*, **2013**, *14*, 984-994.

[3] Bian, L.; Zhu, E.; Tang, J.; Tang, W.; Zhang, F., Recent progress in the design of narrow bandgap conjugated polymers for high-efficiency organic solar cells. *Prog. Polym. Sci.*, **2012**, *37*, 1292-1331.

[4] Kim, Y. H.; Sachse, C.; Machala, M. L.; May, C.; Müller-Meskamp, L.; Leo, K., Highly Conductive PEDOT:PSS Electrode with Optimized Solvent and Thermal Post-Treatment for ITO-Free Organic Solar Cells. *Adv. Funct. Mater.*, **2011**, *21*, 1076-1081.

[5] Ameri, T.; Li, N.; Brabec, C. J., Highly efficient organic tandem solar cells: a follow up review. *Energy Environ. Sci.*, **2013**, *6*, 2390-2413.

[6] Hagfeldt, A.; Boschloo, G.; Sun, L.; Kloo, L.; Pettersson, H.; Dye-Sensitized Solar Cells. *Chem. Rev.*, **2010**, *110*, 6595-6663.

[7] Green, M. A.; Emery, K.; Hishikawa, Y.; Warta, W.; Dunlop, E. D., Solar Efficiency Tables (Version 40). *Prog. Photovoltaics*, **2012**, *20* (5), 606-614.

[8] Yoo, J.; Yu, G.; Yi, J.,Large-area multicrystalline silicon solar cell fabrication using reactive ion etching (RIE). *Sol. Energy Mater. Sol. Cells*, **2011**, *95* (1), 2-6.

[9] Kaltenbrunner, M.; White, M. S.; Głowacki, E. D.; Sekitani, T.; Someya, T.; Sariciftci, N. S.; Bauer, S.,Ultrathin and lightweight organic solar cells with high flexibility. *Nat. Commun.*, **2012**, *3*, 770.

[10] Kim, H.; Gilmore, C. M.; Pique, A.; Horwitz, J. S.; Mattoussi, H.; Murata, H.; Kafafi, Z. H.; Chrisey, D. B., Electrical, optical, and structural properties of indium–tin–oxide thin films for organic light-emitting devices. *J. Appl. Phys*., **1999**, *86*, 6451-6461.

[11] Kumar, A.; Zhou, C, The Race To Replace Tin-Doped Indium Oxide: Which Material Will Win? *ACS Nano*, **2010**, *4* (1), 11-14.

[12] Cairns, D. R.; Witte, R. P.; Sparacin, D. K.; Sachsman, S. M.; Paine, D. C.; Crawford, G. P.; Newton, R. R., Strain-dependent electrical resistance of tin-doped indium oxide on polymer substrates. *Appl. Phys. Lett.*, **2000**, *76* (11), 1425-1427.

[13] Bae, S.; Kim, H.; Lee, Y.; Xu, X.; Park, J. S.; Zheng, Y.; Balakrishnan, J.; Lei, T.; Ri Kim, H.; Song, Y. I.; Kim, Y. J.; Kim, K. S.; Ozyilmaz, B.; Ahn, J-H.; Hong, B. H.; Iijima, S., Roll-to-roll production of 30-inch graphene films for transparent electrodes. *Nat. Nanotechnol.*, **2010**, *5*, 574-578.

[14] Tenent, R. C.; Barnes, T. M.; Bergeson, J. D.; Ferguson, A. J.; To, B.; Gedvilas, L. M.; Heben, M. J.; Blackburn, J. L., Ultrasmooth, Large-Area, High-Uniformity, Conductive Transparent Single-Walled-Carbon-Nanotube Films for Photovoltaics Produced by Ultrasonic Spraying. *Adv. Mater.*, **2009**, *21* (31), 3210-3216.

[15] Geng, H. Z.; Kim, K. K.; So, K. P.; Lee, Y. S.; Chang, Y.; Lee, Y. H., Effect of Acid Treatment on Carbon Nanotube-Based Flexible Transparent Conducting Films. *J. Am. Chem. Soc*., **2007**, *129* (25), 7758-7759.

[16] De, S.; Higgins, T. M.; Lyons, P. E.; Doherty, E. M.; Nirmalraj, P. N.; Blau, W. J.; Boland, J. J.; Coleman, J. N., Silver Nanowire Networks as Flexible, Transparent, Conducting Films: Extremely High DC to Optical Conductivity Ratios. *ACS Nano*, **2009**, *3* (7), 1767-1774.

[17] Kim, D.; Zhu, L.; Jeong, D. J.; Chun, K.; Bang, Y. Y.; Kim, S. R.; Kim, J. H.; Oh, S. K., Transparent flexible heater based on hybrid of carbon nanotubes and silver nanowires. *Carbon*, **2013**, *63*, 530-536.

[18] Zhang, D.; Ryu, K.; Liu, X.; Polikarpov, E.; Ly, J.; Tompson, M. E.; Zhou, C., Transparent, Conductive, and Flexible Carbon Nanotube Films and Their Application in Organic Light-Emitting Diodes. *Nano Lett*., **2006**, *6* (9), 1880-1886.

[19] Gaynor, W.; Burkhard, G. F.; McGehee, M. D.; Peumans, P., Smooth Nanowire/Polymer Composite Transparent Electrodes. *Adv. Mater.*, **2011**, *23* (26), 2905-2910.

[20] Sahin, C.; Elif Selen, A.; Husnu Emrah, U., Optimization of silver nanowire networks for polymer light emitting diode electrodes. *Nanotechnology*, **2013**, *24*, 125202.

[21] Hu, L.; Kim, H. S.; Lee, J. Y.; Peumans, P.; Cui, Y., Scalable Coating and Properties of Transparent, Flexible, Silver Nanowire Electrodes. *ACS Nano*, **2010**, *4* (5), 2955-2963.

[22] (*a*) Zou, J.; Yip, H. L.; Hau, S. K.; Jen, A. K. Y., Metal grid/conducting polymer hybrid transparent electrode for inverted polymer solar cells. *Appl. Phys. Lett*., **2010**, *96*, 203301.

(*b*) Ghosh, D. S.; Chen, T. L.; Pruneri, V., High figure-of-merit ultrathin metal transparent electrodes incorporating a conductive grid. *Appl. Phys. Lett*., **2010**, *96*, 041109.

[23] Gupta, R.; Kulkarni G.U., Holistic Method for Evaluating Large Area Transparent Conducting Electrodes. *ACS Appl. Mater. Interfaces*, **2013**, *5* (3), 730-736.

[24] Moon Kyu, K.; Jong, G. O.; Jae Yong, L.; Guo, L. J., Continuous phase-shift lithography with a roll-type mask and application to transparent conductor fabrication. *Nanotechnology*, **2012**, *23*, 344008.

[25] Kang, M. G.; Guo, L. J., Nanoimprinted Semitransparent Metal Electrodes and Their Application in Organic Light-Emitting Diodes. *Adv. Mater*., **2007**, *19* (10), 1391-1396.

[26] Galagan, Y.; Rubingh, J.-E. J. M.; Andriessen, R.; Fan, C.-C.; Blom, P. W. M.; Veenstra, S. C.; Kroon, J. M., ITO-free flexible organic solar cells with printed current collecting grids. *Sol. Energy Mater. Sol. Cells*, **2011**, *95* (5), 1339-1343.

[27] Galagan, Y.; Zimmermann, B.; Coenen, E. W. C.; Jørgensen, M.; Tanenbaum, D. M.; Krebs, F. C.; Gorter, H.; Sabik, S.; Slooff, L. H.; Veenstra, S. C.; Kroon, J. M.; Andriessen, R., Current Collecting Grids for ITO-Free Solar Cells. *Adv. Energy Mater.*, **2012**, *2*, 103-110.

[28] Gupta, R.; Hösel, M.; Jensen, J.; Krebs, F. C.; Kulkarni, G. U., Current Collecting Grids for ITO-Free Solar Cells. *J. Mater. Chem. C*, **2014**, *2*, 2112–2117.

[29] Gupta, R.; Walia, S.; Hösel, M.; Jensen, J.; Angmo, D.; Krebs, F. C.; Kulkarni, G. U., Solution processed large area fabrication of Ag patterns as electrodes for flexible heaters, electrochromics and organic solar cells. *J. Mater. Chem. A*, **2014**, *2*, 10930-10937.

[30] Yu, J. S.; Kim, I.; Kim, J. S.; Jo, J.; Olsen, T. T. L.; Søndergaard, R. R.; Hösel, M.; Angmo, D.; Jørgensen, M.; Krebs, F. C., Silver front grids for ITO-free all printed solar cells with embedded and raised topographies, prepared by thermal imprint, flexographic and inkjet roll-to-roll processes. *Nanoscale*, **2012**, *4*, 6032-6040.

[31] Han, B.; Pei, K.; Huang, Y.; Zhang, X.; Rong, Q.; Lin, Q.; Guo, Y.; Sun, T.; Guo, C.; Carnahan, D.; Giersig, M.; Wang, Y.; Gao, J.; Ren, Z.; Kempa, K., Uniform Self-Forming Metallic Network as a High-Performance Transparent Conductive Electrode. *Adv. Mater.*, **2014**, *26* (6), 873-877.

[32] Kiruthika, S.; Rao, K. D. M.; Kumar, A.; Gupta, R.; Kulkarni, G. U., Metal wire network based transparent conducting electrodes fabricated using interconnected crackled layer as template. *Mater. Res. Express*, **2014**, *1*, 026301.

[33] Kiruthika, S.; Gupta, R.; Rao, K. D. M.; Chakraborthy, S.; Padmavathy, N.; Kulkarni, G. U., Large area solution processed transparent conducting electrode based on highly interconnected Cu wire network. *J. Mater. Chem. C*, **2014**, *2*, 2089-2094.

[34] (*a*) Li, J. C.; Gong, X.; Wang, D.; Ba, D. C., Electrical switching of molecular thin films filled in metal oxide cracks. *Appl. Phys. A: Mater. Sci. Process*., **2013**, *111* (2), 645-651.

(*b*) Niedermeier, M. A.; Tainter, G.; Weiler, B.; Lugli, P.; Muller-Buschbaum, P., Fabrication of hierarchically structured titania thin films *via* combining nano-imprint with assisted sol–gel templating. J. *Mater. Chem. A*, **2013**, *1*, 7870-7873.

[35] Gupta, D.; Wienk, M. M.; Janssen, R. A. J., Efficient Polymer Solar Cells on Opaque Substrates with a Laminated PEDOT:PSS Top Electrode. *Adv. Energy Mater*., **2013**, *3* (6), 782-787.

[36] Beiley, Z. M.; Christoforo, M. G.; Gratia, P.; Bowring, R. A.; Eberspacher, P.; Margulis, G. Y.; Cabanetos, C.; Beaujuge, P. M.; Salleo, A.; McGehee, M. D., Semi-Transparent Polymer Solar Cells with Excellent Sub-Bandgap Transmission for Third Generation Photovoltaics. *Adv. Mater.*, **2013**, *25* (48), 7020-7026.

Supporting information

Experimental section

Preparation of Ag network derived TCE: Glass substrates were cleaned with soap water, DI water and ethanol, dried with N2 gas. A commercially available acrylic resin dispersion (Ming Ni Cosmetics Co., Guangzhou, China) is used for the preparation of crack forming dispersion. The dispersion is ultrasonicated for 30 min and left over night in an airtight bottle. The suspended solution is filtered with Whatman Filter (1 □m GF/B w/GMF) and further diluted with the diluter (Ming Ni Cosmetics Co., Guangzhou, China), to adjust the concentration of 0.6 g/mL. The final dispersion is spin coating on glass substrate at 3000 rpm for 120 s, followed by thermal evaporation of Ag metal in a vacuum chamber. In the final stage, the acrylic resin template was removed with chloroform. The Ag network is cleaned with chloroform for 2-3 times to remove any residual acrylic resin nanoparticles and heated at 80 °C for 30 min. These Ag network derived TCEs were used for the fabrication of organic solar cell.

Fabrication of polymer solar cell: The Ag network derived TCE and ITO were cleaned with ethanol and dried with N_2 gas. A Zinc acetate solution (109.75 mg zinc acetate dihydrate, 30.5 µL ethanol amine and 1ml methoxyethanole) is mixed, stirred for at least two hours and filtered with 0.2 µm hydrophilic filter. To obtain a 45 nm thick ZnO layer, 100 µL of zinc acetate solution is spin coated on TCE at 4000 rpm for 50 s, followed by heating at 150 °C for 5 min to convert zinc acetate to zinc oxide.[31] Different thicknesses for ZnO layers were obtained by repeating the above procedure. A 2.7 wt% of PCBM:P3HT (0.8:1) in chlorobenzene solution is stirred for 2 hours and filtered with 0.2 µm hydrophobic filter. A 80 µL PCBM:P3HT solution is spin coated on the ZnO coated TCE at 700 rpm for 60 s, followed by annealing at 130 °C for 15 min inside glove box. HTL – Solar PEDOT:PSS (Heraeus-Clevios) is ultrasonicated for 10 minutes and filtered with 0.2 µm hydrophilic filter. A 100 µL of the solution is spin coating on the active layer at 4000 rpm for 90 s and followed by annealing at 130 °C for 15 min in air. In the final step, 60 nm Au is evaporated on PEDOT layer using a thermal evaporator (BOC Edwards, Auto 306, FL 400). Four cells with different ZnO thicknesses (45, 95, 135 and 230 nm) were fabricated, each consisting of five cells (area of each cell: 0.09 -0.13 cm2).

Measurements: Metal fill factors are estimated from imageJ software analysis SEM was carried out using a Nova NanoSEM 600 instrument (FEI Co., The Netherlands). Wyko

NT9100 Optical Profiling System (Bruker, USA) was used for height and depth measurements and Dektak profiler for thickness measurements. Current-voltage characteristics were measured under standard AM 1.5 G spectral conditions at an intensity of 100 mW/cm2 using a solar simulator (Newport-Oriel, 92250A-1000) and an electrometer (Keithley, Model 6517). Light source was regularly calibrated using a silicon solar cell (WPVS cell, ISE Call lab, Freiburg). External quantum efficiencies were measured with a PVE300 photovoltaic device characterization system (Bentham).

SEM images of Ag network

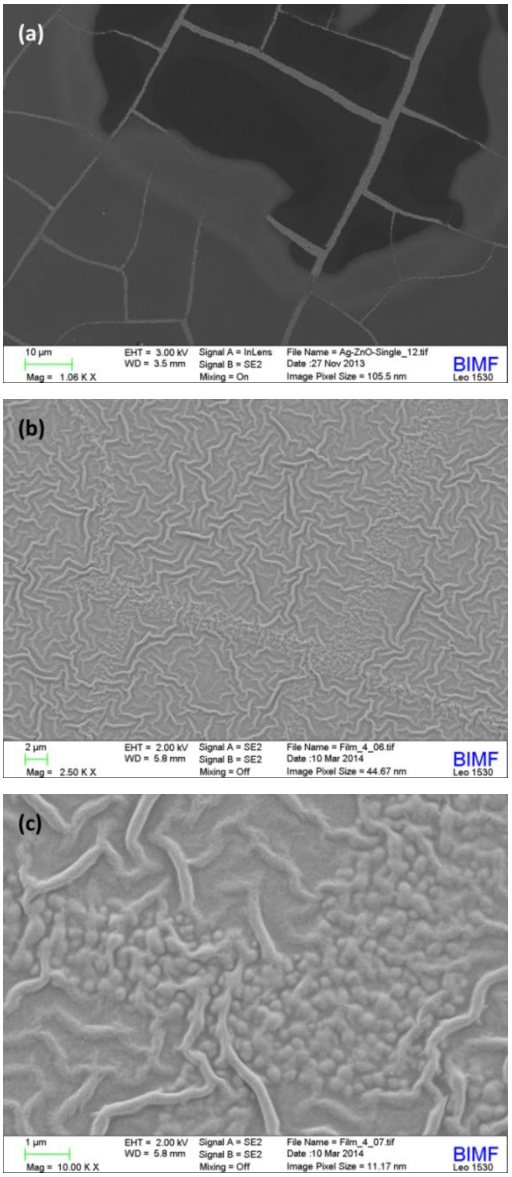

Figure S1. *SEM images for Ag network TCEs in different magnifications with (a) 45 nm ZnO magnified by 1.06K, (b) 135 nm ZnO magnified by 2.50K and (c) 135 nm ZnO magnified by 10.00K. In (c) the underlying Ag network is clearly discernible. The substructures in (b) and (c) are observed at high magnification.*

Current Voltage Characteristics

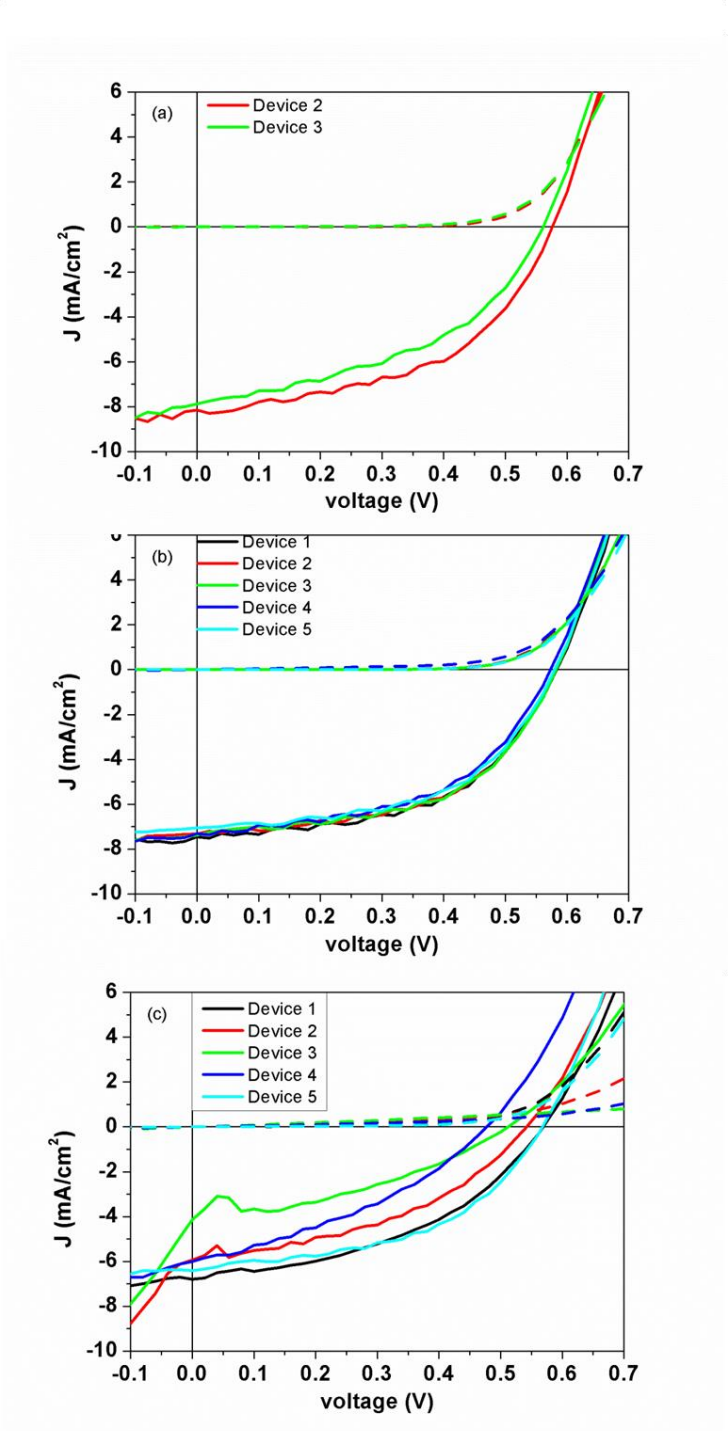

Figure S2. *J-V characteristics of all working Ag wire TCE derived polymer solar cell with (a) 95 nm, (b) 135 nm and (c) 230 nm ZnO layer thicknesses.*

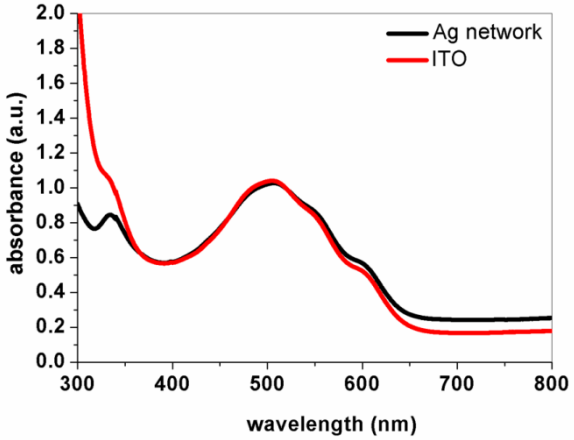

Figure S3. *Absorbance of devices having Ag wire network and ITO TCEs.*

The total absorbance of the (P3HT: PCBM) active layer together with ZnO layer, PEDOT:PSS and TCEs, (Ag network or ITO) is measured. As shown in Fig. S3 the absorbance of the organic layer in both devices is very similar. The only difference corresponds to the difference in the absorption of ITO and Ag network in the UV region.

7 Transparent metal network with low haze and high figure of merit applied to front and back electrodes in semitransparent ITO-free polymer solar cells

Christoph Hunger[a], K. D. M. Rao[b], Ritu Gupta[b], Chetan R. Singh[a], Giridhar U. Kulkarni[b], and Mukundan Thelakkat[a]**

* Corresponding authors

[a] Prof. Dr. Mukundan Thelakkat, Applied Functional Polymers, Macromolecular Chemistry I, University of Bayreuth, D-95440 Bayreuth, Germany.

E-mail: mukundan.thelakkat@uni-bayreuth.de

[b] Prof. Dr. Giridhar U. Kulkarni, Chemistry & Physics of Materials Unit and Thematic Unit of Excellence in Nanochemistry, Jawaharlal Nehru Centre for Advanced Scientific Research, Jakkur P.O., Bangalore 560 064, India.

E-mail: kulkarni@jncasr.ac.in

This manuscript is published in *Energy Technol.*, **2015**, *3* **(**6**)**, 638–645.

Abstract

In the quest for indium-tin oxide (ITO)-free photovoltaics and for building integrated as well as automobile roof applications, novel transparent electrodes for both front and back electrodes are required. Here we report the fabrication and integration of submicrometer transparent silver (Ag) and gold (Au) metal network electrodes, which are invisible to the naked eye, in organic photovoltaic devices. We exploit the idea of using the spontaneous cracking of a polymer layer as template to prepare the metal network. The main challenge is to apply the cracked template approach on top of soluble organic layers and to lift off the template without damaging the photoactive layer. We demonstrate that Ag or Au back electrodes can be fabricated maintaining a transmittance of 80% for the whole visible range. These electrodes exhibit ultralow haze of approximately 5% and an excellent figure of merit value. Moreover, the ITO-free semitransparent polymer solar cell incorporating the Ag/Ag network electrodes exhibits 57% transmittance above 650 nm.

Introduction

Solution-processed organic solar cells have made rapid progress towards technology as a potential source of deriving solar energy in recent years.[1, 2] The major part of research on organic solar cells was in terms of design and development of efficient photoactive materials with new acceptor and donor moieties to improve the power conversion efficiency (PCE).[3, 4] However, the quest for efficient, scalable and rational processing methods for both active layers and electrodes has gained momentum towards application-specific requirements such as large-area processing, low weight, semitransparency, and mechanical resilience for future photovoltaics technologies such as electronic skin, textiles, and building integrated photovoltaics (PV).[1, 2, 5] Here we address the questions concerning the fabrication of indium-tin oxide (ITO)-free electrodes and how to achieve semitransparency in polymer solar cells using these novel electrode materials. In most organic solar cells, ITO serves as a transparent conducting front electrode (TCE) whereas opaque metal films (such as Ag, Au, or Al) are used as back electrodes. ITO is known for its high transparency, reaching approximately 90% in the visible region, and low sheet resistance of 10 Ω/□.[6] But ITO is also scarce and expensive[7] and requires high-temperature processing as well as being brittle so that cracks develop on flexible substrates.[8] Therefore TCE alternatives based on graphene,[9] carbon nanotubes,[10, 11] Ag nanowires (NWs),[12, 13] or printed current-collecting grids from Ag

paste[14, 15] have been developed to replace ITO. Graphene and carbon nanotubes exhibit high transparencies, comparable to ITO, but they suffer from high contact resistances.[9, 10] However, TCEs made from Ag NWs have both high transparency (90% in the visible region) and a sheet resistance as low as 20 Ω/□.[16] To keep the sheet resistance low, a relatively thick layer of well-connected Ag NWs is essential and the layer needs further treatments such as pressing or nano-welding.[17] Printed collecting grids fabricated from Ag paste do not have such problems, but as the dimensions of the printed Ag grid are usually in the range of 200 - 300 mm, it is visible to the naked eye and therefore not ideal as semitransparent electrode in building-integrated or automobile roof photovoltaic applications.[2, 16] One big advantage of organic solar cells with respect to their inorganic counterparts is the semitransparency as well as the color tunability of their photoactive layer. To make the entire solar cell semitransparent, not only the front electrode but also the back electrode need to be transparent. To achieve this, most of these semitransparent solar cells use ITO as front electrode and Ag NWs as back electrode. The Ag NWs itself are filled or blended with PEDOT:PSS, MoO3, ZnO, or ITO particles to yield a PCE of 2–2.5% for P3HT:PCBM blends.[18, 19] Another possibility for a transparent back electrode is based on an ultrathin metal layer. Chen *et al.* demonstrated semitransparent solar cells with the help of an ultrathin Ag layer as back electrode and a low-bandgap (LBG) Polymer/$PC_{[71]}BM$ as photoactive layer.[20] Here, the thickness of the metal layer needs to be very small (< 10 nm) to guarantee adequate transparency, which is usually achieved at the cost of conductivity. There are only a few ITO-free semitransparent polymer solar cells reported in literature. The first report involves the use of PEDOT:PSS both as front and back electrodes resulting in a PCE of 0.5% for the P3HT/$PC_{[61]}BM$ System.[21] On the other hand, a combination of Ag NWs and PEDOT:PSS led to PCEs ranging from 2.0 to 2.3% for polymer solar cells containing P3HT as donor.[22, 23] Very recently a similar electrode combination was also demonstrated for a LBG polymer/ PCBM device.[24] But, it has been demonstrated that metal network electrodes based on cracked templates with network widths ranging from several hundreds of nanometers up to 5 mm can be developed and integrated into electronic devices as replacements for ITO.[25–27] The major advantages of these submicrometer metal network electrodes are their high transmittance and very low sheet resistances. Additionally, this template method is highly scalable. Furthermore, the crack template can be used not only for Ag or Au, but for any metal to form the respective network. However, these metal network electrodes had not been fabricated on top of an organic layer up to now. Moreover, its applicability to diverse surfaces needs to be demonstrated to apply this concept on any kind of surface. Considering the easiness and large-area scalability of

cracked template metal network electrodes, we address the following questions in this work: 1) Is it possible to fabricate a metal network electrode on top of an organic layer by using a cracked template procedure to form a back electrode? 2) Can these metal network electrodes be combined as front as well as back electrodes to realize ITO-free semitransparent solar cells for an organic photoactive layer? The main challenge here is to apply the cracked template approach on top of soluble organic layers without damaging the photoactive layer. This is very critical, as the cracked template needs to be removed by dissolution. We demonstrate for the first time that by a suitable adaptation of the cracked template method, Ag or Au back electrodes can be fabricated maintaining a transmittance of 80% for the whole visible range. To realize this, we first prepared Au network electrodes on top of PEDOT:PSS-coated glass and characterized these for determining the suitability for semitransparent solar cell fabrication. The fundamental properties of a metal network back electrode include haze, transmittance, and sheet resistance, and they are studied using a Au electrode as a typical example. We show that Ag and Au network electrodes can be integrated as front or back electrode depending on the device geometry and without influencing the photoactive layers. For realizing an ITO-free semitransparent solar cell, we chose a P3HT/$PC_{[61]}$BM inverted geometry device. The solar cell characteristics of the ITO-free semitransparent solar cell are compared with those of a reference ITO/Ag opaque as well as ITO/Ag network devices. We realized an ITO-free semitransparent polymer solar cell with a PCE of 1.8% and a transmittance of 57% above 650 nm. These devices, having a Ag network on both sides do not exhibit any differences in performance in either back or front illumination mode. This research work mainly concerns with the relevant issues of electrode fabrication, and we have taken a typical reference photoactive layer (P3HT/$PC_{[61]}$BM) to demonstrate our concept. This is a general approach, which can be transferred to any kind of organic layer, material combination, and metal network as front or back electrode.

Results and Discussion

Fabrication of metal network electrode on PEDOT:PSS

The basic fabrication process flow for the metal network electrodes on top of PEDOT:PSS (≈50 nm) is schematically shown in Figure 1 a. First the precursor dispersion was spin coated onto the PEDOT:PSS surface resulting in spontaneous formation of cracks during drying (Figure S1, Supporting Information). Interestingly, irrespective of the difference in the surface

properties of the glass and PEDOT:PSS, the precursor dispersion cracks on both surfaces in a similar way. Moreover, crack grooves run down to the PEDOT:PSS surface, which is than filled in with Ag or Au by slow thermal evaporation (≈0.2 nm s^{-1}) in vacuum. The crackle layer is easily dissolved away by dipping in chloroform without affecting the PEDOT layer beneath. The lift-off procedure was also optimized using solvents such as ethyl acetate to adapt this template method for applications in solar cells. To study these metal electrodes on top of PEDOT:PSS, a Au metal network was selected as a typical example and several samples of different Au thicknesses in the range of 20–60 nm were prepared following the same procedure as discussed below. A typical metal network electrode, Au (40 nm) network on PEDOT:PSS, was thoroughly characterized by a host of characterization techniques as shown in Figure 1. SEM images and its corresponding energy-dispersive spectroscopy (EDS) maps of the Au network fabricated on top of the PEDOT: PSS are shown in Figure 1b.

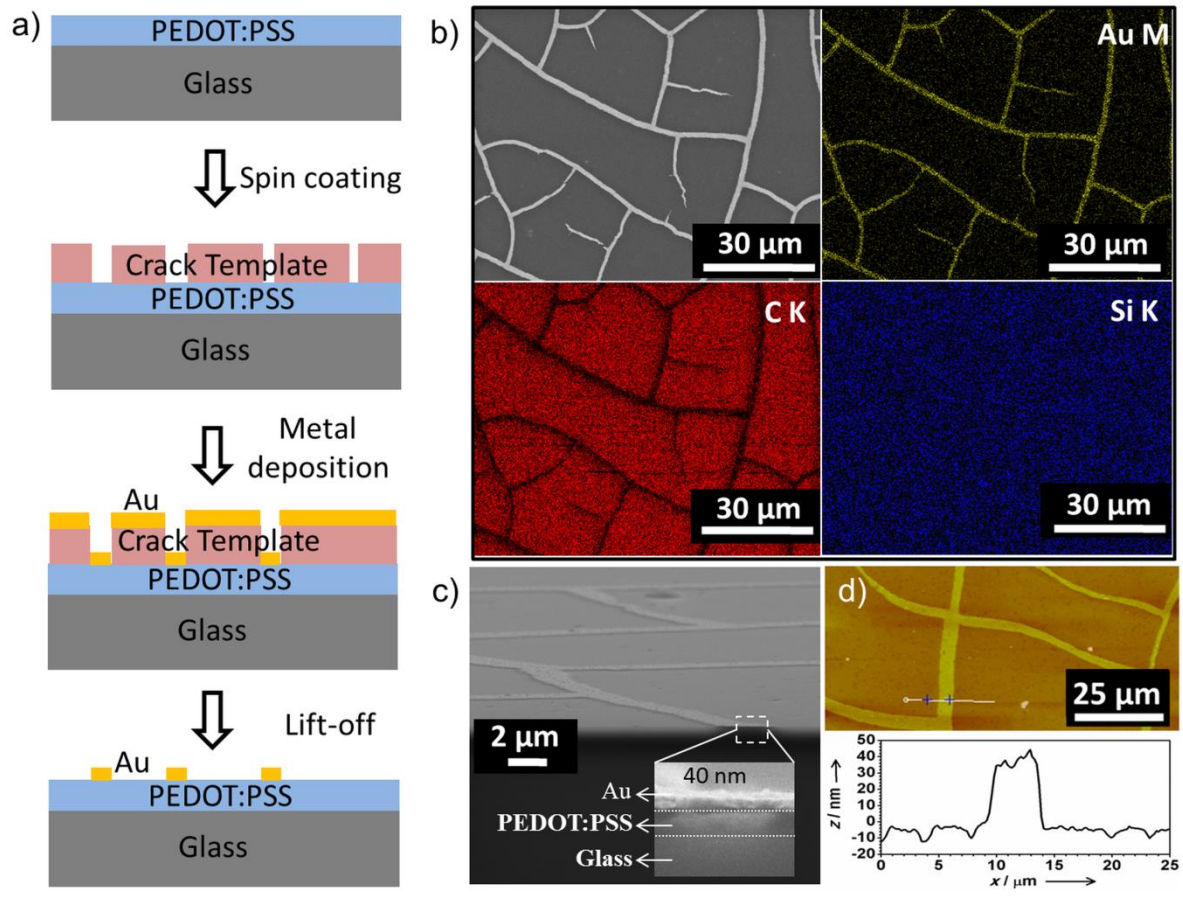

Figure 1. *a) Schematic illustration of preparing a Au metal network electrode on PEDOT:PSS coated glass substrate by spin coating of the crack template, Au deposition and removal of crack template by lift-off. b) SEM image and corresponding EDS maps of Au M, C K, and Si K. c) SEM image showing the cross-sectional view and d) AFM image along with height profile of Au network on PEDOT:PSS layer.*

From the SEM image, it can be seen that the junctions of the network or web are well connected without any defects (Figure 1 b). The Au network structures have a width from several hundreds of nm up to 5 mm and an average cell size (spacing between the grids) of 10–60 mm resulting in metal fill factor of approximately 12%. The metal network is continuous over large areas on the PEDOT:PSS layer (Figure S2, Supporting Information). The Au M, C K, and Si K signals in the EDS map reveal the presence of Au, C, and Si, respectively. As Au is fabricated directly on top of the PEDOT: PSS, the signal from the Au network is clearly visible and the C K signal is the inverse of Au K. This is due to the thickness of Au being more than the penetration depth of secondary electrons, which mask the PEDOT:PSS below it.

The signal from C K (red) arising from PEDOT:PSS is stronger in intensity than Si K (blue) arising from glass substrate, as expected to be the case. Moreover, the uniform distribution of C K signal in the void regions of the network shows that PEDOT:PSS is defect free even upon development of crack template by washing with organic solvents (Figure 1 c). The Si K signal is much weaker, due to the presence of the approximately 50 nm PEDOT:PSS layer as seen from the cross-sectional image in Figure 1d. The good interfacial contact between the Au metal and PEDOT:PSS layer is crucial for efficient charge collection in devices. The atomic force microscopy (AFM) image and the corresponding height profile (Figure 1d) over the network electrode shows the smooth surface of PEDOT:PSS beneath the Au network. As seen from the AFM profile in Figure 1d, the average PEDOT:PSS roughness (Ra) is approximately 5 nm. The Ra of the Au network/PEDOT:PSS electrodes over entire 100x100 mm^2 area is 9 nm, and the peak-to-valley roughness is 47 nm. As the metal fill factor per unit area is considerably low (≈12%), the overall roughness Ra is significantly reduced. The Ag and Au metal networks are very similar and therefore resemble in their properties considerably. Optical and electrical properties of metal network electrode The main properties of concern for a TCE are the optical transmittance, electrical conductivity, haze, and figure of merit (FOM), which gives the electrical/optical conductivity ratio. The electrodes fabricated in this way appear to be highly transparent as seen in Figure 2 a. In this image, the letters behind the electrode indicates high optical transmission. The electrode exhibits a sheet resistance of approximately 3 Ω/□, which is significantly lower (by 3 orders of magnitude) as compared to the PEDOT:PSS that has resistance of approximately 1.5 kΩ/□. The uniformity in resistance is clearly observed in the homogeneous temperature distribution across the thermal image upon subjecting the electrode to a direct current (DC) bias of 6 V (Figure 2 b). Electrothermal joule heating behavior through the transparent electrode is given in Figure S3 (Supporting

Information). The study of the optoelectronic properties for other electrodes with varying Au network thicknesses was conducted in detail. Figure 2 c shows the optical transmission spectra over a broad spectral range corresponding to diffusive transmittance (*TD*) with an average transmittance between 70– 85%. The transmittance of the Au network/PEDOT:PSS electrodes is lowered by 10–15% with respect to PEDOT: PSS thin film, which indicates that the network is highly transparent owing to low metal fill factor. The corresponding specular transmittance (*TS*) spectra are shown in Figure S4 (Supporting Information).

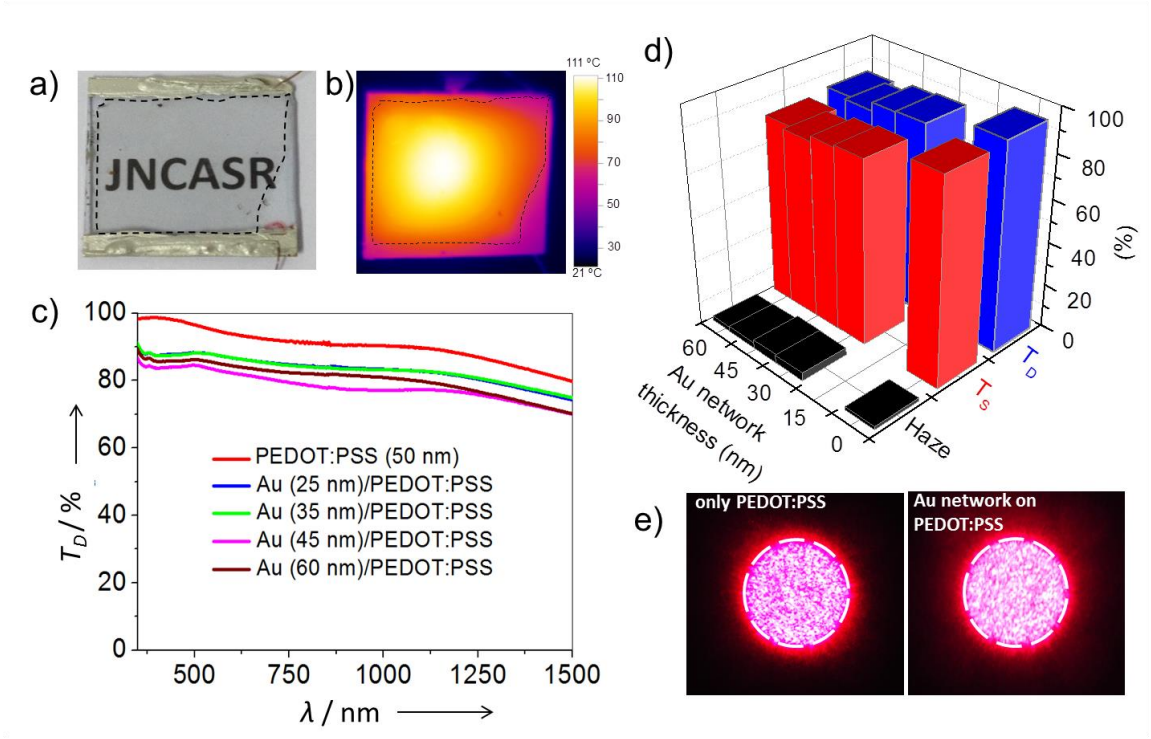

Figure 2. *a) Digital photograph, b) thermal image (at 6 V DC bias) of a Au network on PEDOT:PSS, c) diffusive transmittance spectra (350–1500 nm) for various thicknesses, d) variation in TS, TD, and haze with Au network thickness, e) angular distribution of scattered light from PEDOT:PSS and Au network on PEDOT:PSS. Glass has been taken as reference for transmittance measurement.*

Using average values of *TD* and *TS* as plotted in Figure 2d, the haze of the electrodes is calculated using the following relation: haze (%)=(*TD* − *TS*/*TD*). It refers to the percentage of light diffusely scattered through a transparent surface with respect to the total light transmitted. Haze is an important parameter to determine the optical visibility, especially for those applications where transparency is concerned. Interestingly, the electrodes exhibit an ultralow haze of approximately 5% for metal thicknesses up to 60 nm. The angular distribution of the diffused light is seen in Figure 2e (see Figure S5 for details, Supporting Information). The narrow distribution of the spot shows that specular transmission dominates

over diffusive component with an angular spread for the PEDOT:PSS layer and Au network/PEDOT:PSS electrode, approximately 0.3° and 0.5°, respectively (Figure 2 e). These angular spread values can be lower than those of Ag NW derived TCEs.[28] The ultralow haze values for these electrodes are attributed to the extremely low fill factor and reduced surface roughness. Figure S6 (Supporting Information) shows the interdependence between the transmittance (at 550 nm) and sheet resistance variation for different thicknesses of Au network on top of PEDOT:PSS. The overall resistance remains quite low with increasing transmittance for thinner layers, essentially overcoming the trade-off between the two counteracting properties. To evaluate this trade-off between the sheet resistance (*R*) and transmittance (*T*), the FOM is usually useful.[12] Therefore, the performance of these electrodes is further evaluated by specifying the commonly used FOM based on the electrical/optical conductivity ratio (σ_{DC}/σ_{OP}) calculated using following Equation (1)

$$\text{FOM:} \qquad \sigma_{DC}/\sigma_{OP} = Z_O/2R\left(T^{-1/2}-1\right) \quad (1)$$

To achieve an *R* value of 10 Ω/□ and *T*≈90% requires $\sigma_{DC}/\sigma_{OP} \approx 350$. ITO electrodes having *T*≈97% and *R*≈15–30 Ω/□, exhibit FOM values of 400–800.[12] The FOM for our Au network (60 nm) on PEDOT:PSS is 765.

Solar Cell Preparation & Characterization

Three different solar cell configurations were prepared using the ITO/Ag opaque, ITO/network, and Ag/Ag network as front and back electrodes, respectively. The fabrication steps for a metal network back electrode on top of the photoactive material are schematically shown in Figure 3.

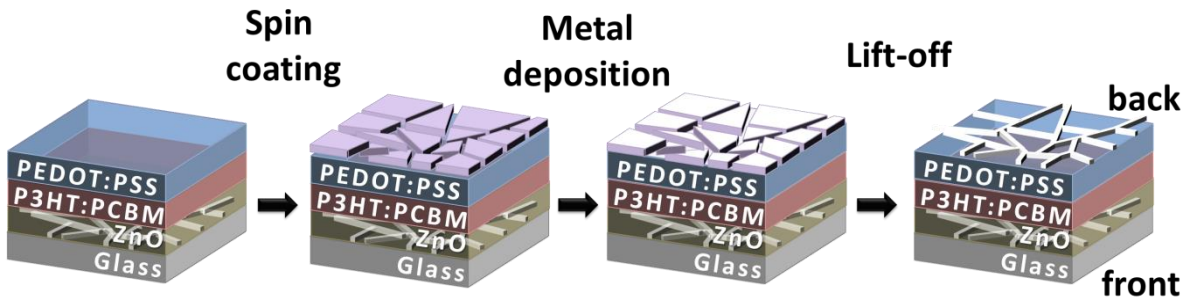

***Figure 3**. Schematics of process steps for the fabrication of ITO-free semitransparent polymer solar cell with a Ag/Ag network as front and back electrodes (glass/ZnO:Ag network/P3HT:PCBM/PEDOT:PSS/Ag network).*

A polymer template layer was spin-coated onto PEDOT: PSS to form spontaneous cracks. After metal deposition, the cracked template needed to be lifted-off by ultrasonication in suitable solvents. For the preparation of the front electrode on a glass substrate, the selection of solvent was not critical and we could use, for example, chloroform. But to remove the template as prepared on top of the photoactive layer coated with PEDOT:PSS, this procedure damaged the device. To find a suitable solvent that does not damage the device, different solvents were tested, and a reference device was ultra-sonicated in these solvents. It was determined that ultra-sonicating in ethyl acetate for 10 s removed the template completely and this treatment had no impact on the solar cell performance (Supporting Information, Figure S7). For the purpose of comparison, all three of the devices using ITO/Ag opaque, ITO/Ag network, and Ag/Ag network as front and back electrodes were fabricated under the same conditions and for the same P3HT/$PC_{[61]}$BM thickness (Figure 4 a). All of the front electrodes were coated with an optimum layer of ZnO to realize the inverted geometry.[27] To guarantee hole extraction/collection at the back electrode, the Ag network electrode was prepared on top of PEDOT:PSS. Both Ag und Au metal networks were tested as back electrodes. As an example, only the Ag network electrodes are discussed here (see Supporting Information for the results on Au network electrodes, Table S1 and Table S2). An optical micrograph of Ag/Ag network device (Figure S8, Supporting Information) clearly shows the formation of submicrometer network structures for both the front and back electrodes. Moreover, the subsequent layer preparation and the fabrication of a Ag network on top of P3HT/$PC_{[61]}$BM layer have no detrimental effects on the underlying layers. It is clear from the photographs shown in Figure 4b that the letters behind the transparent solar cell are clearly visible and both the solar cells with ITO/Ag network and Ag/Ag network are similar in their semitransparency (Figure 4b). The transmittance spectra of the ITO/Ag network and Ag/Ag network devices are shown in Figure 4c. The transmittance of the ITO/Ag network device is 15% at 500 nm (70% beyond 650 nm) whereas the Ag/Ag network device has a comparable transmittance of 13% at 500 nm (57% beyond 650 nm), which is slightly better than published results on Ag NW/PEDOT:PSS electrodes.[22] The low transmittance at 500 nm arises mainly from the intensive absorption of P3HT in this region for the layer thicknesses of approximately 180 nm used here. Further optimization of the P3HT layer thickness may be required to improve the transmittance without sacrificing much on performance. Further, the use of new photoactive materials that absorb in the near infrared with high transmittance in the visible region can result in improved semitransparent solar cells. In this contribution, we were studying the consequences of integrating a metal network electrode on top of a typical organic layer to

elucidate the general validity and feasibility of this approach to any kind of organic solar cell. Therefore, the semiconductor layer was not varied or optimized. In the following, the photovoltaics parameters of all of the three types of devices are discussed in detail. Figure 5a shows the *J–V* characteristics of all three devices, which were measured under front illumination (see Figure S9 for back illumination curves, Supporting Information). The corresponding external quantum efficiency (EQE) spectra for both front and back illumination are given in Figure 5b. The respective values for the open-circuit voltage (V_{OC}), short-circuit current (J_{SC}), fill factor (*FF*), power conversion efficiency (PCE), series resistance (R_S), and shunt resistance (R_{SH}) are summarized in Table 1. As seen in Figure 5, it is feasible to fabricate a metal network back electrode on top of a PEDOT:PSS-coated photoactive layer using the cracked template method described above to obtain considerably efficient photovoltaic devices. The back electrode fabrication is reproducible. The average values and standard derivation for a given number of solar cells are given in the Supporting Information (Table S3), and the data for the best devices are discussed here. All device parameters were obtained by illuminating the devices through a mask and the area of the device is defined by the mask as recommended for solar cell characterization.[29] In many of the published values, this is not the case, and therefore one has to be cautious in comparing the absolute values with those published in literature. In the Supporting Information (Figure S10 and Table S4), we have given the differences in solar cell parameters for the same device if measured correctly with a mask and without a mask, which is often practiced. A reference cell using ITO/Ag opaque exhibits 3.1% PCE here under standard conditions of measurement using a mask and without any artificial layer or additional back reflector.

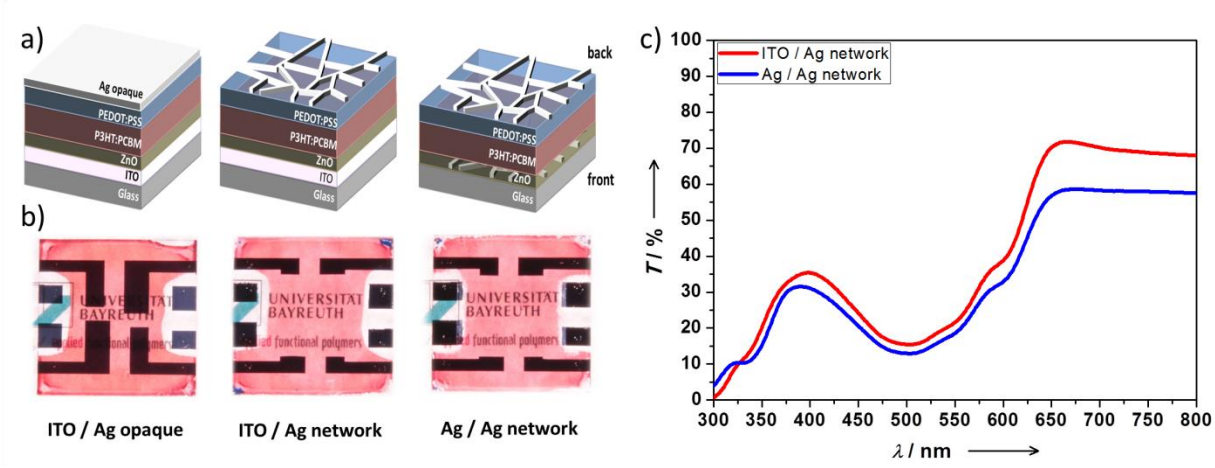

Figure 4. *a) Schematics and b) photographs of all the devices studied: ITO/ Ag opaque, ITO/Ag network, and the ITO-free semitransparent polymer solar cell with Ag/Ag network as front and back electrodes. c) Transmittance of complete devices with ZnO, P3HT/$PC_{[61]}$BM, and PEDOT:PSS for the ITO/Ag network and Ag/Ag network as front and back electrodes, respectively*

For comparison, the ITO/Ag network device shows 2.25% PCE whereas the Ag/Ag network devices exhibit 1.80% PCE. Thus the devices with the metal network as back electrode deliver less photocurrent compared to the ITO/Ag opaque reference device. This may be due to the lack of back reflection in the ITO/Ag network case and both lack of back reflection and decreased transmittance in the Ag/Ag network case. As expected, in the case of ITO/Ag network as well as Ag/Ag network devices, the lack of back reflection decreases the photocurrent as observed in Figure 5 (for reflection spectra of the solar cells please see Figure S11, Supporting Information). Additionally, the Ag/Ag network devices also have a small amount of loss in transmittance at the front electrode due to the thicker ZnO layers as well as Ag network. This observed effect on the front electrode is in agreement with what we observed in our previous work.[27] The observed trend in photocurrent values agrees very well with the measured EQE.

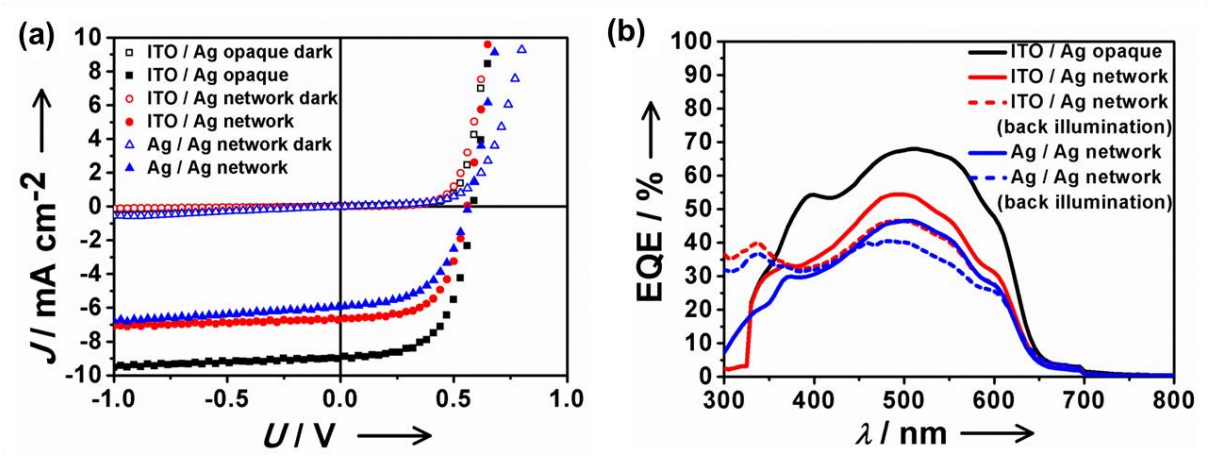

Figure 5. *a) J–V characteristics in the dark (open symbols) and under light (filled symbols) and b) EQE under front and back illumination for all the three types of devices.*

Table 1. Summary of the solar cell parameters for the best devices corresponding to J-V characteristics shown in Figure 5a. Average values and standard derivations are given in Table S3 (Supporting Information).

Cathode / Andode	V_{OC} [mV]	J_{SC} [mAcm^{-2}]	FF [%]	PCE [%]	RS@V_{OC} [Wcm^2]	RSH@J_{SC} [kWcm^2]
ITO/Ag opaque	580	8.78	60.9	3.10	1.37	1.45
ITO/Ag network, front illumination	560	6.67	60.1	2.25	3.29	2.05
ITO/Ag network, back illumination	550	5.95	61.9	2.03	3.51	1.81
Ag/Ag network, front illumination	560	5.90	54.4	1.80	4.22	1.01
Ag/Ag network, back illumination	580	6.16	51.7	1.85	4.24	1.13

Additionally, we verified the effect of front and back illumination for both semitransparent solar cells having ITO/Ag network and the Ag/Ag network as front and back electrodes. For the *J–V* curves (back illumination data in Figure S8, Supporting Information) it does not matter, if the devices are illuminated from the front or back electrode. In the EQE curves, considerable differences are observed in the wavelength range of 300 to 400 nm. Interestingly for both the ITO/Ag network and Ag/Ag network devices in the case of front illumination, the EQE values between 300 and 400 nm are lower, whereas between 400 and 650 nm the EQE values are higher compared to back illumination.

The lower EQE values between 300 and 400 nm are mainly due to optical losses at the front electrode arising from absorption of the glass/ITO/ZnO or glass/ZnO in the respective cases (compared to the Ag network in back illumination) upon illuminating from the front side. To understand the resistance effects, the *J–V* characteristics under illumination for all of the three types of devices were analyzed to obtain R_S and R_{SH} near the open-circuit and short-circuit conditions respectively. All the devices have very low R_S (<5 Ωcm^2) and high R_{SH} values (>1 $k\Omega cm^2$). This results in high *FF* values of 50–60%. The lower *FF* for Ag/Ag network devices correlates well with its highest R_S and lowest R_{SH} values. Thus, replacement of front ITO or back Ag opaque electrode with Ag network leads only to a very small increase in the overall R_S, with no considerable influence on R_{SH}.

Conclusions

The concept of the fabrication of submicrometer metal network electrodes that are invisible to the naked eye using a cracked polymer template is successfully applied to the fabrication of a back electrode on top of a photoactive layer in a solar cell for the first time. Both Ag and Au network electrodes can be used as either front or back electrodes in a polymer solar cell to achieve ITO-free semitransparent devices. Here, the template process is repeatedly applied before and after coating the photoactive layer. The biggest challenge of fabricating a transparent back electrode on top of an organic layer was achieved by optimization of the lift-off procedure for the template. Both the ITO/Ag network and Ag/Ag network devices exhibit considerably good efficiencies of approximately 2% PCE, which is comparable to any other semitransparent electrode system reported for P3HT/$PC_{[61]}$BM blends. The method of cracked template is in principle scalable for large areas, and any kind of evaporable metal can be used in combination with this template approach. Further improvements in PCE and transmittance can be achieved by using other photoactive layers and by additional optimization of the layer thickness. In addition, this is a general approach to fabricate transparent metal electrodes on

top of organic layers, where diverse material combination and type of metal can be used to realize different kinds of optoelectronic devices.

Experimental Section

Fabrication of Ag or Au network by cracked template method on PEDOT:PSS

For the fabrication of metal network electrodes on PEDOT:PSS, we modified the published procedure for a cracked template method on glass.[27] Glass substrates were washed and ultrasonicated in water, acetone, and isopropyl alcohol (IPA), respectively. The substrates were dried using a N_2 gun before use. In the second step, a commercially available acrylic resin nanoparticle dispersion (Ming Ni Cosmetics Co., Guangzhou, China) was diluted to achieve a well-dispersed solution of 0.6 g mL^{-1} concentration using a commercially available diluter (Ming Ni Cosmetics Co., Guangzhou, China). The diluted dispersion was spin coated onto a PEDOT:PSS coated glass substrate at 1000 rpm for 120 s. During drying, this film developed cracks suitable to be used as a template. In the next step, Ag or Au metal was deposited using a thermal evaporator (BOC Edwards, Auto 306, FL 400 and Hind High Vacuum Co., India). In the final step, the cracked template was removed by dissolving in either chloroform or acetone or ethyl acetate.

Solar cell fabrication and characterization

The reference solar cell, ITO/ZnO/P3HT:$PC_{[61]}$BM/PEDOT:PSS/ Ag opaque having an inverted geometry was prepared according to the published procedures.[27] The only difference was the use of structured ITO here. For realizing the devices with ITO as front electrode and Ag or Au network as back electrode, a similar procedure was adopted up to the PEDOT:PSS layer preparation. For the back metal network electrode, the polymer crack template was prepared on the PEDOT:PSS (Clevios HTL Solar) layer as described above, followed by 100 nm metal (Ag or Au) deposition using a thermal evaporator (BOC Edwards, Auto 306, FL 400). The polymer lift-off was performed by ultra-sonication of the entire device in ethyl acetate for 10 s. To realize the semitransparent ITO-free device with Ag network as both front and back electrodes, the published procedure[27] for the front electrode was modified to structure the metal network area using masks, and it was combined with the newly adopted method for the back electrode preparation. The average area of the devices was in the range of 4–9 mm^2 as defined by the area of the light mask. Current–voltage characteristics were measured under N_2 atmosphere using suitable masks under standard AM1.5G spectral conditions at an intensity of 100 $mWcm^{-2}$ using a solar simulator (Newport-

Oriel, 92250A-1000) and an electrometer (Keithley, Model 6517). The light source was regularly calibrated using a silicon solar cell (WPVS cell, ISE Call lab, Freiburg). Near-normal reflectance spectra of full solar cells were obtained using an integrating sphere in a Bentham PVE300 photovoltaic characterization system. External quantum efficiencies were measured using the same Bentham PVE300 photovoltaic device characterization system. For the simplicity of discussion of results, the best solar cell parameters are given. However, average values and the standard derivation for a large number of devices are given in the Supporting Information.

Other characterization methods

SEM was performed using a Nova NanoSEM 600 instrument (FEI Co., The Netherlands). Energy-dispersive spectroscopy (EDS) mapping was performed using an energy-dispersive X-ray analysis (EDAX) Genesis instrument (Mahwah, NJ) attached to the SEM column. AFM measurements were performed using di Innova (Bruker, USA) in contact mode. Standard Si cantilevers were used for normal topography imaging. Wyko NT9100 Optical Profiling System (Bruker, USA) was used for height and depth measurements and Dektak profiler for thickness measurements. A PerkinElmer Lambda 900 UV/visible/near-IR spectrometer was used to perform the transmission and haze measurements of electrodes and device.

Acknowledgements

The financial support from the EU Project “Largecells” (Grant No. 261936), Department of Science and Technology, Government of India, DFG (SFB 840) and the Bavarian State Ministry of Science, Research, and Arts for the collaborative Research Network “Solar Technologies go Hybrid” is gratefully acknowledged. K.D.M.R. thanks UGC for the SRF fellowship and C.H. acknowledges financial support from DFG (GRK 1640) and help in instrumentation and software from Jonas Mayer, University of Bayreuth.

References

[1] Li, G.; Zhu, R.; Yang, Y., Polymer soar cells. *Nat. Photonics*, **2012**, *6*, 153 – 161.

[2] Sondergaard, R.; Hösel, M.; Angmo, D.; Larsen-Olsen, T.T.; Krebs, F. C., Roll-to-roll fabrication of polymer solar cells. *Mater. Today*, **2012**, *15*, 36 –49.

[3] Li, W.; Roelofs, W. S. C.; Turbiez, M.; Wienk, M. M.; Janssen, R. A. J., Polymer solar cells with diektopyrrolopyrrole conjugated polymers as the electron donor and electron acceptor. *Adv. Mater.*, **2014**, *26*, 3304 –3309.

[4] Xu, T.; Yu, L., How to design low bandgap polymers for highly efficient organic solar cells. *Mater. Today*, **2014**, *17*, 11 –15.

[5] Kaltenbrunner, M.; White, M. S.; Głowacki, E. D.; Sekitani, T.; Someya, T.; Sariciftci, N. S.; Bauer, S.,Ultrathin and lightweight organic solar cells with high flexibility. *Nat. Commun.*, **2012**, *3*, 770.

[6] Kim, H.; Gilmore, C. M.; Pique, A.; Horwitz, J. S.; Mattoussi, H.; Murata, H.; Kafafi, Z. H.; Chrisey, D. B., Electrical, optical, and structural properties of indium–tin–oxide thin films for organic light-emitting devices. *J. Appl. Phys.*, **1999**, *86*, 6451-6461.

[7] Kumar, A.; Zhou, C, The Race To Replace Tin-Doped Indium Oxide: Which Material Will Win? *ACS Nano*, **2010**, *4* (1), 11-14.

[8] Cairns, D. R.; Witte, R. P.; Sparacin, D. K.; Sachsman, S. M.; Paine, D. C.; Crawford, G. P.; Newton, R. R., Strain-dependent electrical resistance of tin-doped indium oxide on polymer substrates. *Appl. Phys. Lett.*, **2000**, *76* (11), 1425-1427.

[9] Bae, S.; Kim, H.; Lee, Y.; Xu, X.; Park, J. S.; Zheng, Y.; Balakrishnan, J.; Lei, T.; Ri Kim, H.; Song, Y. I.; Kim, Y. J.; Kim, K. S.; Ozyilmaz, B.; Ahn, J-H.; Hong, B. H.; Iijima, S., Roll-to-roll production of 30-inch graphene films for transparent electrodes. *Nat. Nanotechnol.*, **2010**, *5*, 574-578.

[10] Tenent, R. C.; Barnes, T. M.; Bergeson, J. D.; Ferguson, A. J.; To, B.; Gedvilas, L. M.; Heben, M. J.; Blackburn, J. L., Ultrasmooth, Large-Area, High-Uniformity, Conductive Transparent Single-Walled-Carbon-Nanotube Films for Photovoltaics Produced by Ultrasonic Spraying. *Adv. Mater.*, **2009**, *21* (31), 3210-3216.

[11] Geng, H. Z.; Kim, K. K.; So, K. P.; Lee, Y. S.; Chang, Y.; Lee, Y. H., Effect of Acid Treatment on Carbon Nanotube-Based Flexible Transparent Conducting Films. *J. Am. Chem. Soc.*, **2007**, *129* (25), 7758-7759.

[12] De, S.; Higgins, T. M.; Lyons, P. E.; Doherty, E. M.; Nirmalraj, P. N.; Blau, W. J.; Boland, J. J.; Coleman, J. N., Silver Nanowire Networks as Flexible, Transparent, Conducting Films: Extremely High DC to Optical Conductivity Ratios. *ACS Nano*, **2009**, *3* (7), 1767-1774.

[13] Kim, D.; Zhu, L.; Jeong, D. J.; Chun, K.; Bang, Y. Y.; Kim, S. R.; Kim, J. H.; Oh, S. K., Transparent flexible heater based on hybrid of carbon nanotubes and silver nanowires. *Carbon*, **2013**, *63*, 530-536.

[14] Galagan, Y.; Rubingh, J.-E. J. M.; Andriessen, R.; Fan, C.-C.; Blom, P. W. M.; Veenstra, S. C.; Kroon, J. M., ITO-free flexible organic solar cells with printed current collecting grids. *Sol. Energy Mater. Sol. Cells*, **2011**, *95* (5), 1339-1343.

[15] Galagan, Y.; Zimmermann, B.; Coenen, E. W. C.; Jørgensen, M.; Tanenbaum, D. M.; Krebs, F. C.; Gorter, H.; Sabik, S.; Slooff, L. H.; Veenstra, S. C.; Kroon, J. M.; Andriessen, R., Current Collecting Grids for ITO-Free Solar Cells. *Adv. Energy Mater.*, **2012**, *2*, 103-110.

[16] Carle, J. E.; Helgesen, M.; Madsen, M. V.; Bundgaard, E.; Krebs, F. C., Upscaling from single cells to modules-fabrication of vacuum-and ITO- free polymer solar cells on flexible substrates with long lifetime. *J. Mater. Chem. C*, **2014**, *2*, 1290 –1297.

[17] a) Lee, J.; Lee, P.; Lee, H.; Lee, D.; Lee, S. S.; Ko, S. H., Very long Ag nanowire synthesis and its application in a highly transparent, conductive and flexible metal electrode touch panel. *Nanoscale*, **2012**, *4*, 6408 – 6414

b) Gaynor, W.; Burkhard, G. F.; McGehee, M. D.; Peumans, P., Smooth Nanowire/Polymer Composite Transparent Electrodes. *Adv. Mater.*, **2011**, *23* (26), 2905-2910.

[18] Reinhard, M.; Eckstein, R.; Slobodskyy, A.; Lemmer, U.; Colsmann, A., Solution-processed polymer-silver nanowire top electrodes for inverted semi-transparent solar cells. *Org. Electron*., **2013**, *14* (1), 273 –277.

[19] Zilberberg, K.; Gasse, F.; Pagui, R.; Polywka, A.; Behrendt, A.; Trost, S.; Heiderhoff, R.; Gcrrn, P.; Riedl, T., Highly Robust Indium-Free Transparent Conductive Electrodes Based on Composites of Silver Nanowires and Conductive Metal Oxides. *Adv. Funct. Mater*., **2014**, *24* (12), 1671-1678.

[20] Chen, K.-S.; Salinas, J.-F.; Yip, H.-L.; Huo, L.; Hou, J.; Jen, A. K.-Y., Semi-transparent polymer solar cells with 6% PCE, 25% average visible transmittance and a color rendering index close to 100 for power generating window applications. *Energy Environ. Sci*., **2012**, *5*, 9551 – 9557.

[21] Hau, S. K.; Yip, H.-L.; Zoua, J.; Jen, A. K.-Y, Indium tin oxide-free semi-transparent inverted polymer solar cells using conducting polymer as both bottom and top electrodes. *Org. Electron*., **2009**, *10*, 1401 – 1407.

[22] Yim, J. H.; Joe, S. Y.; Pang, C.; Lee, K. M.; Jeong, H.; Park, J.-Y.; Ahn, Y. H.; de Mello, J. C.; Lee, S., Fully solution-processed semitransparent organic solar cells with a silver nanowire cathode and a conducting polymer anode. *ACS Nano*, **2014**, *8*, 2857 – 2863.

[23] Guo, F.; Zhu, X.; Forberich, K.; Krantz, J.; Stubhan, T.; Salinas, M.; Halik, M.; Spallek, S.; Butz, B.; Spiecker, E.; Ameri, T.; Li, N.; Kubis, P.; Guldi, M. D.; Matt, G. J.; Brabec, C. J., ITO-Free and Fully Solution-Processed Semitransparent Organic Solar Cells with High Fill Factors. *Adv. Energy Mater.*, **2013**, *3* (8), 1062 – 1067.

[24] Guo, F.; Kubis, P.; Stubhan, T.; Li, N.; Baran, D.; Przybilla, T.; Spiecker, E.; Forberich, K.; Brabec, C. J., Fully Solution-Processed Route toward Highly Transparent Polymer Solar Cells. *ACS Appl. Mater. Interfaces*, **2014**, *6*, 18251 – 18257.

[25] Han, B.; Pei, K.; Huang, Y.; Zhang, X.; Rong, Q.; Lin, Q.; Guo, Y.; Sun, T.; Guo, C.; Carnahan, D.; Giersig, M.; Wang, Y.; Gao, J.; Ren, Z.; Kempa, K., Uniform Self-Forming Metallic Network as a High-Performance Transparent Conductive Electrode. *Adv. Mater.*, **2014**, *26* (6), 873-877.

[26] a) Rao, K. D. M.; Gupta, R.; Kulkarni, G. U., Fabrication of Large Area, High-Performance, Transparent Conducting Electrodes Using a Spontaneously Formed Crackle Network as Template. *Adv. Mater. Interfaces*, **2014**, *1*, 1400090;

b) Kiruthika, S.; Gupta, R.; Rao, K. D. M.; Chakraborthy, S.; Padmavathy N.; Kulkarni, G. U., Large area solution processed transparent conducting electrode based on highly interconnected Cu wire network. *J. Mater. Chem. C*, **2014**, *2*, 2089 – 2094.

[27] Rao, K. D. M.; Hunger, C.; Gupta, R.; Kulkarni, G. U., Thelakkat, M., A cracked polymer templated metal network as a transparent conducting electrode for ITO-free organic solar cells. *Phys. Chem. Chem. Phys.*, **2014**, *16*, 15107 –15110.

[28] Preston, C.; Fang, Z.; Murray, J.; Zhu, H.; Dai, J.; Munday, J. N.; Hu, L., Silver nanowire transparent conducting paper-based electrode with high optical haze. *J. Mater. Chem. C*, **2014**, *2*, 1248 –1254.

[29] Gevorgyan, S. A.; Carle, J. E.; Sondergaard, R.; Larsen-Olsen, T. T.; Jorgensen, M.; Krebs, F. C., Accurate characterization of OPVs: Device masking and different solar simulators. *Solar Energy Mater. Solar Cells*, **2013**, 110, 24– 35.

Supporting Information

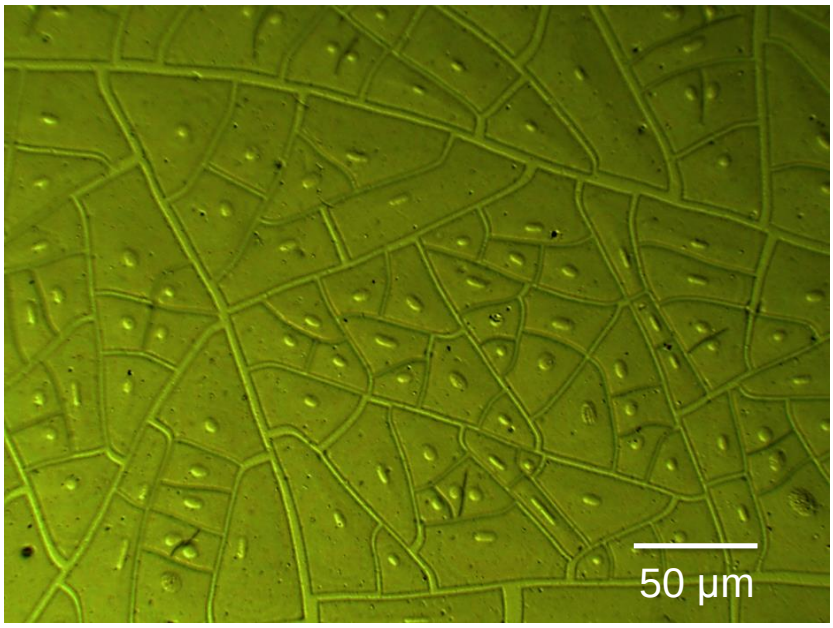

Figure S1. *Optical micrograph of crack patterns formed in polymer template on top of PEDOT:PSS layer.*

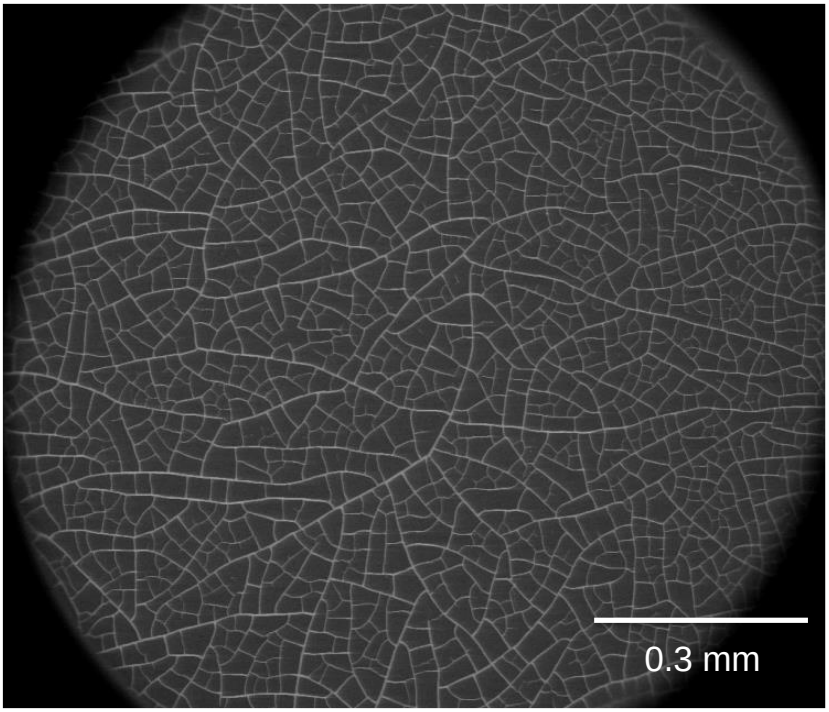

Figure S2. *SEM image (1 mm^2 area) of Au network on top of PEDOT:PSS layer.*

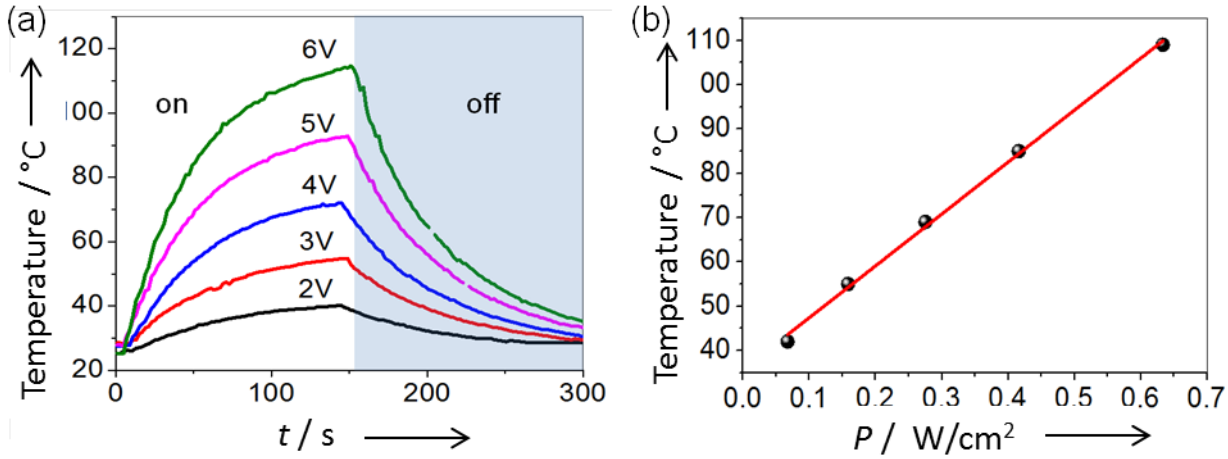

Figure S3. *(a) Temperature profiles as a function of time for a different applied voltages on Au network. (b) The maximum temperature achieved as a function of input power (P).*

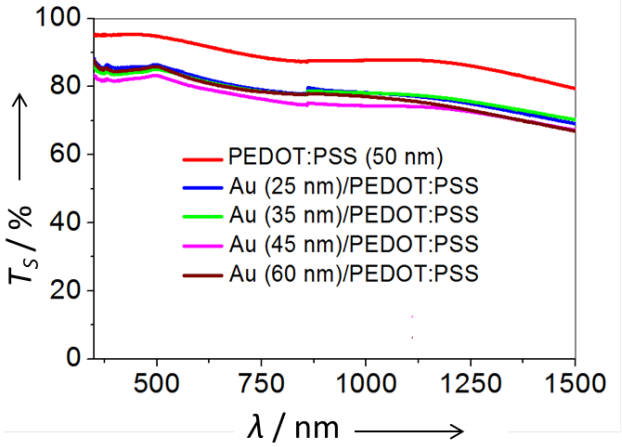

Figure S4. *Specular transmittance (T_S) from 350 to 1500 nm of Au network on top of PEDOT:PSS layer.*

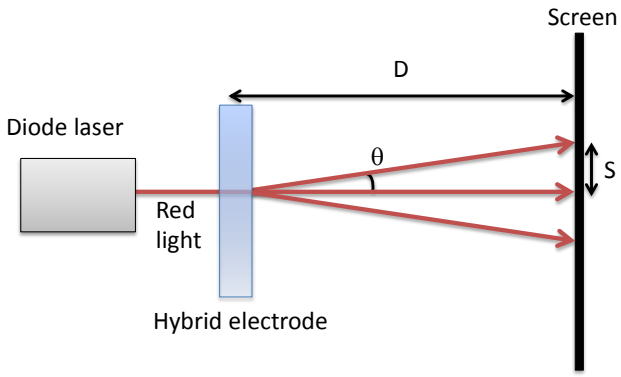

Figure S5. *Schematic illustration of the experimental setup for measuring angular distribution of diffusely scattered light through Au network/PEDOT:PSS electrodes.*

The angular distribution of diffusely scattered light is determined using a simple optical set up with a laser pointer illuminating the electrode surface. The scattered light is directed towards the screen and captured with a camera. The radial spread of the laser light spot is calculated using the following equation: Tan θ = S/D.

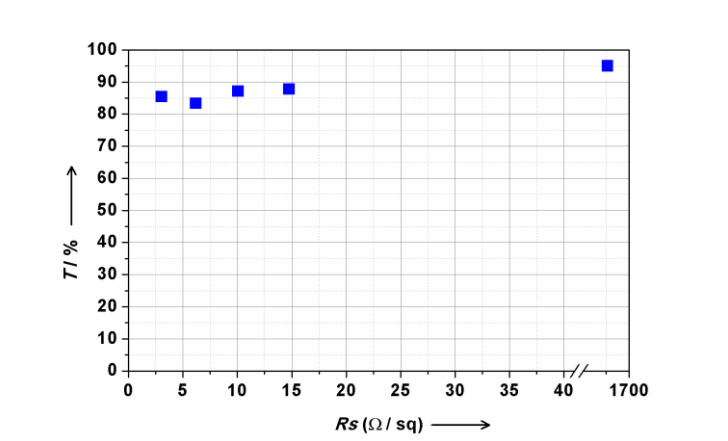

Figure S6. *Transmittance (T) at 550 nm versus sheet resistance (R_S) for Au network on top of PEDOT:PSS (blue squares).*

Table S1. *Summary of the solar cell parameters for the best Au devices measured using mask. Average values and standard derivations are given in Table below.*

cathode/ anode	V_{OC} **[mV]**	J_{SC} **[mA cm^{-2}]**	**FF [%]**	**PCE [%]**	R_S **[Ω cm^2]**	R_{SH} **[kΩ cm^2]**
ITO/Au opaque	570	8.23	61.1	2.86	2.61	1.18
ITO/Au network Front illumination	540	6.49	59.4	2.08	4.57	1.66
ITO/Au network Back illumination	540	5.83	63.1	1.99	4.63	2.02
Ag/Au network Front illumination	560	5.52	51.7	1.60	5.04	1.19
Ag/Au network Back illumination	580	4.45	44.6	1.15	5.66	0.58

Table S2. *Average and standard derivation of the Au solar cell parameters.*

cathode/ anode	V_{OC} **[mV]**	J_{SC} **[mA cm^{-2}]**	**FF [%]**	**PCE [%]**	R_S **[Ω cm^2]**	R_{SH} **[kΩ cm^2]**
ITO/Ag opaque (11 devices)	**491** (± 55)	**7.63** (± 0.39)	**56.7** (± 4.1)	**2.13** (± 0.38)	**3.05** (± 1.12)	**0.96** (± 0.42)
ITO/Ag network (12 devices)	**542** (± 7)	**6.87** (± 0.72)	**52.7** (± 5.5)	**1.95** (± 0.12)	**5.93** (± 2.56)	**1.03** (± 0.49)
ITO/Ag network (12 devices) Back illumination	**552** (± 7)	**5.94** (± 0.20)	**58.8** (± 2.4)	**1.93** (± 0.08)	**6.74** (± 2.04)	**1.68** (± 0.34)
Ag/Ag network (8 devices)	**541** (± 15)	**5.90** (± 0.44)	**45.8** (± 5.0)	**1.46** (± 0.14)	**6.67** (± 3.73)	**0.61** (± 0.37)
Ag/Ag network (8 devices) Back illumination	**562** (± 15)	**4.85** (± 0.79)	**44.7** (± 2.2)	**1.23** (± 0.25)	**8.00** (± 3.36)	**0.52** (± 0.04)

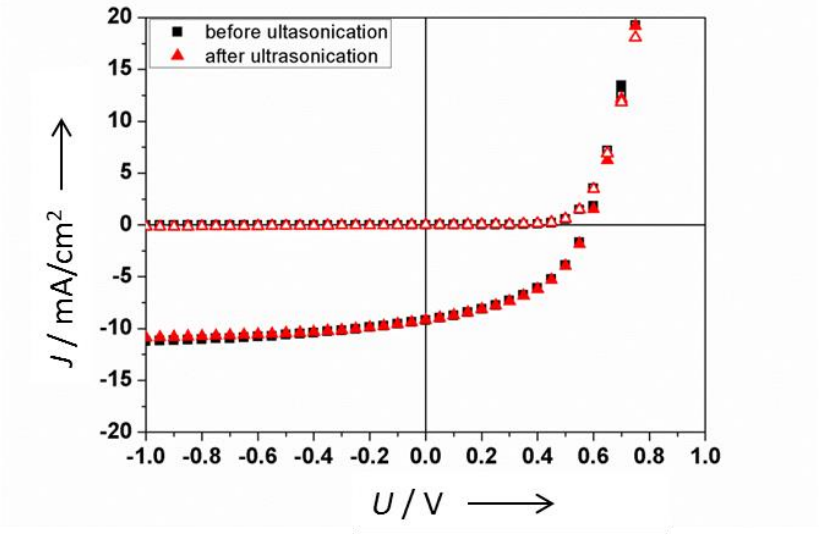

Figure S7. *J-V characteristics of a typical ITO / Ag opaque device before (black) and after 10 seconds ultrasonication in ethyl acetate (red).*

Table S3. *Average and standard derivation of the solar cell parameters for the three types of devices for both front and back illumination.*

cathode/ anode	V_{OC} **[mV]**	J_{SC} **[mA cm^{-2}]**	***FF*** **[%]**	**PCE [%]**	R_S **[Ω cm^2]**	R_{SH} **[kΩ cm^2]**
ITO/Ag opaque (10 devices)	**580** (± 7)	**8.73** (± 0.28)	**59.7** (± 1.8)	**3.03** (± 0.12)	**2.05** (± 0.56)	**1.36** (± 0.35)
ITO/Ag network (14 devices) Front illumination	**544** (± 11)	**6.71** (± 0.36)	**56.5** (± 3.7)	**2.06** (± 0.11)	**2.81** (± 0.83)	**1.00** (± 0.48)
ITO/Ag network (14 devices) Back illumination	**547** (± 10)	**6.01** (± 0.20)	**61.1** (± 2.0)	**2.01** (± 0.09)	**2.93** (± 0.87)	**1.40** (± 0.50)
Ag/Ag network (6 devices) Front illumination	**552** (± 10)	**5.80** (± 0.16)	**50.1** (± 2.8)	**1.61** (± 0.15)	**2.81** (± 0.82)	**0.63** (± 0.22)
Ag/Ag network (6 devices) Back illumination	**568** (± 15)	**5.99** (± 0.24)	**48.8** (± 4.6)	**1.67** (± 0.25)	**2.97** (± 0.80)	**0.62** (± 0.32)

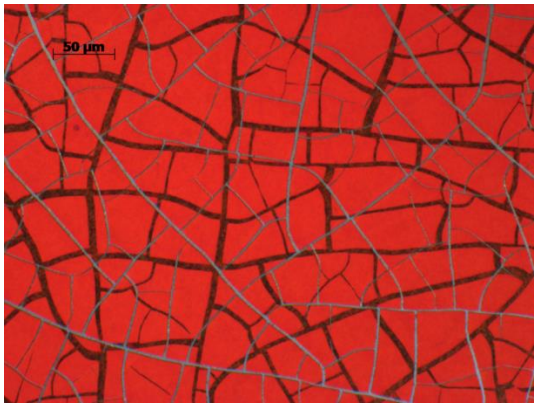

Figure S8. *Optical micrograph of Glass/Ag/ZnO/photoactive layer/PEDOT:PSS / Ag network device seen from the back side. Both front (black) and back (grey) network electrodes are visible.*

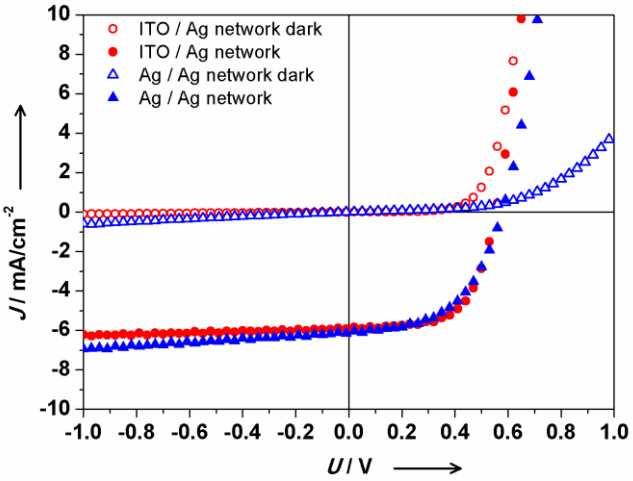

Figure S9. *J-V characteristics of ITO / Ag network device and Ag / Ag network device under back illumination.*

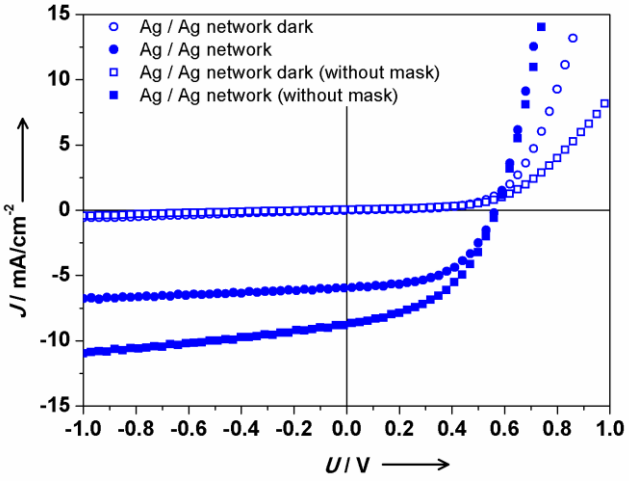

Figure S10. *J-V characteristics of Ag / Ag network device illuminated from front side using mask (circles) and without using mask (squares).*

Table S4. *Summary of the solar cell parameters for the best Ag / Ag network under front illumination.*

cathode/ anode	V_{OC} **[mV]**	J_{SC} **[mA cm^{-2}]**	***FF*** **[%]**	**PCE [%]**	R_S **[Ω cm^2]**	R_{SH} **[kΩ cm^2]**
Ag/Ag network With mask	560	5.90	54.4	1.80	4.22	1.01
Ag/Ag network Without mask	570	8.73	46.7	2.32	6.28	0.32

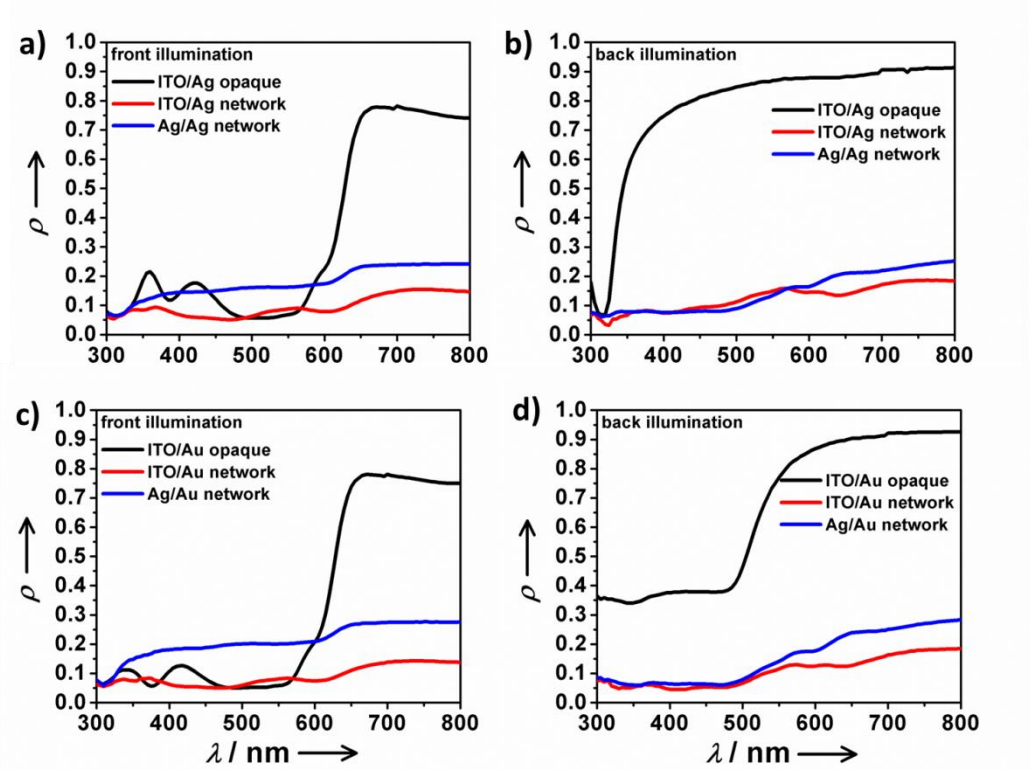

Figure S11. *Reflection spectra of the best devices with Ag back electrode (a) – front illumination, b) – back illumination) and Au back electrode (c) – front illumination, d) – back illumination).*

Comparing the front (a) and back (b) illumination for the ITO/Ag opaque device, it is clear, that in case of the front illumination the light is absorbed by the photoactive layer in the wavelength range 350 nm to 650 nm which lowers the reflection of the Ag opaque electrode compared to the back illumination, where a typical reflection of Ag is observed. For the semitransparent devices ITO / Ag network and Ag / Ag network the reflection is low in the whole wavelength range 300 nm to 800 nm for both, front (a) and back (b) illumination, due to the high transparency of this devices. Only the Ag / Ag network device exhibits a bit higher reflectance than the ITO / Ag network, due to the additional reflectance and light scattering of the Ag network compared to the ITO electrode. For the Au devices (c) and d)) a similar explanation is valid.

8 Technical Appendix

In this technical appendix the transient absorption spectroscopy (TAS) setup is briefly presented which was used to monitor the charge carrier recombination dynamics in chapter 3 and 4.

During the photoinduced charge generation process many intermediate states are involved such as singlet or triplet excited states, charge transfer states and finally charge separated states, so-called polaron states as mentioned in chapter 2. The knowledge of their transition rate constants and hence lifetime is important for understanding the fundamental processes. TAS is a powerful tool to monitor the various intermediate states, since they all exhibit specific optical transitions and TAS is able to resolve these optical transitions spectral as well as in time. TAS can be considered as the change in optical density ΔOD of a sample after photoexcitation provided by a short laser pulse. According to that, ΔOD can be calculated from Eq. 1, where OD is the steady state optical density of the sample and OD_{Exc} is the optical density of the sample after laser excitation. Using Lambert-Beer's law one can calculate the individual optical densities by measuring the respective light intensities, whereas I_0 refers to the light intensity without any sample, and I and I_{EXC} are the light intensity of the sample before and after laser excitation respectively Eq. 2. It is obvious, that I_0 cancels out after rearranging of Eq. 2 leading to Eq. 3. Consequently for calculating ΔOD it is enough to measure just I and I_{EXC}, whereas the both light intensities are proportional to the detector signal.

$$\Delta OD = OD_{EXC} - OD \qquad (1)$$

$$\Delta OD = log\frac{I_0}{I_{EXC}} - log\frac{I_0}{I} \qquad (2)$$

$$\Delta OD = log\frac{I}{I_{EXC}} \qquad (3)$$

The value of ΔOD can be either positive or negative. Positive ΔOD values are ascribed to the absorption species, which are created in consequence of the laser excitation pulse. Such species might be at early times excited states (excitons) such as singlet states $S_1,\ldots S_n$ or triplet states $T_1,\ldots T_n$, charge transfer (CT) states and at later times e.g. in organic photovoltaics (OPV) free charge carriers, or so-called polarons. Negative ΔOD values are ascribed to either stimulated and spontaneous emission of the excited states or to ground state bleaching which

corresponds to the reduction in the concentration of ground states after laser excitation. Depending on the time range of interest two different measurement setups are common: For time scales <1 ns a pump and probe technique is used, where a laser pump pulse serves for sample excitation and a laser probe pulse for sample transmittance measurement. The time resolution is achieved by varying the time delay between pump and probe pulse. At later time scales in the range of nano- to microseconds a laser pump pulse excites the sample, whereas for the sample transmittance measurement a continuous wave from a tungsten or a xenon lamp is used. Both techniques are presented recently in the context of TAS for polymer solar cells by Ohkita *et al.*[1]

In this thesis we focus in chapter 4 and 5 on non-geminate recombination dynamics of charge carriers in OPV, which dominates in the nanosecond to microsecond time scale. Our TAS setup is based on a Laser Flash Photolysis (LFP) LKS80 Spectrometer provided by Applied Photophysics Ltd.. The setup is shown schematically in Figure 1a.

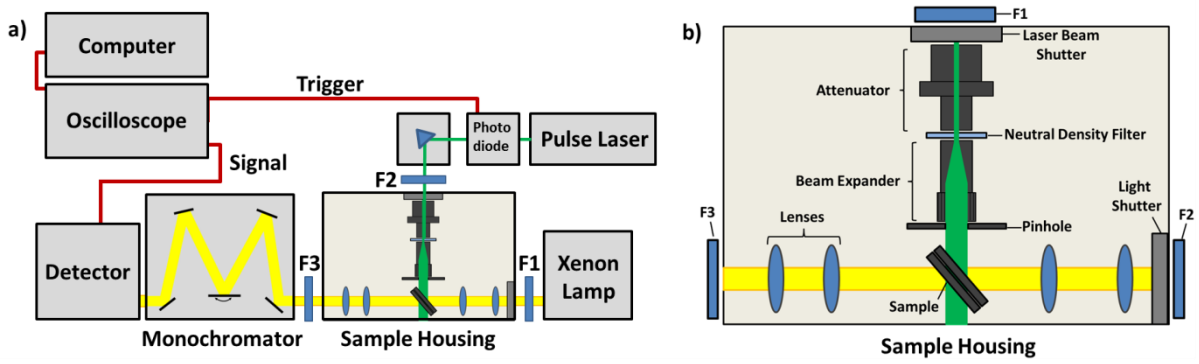

Figure 1. *a) Illustration of transient absorption spectroscopy setup for the nano- to microsecond time range with all important components emphasizes the laser excitation pulse (green) and the white light beam (yellow) as well as important electrical wire connections (red) and b) enlargement of the same sample housing including the optical components as described in the text. F1, F2 and F3 refer to suitable filters as mentioned in the text.*

The pump laser pulse for sample excitation is generated by a laser system (Quantel) consisting of a Q-switched Brilliant B Nd:YAG laser having a fundamental wavelength of 1064 nm, a second (532 nm) and third (355 nm) harmonic oscillator, which pumps an optical parametric oscillator (OPO – Rainbow). This allows us to excite the sample at any wavelength either between 410 and 680 nm using the signal of the OPO and between 720 and 1200 nm using the idler of the OPO. For organic photovoltaics (OPV) the precise choice of excitation wavelength is of special interest, because it allows separate excitation of either the donor or the acceptor. The laser pulse width after the OPO is in the range of 4 to 8 ns whereas the pulse energy is between 30 to 45 mJ (signal) depending on the laser wavelength. The photodiode

after the laser system provides the trigger signal for the oscilloscope, whereas the laser beam is coupled into the sample housing using a prism. In Figure 1b the sample housing is enlarged to discuss the individual components in detail. The short pass filter F1 has a cut-off wavelength of around 700 nm and blocks the residual fundamental wavelength at 1064 nm. This is especially important for measurements in the NIR range, to avoid any scattering of the fundamental wavelength towards the detector. The laser beam shutter is software controlled and enables automated measurements with and without laser excitation. In the next step the laser pulse energy is reduced by a laser beam attenuator consisting of two air-spaced Glan-Taylor calcite polarizers. By the rotation of one of the polarizer the transmission can be tuned from maximum transmission at 0° to zero transmission at 90°. However, in the region between 70° to 90° the intensity profile of the laser beam is getting unequal due to light scattering effects and hence a neutral density Filter is placed after the attenuator to reduce the pulse energy down to several µJ. The laser beam expander (Galilean type telescope) enlarges the beam diameter for an optimal overlap between laser pulse and white light beam to achieve a sufficient signal to noise ratio. A pinhole allows the adjustment of a desired beam diameter and cuts the beam in shape. Finally, the laser beam excites the sample, which is place in approximately 45° with respect to the laser beam and the white light beam. The sample itself is usually measured under nitrogen in a suitable sample holder. The energy of the laser pulse is measured at the place of the sample using a QE25 energy detector (Gentec). For determination of ΔOD according to Eq. 3 the light intensity with (I) and without (I_{EXC}) laser excitation need to be measured. For that a stabilized xenon lamp provides a white light beam, which passes the sample in the sample housing (Figure 1a). The filter F3 blocks any scattered light from the excitation laser pulse. A monochromator enables the selection of the desired wavelength and finally a detector measures the light intensities I and I_{EXC}. The detector is connected with an oscilloscope (DSOS104A - Agilent) for data acquisition, which than forwards the data to a computer for data analysis and storage. Depending upon the measurement wavelength range one has to select the right grating in the monochromator as well as the right detector. Two detector types are available, a photomultiplier tube (PMT – R928 – Hamamatsu Photonics) for the visible (VIS) wavelength range between 300 to 850 nm and an indium gallium arsenide (InGaAs – HCA-S-200M-IN – Femto) photodiode for the near infrared (NIR) wavelength range between 870 to 1700 nm. Whereas light intensity provided by the xenon lamp is high enough for the NIR detector, the PMT requires much higher light intensities for sufficient photocathode currents. Therefore, the xenon lamp is electrically pulsed for few milliseconds by a capacitor discharge. This white light flash leads

to an increase in light intensity by more than 35 times in the VIS range. The TAS measurement including the laser excitation is carried out within the constant plateau of the white light flash [2]. The white light flash is a characteristic for the classical LFP setup. However, in OPV the charge carrier recombination dynamics is highly dependent on the charge carrier density of the sample and the white light flash indeed leads to an increase in charge carrier density already before the laser excitation. Therefor the sample has to be protected from any light which is not needed for measurement. This can be realized by using a second monochromator on the right side of the sample just between the sample housing and the xenon lamp. In this case, both monochromators are set to the same wavelength. Another method is to use a suitable Filter F2 as seen from Figure 1b. A comparison between both methods for the transient absorption monitored at 700 nm of a P3HT:PBI 1 (1:2 by weight) blend is shown in Figure 2b. Figure 2a shows the chemical structures of the donor polymer P3HT and the perylene bisimides (PBI) PBI 1 or PBI 2.

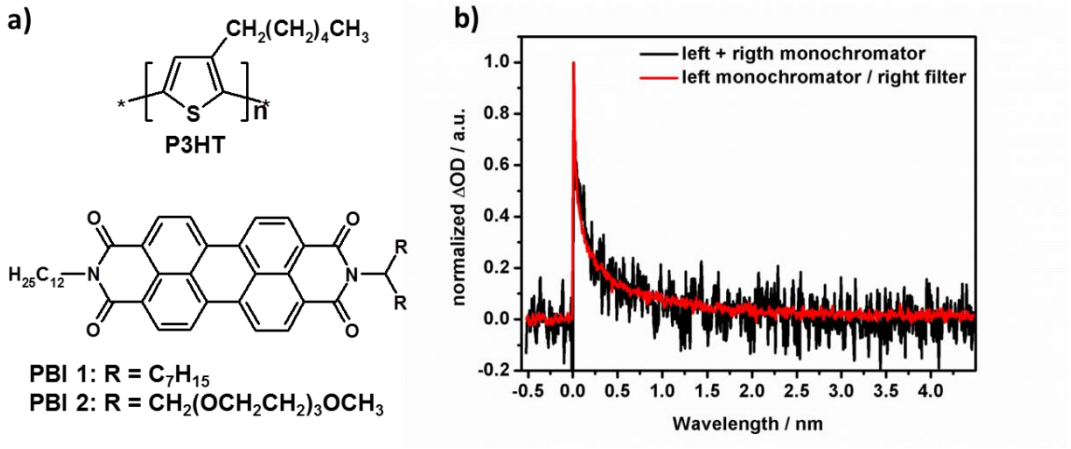

Figure 2. *a) Chemical structures of P3HT, PBI 1 and PBI 2 used for blend samples. b) The comparison in normalized transient absorption decay using an additional monochromator between the sample housing and the xenon lamp (black) versus using a long pass filter F2 instead, having a cut-on wavelength of 550 nm. The transient absorption decay was taken at 700 nm for a P3HT:PBI 1 (1:2 by weight) blend after excitation at 500nm with 850 µJ / cm² and 50 averages.*

Both measurements in Figure 2b show similar decay dynamics, however, the noise is much higher, when using a monochromator. Here the second monochromator between sample housing and xenon lamp reduces the overall light intensity for the PMT leading to an increase in noise. In contrast to that, using a suitable long pass filter with a cut-on wavelength at 550 nm improves the signal to noise ratio enormously. We therefore decided to measure with suitable long pass filters F2 for protecting the sample from unnecessary light exposure. However, the question of using a monochromator or a long pass filter at this place always

needs to be answered with respect to the desired measurement wavelength. Especially the measurement in the ground state bleach region might require the use of two monochromators. For analysis of recombination dynamics in OPV most important is the positive transient absorption of the polaron, which usually occurs red shifted from the ground state absorption of the blend, e.g. for many donor polymers in the NIR region. In this case it is often sufficient to measure with a suitable long pass filter F2. However, the choice of the right Filter F2 is important to ensure that no light from the xenon lamp is absorbed by the blend system. This is demonstrated in figure 3 using a P3HT:PBI 2 (1:2 by weight) blend.

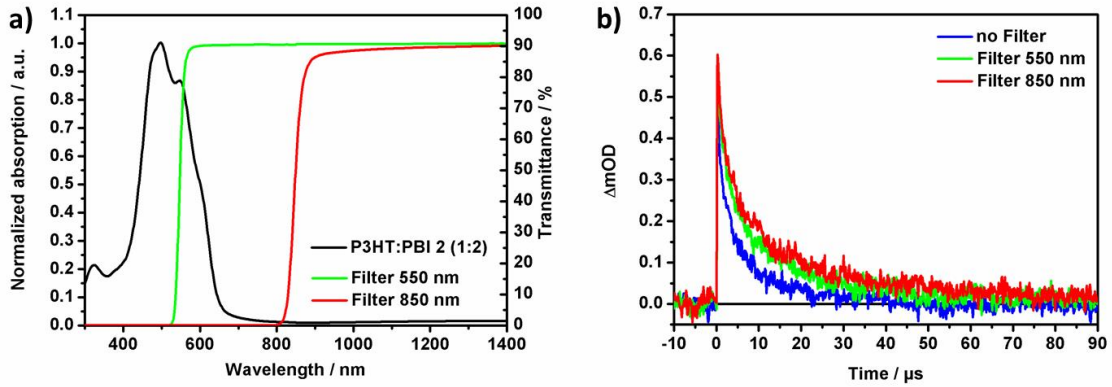

Figure 3. *a) Normalized absorption of P3HT:PBI 2 (1:2 by weight) blend (black) and transmittance spectra of long pass filters F2 having a cut-on wavelength of 550 nm (green) and 850 nm (red). b) Transient absorption decay dynamics of the same blend at 970 nm after excitation at 500nm with 130 µJ / cm^2 and 100 averages using either the respective long pass filters F2 or without any filter.*

As seen from Figure 3a, the blend light absorption is between 400 to 650 nm. The transmittance spectra of two long pass filter F2 are shown as well having a cut-on wavelength of either 550 nm (filter 550 nm) or 850 nm (filter 850 nm). Using the filter 550 nm the sample partially absorbs light between 550 nm and 650 nm, whereas using filter 850 nm, no light is absorbed by the sample. The light absorption leads to charge carrier generation prior the laser excitation and hence an increase in charge carrier density. This might accelerate the decay dynamics by using filter 550 nm (green) compared to filter 850 nm (red) as seen from Figure 3b. This effect is even enhanced, when no filter is used (blue). Especially in the VIS range, where pulsing of the lamp is needed, a suitable long pass filter F2 has to be taken in order to avoid accelerated decay dynamics due to the high light intensities.

References

[1] Ohkita, H.; Tamai, Y. ; Benten, H. ; Ito, S. Transient Absorption Spectroscopy for Polymer Solar Cells, *IEEE Journal* **2015**, doi: 10.1109/JSTQE.2015.2457615

[2] User Manual LKS80 Spectrometer provided by Applied Photophysics Ltd., September 2012

9 List of Publications

Rao, K. D. M.; **Hunger, C.**; Gupta, R.; Kulkarni, G. U., Thelakkat, M., A cracked polymer templated metal network as a transparent conducting electrode for ITO-free organic solar cells. *Phys. Chem. Chem. Phys.*, **2014**, *16*, 15107 –15110.

Hunger, C.; Rao, K. D. M.; Gupta, R.; Singh, C. R.; Kulkarni, G. U., Thelakkat, M., Transparent Metal Network with Low Haze and High Figure of Merit applied to Front and Back Electrodes in Semitransparent ITO-free Polymer Solar Cells. *Energy Technol.*, **2015**, *3* (6)**,** 638–645.

10 Danksagung / Acknowledgment

An dieser Stelle möchte ich mich bei all denen bedanken, die durch ihre Unterstützung und Begleitung zum Gelingen dieser Arbeit beigetragen haben.

Zuerst und ganz besonders möchte ich mich bei meinem Betreuer Herrn Prof. Dr. Mukundan Thelakkat für die Möglichkeit bedanken, die Arbeit bei ihm in dem spannenden Themenumfeld der organischen Photovoltaik anzufertigen. Seine Offenheit gegenüber neuen Ideen und Konzepten schätze ich sehr, welche auch maßgeblich zur Entstehung dieser Dissertation beigetragen. Danken möchte ich ihm auch für die gute Betreuung der Arbeit und die hilfreichen und interessanten Diskussionen, auch außerhalb der Forschung. Außerdem bin ich ihm dankbar für die zahlreichen nationalen und internationalen Konferenzen und Projekttreffen an denen ich teilnehmen durfte sowie für zwei Forschungsaufenthalte an der TU Einhoven / Niederlande und der University of Madras / Indien.

At this point I also would like to thank my cooperation partners at the TU Eindhoven Prof. René Janssen, Dr. Martijn Wienk and Dr. Weiwei Li for the possibility to work in their laboratory and to learn a lot details about organic solar cell fabrication. Likewise, I thank Prof. Dr. Giridhar U. Kulkarni and Dr. Mallik Arjun Rao from the JNCASR Bangalore for the fruitful collaboration regarding the transparent metal network electrode. Many thanks also to Prof. Dr. Perumal Ramamurthy and his workgroup from the University of Madras for a great time and research stay in India and making me familiar with laser flash photolysis. In this context I also would like to greatly thank Peter Lachmann from Applied Photophysics for helping me to modify the laser flash photolysis setup for our purpose.

Herzlichen Dank an meine ehemaligen und aktuellen Kollegen der Arbeitsgruppe Angewandte Funktionspolymere und des Lehrstuhls Makromolekulare Chemie I für die freundschaftliche Aufnahme sowie angenehme & hilfsbereite Atmosphäre und einer schönen und erlebnisreichen Zeit auch außerhalb der Laborräume. Für die Unterstützung und hilfreichen Diskussionen bei verschiedenen Messungen möchte ich mich besonders bei Dr. Tanaji Gujar, Dr. Chetan Raj Singh, Jonas Mayer, David Heinrich und Andreas Schedl bedanken, ebenso wie bei Martina Schmidt für die sehr nette und angenehme Büroatmosphäre. Außerdem möchte ich bei Petra Weiß, Christina Wunderlich und Claudia Geier für die Erledigung vielerlei organisatorischen und bürokratischen Angelegenheiten

während der ganzen Zeit herzlich bedanken. Ihr alle habt direkt oder indirekt zur Entstehung der Arbeit beigetragen – vielen herzlichen Dank dafür!

Dem Graduiertenkolleg 1640 der Deutschen Forschungsgemeinschaft danke ich außerdem für die finanzielle Unterstützung.

Vielen lieben Dank auch meinen Freunden genauso wie meiner Familie, die mich stets unterstützt hat und die ganze Arbeit, wenn auch aus gewisser räumlicher und fachlicher Entfernung, sehr interessiert verfolgte. Ganz besonders möchte ich mich auch bei meiner lieben Hana bedanken! Ohne Dich wäre alles nur halb so schön und doppelt beschwerlich. Von Herzen danke ich Dir für Dein Verständnis und Deinen Rückhalt besonders auch in der Endphase dieser Arbeit.

Vielen Dank!

11 Erklärung

nach der Promotionsordnung der BayNAT in der Fassung vom 20. März 2014

(§ 8 S. 2 Nr. 6 PromO)

Hiermit erkläre ich mich damit einverstanden, dass die elektronische Fassung meiner Dissertation unter Wahrung meiner Urheberrechte und des Datenschutzes einer gesonderten Überprüfung hinsichtlich der eigenständigen Anfertigung der Dissertation unterzogen werden kann.

(§ 8 S. 2 Nr. 8 PromO)

Hiermit erkläre ich eidesstattlich, dass ich die Dissertation selbständig verfasst und keine anderen als die von mir angegebenen Quellen und Hilfsmittel benutzt habe.

(§ 8 S. 2 Nr. 9 PromO)

Ich habe die Dissertation nicht bereits zur Erlangung eines akademischen Grades anderweitig eingereicht und habe auch nicht bereits diese oder eine gleichartige Doktorprüfung endgültig nicht bestanden.

(§ 8 S. 2 Nr. 10 PromO)

Hiermit erkläre ich, dass ich keine Hilfe von gewerbliche Promotionsberatern bzw. -vermittlern in Anspruch genommen habe und auch künftig nicht nehmen werde.

.....

Ort, Datum, Unterschrift